MESOSIDERITE FORMATION: REDOX FROM THE METAL PERSPECTIVE

by

LINDSAY R. CAVES

Bachelor of Science, 2016
University of Tennessee
Knoxville, TN.

Submitted to the Graduate Faculty of the
College of Science and Engineering
Texas Christian University
in partial fulfillment of the requirements
for the degree of

Master of Science

August 2019

Acknowledgements

I would first like to thank my thesis advisor, Dr. Rhiannon Mayne, for providing a research project that allowed me to study a unique group of meteorites and broaden my knowledge of planetary geology. She invested a great deal of her time teaching me and always reminded me to have confidence in myself. She fueled my motivation with many Starbucks drinks and never let me forget to take a break from working to eat some lunch.

I would also like to thank my committee member, Dr. Richard Hanson, for expanding my understanding of geology and for creating an encouraging classroom environment where I felt comfortable asking any question that came to mind. His ample amount of patience and dry sense of humor was essential for turning me into the geologist that I am today. I thank him for choosing me as his field assistant and providing me with the opportunity to stare at ancient Namibian volcanic rocks face-to-face. Even though he made me sleep on the African ground for the better part of six weeks, it was an experience I will cherish forever.

Next, I would like to thank my committee member, Dr. Timothy McCoy, for the considerable amount of his free time spent on brainstorming ideas and writing with me. These research findings would not be nearly as interesting without his help and guidance. I would also like to thank him for his attempt at convincing me that I am "the 3rd smartest person to work on mesosiderites".

Lastly, I would like to thank my family and friends that have given me an enormous amount of emotional support over the past two years. A special thanks goes to my boyfriend, Tyler Fee, for keeping my sanity intact and enduring my countless number of mental breakdowns. I also give a huge thanks to my aunt, Rebecca Winter, for opening her home to me when my teaching assistant stipend finally dwindled away.

Table of Contents

List of Figures

List of Tables

1.0 Introduction

During early Solar System history, planetesimals collided and consolidated into planetary bodies. Asteroids are the smaller bodies that remained after planetary formation. Because of their size, asteroids cooled much more quickly than the terrestrial planets. In fact, some terrestrial planets exhibit active geologic processes, such as volcanism (Earth and Venus) and tectonism (Earth, Mars, and Mercury), which indicate that these planets still have hot interiors. These processes continue to erase terrestrial planets' earliest history by constantly reshaping and reprocessing their surfaces and interiors. Asteroids were not subject to this activity after their formation, because of their fast cooling rate; they have remained almost unaltered since early Solar System history. As a result, the study of meteorites derived from asteroids provides insights to a time period that terrestrial planets do not preserve, advancing our understanding of planetary formation and, in turn, Solar System evolution.

Asteroidal meteorites are widely studied; however, that does not mean they are all well understood. The mesosiderites are an example of such a group labeled as enigmatic. Mesosiderites are breccias consisting of core (metal) and crustal (basaltic) material, with little to no mantle material present (Powell, 1971; Mittlefehldt *et al.*, 1998). It is hard to model the formation of a group that consists of such a mixture. The research presented here examines the metal within mesosiderites to better understand the processes that occurred during the metal-silicate mixing phase of their formation. This, in turn, elucidates processes that took place during the early history of the Solar System while planetary bodies were still forming.

2.0 Background

2.1 Classification Schemes

Mesosiderites are composed of roughly equal parts Fe-Ni metal and a crustal silicate component, which consists of brecciated igneous lithologies and mineral clasts in a fine-grained fragmental igneous matrix (Powell, 1971; Floran, 1978). The primary minerals within the basaltic clasts of mesosiderites are low-Ca pyroxene, plagioclase, and Fe-Ni metal; accessory minerals include olivine, troilite, tridymite, chromite, apatite, whitlockite, merrillite, augite, ilmenite, and rutile (Powell, 1971; Floran, 1978).

Mesosiderites have been classified in several different ways. Powell (1971) classified mesosiderites based on their mineralogy and textural features. He assigned mesosiderites to three subgroups distinguished by degree of brecciation, recrystallization, and the presence of reaction textures between silicates. This scheme was later revised to focus more on the metamorphism that each mesosiderite has experienced by defining three metamorphic subgroups (1-3) and a fourth subgroup labeled as impact melt breccias (4) (Table 1) (Floran, 1978; Hewins, 1984). Hewins (1984, 1988) further divided mesosiderites into three classes (A, B, and C) by considering the modal mineralogy of the silicate portion (Table 2; Fig. 1). In the current literature, mesosiderites are classified by combining both schemes. Samples labeled as anomalous are not assigned to either a class or number because of unique characteristics.

Table 1. Revised criteria for mesosiderite classification (Powell, 1971; Floran, 1978).

Metamorphic			Igneous
Subgroup 1	**Subgroup 2**	**Subgroup 3**	**Subgroup 4**
Slightly recrystallized	Moderately recrystallized	Highly recrystallized	Impact melts
Pronounced cataclastic textures	Cataclastic textures recognizable in thin section	No cataclastic angularity at thin section scale, brecciation only seen macroscopically	Clast-rich, igneous and metaigneous textures; also contains individual clasts displaying impact-melt origin petrographic features
Very fine-grained matrices and angular clasts, many grains less than 10 μm	Fine-grained material coaser than subgroup 1, most grains exceed 10 μm	No extremely fine-grained silicates, most grains exceed 100 μm	Silicate portions display igneous textures similar to terrestrial basalts
Textural heterogeneity obvious on microscopic scale	Textural heterogeneity observable on microscopic scale, but less pronounced	Microscopic silicate textures relatively homogenous	
Silicate fragment grain boundaries not intergrown; sutured contacts only in lithic fragments	Some sutured contacts occur between smaller silicate grains; silicate grain intergrowth visible between small matrix grains and large fragments	Silicate grains of all sizes display interlocking boundaries	
Abundant pigeonite; inversion to opx* not apparent	Minor abundance of pigeonite; displays partial inversion to opx*	Accessory pigeonite only; shows thorough inversion to opx*	
	Distinctive pyx/plag* poikiloblastic textures poorly developed	Distinctive pyx/plag* poikiloblastic textures well developed	
Olivine reaction rims vary significantly in subgroups and throughout individual samples, although subgroup 1 displays characteristic fine-grained mantles			

*opx – orthopyroxene, pyx – pyroxene, plag – plagioclase

Table 2. Silicate modal mineralogy criteria for mesosiderite petrologic classes A/B/C (Hewins, 1984, 1988).

Class A	Class B	Class C
Greater amount of plagioclase and cpx* than opx*; basaltic in composition	Greater amount of opx* than plagioclase; more ultramafic in composition	Contains almost exclusively opx*; RKPA 79015 is the sole sample of this class

*cpx – clinopyroxene, opx – orthopyroxene

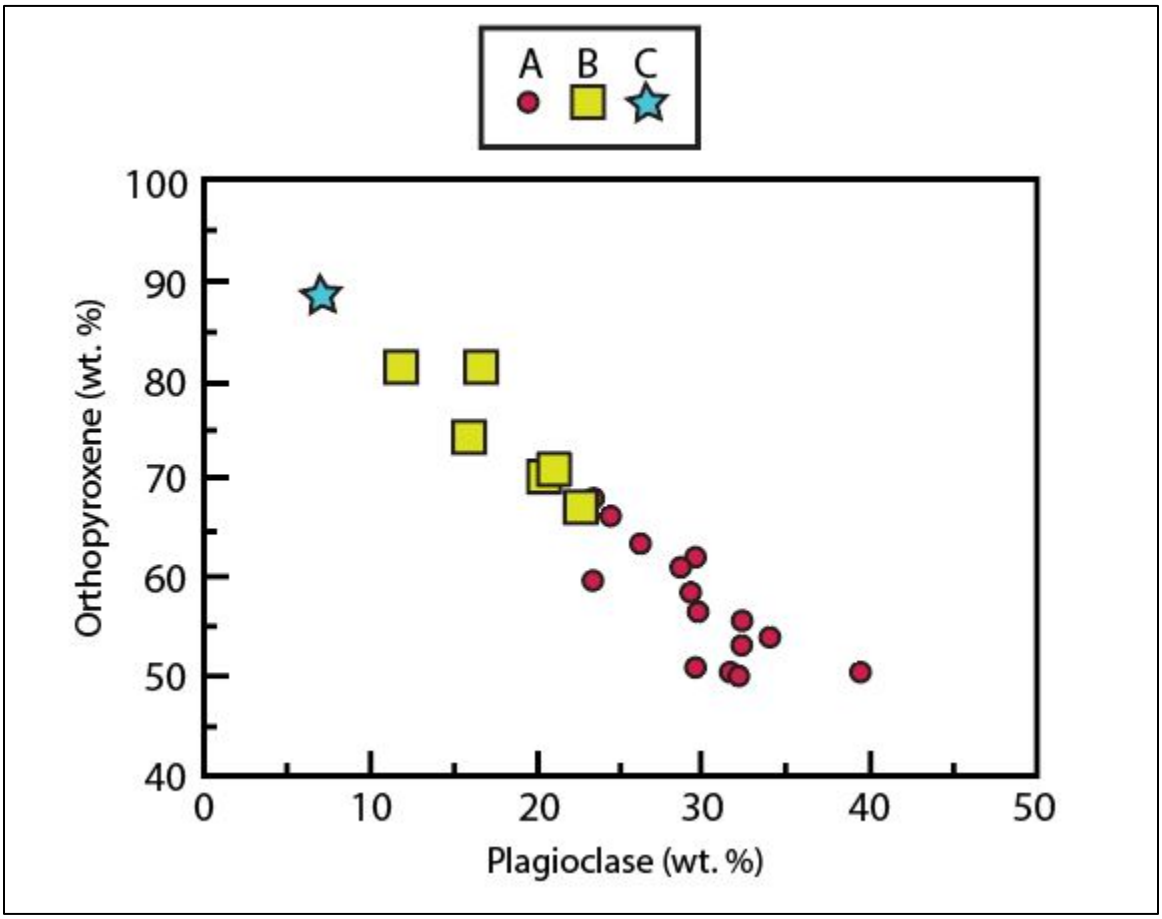

Figure 1. Orthopyroxene wt. % vs. plagioclase wt. % for mesosiderites groups A, B, and C. Class A mesosiderites show more basaltic compositions compared to class B, which shows ultramafic compositions. Adapted from Mittlefehldt *et al.* (1998).

2.2 Proposed Relationships to Other Meteorite Groups

Understanding where certain meteorites originated from and how they formed allows us to determine how different planetary bodies evolved and what processes took place during and after their formation. Linking different groups of meteorites to the same parent body provides a more detailed story of how the asteroids and planets evolved over time. Mesosiderites have been proposed to be genetically related to several groups, as detailed below.

2.2.1 Insights from Silicate Compositions

Previous studies have proposed that mesosiderite silicates are genetically related to the howardite, eucrite, and diogenite (HED) meteorite clan, due to strong similarities between their mineralogy, textures, and bulk compositions (Powell, 1971; Floran, 1978; Rubin and Jerde, 1987; Rubin and Mittlefehldt, 1992; Mittlefehldt *et al*., 1998). The HEDs are the largest group of crustal igneous meteorites and are believed to originate from the asteroid 4 Vesta. However, there are fundamental differences between the compositions of HED and mesosiderite silicates, such as the Fe-Mn-Mg systematics in pyroxene – possible explanations for this are discussed in section 2.3.2.

Although mesosiderite silicates share strong geochemical similarities to those in basaltic and cumulate eucrites, basaltic clasts of mesosiderites show more complex rare-earth-element (REE) patterns (Fig. 2) (Rubin and Mittlefehldt, 1992; Mittlefehldt *et al*., 1998). REE patterns give us a better understanding of the evolution of parental magmas. Different concentrations/depletions of trace elements, given relative to a standard (chondrites), can determine how primitive or evolved the source magma was at the time of crystallization. For example, a low percent partial melt will produce a magma that is concentrated in light rare-earth-elements (LREE) and depleted in heavy rare-earth-elements (HREE), because LREE are less compatible and preferentially partition into the melt. The residue left behind will then be depleted in LREE and, under the right conditions,

will produce partial melts that have lower concentrations of LREE than the initial partial melt. This causes separate generations of rocks on one parent body to produce differing REE patterns.

The major element compositions of some basaltic clasts in mesosiderites lie within the range of basaltic eucrites and produce REE patterns that are nearly identical to basaltic eucrites (*e.g.*, Mount Padbury basalt clast), suggesting they could be related (Fig. 2) (Mittlefehldt, 1979). However, many mesosiderite basaltic clasts differ in major element composition and show REE element patterns distinct from basaltic eucrites (e.g. Patwar basalt clast RV-02) (Fig. 2) (Mittlefehldt, 1979). Some mesosiderite gabbroic clasts are similar in major and trace element compositions to cumulate eucrites (e.g. Vaca Muerta pebble 5) (Fig. 2) (Mittlefehldt *et al.*, 1998); however, cumulate eucrites show more heterogeneity within their major and trace element compositions making it difficult to determine a relationship with the mesosiderite gabbroic clasts (Mittlefehldt *et al.*, 1998). Many mesosiderite gabbroic clasts are similar in major element composition to cumulate eucrites but are strongly depleted in LREE and exhibit extreme positive Eu anomalies (e.g. Vaca Muerta pebble 18) (Fig.2) (Mittlefehldt *et al.*, 1998). In general, some mesosiderite basaltic and gabbroic clasts are indistinguishable from known eucrites while others suggest a unique petrogenetic history.

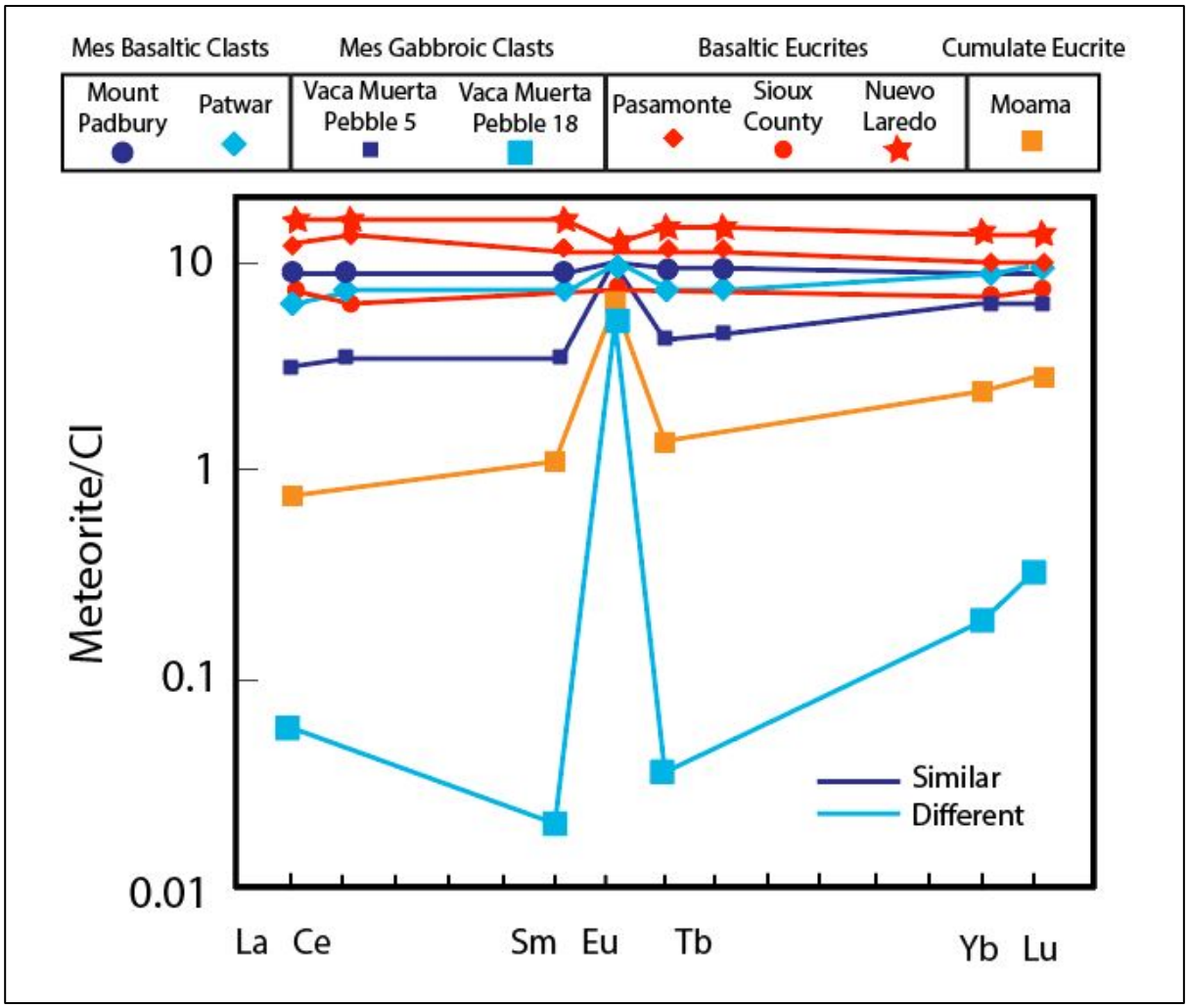

Figure 2. The mesosiderite basaltic clast in Mount Padbury shows a REE pattern similar to basaltic eucrites, but the Patwar basaltic clast displays a pattern unknown to those meteorites. The REE pattern of Vaca Muerta pebble 18 is strongly depleted in LREE compared to cumulate eucrites. Although some mesosiderite clasts are nearly identical to eucrites, these differences suggest they are not petrogenetically related to eucrites. Mesosiderites: Mount Padbury, Patwar, Vaca Muerta. Eucrites: Sioux County, Pasamonte, Nuevo Laredo, and Moama. All data is normalized to CI-chondrite values from McDonough and Sun (1995). Adapted from Mittlefehldt *et al*. (1998).

Oxygen isotopic studies can link, or separate, different classes of meteorites based on the isotopic reservoir from which their parent bodies formed. There are three stable isotopes of oxygen: ^{16}O, ^{17}O, and ^{18}O. It is thought that the proportions of these isotopes varied depending on location within the protoplanetary disk. As a result, each planetary body has a unique oxygen isotope composition, which was dictated by its location during its formation. Fractionation can cause the proportion of isotopes to change through chemical and physical processes; however, this fractionation behavior is well understood and compositions of meteorites from a single parent body (*e.g.*, the HEDs) will plot on a mass fractionation line, which is determined by plotting oxygen isotope abundances of samples relative to a standard. Different classes of meteorites that fall along the same fractionation line are suggested to have formed from either the same parent body, or parent bodies that formed in similar environments within the protoplanetary disk (Clayton, 2005). Greenwood *et al.* (2006) coupled oxygen isotope analyses with laser assisted fluorination techniques to reveal small variations that otherwise could not have been seen; for example, prior to this technique the HEDs, pallasites, and mesosiderites could not be distinguished from one another (Clayton, 2005). The results of Greenwood *et al.* (2006) showed no distinct difference in the mass fractionation lines between the mesosiderites and the HED clan of meteorites (Fig. 3) but were able to differentiate the pallasite grouping as separate. This suggests that the HEDs and mesosiderites could be genetically related.

The HED clan is believed to originate from the asteroid 4 Vesta. Initial evidence of the HED-Vesta connection came from the spectral study McCord *et al.* (1970), which showed that the visible/near-infrared (VISNIR) reflectance spectrum of Vesta was similar to eucrites of the HED clan of meteorites. Spectral studies of the asteroid belt, *e.g.* Wisdom (1985), have shown that Vesta has a unique spectrum, which strengthened the argument for Vesta as the HED parent body. In

addition, the NASA Dawn mission orbited Vesta for 14 months, beginning in July 2011. The results from Dawn significantly strengthened the hypothesis that the HEDs originated from Vesta as it identified all three as lithologies on the surface (McSween *et al*., 2013). The lack of meteorites representing samples of asteroid mantles (olivine-rich achondrites) furthered the argument that the HEDs originated from Vesta, because the basaltic crust sampled by the HEDs must still be intact on a differentiated asteroid (Consolmagno and Drake, 1977). However, Wasson and Wetherill (1979) noted that Vesta is not near to any resonances within the main asteroid belt that could deliver fragments to Earth, making a Vestan origin for HEDs dynamically unlikely. The discovery of vestoids, smaller asteroidal bodies with similar spectral characteristics to Vesta, located near to the 3:1 resonance provided a solution for this problem (Binzel and Xu, 1993; Lazarro *et al.*, 2000; Hardersen *et al*., 2004; Sunshine *et al*., 2004; Roig *et al*. 2008). If the mesosiderites originated from the HED parent body, there should be spectral evidence of their existence on Vesta or the vestoids. However, Dawn's Gamma Ray and Neutron Detector (GRaND) mapping of specific elements, *e.g*. Fe, Mg, Si, on Vesta shows no evidence of a concentration of Fe, which would be expected if the metal-rich mesosiderite material was present (Prettyman *et al*., 2012). Therefore, it is more likely that the mesosiderites did not originate from the HED parent body, but instead, formed on a body with a similar composition and petrogenesis to the asteroid 4 Vesta.

A recent study suggested that the HED clan of meteorites originated from the IIIAB iron parent body due to a strong correlation between their O and Cr isotopes (Wasson, 2013). Wasson states that this evidence is more compelling than the spectral evidence received from the Dawn mission, which promoted 4 Vesta as the HED parent body. However, due to the evidence presented above, the consensus of the scientific community is that the HEDs and IIIABs are from separate parent bodies.

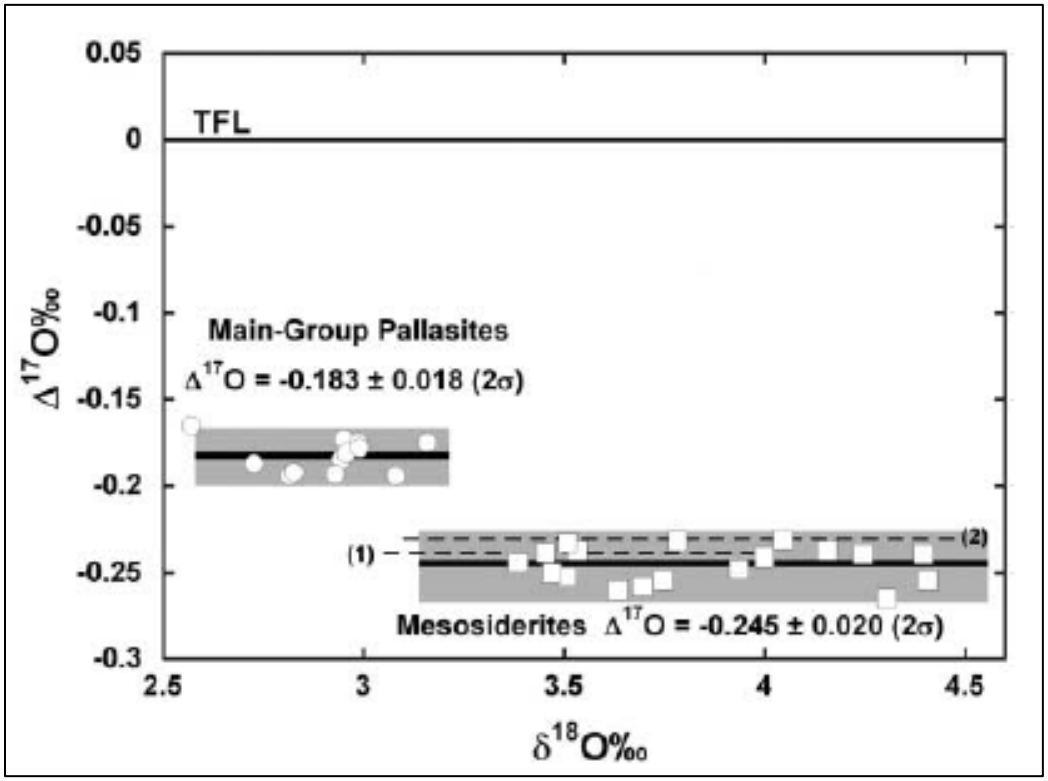

Figure 3. Oxygen-isotope plot comparing mesosiderites to main-group pallasites and HEDs. Dashed lines (1) and (2) represent HED meteorite data that plot within the 2σ error bar of mesosiderites (gray shaded box). TFL represents the terrestrial fractionation line. Deviation from the TFL line shows that these meteorites originated from bodies formed in different comsochemical environments (Greenwood *et al.*, 2006).

2.2.2 Insights from Metal Compositions

Data from Wasson *et al.* (1974; 1998) and Hassanzadeh *et al.* (1990) show that the mesosiderite metal compositions fall within IIIAB iron compositions, which indicates a relationship between the mesosiderite metal and the IIIAB irons. However, like the silicates, the metal compositions of mesosiderites show some distinct differences when studied in detail. IIIAB irons are meteorites composed mostly of metal that was molten in its early history. These iron meteorites are proposed to have formed by fractional crystallization of a core inside a planetary body (Wasson, 1999; Chabot and Drake, 1999). This formation mechanism is supported by the magmatic trends seen within their siderophile element contents, *e.g.* variation of Ir with little variation in Ga contents (Fig. 4). The mesosiderites do not show similar magmatic trends, and instead, the metal in class A and B samples contains relatively constant Ir/Ni ratios with varying Ga concentrations (Fig. 4). The sole member of mesosiderite class C, RKPA 79015, has been classified as anomalous due to the lower Ir/Ni ratio of its metal compared to class A and B mesosiderites. Studies have suggested differences in Ga concentrations could be a result of reactions taking place between the metal and the silicate phases in mesosiderites (Hassanzadeh *et al.*, 1990; Wasson *et al.*, 1974, 1998). If this is true, it would allow for IIIAB irons to be genetically linked to mesosiderites.

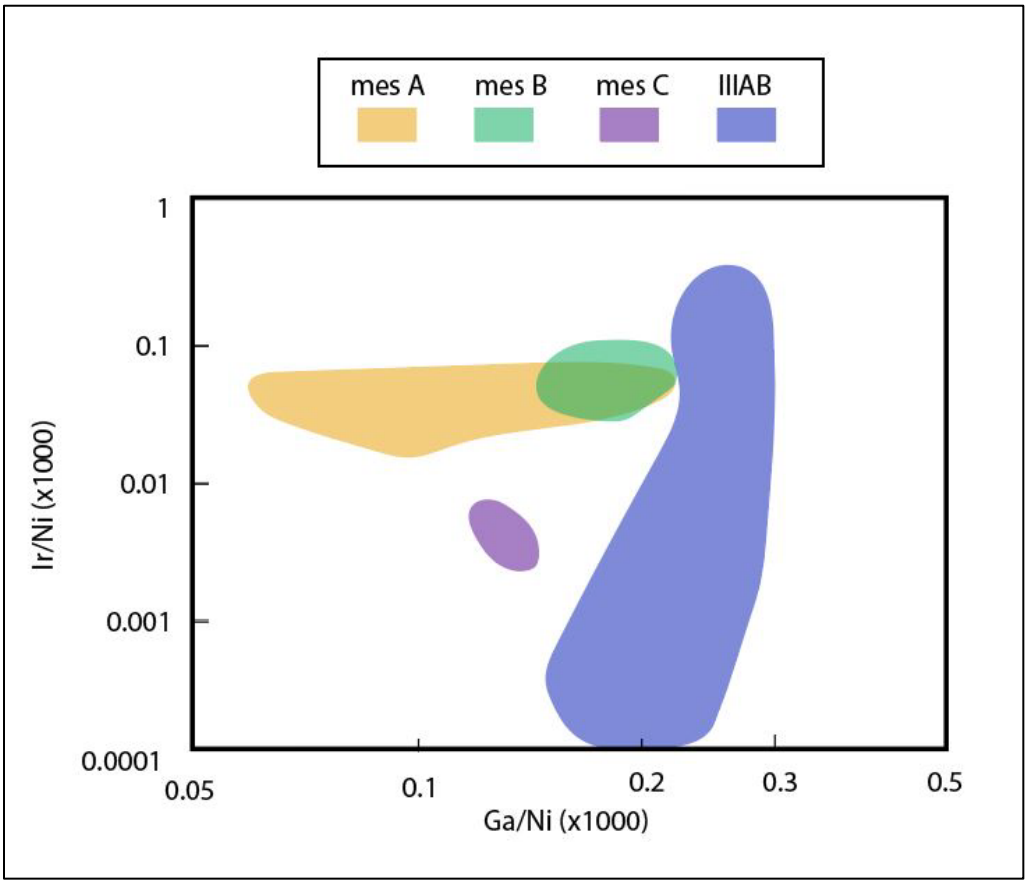

Figure 4. Mesosiderite metal compared to IIIAB irons on a plot of Ir/Ni vs. Ga/Ni. Mesosiderite compositional classes A, B, and C do not show the same magmatic siderophile element trend as the IIIAB irons. (Wasson *et al*., 1974, 1998; Hassanzadeh *et al.*, 1990) Adapted from Mittlefehldt *et al*. (1998).

2.3 Mesosiderite Formation

The formation of mesosiderites can be divided into three main stages: (1) Initial crystallization of mesosiderite silicates followed by a period of intense brecciation; (2) Mixing of metal and silicates, resulting in local partial melting, recrystallization of silicates, and rapid cooling; (3) Deep burial and slow cooling (*e.g*. Powell, 1969, 1971; Floran, 1978; Hewins, 1984, 1988; Wasson and Rubin, 1985; Rubin and Jerde, 1987; Bogard *et al*., 1990; Haack *et al*., 1996; Hopfe and Goldstein, 2001; Scott *et al*., 2001). Many authors have proposed various models to explain the complex formation of mesosiderites and how they may relate to other meteorite groups.

2.3.1 Stage 1: Initial Crystallization

Silicates

The earliest formation model proposed that mesosiderites and HEDs evolved on the same parent body (Powell, 1971). In this model, near-surface melting caused magmatic activity to locally segregate the metal fraction and the silicate fraction prior to core formation (Fig. 5a). The silicate fraction then continued to differentiate, resulting in heterogeneities at the surface. Powell (1971) originally described the petrogenesis of the silicates prior to mixing with the metal by examining the mineralogy of the subgroup 1 mesosiderites. This subgroup of mesosiderites represents the samples that best preserve the mineralogy closest to its original state because they have experienced the least amount of metamorphism. Powell (1971) studied various lithic fragments and concluded that the silicate portion of mesosiderites originated from a large body that had experienced extensive differentiation, like the HED parent body. This study suggested that lithic fragments containing pigeonite with narrow augite lamellae were produced by melts saturated with SiO_2 and formed shallow intrusive rocks similar to eucrites. The varying grain sizes and extent of magmatic zoning in the pyroxenes reflect a range of cooling environments (Powell,

1971). The monomineralic lithic fragments of subgroup 1 mesosiderites represent cumulate rocks, such as dunites, orthopyroxenites, and anorthosites, which implies that larger differentiated igneous bodies were present on the mesosiderite parent body. These coarse-grained fragments were interpreted as magmatic segregations formed from differentiated liquids of varying degrees (Powell, 1971; Floran, 1978). Reaction coronas on the few olivine-rich fragments present in the subgroup 1 mesosiderites show evidence of disequilibrium with the surrounding matrix, and the olivine was described as "foreign" to the mesosiderite silicates (Prior, 1918). Prior (1918) suggested that the minor amount of olivine was associated with the metal portion of mesosiderites; however, (Powell, 1971) claims that the high Ni content of the olivine is in disagreement with a genetic relationship with the metal. After initial crystallization of the mesosiderite silicates, impact events caused extensive brecciation resulting in cataclastic features and textural heterogeneity of mesosiderites (Table 1; Fig. 5b) (Powell, 1971; Floran, 1978).

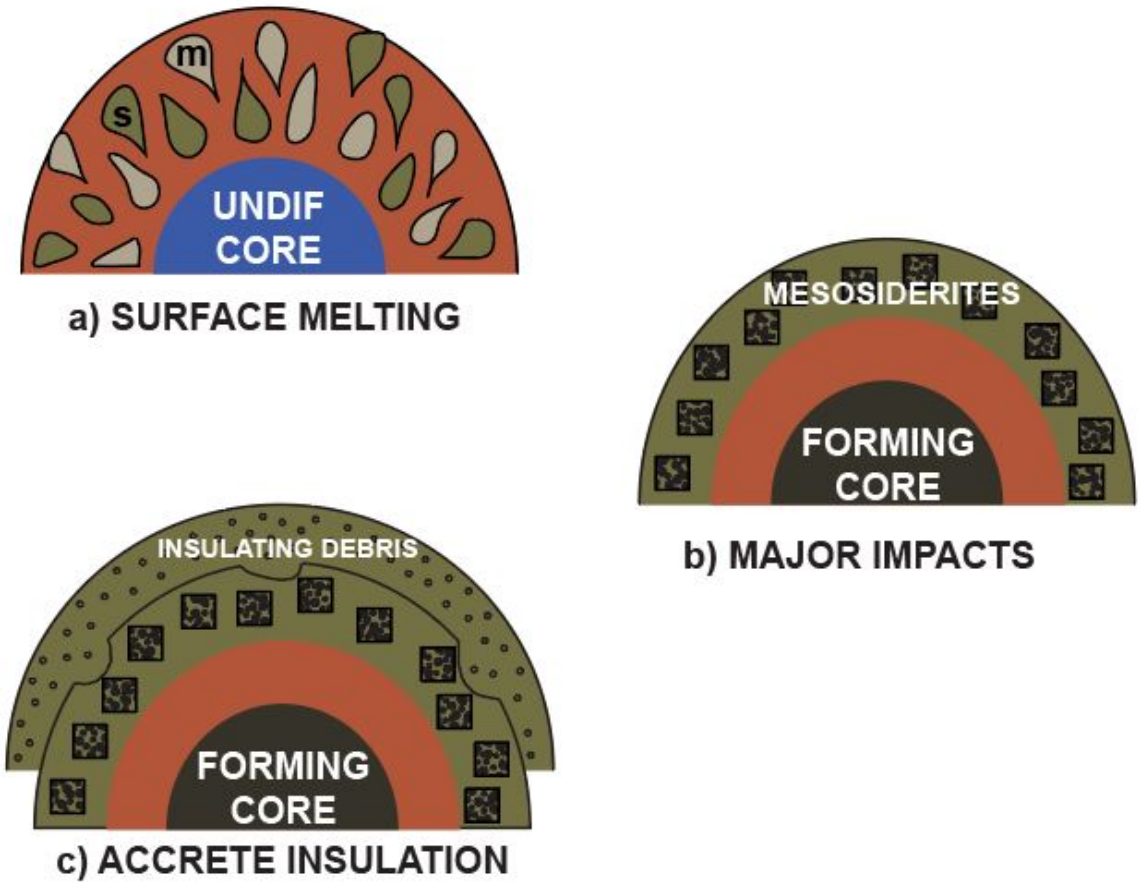

Figure 5. Mesosiderite formation model showing: a) near-surface melting causing segregation of metallic and silicate melts prior to core formation b) extensive brecciation producing mesosiderites by metal-silicate mixing and c) deep burial underlying an insulating layer of debris (Powell, 1971). Adapted from (Hewins, 1983).

Metal

Results from electrical conductivity tests performed on mesosiderites show that the metal is interconnected throughout the samples, forming three-dimensional networks (Powell, 1969; 1971). This suggests that the metal was molten at the time of mixing, although it has been shown that metal can redistribute at subsolidus temperatures in chondrites (Dodd and Van Schmus, 1967). If this is possible for mesosiderites, it could support the idea that previously disconnected metal masses could redistribute to form interconnected three-dimensional networks through the matrix of the silicates, allowing the metal to equilibrate (Powell, 1971). Other researchers have proposed that the large, metal nodules seen in mesosiderites were mixed in a solid state due to the "random magnetic polarity and well-sorted nature" of the nodules (Wilson, 1972; Floran, 1978). The problem of "random magnetic polarity" of mesosiderite nodules will be returned to in the discussion. Delaney *et al.* (1981) argue that if mesosiderites are genetically related to the HED suite of meteorites, then vugs observed in eucritic meteorites and intricate metal-silicate boundaries in mesosiderites are evidence for molten metal at the time of mixing. These vugs represent areas from which molten metal had escaped. Wasson and Rubin (1985) and Hassanzadeh *et al.* (1990) suggested that the restricted range in Ir/Ni ratios in mesosiderite metal (Fig. 4) indicates that the metal was undifferentiated, and therefore molten, at the time of mixing.

2.3.2 Stage 2: Metal-Silicate Mixing

Physical Mixing Mechanisms

Some models propose that the silicates and metal originated on the same parent body and were mixed together by impacting and brecciation at the surface. The Powell (1971) model suggested that fluctuating degrees of brecciation took place through the process of impacts, which generated the monomict eucrites and the polymict, metal-poor howardites. The monomict eucrites

represent a small degree of mixing, while the polymict, metal-poor howardites were produced by an extensive amount of mixing of only silicate components. The mesosiderites were then manufactured by a similar degree of mixing to the howardites but included mixing of metal with the silicates (Fig. 5a, 5b); however, this model does not provide an explanation for the low amount of olivine in mesosiderites. Powell (1971) claimed that the heat produced by the impactors could have resulted in local partial melting, but that most lithologies were still mixed as solids.

Delaney *et al.* (1981) also proposed a mixing model that required the silicates and metal to originate from the same parent body. In this model, near-surface melting caused metallic liquid to segregate into a layer deep inside the body during differentiation prior to core formation (Fig. 6). A large impacting event produced a basin that extended down into the metallic layer allowing for crustal silicate debris and metallic liquid to mix together forming mesosiderites. Delaney *et al.* (1981) also suggests that the formation of a liquid metallic shell deep inside a differentiating asteroid would be gravitationally unstable causing disruption in the mantle and crust, which could allow for turbulent mixing to produce stony-iron meteorites, but this model does not account for the low abundance of olivine in mesosiderites if the metallic shell layer was overlain by a mantle.

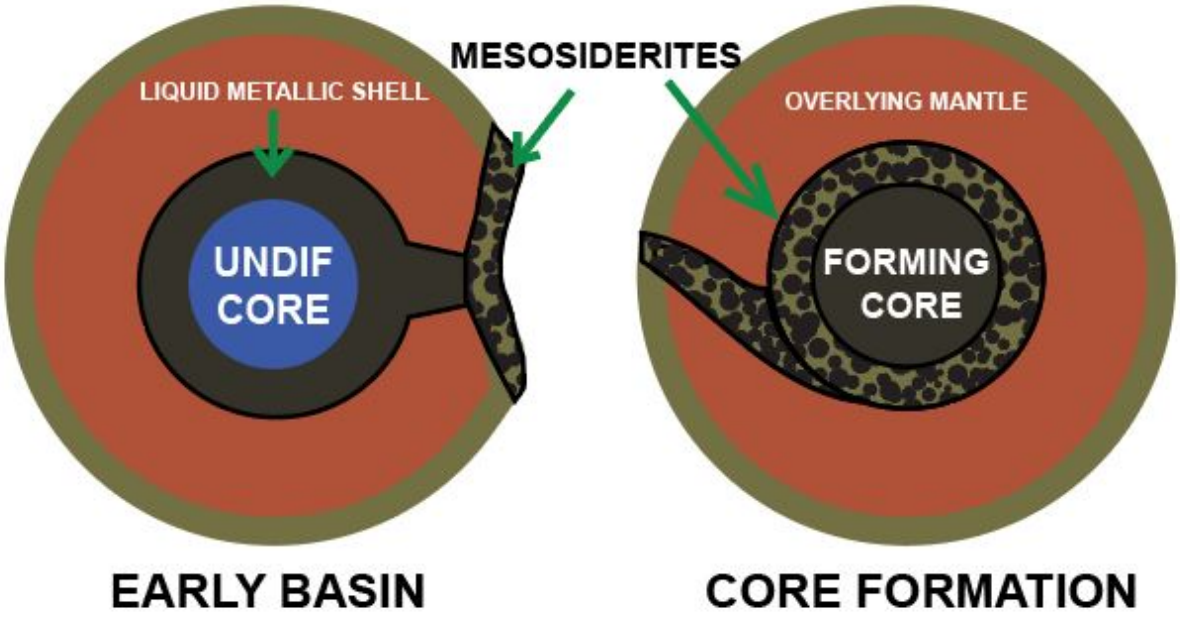

Figure 6. Early basin and core formation scenarios from Delaney *et al.* (1981). (Left) Excavation of a giant impact basin prior to core formation allowed crustal debris to mix with the buried metallic shell. (Right) As the core was forming, the overlying mantle and crust turbulently mixed with the gravitationally unstable liquid metallic shell. Adapted from Hewins (1983).

Greenberg and Chapman (1984) invoked crustal foundering, or sinking, to the core-mantle boundary for mesosiderite formation (Fig. 7). This model suggests that crustal blocks sank through a largely liquid asteroidal body down to the top of the liquid core. However, the required high temperature of the liquid core, assuming it is insulated by a molten mantle, would not be able to produce the textures and thermal history displayed in the mesosiderite silicates. If crustal material survived its descent through the underlying mantle, it would have completely melted at the liquid core boundary until the metal cooled below the liquidus. For these reasons, impact-related models are more popular for mesosiderite formation.

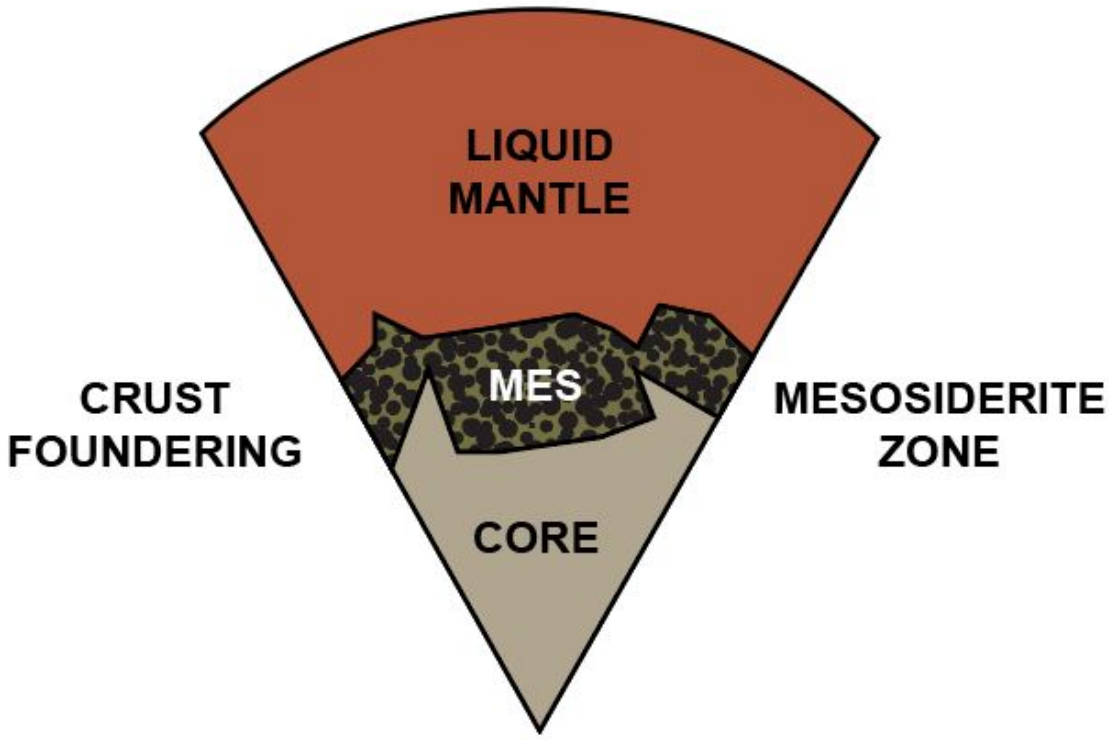

Figure 7. Greenburg and Chapman (1984) formation model displaying crustal blocks sinking through liquid mantle that formed the mesosiderites near the core-mantle boundary of an asteroid. Adapted from Hewins (1983)

The formation model proposed by Wasson and Rubin (1985) suggested low-velocity impacts of metallic core fragments onto the regolith of a differentiated asteroid to produce mesosiderites (Fig. 8). This model requires that the impacting process took place during the early stages of planetary formation when small bodies were still growing. Wasson and Rubin (1985) suggested that disrupting an actively differentiating and growing asteroid would strip away weak crustal and mantle components, leaving behind the core in fragments. The core fragments could then accrete onto the crustal layers causing metal-silicate mixing and brecciation (Fig. 8). If impacting had persisted, multiple generations of breccias would have been produced and resulted in the finer silicate grain sizes and metal distribution that is observed in mesosiderites. This model attributes the metamorphism and melting in mesosiderites to the heat produced by persistent impacts. Wasson and Rubin (1985) suggest that the indistinguishable isotopic and chemical compositions between the howardites and the mesosiderites indicate that they most likely formed on the same parent body or one very similar (Wasson and Rubin, 1985). Because howardites contain much less metal than mesosiderites, they suggest that mesosiderites formed in close vicinity to the impact sites where the core fragments were accreted.

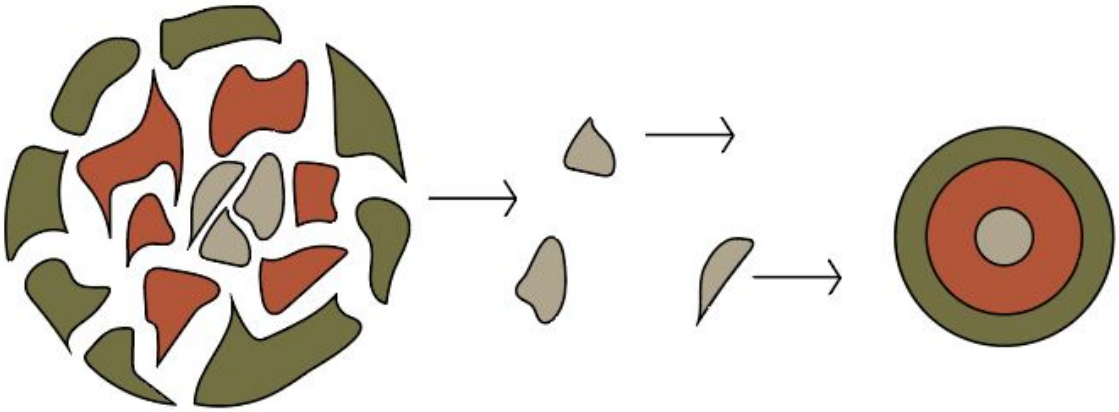

Figure 8. Formation model showing actively growing asteroid broken apart by impacts leaving stripped core fragments free to accrete by low-velocity impacts onto the surface of an asteroid body, allowing for metal-silicate mixing (Wasson and Rubin, 1985).

Rubin and Jerde (1987) proposed three different scenarios for the origin of mesosiderites. In the first scenario, mesosiderites and the HEDs did not share the same parent body, and the mesosiderite parent body was more heavily impacted than the HED parent body producing the range in textures seen in mesosiderites. The second model suggests both suites of meteorites were derived from the same parent body, although the areas of the regolith that contained the mesosiderites experienced more significant impacting from accreted core fragments at low velocities, similar to the Wasson and Rubin (1985) model. The coarse, metallic particles from the accreted core fragments retained enough heat to cause melting of parts of the regolith, resulting in subgroup 4 mesosiderites. The third scenario suggests a common parent body for the HEDs and the mesosiderites, and the entire regolith experienced similar amounts of impacting. The areas containing HED material and no metal were brecciated into fine particles that cooled rapidly from radiation, while the areas that produced mesosiderites and were abundant in metal retained enough heat to allow the regolith to weld together into coarser material.

A study by Scott *et al.* (2001) did not favor the HED parent body as the parent body for mesosiderites. They suggested that a projectile about 50-150 km in diameter collided with a 200-400 km diameter asteroid containing a molten metal core (Fig. 9). This model attributes the low amount of olivine in the mesosiderites as a result of the redistributed mantle material being excluded from the metallic regions of the re-accreted body. Because the mantle material would have been hotter and larger in volume than the crustal material, the metal favored crystallizing with the crustal material, which allowed the olivine to separate from the region gravitationally. The initial rapid cooling rate was suggested to be a result of hot and cold ejecta mixing and equilibrating locally. In support of their model, Scott *et al.* (2001) cite the fact that only a few olivine-rich (A-type) and metal-rich (M-type) asteroids have been recognized, which suggests that

stripping of mantles from metallic cores during large impacting events was not uncommon at this time (Scott *et al*., 2001).

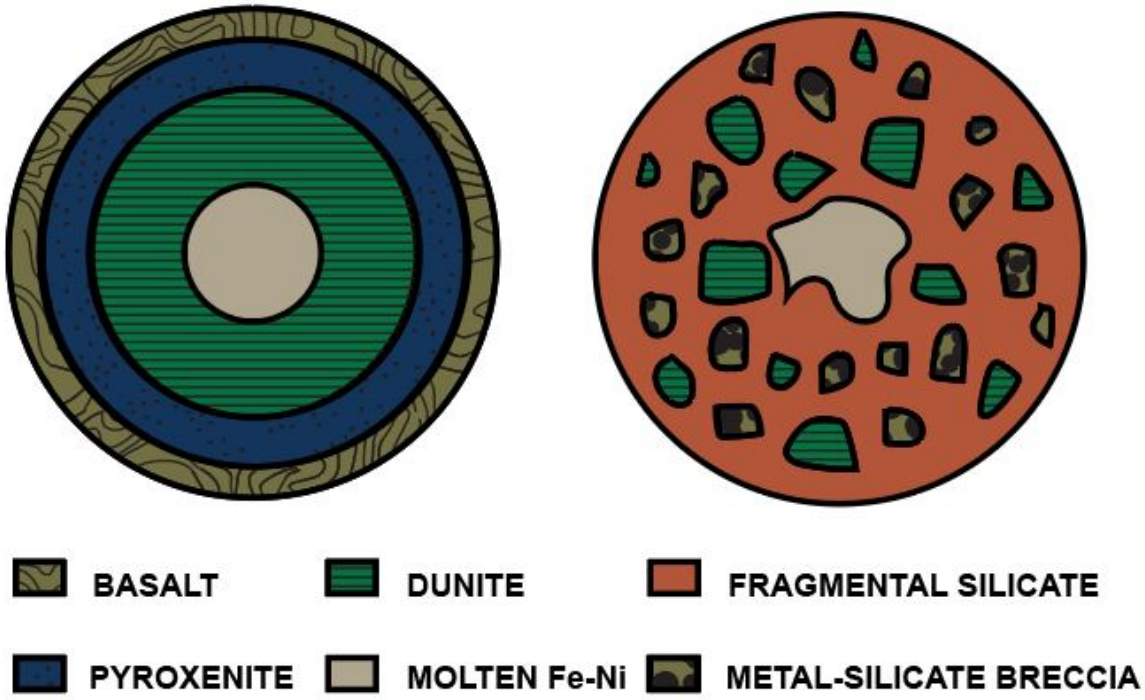

Figure 9. (Left) Differentiated asteroid displaying layers and a molten core. **(Right)** After hypervelocity collisions, deeply buried masses of mesosiderite material are displaced from the site of the collision with a projectile that mixed the metal and silicate portions. Adapted from Scott *et al*. (2001).

Proposed Reactions Produced by Metal-Silicate Mixing

Researchers have attributed the high amounts of certain phases present in some mesosiderites to redox reactions between the metal and silicates during the mixing stage of their formation (Powell, 1971; Nehru *et al.*, 1978; Floran, 1978; Agosto *et al.*, 1980; Delaney *et al.*, 1981; Harlow *et al*., 1982; Agosto, 1985; Hassanzadeh *et al.*, 1990; Mittlefehldt, 1990). For every oxidation reaction, there is a subsequent reduction reaction, hence the term "redox reaction". In simple terms, oxidation refers to the increase in the oxidation state of an element (loss of electrons by an atom called the reducing agent); reduction is the reverse process (addition of electrons to an atom called the oxidizing agent) (Mason, 1949). Many elements can exist in multiple oxidation states. For example, iron can be present in three oxidation states (Fe^{o}, Fe^{2+}, Fe^{3+}). In geologic systems, oxygen fugacity, or the availability of oxygen to react, is used as a variable to determine the potential for iron to occur in either a more oxidized state or a more reduced state (Frost, 1991). In an environment with low oxygen fugacity, iron can exist as metallic iron, and at high oxygen fugacity, iron can exist in its divalent (Fe^{2+}, ferrous) and/or trivalent (Fe^{3+}, ferric) states (Frost, 1991). The presence of magnesium and titanium also stabilizes ferrous iron (Fe^{2+}), allowing it to exist in environments with higher oxygen fugacity because it substitutes readily for those ions (Frost, 1991). This tells us that the Fe/Mg ratio of silicates, the compositions of Fe-Ti oxides present, and oxygen fugacity are directly correlated and determine the redox reactions that can take place in a geochemical system (Frost, 1991).

As stated previously, mesosiderites are approximately 50% Fe-Ni metal, and 50% crustal silicates, some of which contain Fe. If redox reactions took place during the metal-silicate mixing event, one would expect the oxidized elements to be depleted in the metal and enriched in the silicates, while the reduced elements would be depleted in the silicates and enriched in the metal,

depending on the reaction. Some of the elements that have previously been discussed in the literature as participating in such redox reactions are Fe, P, Si, W, and Ga.

Delaney *et al.* (1981) suggested that if redox reactions took place between the metal and silicate phases, the Fe-Mn-Mg systematics would be altered in the orthopyroxenes. Mittlefehldt (1990) proposed that the majority of mesosiderite basalts and gabbros were produced by remelting of previously existing igneous rocks. He observed the effects of redox reactions, showing that the pyroxenes in the mesostasis of the remelted lithologies were richer in MgO than pyroxenes in the non-mesostasis portion. This is not a typical magmatic pattern, which suggests metamorphic redox reactions took place. Fe^{2+} and Mn^{2+} are considered homologous elements and will not fractionate during partial melting or fractional crystallization (*i.e.*, the ratio Fe/Mn remains constant), creating vertical trends when plotted versus Fe/Mg, while Fe/Mg tends to increase during fractional crystallization, as pointed out by Mittlefehldt (1990) (Fig. 10a). He argued that augite found in mesosiderites was a result of late stage crystallization during FeO reduction in the silicate matrix (Mittlefehldt, 1990). He notes that pigeonite has a higher Fe/Mg ratio than augite, and states that the abundance of augite in mesosiderites compared to the HEDs is caused by FeO reduction driving the liquid into the liquidus field for pigeonite + augite (Mittlefehldt, 1990). The Fe/Mn and Fe/Mg systematics of mesosiderite pigeonite and augite were compared to pyroxene present in HED clasts, which showed vastly different trends (Fig. 10b) (Mittlefehldt, 1990). The HED clasts display a trend typical of normal magmatic fractional crystallization, while the mesosiderite mesostasis pyroxenes show a trend representing FeO reduction. This could explain why the mesostasis pyroxenes have higher MgO content than the non-mesostasis pyroxenes and gives evidence for this process taking place where the metal and silicates are mixing (Mittlefehldt, 1990).

It has been discussed by other authors that if FeO has been reduced from pyroxenes, some of it most likely accumulated in chromite and ilmenite in the mesostasis and reaction rims, which resulted in pyroxene with lower Fe/ (Fe + Mg) ratios than the adjacent olivine (Powell, 1971; Delaney *et al*., 1981; Mittlefehldt, 1990). This provides evidence for the occurrence of subsolidus metal-silicate reactions because the Mn/Mg ratio shows no change in the pyroxenes, which would typically happen if the pyroxene was present during magmatic reduction (Mittlefehldt, 1990).

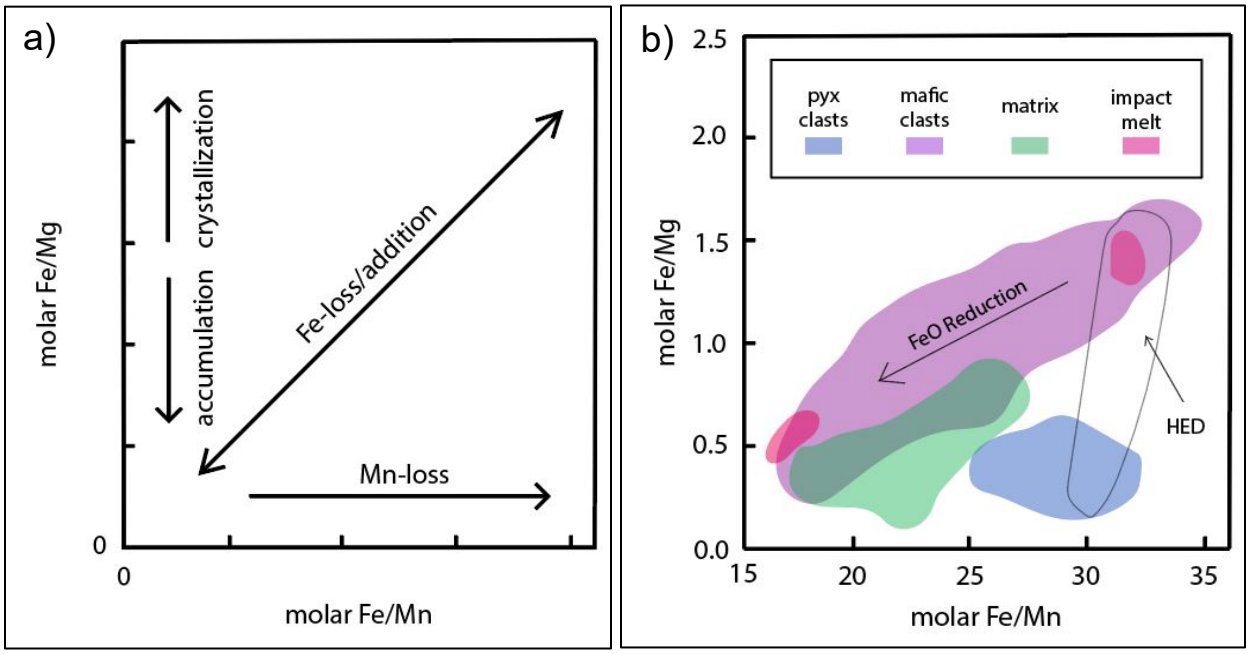

Figure 10. a) Typical trends seen in molar Fe/Mg vs. Fe/Mn ratios caused by different processes (fractional crystallization/ crystal accumulation/ FeO reduction). Adapted from (Goodrich and Delaney, 2000). **b)** Mesosiderite pyroxene data compared to HED data. HED data show typical igneous trends, while mesosiderites show trends of Fe loss, possibly due to redox reactions (Mittlefehldt, 1990). Adapted from Mittlefehldt *et al.* (1998).

The phosphate merrillite ($Ca_3(PO_4)_2$) has also been attributed to redox reactions in the silicate matrix in mesosiderites by oxidation of P contained in the metal (Fuchs, 1969; Powell, 1971; Nehru *et al*., 1978; Delaney *et al*., 1981; Harlow *et al*., 1982; Mittlefehldt, 1990). High concentrations of REE are not observed in mesosiderite merrillite unlike the phosphates in achondrites (Harlow *et al*., 1982). These high concentrations in achondrites are a typical feature of igneous fractionation, suggesting that mesosiderite phosphates are not a product of this process. Phosphate concentration in mesosiderites is five times higher than in eucrites and howardites (Powell, 1971), and merrillite is a modally abundant phase in mesosiderites (Harlow *et al*., 1982). This discrepancy between the HED clan and mesosiderite group can be explained if mesosiderite phosphates are a result of oxidation, not fractionation, of phosphorus that is dissolved in the metal.

The average modal abundance of tridymite has been determined to be 8% for basaltic clasts in mesosiderites (McCall, 1966), and only 4% in eucrites (Delaney *et al*., 1981), but redox reactions can also explain this discrepancy. Igneous fractionation can cause enrichment in FeO, CaO, and SiO_2, but this would also cause an enrichment in alkalis. Only a slight increase in Na(+K) is seen in mesosiderites, showing that igneous fractionation is not a probable cause of the high modal silica abundance (Harlow *et al*., 1982). It has been suggested that reduction of FeO by P would result in the generation of metallic Fe and excess free silica (Table 3) (Mittlefehldt *et al*., 1979; Agosto *et al*., 1980), although additional reactions have been considered due to the lack of correlation between silica and merrillite (Harlow *et al*., 1982).

Table 3. Relevant oxidation/reduction chemical reactions between silicates and metal in mesosiderites (Agosto, 1985).

$3CaMgSi_20_6 + 5FeSiO_3 + 2[P]^{Fe} = Ca_3(PO_4)_2 + 3MgSiO_3 + 8SiO_2 + 5Fe$
$45(Ca_{.09}Mg_{.56}Fe_{.35})SiO_3 + 2[P]^{Fe} = Ca_3(PO_4)_2 + 35(Ca_{.03}Mg_{.72}Fe_{.25})SiO_3 + 10SiO_2 + 7Fe + O_2$

The presence of tridymite is correlated with coronas, or reaction rims, of fine-grained pyroxene and/or chromite around olivine grains showing disequilibrium with the silicate matrix where the redox reactions are proposed to occur (Powell, 1971). The formation of this texture is a result of the instability of the Mg-rich olivine in the presence of tridymite; the coronas form a barrier between the olivine and the matrix (Powell, 1971; Floran, 1978; Delaney *et al.*, 1981). Tridymite does not exist in the mesosiderites that do not show coronas around olivine grains (Nehru *et al*., 1980), which explains the variation of these coronas between the subgroups (Table 1) (Powell, 1971; Floran, 1978; Delaney *et al.*, 1981).

Differing siderophile element concentrations of fractionated iron meteorites and the mesosiderite metal phase also provide evidence for redox reactions during the metal-silicate mixing event. As mentioned above, the mesosiderite metal does not follow the near vertical, magmatic trend in siderophile elements that the IIIAB irons show (Fig. 4). Compositional group B mesosiderites plot high in Ga, while variations from low to high Ga are seen in compositional group A mesosiderites, but both classes show no variation in Ir content (Hassanzadeh *et al.*, 1990; Wasson *et al.*, 1974, 1998). Wasson and Rubin (1985) propose that the differing metal compositions could indicate that the metal in class A mesosiderites accreted in a distinct regolithic region from class B mesosiderites. However, it could reflect redox reactions taking place between the metal and the silicates (Hassanzadeh *et al.*, 1990; Wasson *et al.*, 1974). W and Ga can be affected by reduction processes and should be examined more closely to determine if the differences between the IIIAB iron and mesosiderite metal can be explained through metal-silicate reactions.

2.3.3 Stage 3: Slow Cooling

Metal

Powell (1971) claims that the "textural relationships indicate that the kamacite-taenite structures observed in the mesosiderite metal developed *in situ*, after metal-silicate physical relationships were established". Cooling rates for the metal, based on kamacite-taenite structures, were originally determined to be as slow as 0.1°C per million years (Powell, 1969), but have since been revised to 1.0°C per million years (Narayan and Goldstein, 1985). This is the slowest cooling rate calculated for any type of meteorite to date. The IIIAB iron metallographic structures also reveal slow cooling rates of 3-75°C per million years (Mittlefehldt *et al.*, 1998). The slow cooling rate for mesosiderites can be interpreted in two different ways within the temperature range of 500-350°C (Powell, 1971). The first is continuous slow cooling, and the second, rapid cooling to low temperatures preceding a reheating event to 500°C followed by slow cooling to 350°C (Powell, 1971). The metal of mesosiderites suggest these meteorites were cooled very slowly; however, the cooling rates determined by mesosiderite silicates indicate a more complex thermal history.

Silicates

Modeling of element distribution in individual silicate minerals and Ar diffusion in bulk silicates has been used to determine the cooling history of mesosiderites. Original cooling rates of the silicates were determined to be 1° to 100°C per annum estimated by Delaney *et al.* (1981) but were recalculated to ~ 2°C per annum from Fe-Mg diffusion in clinopyroxene overgrowths on orthopyroxene cores (Jones, 1983). These values were recalculated based on evolving information on diffusivity in pyroxenes, although these values are 6 to 8 orders of magnitude higher than

cooling rates constrained by metal structures in mesosiderites. Ganguly *et al.* (1994) reinvestigated data from two mesosiderites studied in Delaney *et al.* (1981) using more complex cooling models to produce a cooling rate of ~ 14°C per thousand years at 1150°C and 5°C per thousand years at 600°C. This study also suggested cooling rates of the silicates could have been less than 1°C per million years at a temperature of 250°C based on cation ordering in orthopyroxenes. All estimated cooling rates for mesosiderite pyroxenes are much higher than metallographic cooling rates; however, Bogard *et al*. (1990) suggest that Ar-Ar release profiles are in agreement with slow cooling at low temperatures estimated by metallographic structures. The mineralogical and textural evidence for surficial formation, indicated by mesosiderite silicates, is in disagreement with the significantly slow cooling rates experienced by these meteorites making it difficult for scientists to explain their last stage of formation.

Two separate mechanisms have been suggested in the literature to produce the slow cooling rates of the metal; the first requires a blanket layer of ejecta and debris that insulates the mesosiderites allowing for significant heat retention for an extended period of time, and the second involves deep burial of mesosiderites to place them at an appropriate depth to produce slow cooling rates. Powell (1971) proposed that additional low velocity impacts assembled an insulating layer of debris that buried the regolith, which changed the cooling environment drastically after metal and silicates mixed (Fig. 5c). Once the material was buried, the metal re-organized into three-dimensional networks, recrystallization of the silicates took place, and metallographic structures began to form. This study suggests the variations in recrystallization (subgroups 1-4) seen in the mesosiderites are a result of the depth at which each subgroup was buried (Powell, 1971). The crustal foundering model proposed by Greenburg and Chapman (1984) predicted that mesosiderite formation would occur at a great enough depth to produce the slow cooling features of the metal

(Fig. 7). Wasson and Rubin (1985) infer that the slow cooling rates of the metal are a result of low temperature thermal annealing (altering the physical or chemical make-up of the metal), or thermal cycling at the surface of the parent body for an extended period to produce the metallographic structures used to determine cooling rates.

No single formation model has been proposed that can accurately explain the lithologies found in mesosiderites and their unique textures, the absence of mantle material, the slowest coolest rates known for meteorites, and the difference in cooling rates between the silicates and metal. To better understand the formational history of these meteorites, each stage of formation must be examined in depth.

3.0 Project Description

This research aims to better understand processes that took place during the second stage of mesosiderite formation, metal-silicate mixing. While many studies have examined evidence for redox reactions during metal-silicate mixing, they have primarily focused on the silicates (*e.g.*, Harlow *et al*., 1982; Agosto *et al*., 1985; Mittlefehldt, 1990). Most research of mesosiderites was conducted during a time when instrumentation could not effectively analyze metal compositions. Metal studies used instrumental neutron activation analysis (INAA), which can only measure a few elements at a time within the metal, making it difficult to interpret the effects of redox reactions from the metal. Over the past decade, the development of laser ablation-inductively coupled plasma-mass spectrometry (LA-ICP-MS) has allowed for the identification of a full suite of siderophile elements within the metal. Mesosiderite metal should also preserve evidence of redox reactions if they occurred; depletions in readily oxidizable elements (*e.g.*, W, P) would be expected in the metal most closely associated with the silicates, referred to here as matrix metal, relative to metal clast (nodule) material.

In order to assess this hypothesis, we compare the texture, metallography, mineralogy, and major, minor, and trace element composition of both the matrix and clast metal within five mesosiderites. For this research, we have defined metal clasts as metal not in contact with silicates and matrix metal as metal in close contact with surrounding silicates. These samples span the range of petrologic classes (A-C, anomalous) and, in order to see past the last stage of mesosiderite formation (cooling), only samples that exhibit a low degree of metamorphism (subgroup 1) were chosen. They provide us with the best opportunity to assess the evidence for redox reactions within the metal portion of mesosiderites.

4.0 Methods

4.1 Sample Selection

During the preliminary stages of this study, hand samples of 26 mesosiderites from the Smithsonian Institution's National Museum of Natural History Meteorite Collection were examined. Five polished sections were selected from this group that are characteristic of all petrologic classes of mesosiderites, including anomalous samples. The specimens chosen for this study are Crab Orchard (USNM1590), Chinguetti (USNM 3205), Chaunskij (USNM 3256), RKPA 79015, Vaca Muerta (USNM 1682). Crab Orchard and Vaca Muerta are classified as petrologic class A mesosiderites, and Chinguetti is classified as petrologic class B. All three of these meteorites fall into the subgroup 1 category of recrystallization. RKPA 79015 is the only member of the petrologic class C and it, as well as Chaunskij, is classified as anomalous.

4.2 SEM Elemental Mapping

The FEI NovaSEM 600 scanning electron microscope in the Department of Mineral Sciences at the Smithsonian Institution's National Museum of Natural History was used to produce

back-scattered electron images and elemental x-ray images for each polished section. Full spectrum mapping was used to produce both elemental and multi-element maps, which were used to select areas of interest for electron microprobe analysis (EMPA) and laser ablation-inductively coupled plasma-mass spectrometry (LA-ICP-MS) analyses.

The SEM maps were collected through a quadrant system starting at the upper left-hand corner of the sample, creating a tile labeled (0,0) (Fig. 11). The SEM traverses to the right across the sample creating tiles labeled (0,1), (0,2), etc., and then drops down to the next row, beginning at the left again, with a tile labeled (1,0). The SEM continues in this manner until the entire sample is mapped in tiles labeled by their position. Each tile includes an area of the sample that is overlapped with the tile above it and beside it, making it possible to align the tiles into a complete map of the section. The number of tiles used to map each section is based on the overlap necessary to map the entire section, and the resolution used to map the area of the section.

Each tile consists of multiple elemental x-ray maps that are layered on top of each other. For this study, we collected data for the elements Al, Ca, Co, Cr, Cu, Fe, K, Mg, Mn, Na, Ni, O, P, S, Si, Ti, and V, along with BSE images of each sample. Once the tiles are placed in their quadrant positions and the overlap is matched, the tiles corresponding to the same elemental data are merged into one layer (*e.g.*, all Ni tiles). This is done for each element, producing a suite of elemental maps for each section. Each individual elemental map is assigned a specific color and shows the distribution of the element across the section by a gradient of color; areas where the color is brightest show where the element is concentrated. All maps collected are provided in Appendices B-F.

In this study, multi-element maps were made using the elements Fe, Ni, and P to identify the different metal phases and P-bearing minerals present in each sample. These maps were made

by layering the colored Fe, Ni, and P maps on top of each other, and making each layer slightly transparent (Fig. 12). The transparency allows the colors of each map to show through and combine making it possible to identify certain phases that contain Fe, Ni, and/or P.

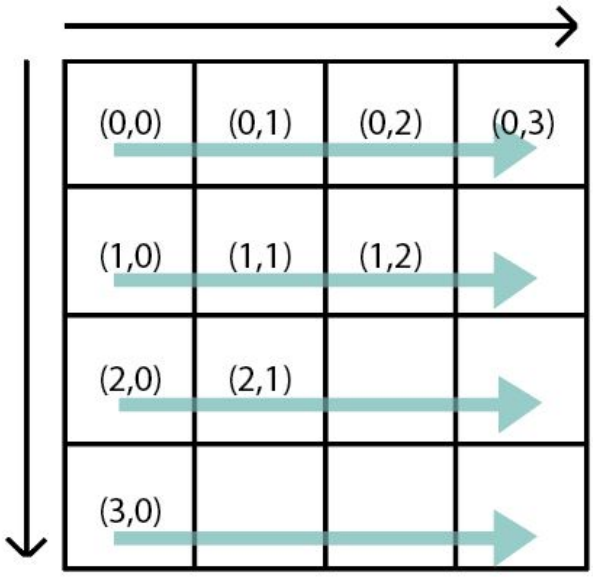

Figure 11. Quadrant grid of SEM mapping. Blue arrows indicate the direction in which the SEM maps.

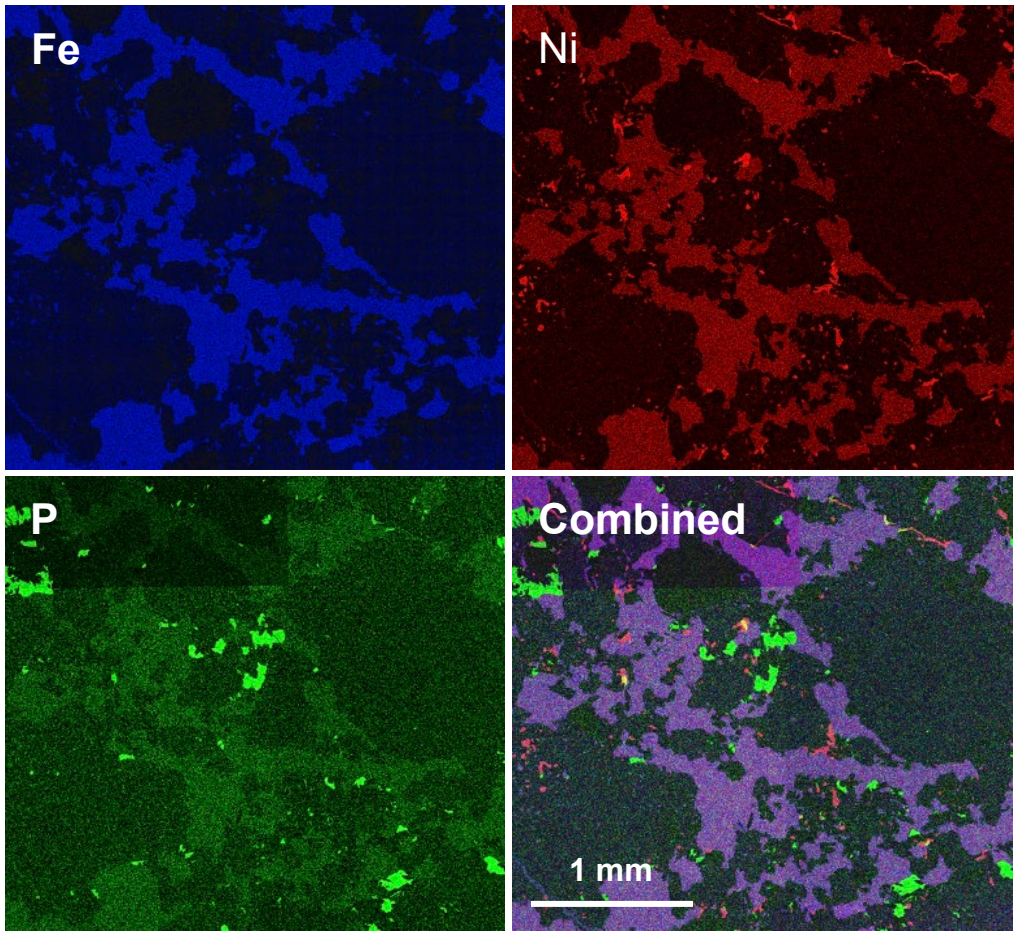

Figure 12. Separate elemental maps of Fe, Ni, and P next to a combined multi-element map showing distribution of all 3 elements together.

4.3 Electron Microprobe Analysis

Electron microprobe analyses of mesosiderite metal were obtained using the JEOL 9800R/5 at the Smithsonian Institution's National Museum of Natural History in the Department of Mineral Sciences. Elements analyzed were Fe, Ni, Si, S, P, Co, Cu, and Cr. Operating conditions included a fully focused beam, a current of 30 nA, and accelerating voltage energy of 20 keV. Standards used for microprobe analyses included Ni10Fe, S3.22Fe, troilite, schreibersite, and metallic Co, Cu, and Cr.

4.4 Laser Ablation-Inductively Coupled Plasma-Mass Spectrometry

Minor and trace element analyses by LA-ICP-MS were conducted at the University of Maryland. The LA-ICP-MS analyses were calibrated using the Ni concentration measured for the closest EMPA analysis. In some cases, multiple LA-ICP-MS spots were referenced to the same microprobe analyses. Analyses were made on both matrix metal and metal clast phases for samples Crab Orchard and Chinguetti. Crab Orchard and Chinguetti metal clasts were analyzed in 2 runs, the first of which produced anomalously low Ge concentrations, which we exclude from the data set presented. Metal clasts were analyzed in Chaunskij and RKPA 79015. One large, isolated metal clast was analyzed in Vaca Muerta. Locations of LA-ICP-MS measurements are shown in Figures 13-17. All analyses, excluding runs for Vaca Muerta, were performed using a spot diameter of 80 μm and a 7Hz laser repetition rate. Spot diameter for Vaca Muerta analyses ranges from 35 to 40 μm. Standards used to calibrate the instrument include iron meteorites Hoba (IVB), North Chile (IIAB), and Coahuila (IIAB). Best data runs for each sample were chosen by lowest relative standard deviation (RSD) values. Data was normalized to CI-chondrite values given by McDonough and Sun (1995) and plotted on a logarithmic scale in order of increasing volatility.

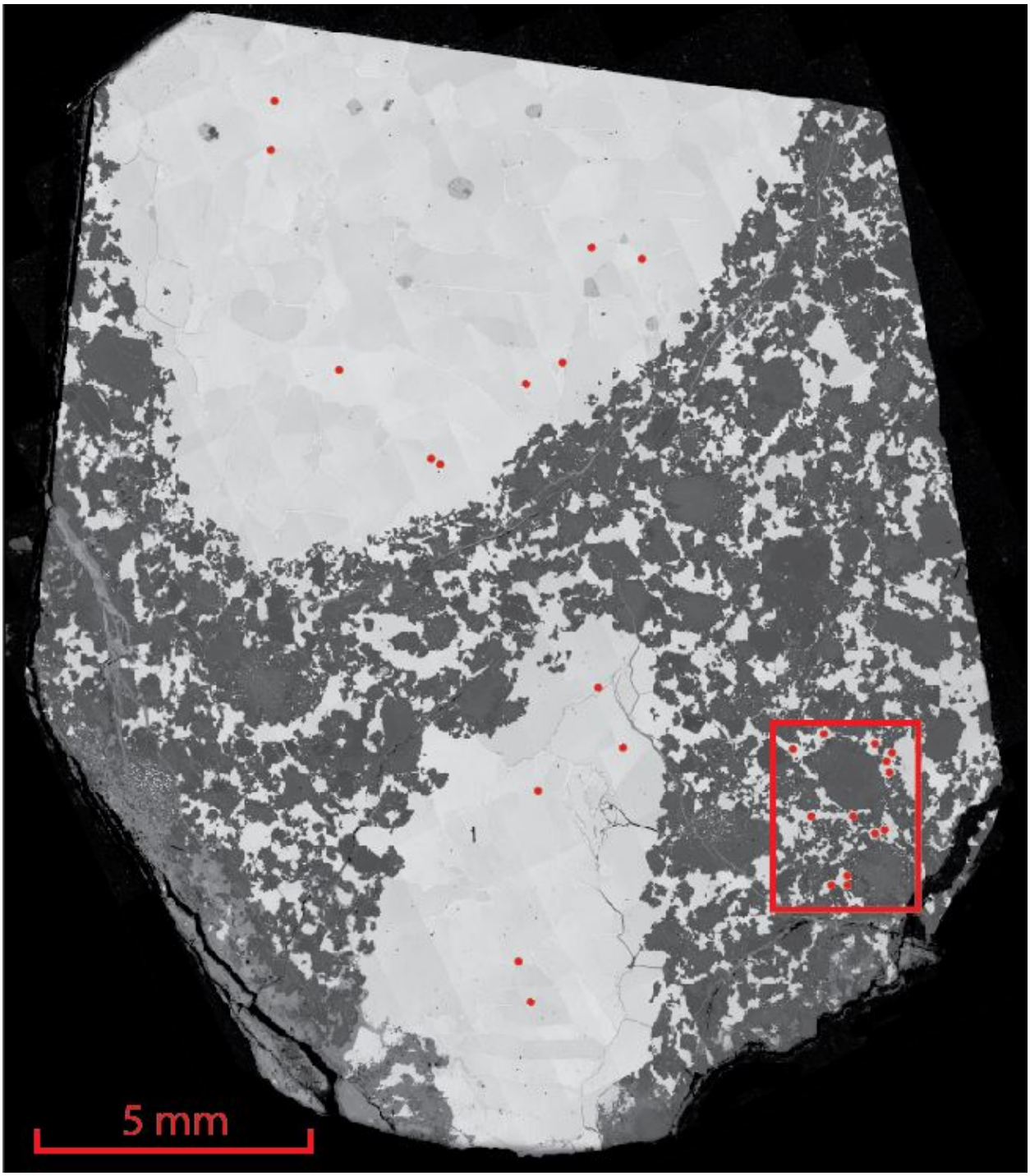

Figure 13. Back-scattered electron image of Crab Orchard. Red spots indicate LA-ICP-MS locations. Matrix metal locations are outlined by a red box.

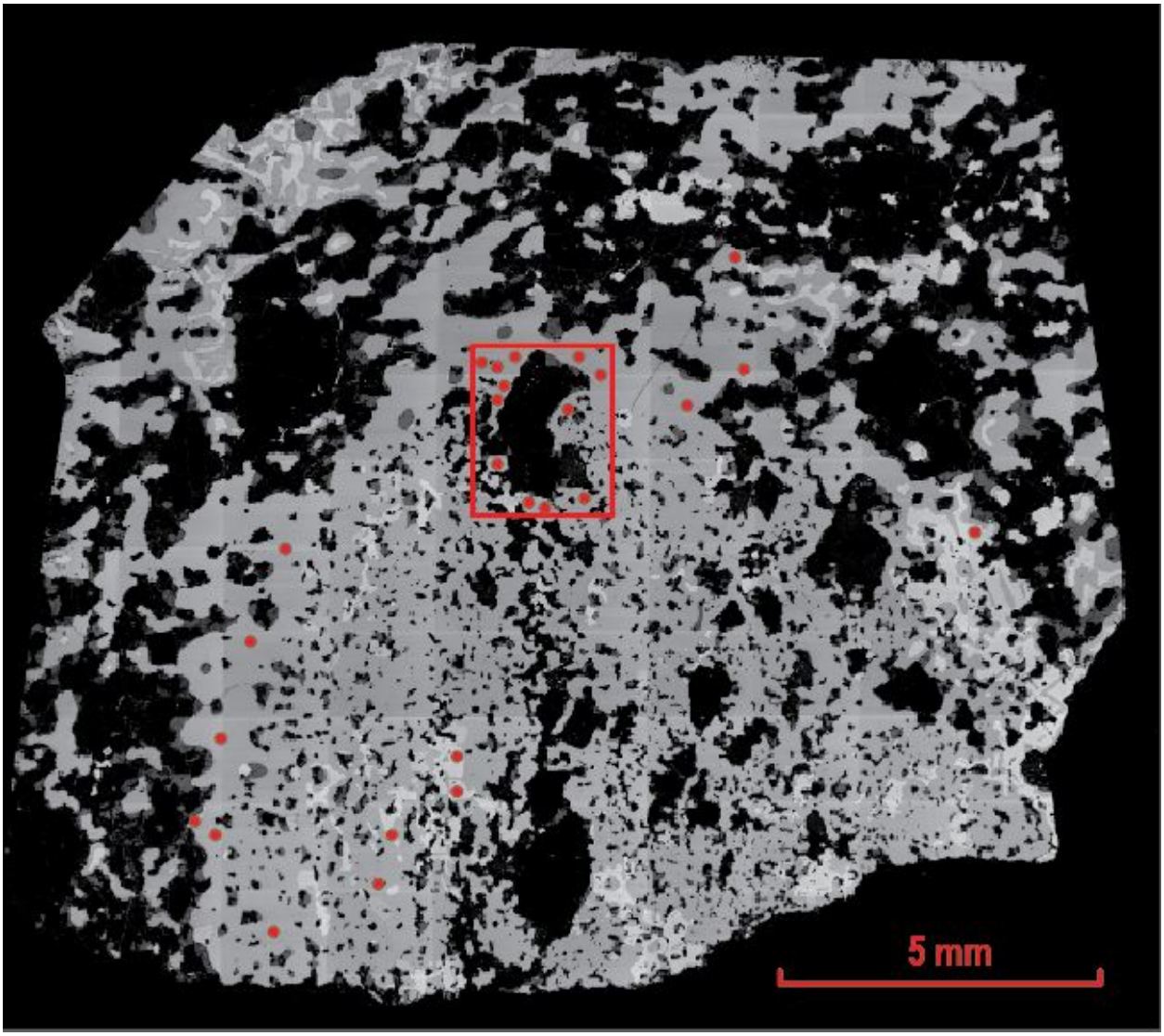

Figure 14. Back-scattered electron image of Chinguetti. Red spots indicate LA-ICP-MS locations. Matrix metal locations are outlined by a red box.

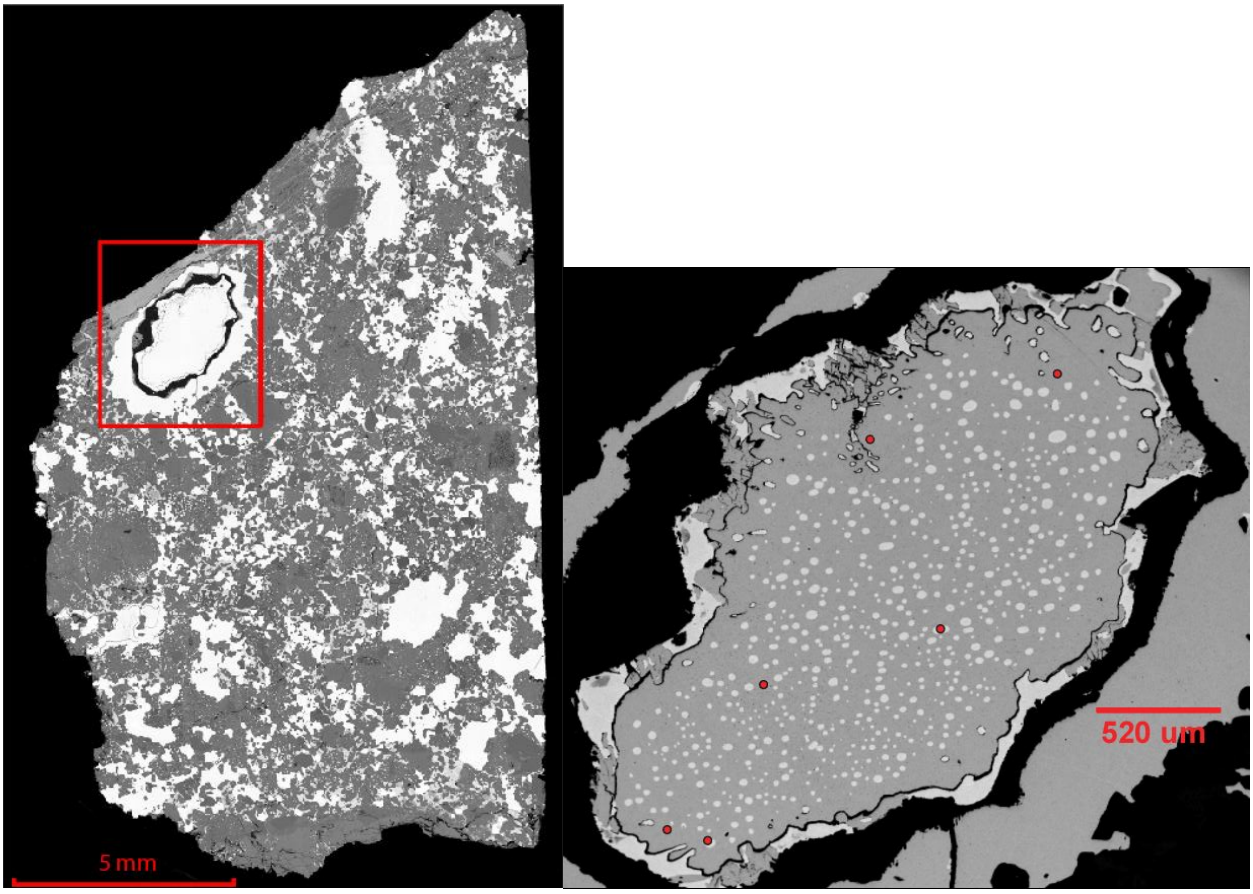

Figure 15. (Left): Full back-scattered electron image of Vaca Muerta showing outline of metal clast in red box. **(Right):** Close up of metal clast. Red spots indicate LA-ICP-MS locations.

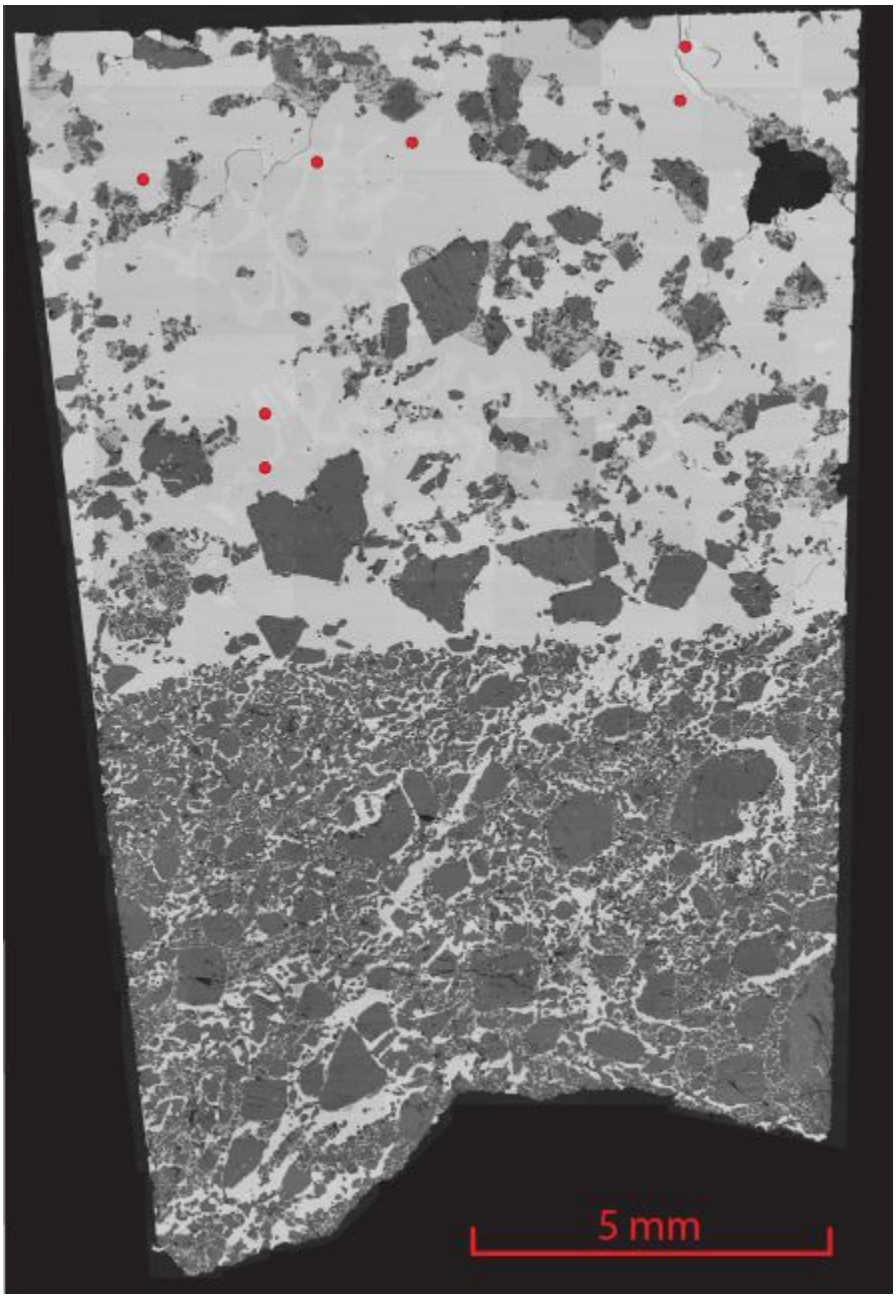

Figure 16. Back-scattered electron image of RKPA 79015. Red spots indicate LA-ICP-MS locations.

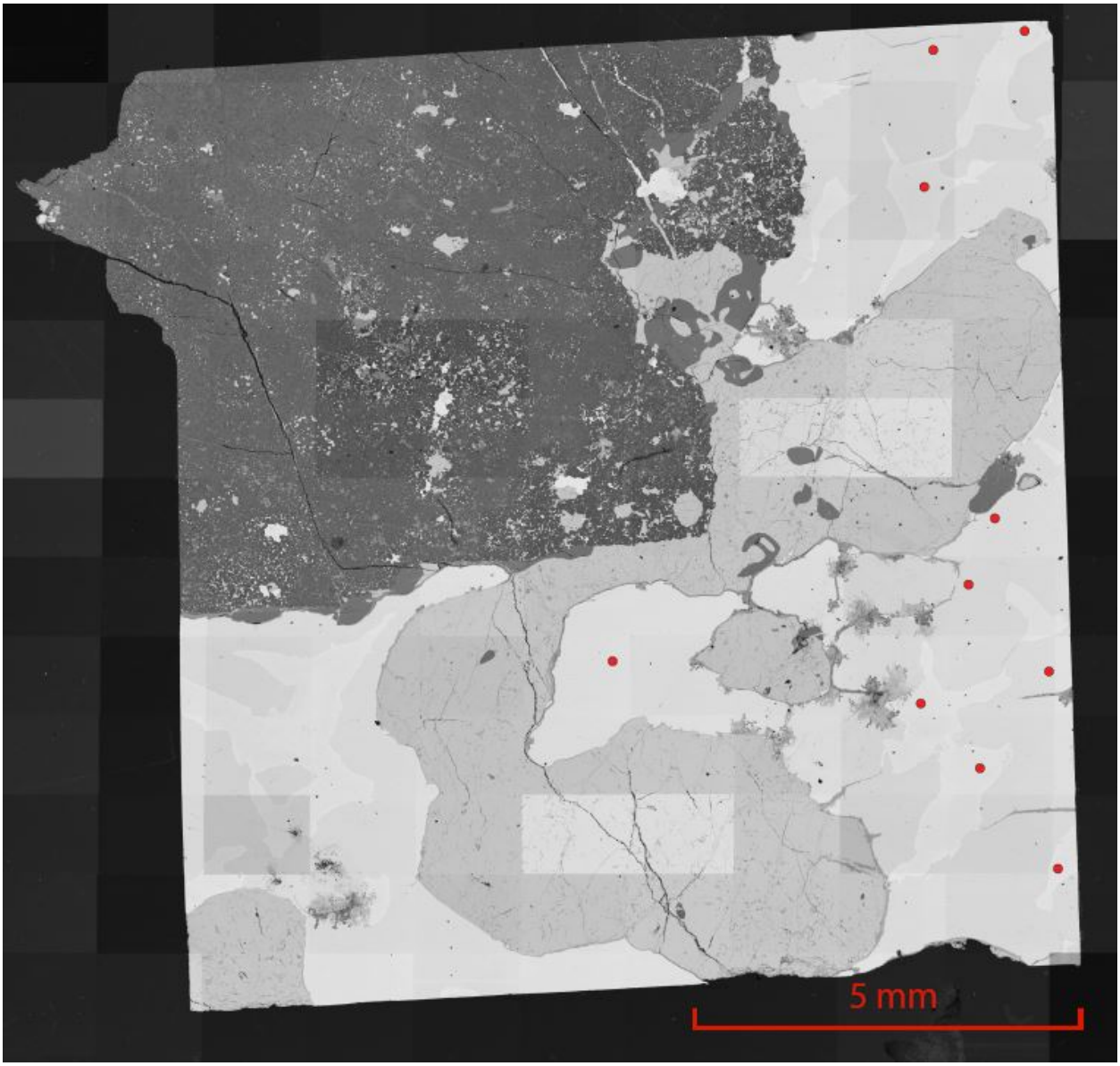

Figure 17. Back-scattered electron image of Chaunskij. Red spots indicate LA-ICP-MS locations.

5.0 Results

Coordinated petrologic and major and minor element chemical analyses allow differences in chemistry potentially related to redox reactions to be placed in the context of spatial relationships. Multi-element maps produced from combining individual elements illustrate the relationship between clasts and matrix and the mineralogy and textures in each. Mapping of Fe, Ni and P allow identification of kamacite, taenite, phosphates and the phosphide schreibersite. Elements Fe and P are redox sensitive elements, while Ni is not. Examining the distribution of these elements provides insight into the oxidation state of the environment, depending on specific minerals that are present and their spatial/textural relationships. Zonation, or the lack thereof, in the metal will be evident through the distribution of Ni, which gives a visual representation of composition. Measurements of siderophile elements from EMPA and LA-ICP-MS produce a quantitative analysis of the composition of the metal. Some of my samples show clear separation between metal clasts and matrix metal, while others do not. For the latter, LA-ICP-MS analyses that are labeled as matrix have been measured from metal in close contact with silicate clasts. Matrix metal has been analyzed for two of the samples in this study, Crab Orchard and Chinguetti.

5.1 Multi-Element Mapping

Crab Orchard (A1) matrix and clast metal are clearly distinguished, with metal clasts sometimes exceeding 1 cm in diameter (Fig. 18). The clasts exhibit a Widmanstätten pattern with kamacite lamellae of 0.75 to 1 mm in width and L/W (length/width) of ~ 3. Minor troilite and rare schreibersite are observed within the clasts, but phosphate and silicates are absent. Matrix metal is intimately mixed with the silicates and occurs as grains up to ~ 2 mm in size. Kamacite dominates the matrix metal grains with taenite occurring rarely as grains on the order of 100 μm long. Metal

clasts contain approximately 30 % taenite, and the matrix metal contains approximately 5 to 10 % taenite. Schreibersite is present in the matrix, but phosphates are the dominant P-bearing phase.

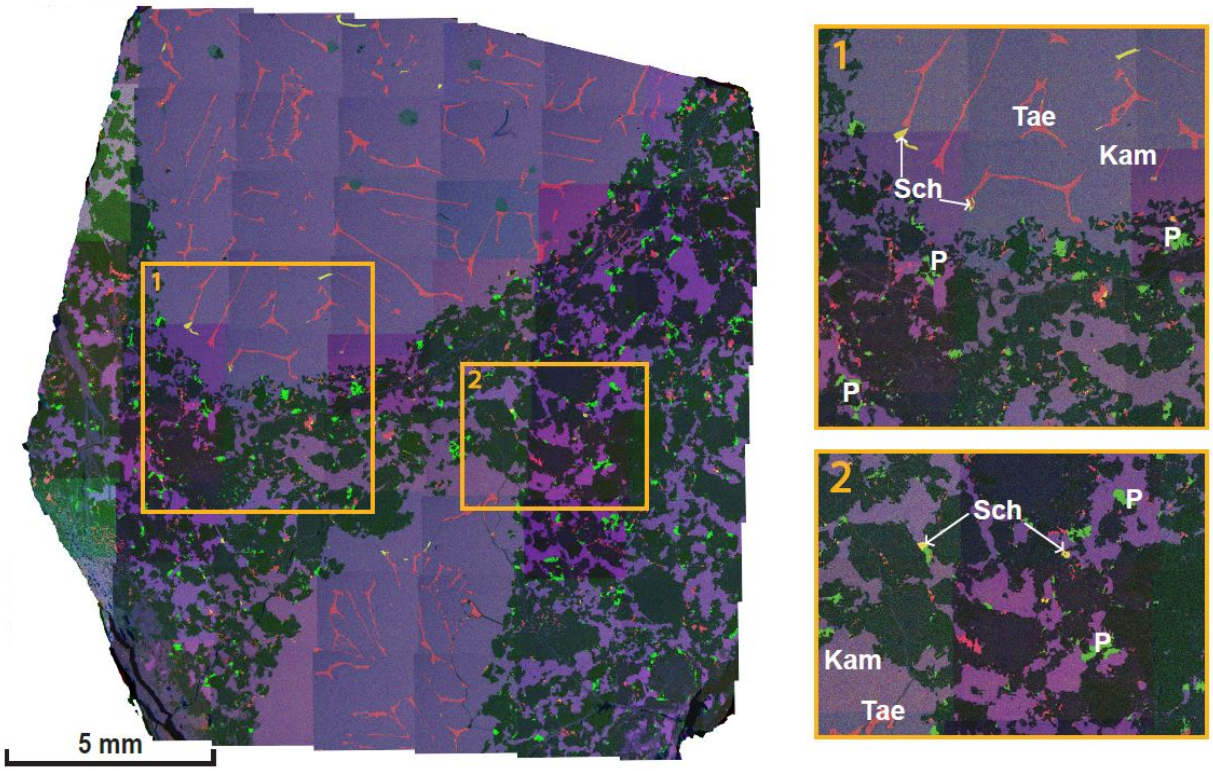

Figure 18. Multi-element x-ray map showing the distribution of Fe, Ni, and P in Crab Orchard. Kamacite (blue/purple), taenite (red), schreibersite (yellow), phosphate (green), silicates (black). Phosphates occur in association with silicates in the matrix. Schreibersite is the only P-bearing phase found in the metal clasts of Crab Orchard. Taenite rarely occurs in the matrix metal.

The distinction between metal clasts and matrix metal in Chinguetti (B1) is not as clear as within Crab Orchard (Fig. 19). The metal consists mostly of kamacite with amoeboid patches of taenite that range from 0.5 to 1 mm in length. Taenite makes up approximately 15 to 20 % of the metal throughout the sample, and taenite is not present in the area where matrix metal is analyzed for Chinguetti. In this sample, schreibersite grains ranging from 100 to 300 μm in size are the dominant P-bearing phase and are concentrated towards the center of the section. Rare phosphate is also present and generally occurs on the edges of silicate grains.

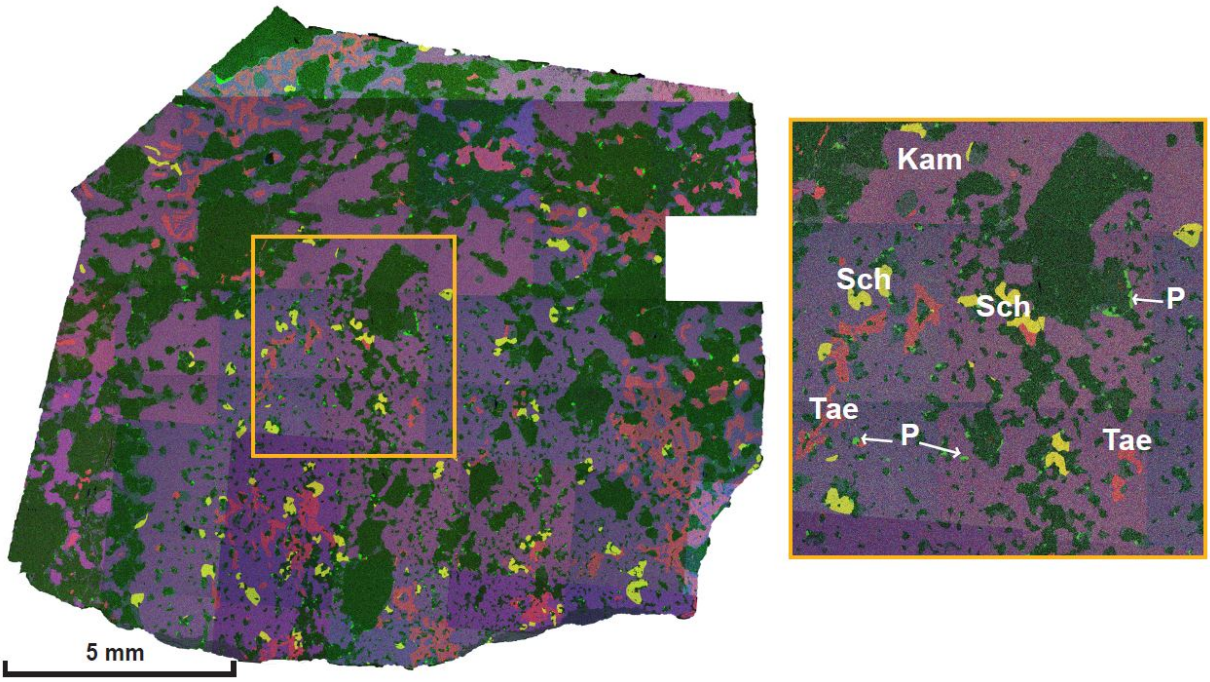

Figure 19. Multi-element x-ray map showing the distribution of Fe, Ni, and P in Chinguetti. Kamacite (blue/purple), taenite (red), schreibersite (yellow), phosphate (green), silicates (black). Metal clasts and matrix metal are not clearly distinguished in this sample. Phosphates occur as small grains associated with silicate clasts. Schreibersite forms larger grains and sometimes borders taenite.

Vaca Muerta (A1) exhibits unclear distinction between metal clasts and matrix metal, much like Chinguetti, except for one isolated metal clast (Fig. 20). The metal in Vaca Muerta is more intimately mixed with silicates than in Chinguetti. The large isolated metal clast that is separated from surrounding material, ~ 3.5 mm in length, consists of kamacite with scattered taenite blebs ranging from ~ 20 to 60 μm in size and taenite grains ~ 0.7 mm in length along the edges. This clast sits inside a rim of kamacite ~ 0.5 mm in width. Kamacite dominates the metal that is intimately mixed with the silicates, and taenite rarely occurs in patches up to 0.6 mm in length. The metal clast contains approximately 35 to 40 % taenite, and the matrix metal contains approximately 10 to 15 % taenite. Rare schreibersite grains up to ~ 30 μm in size are present only in the isolated metal clast and the outer kamacite rim. Phosphate is not present in the isolated clast but is abundant throughout the mixed metal and ranges in size from ~ 100 μm to 0.5 mm in length.

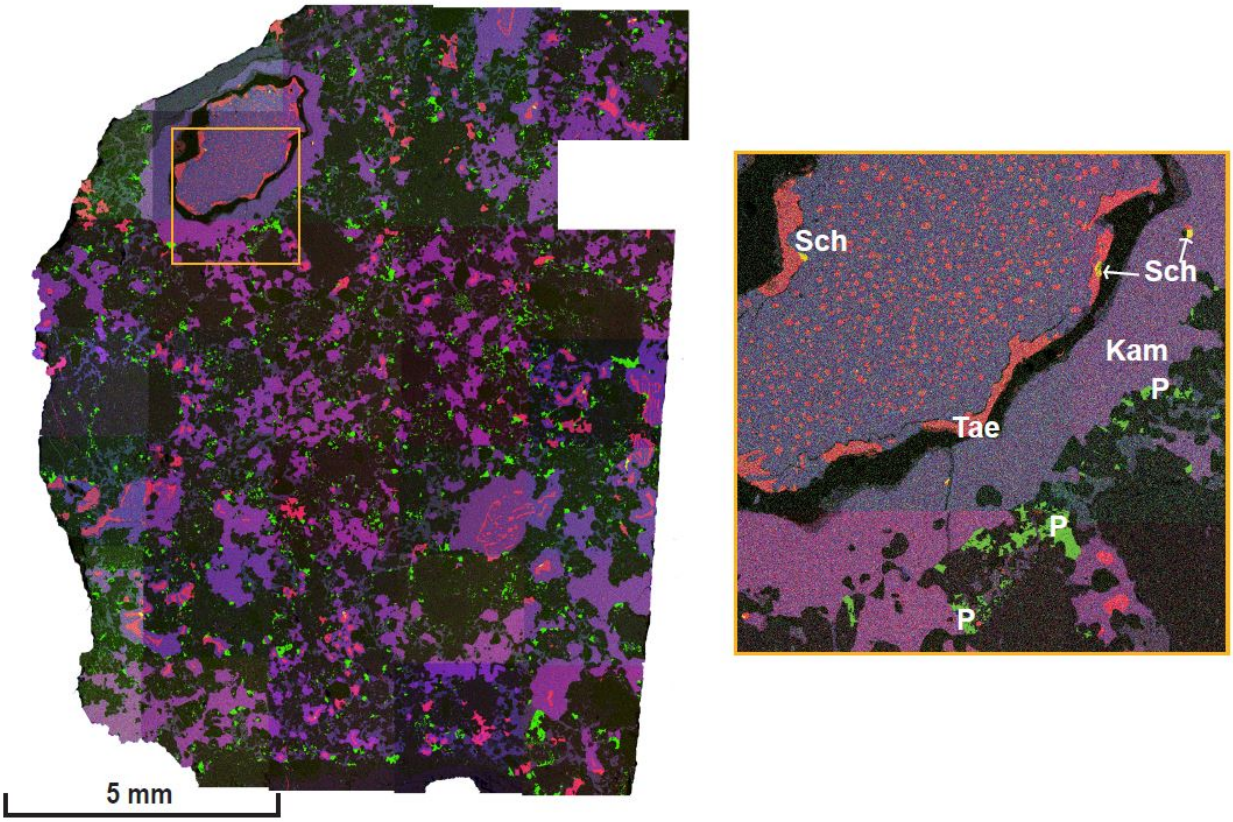

Figure 20. Multi-element x-ray map showing the distribution of Fe, Ni, and P in Vaca Muerta. Kamacite (blue/purple), taenite (red), schreibersite (yellow), phosphate (green), silicates (black). A few very small grains of schreibersite exist in the isolated metal clast. Phosphate grains are larger and abundant in the matrix. Taenite forms small blebs in the isolated metal clast and partially rims the outer edge.

The multi-element map of Fe, Ni, and P for RKPA79015 (C-an) contains a gradual transition from clast to matrix metal along the length of the section (Fig. 21). In the clast, kamacite exhibits an amoeboid texture, and both schreibersite and phosphate are present. Schreibersite occurs as grains ranging from 0.3 to 1 mm, and phosphates occur in grains on the order of 100 μm, which are directly associated with isolated silicate clasts within the metal clast. Matrix metal is intimately mixed with silicates and occurs in an interconnected vein network with individual veins having lengths up to ~ 1.75 mm. Kamacite dominates the matrix metal with rare taenite grains of ~ 100 μm in size. The metal clast contains approximately 15 to 20 % taenite, and the matrix metal contains approximately less than 5 % taenite. Phosphates occur sporadically throughout the matrix metal in grains ~ 100 μm in size. Small schreibersite grains, ~ 100 μm in size, occur throughout the matrix but are less common. Schreibersite is also present locally in larger grains ~ 0.1 to 1 mm in length.

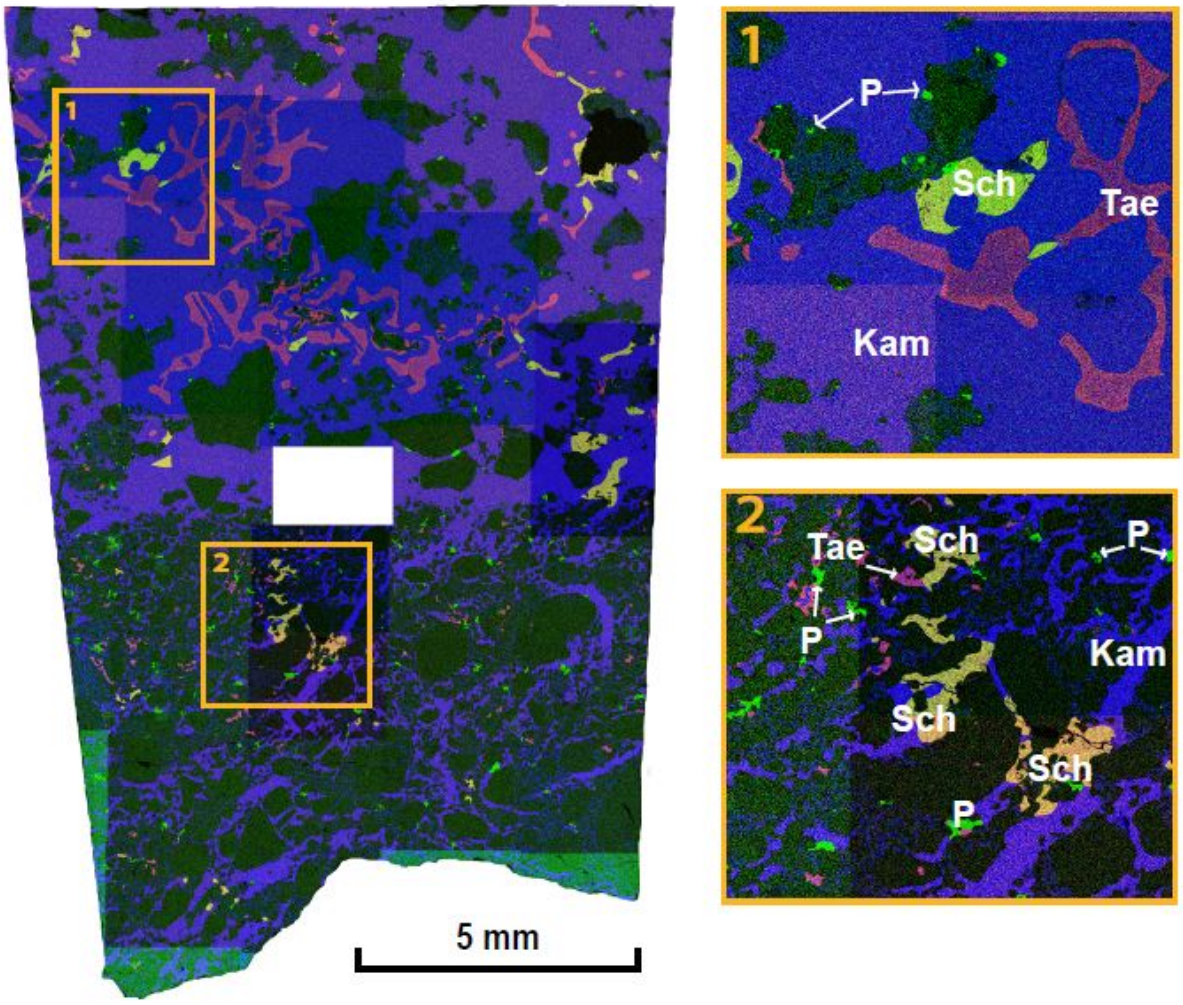

Figure 21. Multi-element x-ray map showing the distribution of Fe, Ni, and P in RKPA 79015. Kamacite (blue/purple), taenite (red), schreibersite (yellow), phosphate (green), silicates (black). Metal shows a gradual transition from matrix to clast. Phosphate grains are much smaller than schreibersite grains and are associated with isolated silicate clasts within the metal clast and with silicates in the matrix metal. Taenite rarely occurs in the matrix metal.

My sample of Chaunskij (an) (Fig. 22) consists mostly of a massive metal clast, ~ 1 cm wide, and a silicate clast, ~ 0.5 cm x 0.5 cm. Metal is rare within the silicate clast, and ranges from ~ 100 μm to 0.5 mm in size. Kamacite exists as amoeboid patches in the metal clast, and a large sinuous grain of troilite is present in the metal clast that reaches up to ~ 0.4 cm. The metal clast contains approximately 20 to 25 % taenite, and the matrix metal within the silicate clast contains approximately 10 % taenite. Schreibersite grains (~ 0.3 mm long) exist only in the metal clast in close association with both taenite and troilite. Phosphate grains, ~ 0.5 to 1 mm in size, are present in the metal clast and along the edges of the large silicate clast; smaller phosphates on the order of ~ 100 μm also exist in the matrix metal.

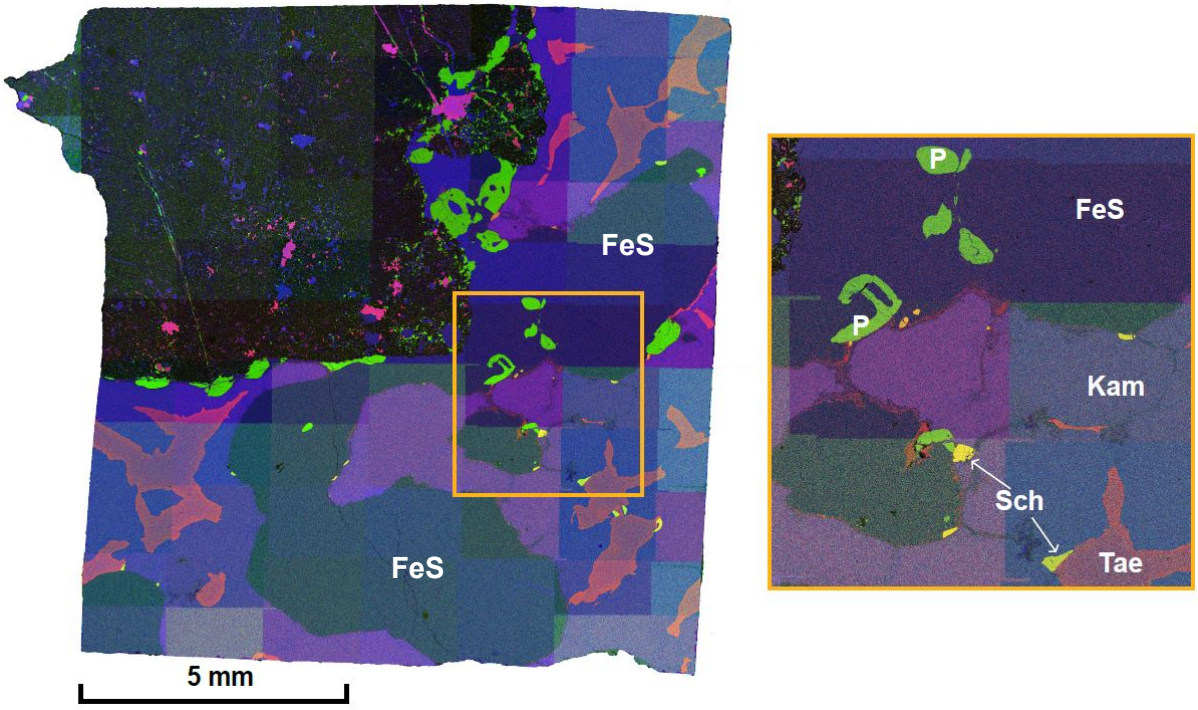

Figure 22. Multi-element x-ray map showing the distribution of Fe, Ni, and P in Chaunskij. Kamacite (blue/purple), taenite (red), schreibersite (yellow), phosphate (green), silicates (black). Chaunskij consists of metal clasts containing one large silicate clast and a large sinuous grain of troilite. Phosphates are larger in size than schreibersite and are mostly associated with the outer edge of the large silicate clast. Small schreibersite grains occur along the edges of taenite and troilite in the metal clast.

5.2 Major Element Chemistry

Only EMPA analyses that correspond to subsequent LA-ICP-MS analyses are presented here. All EMPA analyses can be found in Appendix A. Kamacite was the only metal phase analyzed in the matrix metal due to the small size and abundance of taenite in the matrix.

EMPA of kamacite and taenite in Crab Orchard (Tables 4, 5) for Fe, Ni, and Co demonstrate relative homogeneity within each phase. Kamacite within the metal clasts exhibits compositions of 6.51 to 7.03 wt. % Ni and 0.69 to 0.76 wt. % Co, with taenite ranging from 36.9 to 40.5 wt. % Ni and 0.25 to 0.31 wt. % Co. Only kamacite could be analyzed in the matrix, yielding a range of values from 4.47 to 6.26 wt.% Ni and 0.15 to 0.19 wt. % Co. Analyses of Si, S, P, Cr, and Cu were below detection limits.

Table 4. Electron microprobe data locations given correspond to relevant LA-ICP-MS analyses for Crab Orchard metal clasts. All EMPA data for Crab Orchard clasts are given in Appendix A-1.

Location	***Fe***	***Ni***	***Co***	***Total***
	Kamacite			
2	92.31	6.96	0.74	100.01
3	92.43	7.01	0.75	100.19
10	93.53	6.51	0.72	100.76
21	92.22	7.03	0.76	100.01
23	92.80	6.62	0.76	100.18
25	92.59	6.85	0.71	100.15
38	92.28	6.70	0.69	99.67
	Taenite			
1	59.62	38.88	0.30	98.8
11	60.59	39.26	0.28	100.13
16	61.08	39.13	0.25	100.46
17	59.72	40.54	0.26	100.52
24	59.91	38.76	0.28	98.95
26	61.97	36.89	0.31	99.17
37	59.99	39.75	0.30	100.04

Table 5. Electron microprobe data locations given correspond to relevant LA-ICP-MS analyses for Crab Orchard matrix metal. All EMPA data for Crab Orchard matrix metal are given in Appendix A-2.

Location	***Fe***	***Ni***	***Co***	***Total***
	Kamacite			
Ap10a13	93.125	6.038	0.161	99.324
Ap10a14	92.759	6.218	0.171	99.148
Ap10a15	93.112	6.047	0.162	99.321
Ap10a16	92.722	5.505	0.165	98.392
Ap10a17	92.722	5.505	0.165	98.392
Ap10a18	93.039	6.266	0.159	99.464
Ap10a19	93.112	6.047	0.162	99.321
Ap10a20	94.586	4.469	0.194	99.249
Ap10a21	94.586	4.469	0.194	99.249
Ap10a22	92.104	6.22	0.187	98.511
Ap10a23	93.394	5.954	0.176	99.524
Ap10a24	92.519	6.196	0.166	98.881
Ap10a25	93.045	5.644	0.181	98.87
Ap10a26	92.806	6.261	0.188	99.255
Ap10a27	94.053	5.606	0.192	99.851
Ap10a28	93.02	5.889	0.147	99.056

EMPA for Fe, Ni, and Co of kamacite and taenite in Chinguetti (Tables 6, 7) are slightly more heterogeneous than Crab Orchard but are relatively homogeneous overall. Kamacite compositions not closely associated with silicate clasts range from 5.63 to 6.82 wt. % Ni and 0.75 to 0.80 wt. % Co. Taenite compositions in the same area range from 35.6 to 40.8 wt. % Ni and 0.29 to 0.36 wt. % Co. Kamacite in metal that is closely associated with silicate clasts ranges from 5.55 to 6.66 wt. % Ni and 0.23 to 0.27 wt. % Co. Taenite was not analyzed for the metal closely associated with silicate clasts because of the small size of the grains.

Table 6. Electron microprobe data locations given correspond to relevant LA-ICP-MS analyses for Chinguetti metal clast. All EMPA data for Chinguetti clast are given in Appendix A-3.

Location	***Fe***	***Ni***	***Co***	***Total***
		Kamacite		
1	93.50	6.02	0.78	100.3
2	93.00	6.75	0.75	100.5
4	93.04	6.62	0.79	100.45
5	93.39	6.66	0.80	100.85
6	92.64	6.82	0.78	100.24
11	92.45	6.65	0.77	99.87
12	92.33	6.63	0.78	99.74
30	94.20	5.63	0.76	100.59
		Taenite		
14	60.67	38.63	0.34	99.64
16	63.85	35.56	0.33	99.74
26	63.64	35.74	0.36	99.74
27	58.57	40.75	0.30	99.62
31	61.57	37.58	0.29	99.44

Table 7. Electron microprobe data locations given correspond to relevant LA-ICP-MS analyses for Chinguetti matrix metal. All EMPA data for Chinguetti matrix metal are given in Appendix A-4.

Location	***Fe***	***Ni***	***Co***	***Total***
		Kamacite		
My12a11	95.438	5.984	0.267	101.689
My12a12	96.635	5.552	0.242	102.429
My12a13	94.562	6.666	0.254	101.482
My12a14	95.495	6.521	0.247	102.263
My12a15	96.433	6.079	0.245	102.757
My12a16	95.969	6.361	0.232	102.562
My12a17	95.969	6.361	0.232	102.562
My12a18	96.09	6.132	0.239	102.461
My12a20	95.61	5.689	0.247	101.546
My12a21	95.132	6.059	0.235	101.426
My12a22	94.833	6.363	0.229	101.425
My12a23	94.833	6.363	0.229	101.425
My12a24	95.536	6.23	0.242	102.008
My12a25	95.666	6.436	0.265	102.367
My12a26	94.663	6.571	0.245	101.479

Major element concentrations (Fe, Ni, Co) of kamacite and taenite in the Vaca Muerta isolated metal clast (Table 8) show the greatest homogeneity of all the samples studied. The isolated metal clast was the only metal analyzed for this sample. Kamacite compositions range from 5.43 to 5.55 wt. % Ni and 0.80 to 0.82 wt. % Co, and taenite compositions range from 42.5 to 43.2 wt. % Ni and 0.25 to 0.27 wt. % Co.

Table 8. Electron microprobe data locations given correspond to relevant LA-ICP-MS analyses for Vaca Muerta metal clast. All EMPA data for Vaca Muerta clast are given in Appendix A-5.

Location	***Fe***	***Ni***	***Co***	***Total***
	Kamacite			
1	94.28	5.46	0.81	100.55
13	93.93	5.55	0.80	100.28
15	94.37	5.43	0.82	100.62
	Taenite			
5	56.33	42.55	0.27	99.15
7	56.78	42.47	0.25	99.50
12	55.58	43.17	0.27	99.02

As with the type A and B mesosiderites presented above, kamacite major element concentrations (Fe, Ni, Co) in RKPA 79015 do not show much variation (Table 9). Kamacite compositions range from 6.28 to 7.08 wt. % Ni and 0.73 to 0.84 wt. % Co; whereas, taenite concentrations show a greater range from 32.3 to 39.3 wt.% Ni and 0.29 to 0.56 wt. % Co.

Table 9. Electron microprobe data locations given correspond to relevant LA-ICP-MS analyses for RKPA 79015 metal clast. All EMPA data for RKPA 79015 clast are given in Appendix A-6.

Location	***Fe***	***Ni***	***Co***	***Total***
	Kamacite			
8	93.15	6.61	0.80	100.56
15	92.70	6.85	0.76	100.31
29	93.10	7.02	0.78	100.9
	Taenite			
5	64.59	34.69	0.35	99.63
30	59.87	39.32	0.29	99.48
35	61.58	37.75	0.32	99.65

EMPA of kamacite and taenite major element concentrations (Fe, Ni, and Co) in Chaunskij indicate greater heterogeneity in the metal clast compared to types A, B, and C mesosiderites (Table 10). Kamacite compositions range from 4.98 to 7.09 wt.% Ni and 0.79 to 0.94 wt. % Co, and taenite ranges from 23.4 to 35.8 wt.% Ni and 0.35 to 0.52 wt. % Co.

Table 10. Electron microprobe data locations given correspond to relevant LA-ICP-MS analyses for Chaunskij metal clast. All EMPA data for Chaunskij clast are given in Appendix A-7.

Location	***Fe***	***Ni***	***Co***	***Total***
	Kamacite			
2	93.29	6.78	0.85	100.92
11	92.97	6.81	0.83	100.61
13	92.70	6.77	0.84	100.31
16	92.61	7.01	0.86	100.48
38	92.83	6.86	0.89	100.58
	Taenite			
4	68.01	32.51	0.36	100.88
8	68.54	31.05	0.38	99.97
19	71.23	27.85	0.46	99.54
20	72.03	27.65	0.42	100.1
21	63.35	35.79	0.36	99.5

5.3 Minor and Trace Element Chemistry

Minor and trace element analyses of Crab Orchard matrix and clast metal (Tables 11, 12; Fig. 23) illustrate that both are enriched at ~ 10 × CI for both highly and moderately refractory siderophile elements. In contrast, the volatile siderophiles are depleted at ~ 0.1 to 1 × CI. As only kamacite was measured in the matrix, clast and matrix kamacite compositions are compared in Figure 23. For most highly and moderately refractory siderophile elements, there is no significant compositional difference between matrix and clast metal. Notable exceptions are Mo, whose concentration is higher in the clast kamacite, and Pd, whose concentration is lower in the clast kamacite. Au, Cu, and P are at higher concentrations in the clast compared to the matrix, although the data for P are limited. Notably, Mo in the matrix metal exhibits a pronounced depletion relative to adjacent elements of similar volatility.

In addition to differences between matrix and clast kamacite, differences between kamacite and taenite within the Crab Orchard clasts are observed (Table 12; Fig. 24). Relative to kamacite, taenite exhibits higher concentrations in most siderophile elements at ~ 20 to 30 × CI. Exceptions are Co, Fe, and P in which taenite is slightly to strongly depleted relative to kamacite. These depletions are likely correlated with the elements' affinity for kamacite compared to taenite.

Table 11. Siderophile element abundances for Crab Orchard matrix metal collected by LA-ICP-MS.

Location	***Re***	***Os***	***W***	***Ir***	***Mo***	***Ru***	***Pt***	***Rh***	***Co***	***Ni***	***Fe***	***Pd***	***Au***	***Cu***	***P***	***Ga***	***Ge***
	ppm	ppm	ppm	ppm	ppm	ppm	ppm	ppm	ppm	wt.%	wt. %	ppm	ppm	ppm	ppm	ppm	ppm
										Kamacite							
Ap10a13	0.51	3.2	0.7	3.5	6.5	4.7	6.8	1.0	4981	6.04	93.1	1.7	0.24	29	168	7.6	41
Ap10a14	0.75	5	0.7	3.7	4.6	5	8.5	0.8	6121	6.22	92.8	1.8	0.39	32	255	9.2	53
Ap10a15	0.35	4.4	0.8	3.7	3.6	5.4	8.1	1.0	5172	6.05	93.1	2	0.35	31	195	8.4	52
Ap10a16	0.42	4.1	0.8	4.5	3.7	5.2	7.7	1.0	5441	5.51	92.7	2.5	0.35	21	128	9.4	61
Ap10a17	0.43	4.8	0.8	4.1	3	5.2	8	0.9	4948	5.51	92.7	1.9	0.39	22	153	8.4	54
Ap10a18	0.41	4.8	0.8	4.4	3.8	6.1	8.1	1.1	5361	6.27	93.0	1.9	0.39	25	172	9.3	61
Ap10a19	0.41	5.1	1.0	4.9	3.8	6.2	9.1	1.0	5496	6.05	93.1	2.1	0.5	29	200	9.2	56
Ap10a20	0.4	4.5	0.7	4.1	1.9	5	7.8	1.0	4775	4.47	94.6	1.4	0.36	15	116	8.8	51
Ap10a21	0.47	4.4	0.7	3.8	3	5.1	7.9	0.9	4579	4.47	94.6	1.8	0.37	17	136	8.2	53
Ap10a22	0.37	5.3	0.8	4.4	3.8	4.6	9.2	1.1	5919	6.22	92.1	2.6	0.52	33	215	10.7	67
Ap10a23	0.45	4.8	0.9	4.2	3.7	5.2	8.3	1.0	5075	5.95	93.4	2	0.53	30	203	10.3	58
Ap10a24	0.44	5.1	0.9	4.7	4.5	6.3	8.5	1.1	5246	6.19	92.5	2.5	0.59	32	202	10.4	60
Ap10a25	0.48	4.9	0.9	4.6	3.5	5.8	8.9	1.1	5378	5.64	93.0	1.9	0.44	24	148	9.8	68
Ap10a26	0.39	5.7	0.9	4.5	3.9	5.7	10	1.1	5652	6.26	92.8	1.8	0.51	33	200	10.5	59
Ap10a27	0.49	4.1	0.8	3.6	3.2	4.9	8.3	1.0	5000	5.61	94.1	2.2	0.51	29	210	8.6	57
Ap10a28	0.45	4.7	1.0	3.9	5.1	5.4	9.5	1.1	5163	5.89	93.0	2.2	0.52	29	196	9.5	54
Average	0.45	4.7	0.8	4.2	3.8	5.4	8.4	1.0	5269	5.77	93.2	2.0	0.44	27	181	9.3	57
Std. Dev.	0.09	0.6	0.1	0.4	1.0	0.5	0.8	0.1	403	0.57	6.91	0.3	0.09	5.6	37.3	0.9	6.5
CI-norm Average	11.7	9.58	8.89	9.16	4.27	7.56	8.33	7.81	10.5	5.50	5.06	15.5	3.12	0.22	0.17	1.01	1.82

Data are normalized to CI-chondrite abundances (McDonough and Sun, 1995).

Table 12. Siderophile element abundances for Crab Orchard metal clasts collected by LA-ICP-MS.

Location	*Re*	*Os*	*W*	*Ir*	*Mo*	*Ru*	*Pt*	*Rh*	*Co*	*Ni*	*Fe*	*Pd*	*Au*	*Cu*	*P*	*Ga*	*Ge*
	ppm	ppm	ppm	ppm	ppm	ppm	ppm	ppm	ppm	wt.%	wt. %	ppm	ppm	ppm	ppm	ppm	ppm
	Kamacite																
2	0.5	5.7	1.1	4.8	7.7	5.9	10	1.4	5106	6.96	94.6	3.2	0.77	75	--	--	--
3	0.49	5.6	1.0	4.8	8.0	7.1	9.9	1.3	5280	7.01	91.1	2.6	0.68	77	--	--	--
10	0.46	5.5	0.92	4.8	7.5	6.1	8.3	1.1	4862	6.51	86.5	2.7	0.85	48	--	9.7	50
21	0.55	5.7	0.84	5.0	7.7	5.2	8.9	1.1	5183	7.03	98.0	2.4	1.1	57	--	11	54
23	0.56	5.2	0.99	4.6	7.0	6.6	9.3	1.2	5107	6.62	91.8	2.8	0.67	76	405	--	--
25	0.48	6.4	1.3	5.3	7.3	6.7	9.9	1.1	5133	6.85	95.3	3.0	0.77	75	428	--	--
38	0.47	6.3	0.79	5.0	7.0	6.7	9.4	1.1	5243	6.70	96.5	2.6	1.0	54	352	11	58
Average	0.50	5.8	0.99	4.9	7.4	6.3	9.4	1.2	5130	6.81	93.4	2.7	0.84	66	395	10.6	54
Std. Dev.	0.04	0.4	0.17	0.2	0.4	0.6	0.6	0.1	136	0.20	3.90	0.3	0.17	13	39.0	0.8	3.8
CI-norm Average	12.7	11.8	10.6	10.8	8.25	8.92	9.32	9.14	10.3	6.49	5.16	4.97	5.99	0.55	0.37	1.2	1.7
	Taenite																
1	0.76	8.7	1.1	8.0	10	22	15	2.3	1139	38.9	61.5	19	3.3	1270	--	--	--
11	0.91	11	1.4	8.1	14	25	16	2.3	1096	39.3	63.0	19	6.0	1072	43.7	65	127
16	0.68	8.1	1.3	6.5	11	20	14	1.8	996	39.1	56.6	16	5.9	1116	--	67	132
17	0.78	9.6	1.3	7.3	12	21	16	1.9	1113	40.5	62.3	17	6.1	1140	40.1	72	135
24	0.69	9.4	1.1	6.5	11	20	15	2.0	1115	38.8	61.0	17	3.7	1376	--	--	--
26	0.89	9.5	1.1	8.0	12	22	16	2.3	1284	36.9	64.5	19	3.5	1257	55.2	--	--
37	0.76	9.6	1.0	7.7	11	19	14	1.7	1111	39.8	61.1	15	5.2	1092	--	66	127
Average	0.78	9.4	1.2	7.4	12	21	15	2.1	1122	39.0	61.4	18	4.8	1189	46.3	67	130
Std. Dev.	0.09	0.8	0.1	0.7	1.2	2.0	0.8	0.2	84.8	1.12	2.46	1.7	1.3	113	7.89	2.9	4.0
CI-norm Average	19.8	19.1	12.6	16.4	12.9	30.2	15.0	15.8	2.24	37.2	3.39	31.9	34.3	9.91	0.04	7.33	4.20

Data are normalized to CI-chondrite abundances (McDonough and Sun, 1995). Dashes indicate concentrations below detection limits.

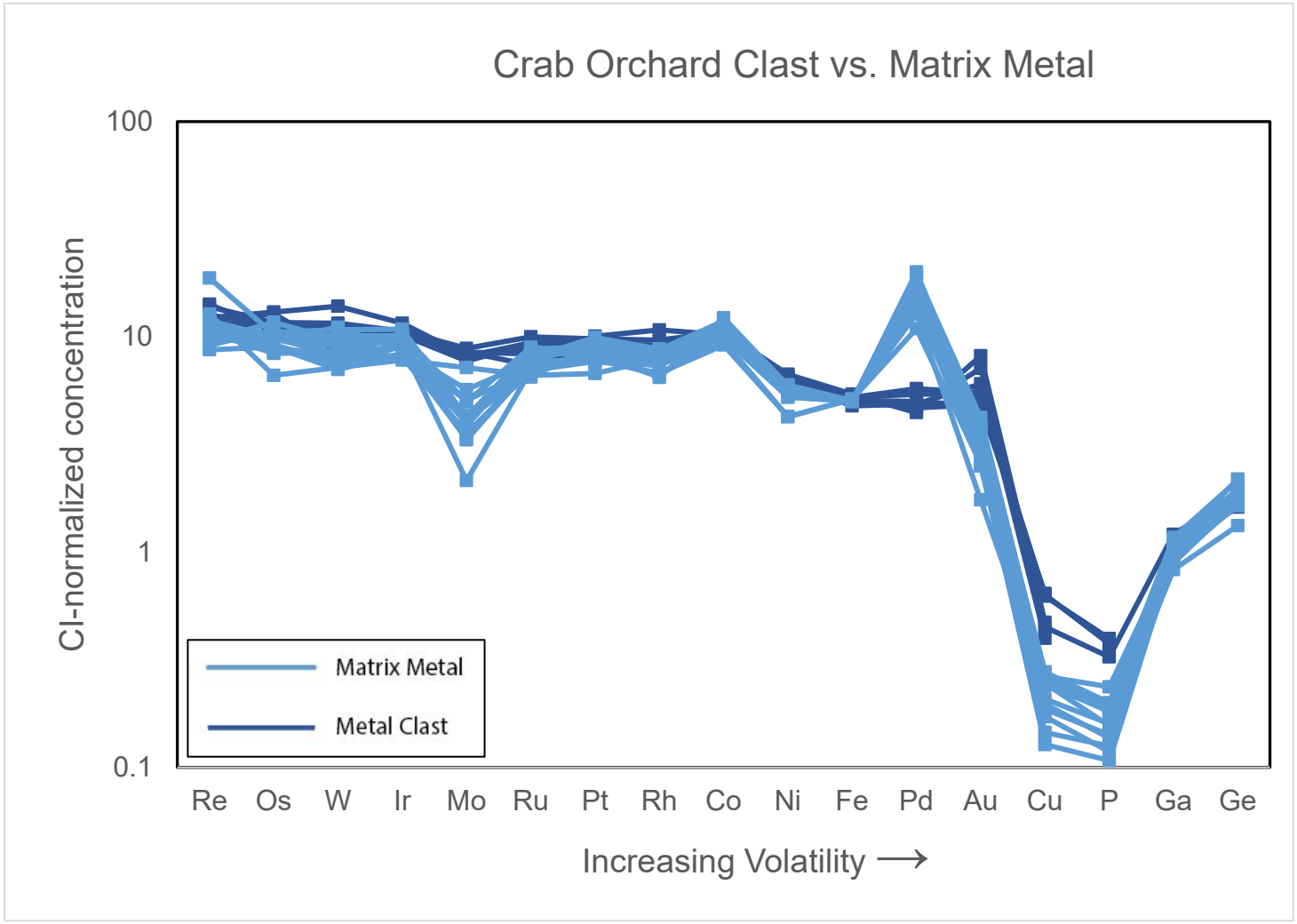

Figure 23. Comparison of Crab Orchard metal clast kamacite and matrix metal kamacite compositions. Metal clast siderophile concentrations (dark blue), matrix metal siderophile concentrations (light blue). Plot shows the depletions of Mo, Cu, and P and an enrichment of Pd in the matrix metal compared to the metal clasts.

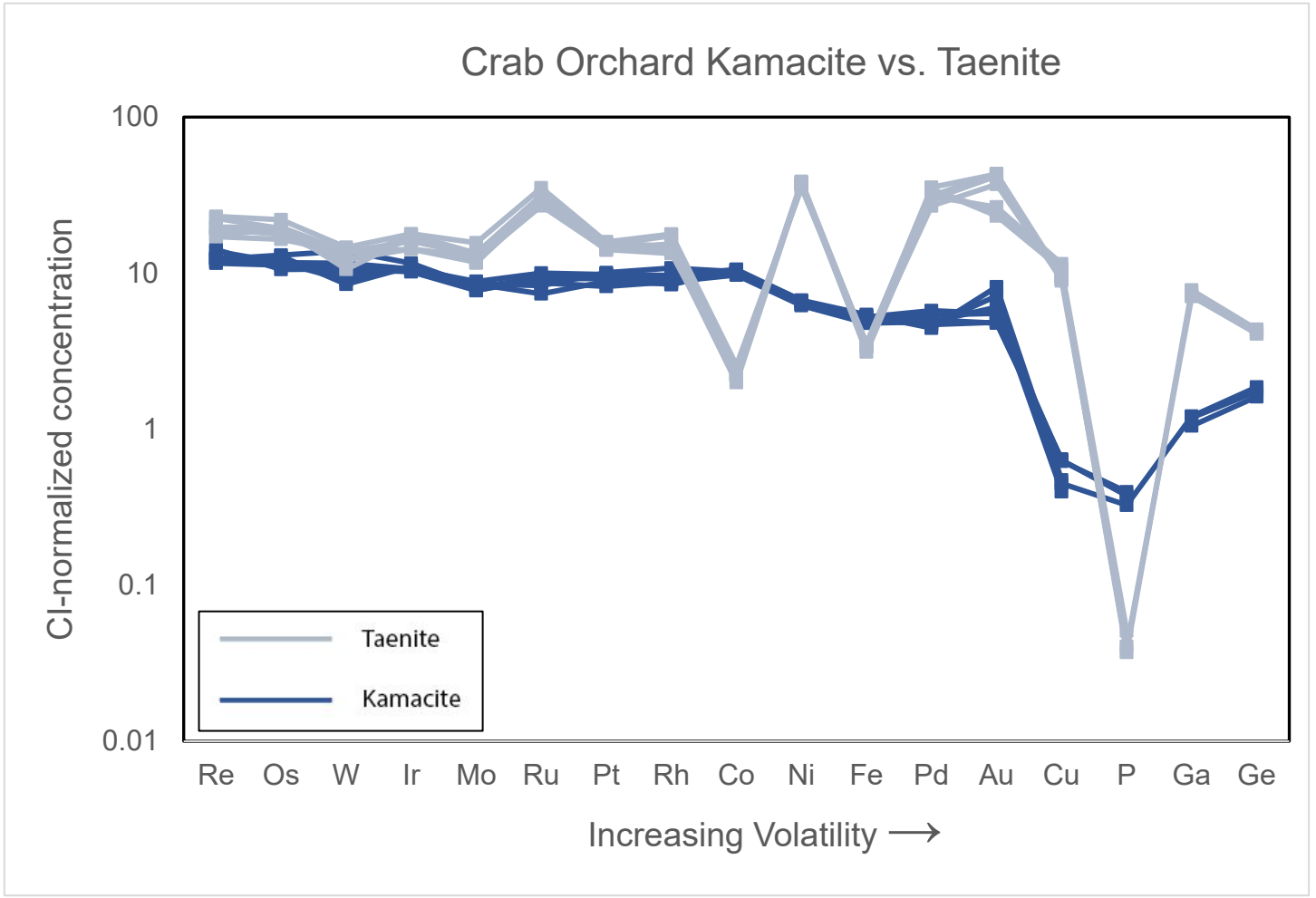

Figure 24. Data plot showing siderophile element concentrations distributed into metal phases kamacite and taenite in Crab Orchard metal clasts.

Chinguetti matrix and clast kamacite compositions are compared in Figure 25. Highly and moderately refractory siderophile elements in the matrix and clast metal are enriched at ~ 10 to 13 × CI (Tables 13, 14; Fig. 25). The volatile siderophile elements show a depletion at ~ 0.1 to 1 × CI. Concentrations of highly and moderately refractory siderophile elements do not different significantly between matrix and clast metal and both show a depletion in Mo relative to elements of similar volatility. The average concentration of Mo in the matrix metal is ~ 4.5 × CI, and ~ 6 × CI in the clast metal. In contrast to Crab Orchard, Pd is not enriched in the matrix metal and the concentration of Pd in both the matrix and clast kamacite is ~ 4 to 4.5 × CI. Matrix metal shows depletions in Cu and P compared to the metal clast, similarly to Crab Orchard, but Au concentrations are significantly enriched in the metal clast.

Differences in kamacite and taenite in the metal clast in Chinguetti are shown in Figure 26. Taenite exhibits higher concentrations of most siderophile elements (~ 15 to 30 × CI), relative to kamacite (Table 14; Fig. 26). Much like Crab Orchard, the exceptions are Co, Fe, and P, which exhibit a range of depletions compared to kamacite. As with Crab Orchard, these depletions are expected with the higher Ni content of taenite relative to kamacite.

Table 13. Siderophile element abundances for Chinguetti matrix metal collected by LA-ICP-MS.

Location	***Re***	***Os***	***W***	***Ir***	***Mo***	***Ru***	***Pt***	***Rh***	***Co***	***Ni***	***Fe***	***Pd***	***Au***	***Cu***	***P***	***Ga***	***Ge***
	ppm	ppm	ppm	ppm	ppm	ppm	ppm	ppm	ppm	wt.%	wt. %	ppm	ppm	ppm	ppm	ppm	ppm
	Kamacite																
My12a11	0.42	5.2	0.96	5.0	4.1	7.1	8.7	1.13	6153	5.98	95.4	1.8	0.39	41	206	10	60
My12a12	0.48	5.5	0.77	4.7	3.4	6.1	7.8	1.14	5796	5.55	96.6	1.8	0.4	35	143	9.8	59
My12a13	0.57	5.2	1.00	5.1	4.4	5.9	8.4	1.2	6430	6.67	94.6	2.1	0.44	51	249	11	65
My12a14	0.5	6.1	0.88	5.2	4.1	6.6	8.8	1.11	5879	6.52	95.5	2.1	0.45	51	228	11	60
My12a15	0.61	7.2	1.10	6.1	4.6	6.9	9.7	1.37	6697	6.07	96.4	2.1	0.47	40	182	11	67
My12a16	0.58	6.5	0.93	5.8	4.3	5.9	9.6	1.2	6285	6.36	96.0	2.4	0.46	51	245	12	63
My12a17	0.53	6.9	0.89	5.9	4.8	6.0	9.4	1.19	6420	6.36	96.0	1.9	0.49	48	247	11	60
My12a18	0.54	6.4	0.89	5.7	4.0	5.9	9.5	1.13	5575	6.13	96.1	2.0	0.44	41	172	9.6	54
My12a20	0.64	7.4	0.77	6.5	3.8	6.8	9.8	1.13	6053	5.69	95.6	2.2	0.38	39	140	9.5	60
My12a21	0.58	7.5	0.75	6.2	3.7	6.6	9.8	1.26	6150	6.10	95.1	2.4	0.36	44	186	10	58
My12a22	0.68	7.6	0.99	6.4	3.9	6.4	10	1.14	6138	6.36	94.8	2.3	0.49	55	258	11	64
My12a23	0.61	7.8	1.10	6.5	4.7	6.8	10	1.47	6191	6.36	94.8	2.3	0.51	53	269	11	63
My12a24	0.58	7.3	1.20	6.0	3.8	7.1	11	1.13	6916	6.23	95.5	2.4	0.49	47	231	11	64
My12a25	0.48	5.3	0.85	4.8	3.7	5.2	8.8	1.22	6081	6.44	95.7	2.1	0.5	58	261	11	65
My12a26	0.61	5.7	1.10	5.4	3.8	6.6	8.9	1.13	6565	6.57	94.7	2.5	0.51	57	323	13	64
Average	0.56	6.5	0.94	5.7	4.1	6.4	9.4	1.20	6222	6.22	95.5	2.2	0.45	47	223	11	62
Std. Dev.	0.07	0.9	0.13	0.6	0.4	0.5	0.8	0.10	348	0.31	6.32	0.2	0.05	7.1	50.6	0.9	3.5
CI-norm Average	14.2	13.3	10.1	12.5	4.52	8.99	9.28	9.21	12.4	5.93	5.28	3.91	3.23	0.39	0.21	1.19	1.99

Data are normalized to CI-chondrite abundances (McDonough and Sun, 1995).

Table 14. Siderophile element abundances for Chinguetti metal clast collected by LA-ICP-MS.

Location	*Re*	*Os*	*W*	*Ir*	*Mo*	*Ru*	*Pt*	*Rh*	*Co*	*Ni*	*Fe*	*Pd*	*Au*	*Cu*	*P*	*Ga*	*Ge*
	ppm	ppm	ppm	ppm	ppm	ppm	ppm	ppm	ppm	wt.%	wt. %	ppm	ppm	ppm	ppm	ppm	ppm
	Kamacite																
1	0.55	5.5	1.1	5.3	4.9	7.1	11	1.2	5775	6.04	93.5	2.5	0.65	65	289	9.6	--
2	0.37	4.4	0.88	4.1	3.8	4.5	8.1	0.94	5262	6.75	87.6	2.1	1.1	58	--	8.9	53
4	0.47	5.1	0.96	5.0	5.5	7.4	11	1.3	6018	6.62	97.2	2.6	--	74	397	11	69
5	0.40	4.4	0.87	5.0	6.0	6.9	10	1.2	6130	6.66	92.3	2.1	--	84	--	11	66
6	0.65	4.7	0.70	4.7	6.8	5.7	9.6	1.2	6186	6.82	--	2.2	1.4	77	299	11	68
11	0.56	7.6	0.94	6.2	4.8	7.1	10	1.1	5691	6.19	92.5	2.7	0.64	76	274	8.9	--
12	0.52	6.6	0.99	6.0	4.1	8.8	11	1.3	5438	7.25	92.3	3.1	0.69	159	273	10	--
30	0.70	6.5	0.74	6.3	4.3	6.8	11	1.3	5909	6.63	98.0	2.2	--	60	--	9.4	59
Average	0.53	5.6	0.90	5.3	5.0	6.8	10	1.2	5801	6.62	93.3	2.4	0.89	82	306	10	63
Std. Dev.	0.11	1.2	0.13	0.8	1.0	1.3	1.0	0.1	327.4	0.37	3.47	0.4	0.33	33	51.7	0.9	6.7
CI-norm Average	13.4	11.4	9.63	11.7	6.00	9.57	10.1	9.20	11.6	6.30	5.16	4.41	6.35	0.68	0.28	1.09	2.02
	Taenite																
14	0.66	7.8	1.3	6.7	8.6	19	14	1.9	1219	36.2	60.7	18	3.6	1527	56.3	58	--
16	0.78	9.3	1.1	7.8	9.0	17	14	2.3	1691	37.1	63.9	16	2.9	1515	54.1	46	--
26	0.74	7.5	1.3	7.2	9.1	20	17	2.3	1540	33.3	63.6	17	3.0	1334	60.3	45	--
31	0.78	6.0	1.6	6.3	7.0	18	15	1.7	1095	37.6	61.0	15	6.0	1215	57.2	56	125
Average	0.74	7.6	1.3	7.0	8.4	19	15	2.0	1386	36.0	62.3	17	4.0	1398	57.0	51	125
Std. Dev.	0.05	1.2	0.2	0.6	0.9	1.3	1.6	0.3	248.9	2.08	1.58	1.1	1.3	133.5	2.57	6.6	--
CI-norm Average	18.7	15.6	14.2	15.4	9.37	26.5	15.0	15.8	2.77	34.3	3.44	30.1	27.8	11.6	0.05	5.58	4.03

Data are normalized to CI-chondrite abundances (McDonough and Sun, 1995). Dashes indicate concentrations below detection limits.

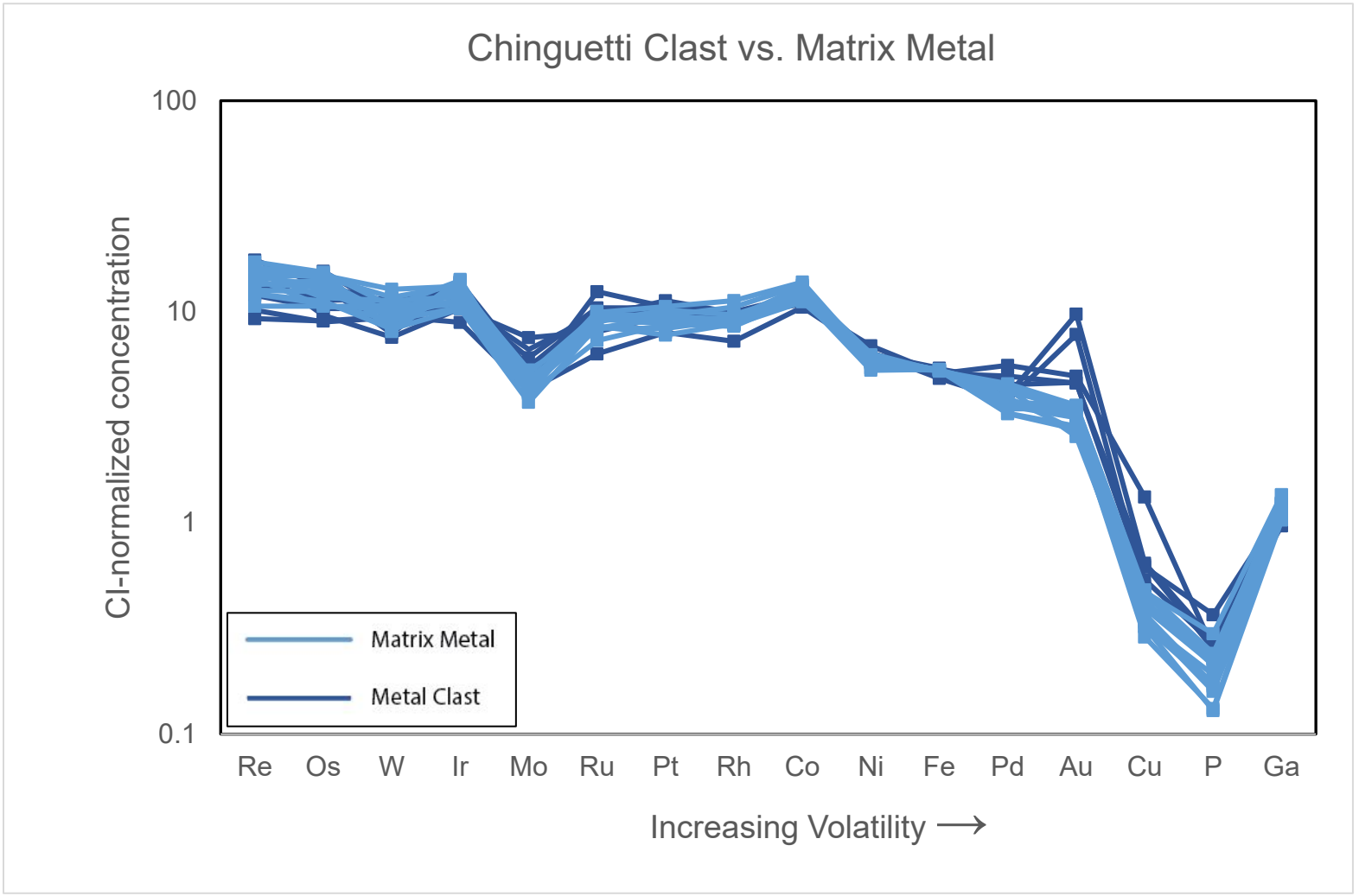

Figure 25. Comparison of Chinguetti metal clast kamacite and matrix metal kamacite compositions. Metal clasts siderophile concentrations (dark blue), matrix metal siderophile concentrations (light blue). Plot shows the depletions of Cu, and P of the matrix metal compared to the metal clasts. Matrix metal does not show an enrichment in Pd, but the metal clast is enriched in Au compared to the matrix metal.

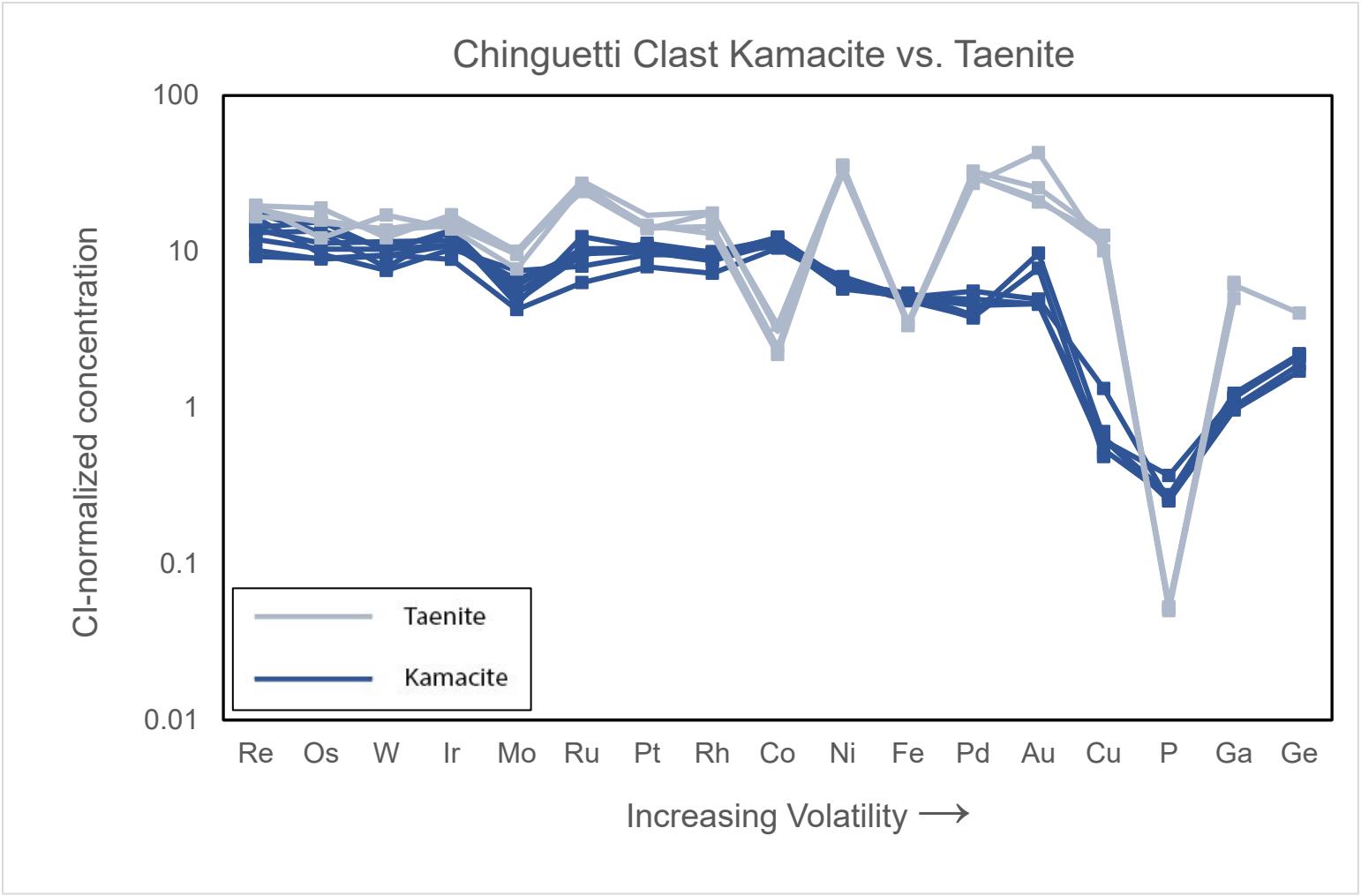

Figure 26. Data plot showing siderophile element concentrations distributed into metal phases kamacite and taenite in the Chinguetti metal clast.

Vaca Muerta kamacite concentrations of highly and moderately refractory siderophile elements are relatively unfractionated and occur at ~ 10 × CI, with a depletion of volatile siderophiles at ~ 0.1 to 1 × CI (Table 15; Fig. 27). Overprinted on this are depletions of Mo relative to elements of similar volatility, Ir and Ru. Although data for volatile siderophiles in kamacite and taenite are limited, Vaca Muerta exhibits enrichments of most siderophile elements in taenite relative to kamacite with the exception Co, Fe, and P, as also observed in Crab Orchard and Chinguetti.

Table 15. Siderophile element abundances for Vaca Muerta metal clast collected by LA-ICP-MS.

Location	***Re***	***Os***	***W***	***Ir***	***Mo***	***Ru***	***Pt***	***Rh***	***Co***	***Ni***	***Fe***	***Pd***	***Au***	***P***	***Ga***
	ppm	ppm	ppm	ppm	ppm	ppm	ppm	ppm	Ppm	wt.%	wt. %	ppm	ppm	ppm	ppm
	Kamacite														
1	0.48	3.6	--	3.5	6.3	5.3	7.4	0.89	5744	3.82	94.3	1.9	--	--	3.2
13	0.46	4.2	0.87	4.1	4.3	5.0	10	1.0	5385	6.99	93.9	2.9	0.75	114	6.0
15	0.37	4.2	0.75	3.8	3.6	6.8	7.6	0.89	5170	4.46	94.4	2.0	0.58	111	3.4
Average	0.43	4.0	0.81	3.8	4.7	5.7	8.5	0.95	5433	5.09	94.2	2.3	0.67	113	4.2
Std. Dev.	0.06	0.4	0.08	0.3	1.4	1.0	1.7	0.09	290.3	1.68	0.23	0.5	0.12	2.1	1.5
CI-norm Average	11.0	8.12	8.71	8.36	5.27	8.03	8.39	7.27	10.9	4.85	5.20	4.17	4.77	0.10	0.46
	Taenite														
5	0.28	7.5	0	6.0	2.3	12	14	1.4	857	59.8	56.3	37	7.4	--	51
7	0.49	8.5	1.2	6.9	5.1	18	13	1.4	916	41.7	55.6	27	7.3	--	45
12	--	12	--	--	--	--	--	--	--	49.0	55.6	28	9.5	--	53
	0.69	9.1	--	6.1	2.5	--	6.8	--	--	60.0	55.6	26	5.9	--	56
	--	8.5	1.6	5.4	4.5	16	12	1.5	1092	47.3	55.6	24	6.8	--	44
Average	0.49	9.5	1.4	6.1	3.6	15	10	1.5	955	51.6	55.7	29	7.4	--	50
Std. Dev.	0.20	1.6	0.3	0.6	1.4	3.5	3.1	0.01	122.2	8.06	0.34	5.0	1.3	--	5.03
CI-norm Average	12.33	18.55	14.99	13.42	4.02	21.69	11.27	11.12	1.91	49.10	3.08	51.99	52.58	--	5.43

Data are normalized to CI-chondrite abundances (McDonough and Sun, 1995). Dashes indicate concentrations below detection limits.

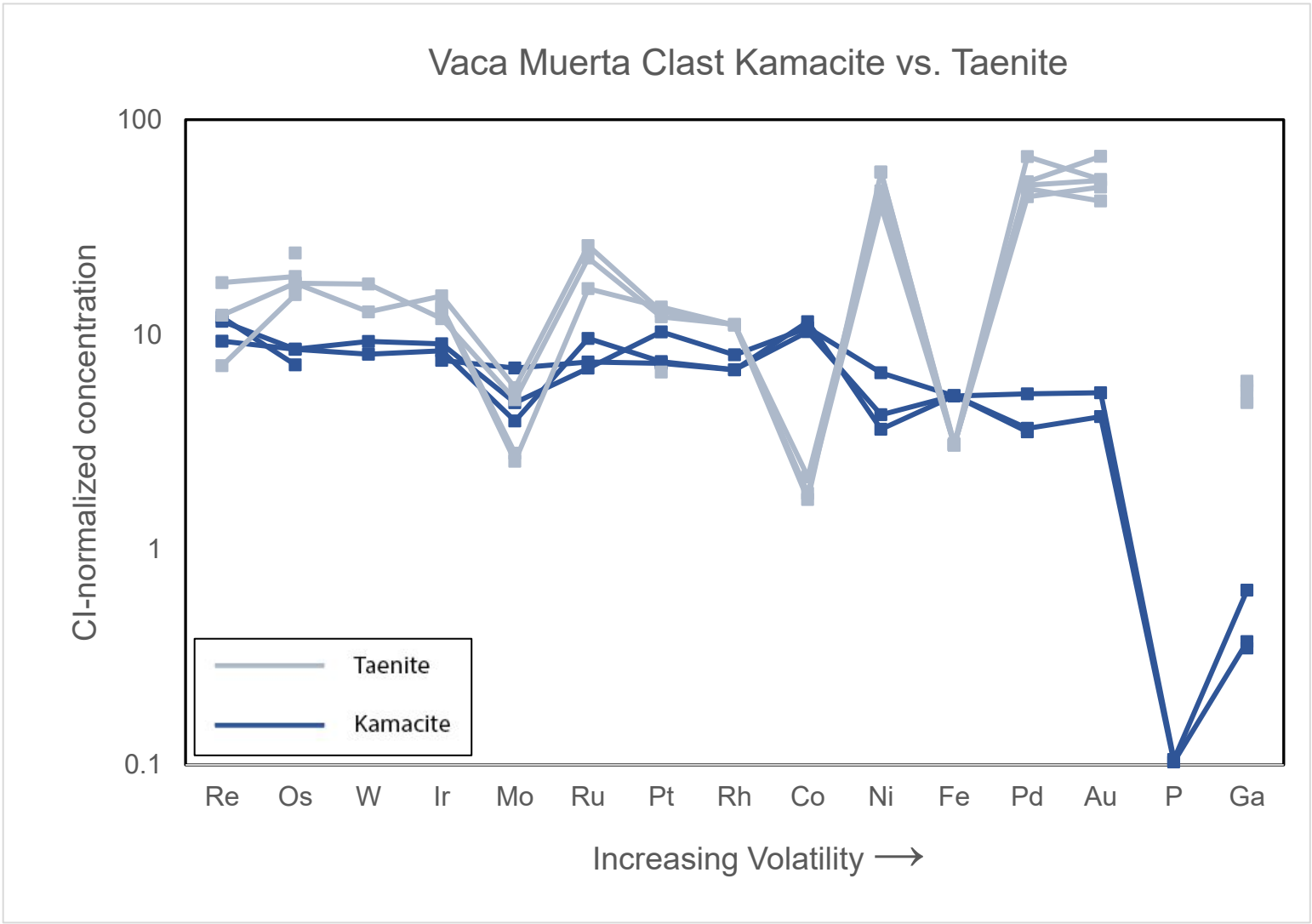

Figure 27. Data plot showing siderophile element concentrations distributed into metal phases kamacite and taenite in the Vaca Muerta metal clast.

In contrast to the type A and B mesosiderites analyzed in this study, the highly refractory siderophile elements Re, Os, and Ir in RKPA 79015 are depleted (~ 1 to 3 × CI) relative to the moderately refractory siderophile elements (~ 3 to 5 × CI) (Table 16; Fig. 28). The volatile siderophiles exhibit depletions relative to the moderately refractory siderophile elements, although these depletions are less marked compared to the type A and B mesosiderites. For example, Ga and Ge occur at ~ 1 to 6 × CI in RKPA79015 compared to ~ 0.1 to 1 × CI in type A and B mesosiderites. As with type A and B mesosiderites, taenite shows higher concentrations in most siderophile elements, excluding Co, Fe, and P.

Table 16. Siderophile element abundances for RKPA 79015 metal clast collected by LA-ICP-MS.

Location	***Re***	***Os***	***W***	***Ir***	***Mo***	***Ru***	***Pt***	***Rh***	***Co***	***Ni***	***Fe***	***Pd***	***Au***	***Cu***	***P***	***Ga***	***Ge***
	ppm	ppm	ppm	ppm	ppm	ppm	ppm	ppm	ppm	wt.%	wt. %	ppm	ppm	ppm	ppm	ppm	ppm
	Kamacite																
8	0.045	0.70	0.57	0.77	6.1	3.7	3.6	1.0	4922	6.61	86.8	2.3	0.80	52	602	8.8	38
15	0.095	0.81	0.71	1.0	6.9	4.5	4.1	1.0	5341	6.85	89.2	2.8	0.80	54	612	8.4	43
29	0.061	0.93	0.67	0.90	5.8	3.8	3.6	0.9	5055	7.02	88.1	2.9	1.0	60	625	8.5	42
Average	0.067	0.82	0.65	0.87	6.2	4.0	3.8	1.0	5106	6.83	88.0	2.7	0.88	55	613	8.5	41
Std. Dev.	0.025	0.11	0.07	0.09	0.6	0.4	0.3	0.1	214	0.21	1.20	0.3	0.1	3.9	11.7	0.2	2.6
CI-norm Average	1.70	1.66	7.01	1.92	6.92	5.63	3.75	7.45	10.2	6.50	4.86	4.86	6.26	0.46	0.57	0.93	1.32
	Taenite																
5	0.10	1.4	0.73	1.2	10	10	6.0	1.6	1323	34.7	60.5	17	3.8	943	61.2	38	76
30	0.094	1.4	0.80	1.4	7.9	10	7.1	1.4	1361	39.3	55.8	23	6.6	1246	93.8	61	93
35	0.063	0.90	0.69	0.81	9.6	12	5.3	1.6	1102	37.8	52.6	18	4.0	957	45.1	44	84
Average.	0.090	1.2	0.74	1.1	9.3	11	6.2	1.5	1262	37.3	56.3	19	4.8	1049	66.7	48	84
Std. Dev.	0.020	0.28	0.06	0.3	1.2	1.2	0.9	0.1	140	2.35	3.98	3.4	1.5	171	24.8	12	8.9
CI-norm Average	2.17	2.50	7.94	2.49	10.3	15.0	6.11	11.8	2.52	35.5	3.11	34.9	34.3	8.74	0.06	5.20	2.72

Data are normalized to CI-chondrite abundances (McDonough and Sun, 1995).

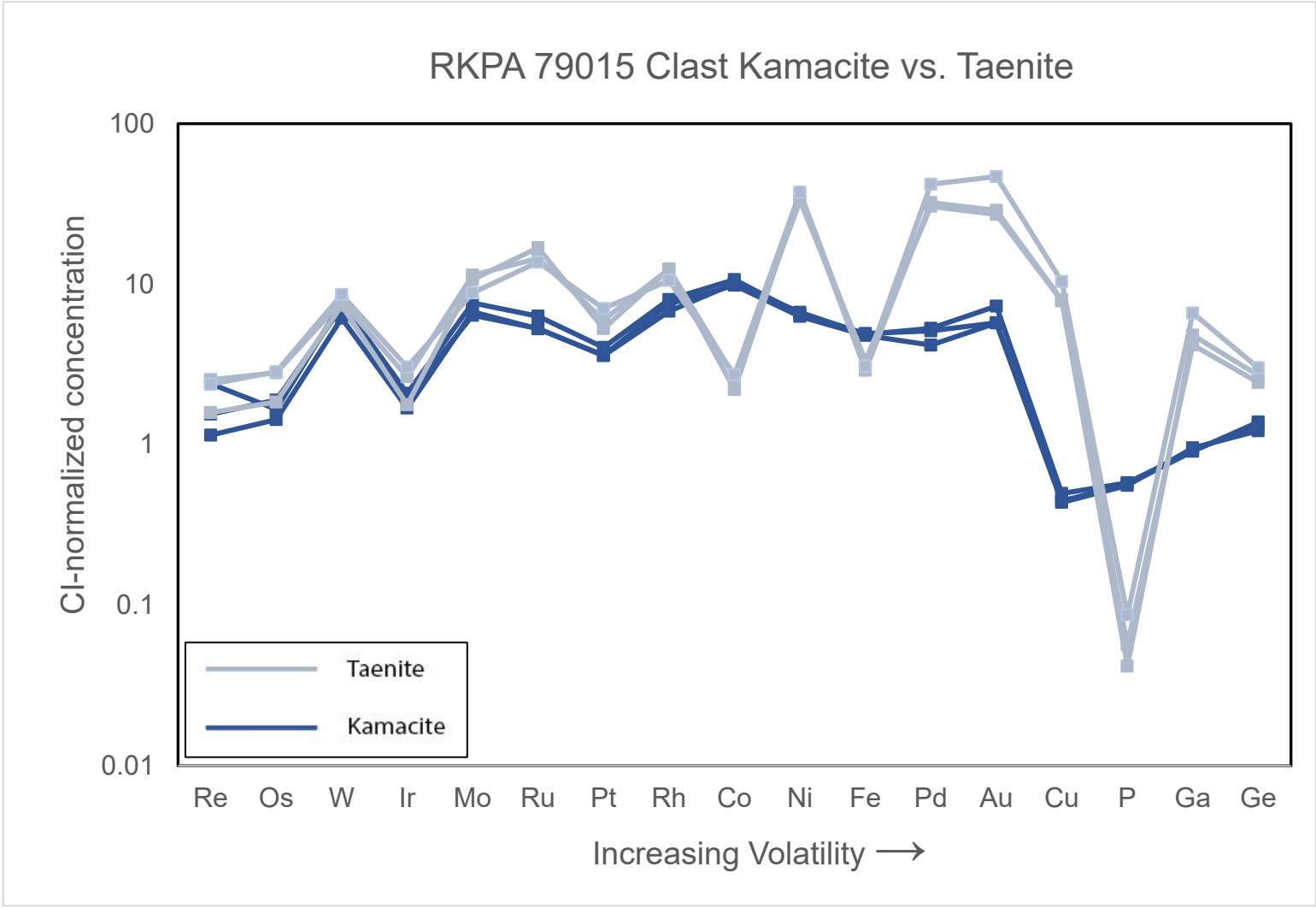

Figure 28. Data plot showing siderophile element concentrations distributed into metal phases kamacite and taenite in the RKPA 79015 metal clast.

The Chaunskij metal clast shows depletions in Re, Os, and Ir (~ 0.3 to 0.5 × CI) in comparison to the moderately refractory siderophile elements (~ 10 × CI). This same pattern occurs in the type C mesosiderite RKPA 79015, but the highly refractory siderophile depletion in Chaunskij is of greater magnitude (Table 17; Fig. 29). Volatile siderophile element concentrations are depleted relative to moderately refractory siderophiles, with similar Cu and P concentrations to the class A and B mesosiderites Crab Orchard, Chinguetti, and Vaca Muerta (0.2 to 0.5 × CI). Much like types A, B, and C mesosiderites, taenite shows higher concentrations of most siderophile elements, except Co, Fe, and P.

Table 17. Siderophile element abundances for Chaunskij metal clast collected by LA-ICP-MS.

Location	***Re***	***Os***	***W***	***Ir***	***Mo***	***Ru***	***Pt***	***Rh***	***Co***	***Ni***	***Fe***	***Pd***	***Au***	***Cu***	***P***	***Ga***	***Ge***
	ppm	ppm	ppm	ppm	ppm	ppm	ppm	ppm	ppm	wt.%	wt. %	ppm	ppm	ppm	ppm	ppm	ppm
	Kamacite																
2	0.011	0.078	0.18	0.079	5.4	0.76	0.54	0.45	6499	6.78	99.9	2.4	0.68	52	188	3.4	14
11	0.013	0.15	0.23	0.22	3.8	2.0	0.82	0.57	6777	6.81	--	2.9	0.72	59	251	4.1	18
13	0.0056	0.20	0.13	0.19	4.9	1.6	0.72	0.45	6278	6.77	94.3	2.8	0.71	58	237	4.3	16
16	0.0094	0.21	0.26	0.22	4.8	1.6	0.71	0.49	6546	7.01	94.9	2.9	0.65	74	271	4.9	18
38	0.021	0.15	0.15	0.20	5.6	1.7	0.79	0.51	6762	6.86	98.6	2.8	0.75	61	115	5.1	17
Average	0.012	0.16	0.19	0.18	4.9	1.5	0.72	0.49	6572	6.85	96.9	2.8	0.70	61	212	4.4	17
Std. Dev.	0.0057	0.05	0.05	0.06	0.7	0.5	0.11	0.05	206	0.10	2.75	0.2	0.04	8.1	62.5	0.7	1.7
CI-Norm Average	0.30	0.32	2.07	0.40	5.47	2.17	0.71	3.78	13.1	6.52	5.39	5.03	5.00	0.51	0.20	0.48	0.53
	Taenite																
4	0.0024	0.15	0.31	0.10	7.6	3.0	0.78	0.76	1739	32.5	67.7	15	2.7	923	53	17	28
8	--	0.14	0.27	0.091	7.3	2.8	0.76	0.79	1921	31.1	69.7	15	2.8	829	36	15	27
19	0.025	0.34	0.22	0.16	6.4	1.7	0.88	0.72	1819	27.9	58.6	14	2.5	754	46	15	24
20	0.022	0.19	0.31	0.19	6.2	2.6	0.67	0.79	2319	27.7	68.1	13	1.9	683	61	12	22
21	0.010	0.50	0.26	0.38	8.1	3.1	1.0	0.99	2320	35.8	82.9	18	3.0	1017	53	20	34
Average	0.015	0.26	0.27	0.18	7.1	2.6	0.82	0.81	2024	31.0	69.4	15	2.6	841	50	16	27
Std. Dev.	0.012	0.16	0.04	0.12	0.8	0.6	0.13	0.10	278	3.38	8.71	1.9	0.4	133	9.4	2.9	4.6
CI-Norm Average	0.38	0.53	2.96	0.41	7.94	3.71	0.82	6.21	4.05	29.5	3.83	27.5	18.5	7.01	0.05	1.73	0.86

Data are normalized to CI-chondrite abundances (McDonough and Sun, 1995). Dashes indicate concentrations below detection limits.

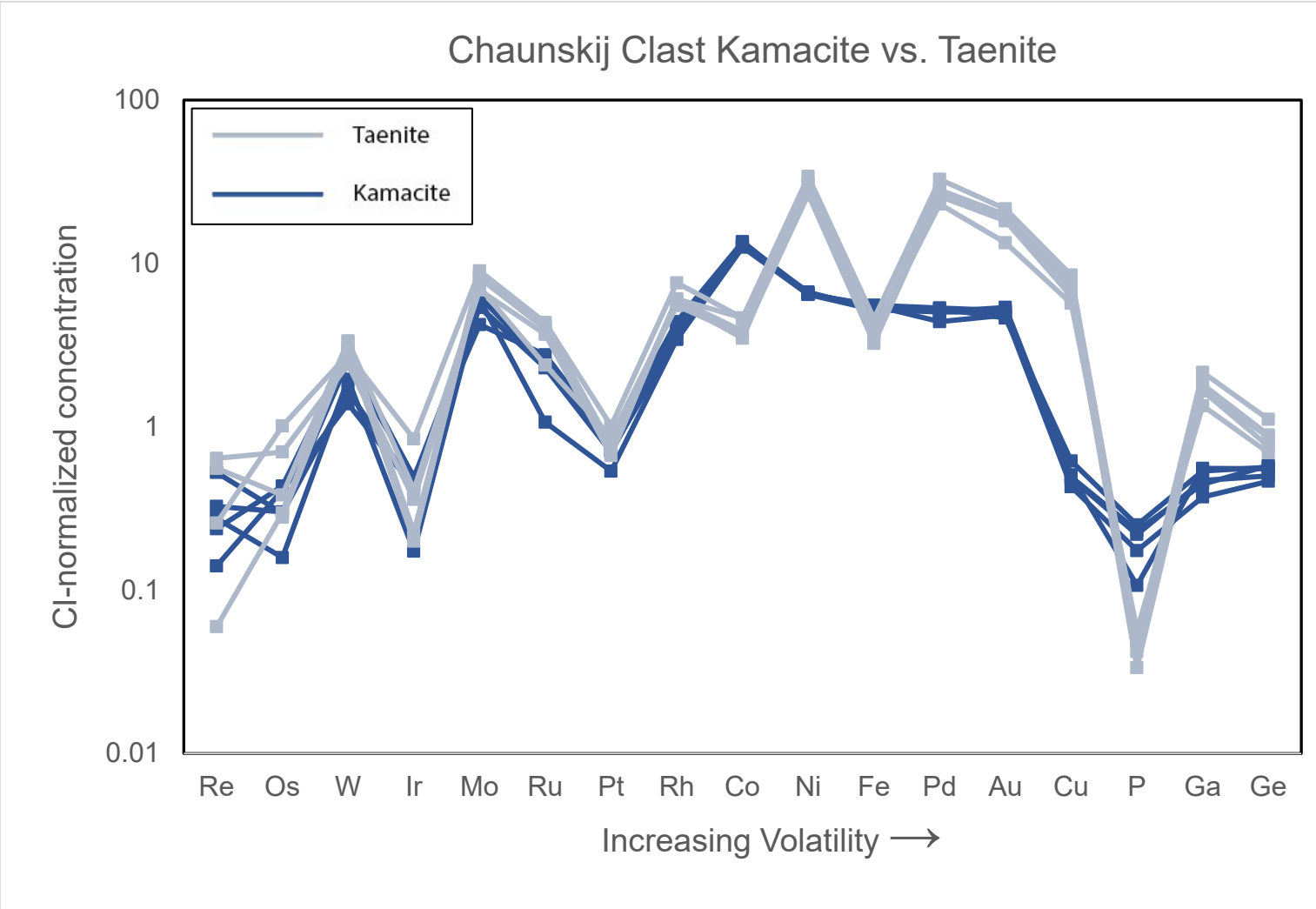

Figure 29. Data plot showing siderophile element concentrations distributed into metal phases kamacite and taenite in the Chaunskij metal clast.

6.0 Discussion

Our results elucidate the three main stages of mesosiderite formation – initial crystallization, metal-silicate mixing, and slow cooling. Although our primary interest is redox reactions that occurred during metal-silicate mixing, our data can be used to examine all three stages. Here we address each stage from most recent to earliest from the perspective of metal textures, metallography, mineralogy, and major, minor, and trace element composition.

6.1 Slow Cooling

In this study, we chose subgroup 1 mesosiderites, which are defined as the least metamorphosed. This classification scheme is based only on silicate textures and mineralogy (Powell, 1971; Floran, 1978). Notably, subgroup 1 samples contain pigeonite that has not inverted to orthopyroxene (Powell, 1971; Floran, 1978). In contrast, metal clasts commonly contain exsolved kamacite and taenite, reflective of the faster diffusion rates in metallic alloys compared to silicates (Ganguly, 2002; Chakraborty, 2008). The slow cooling of mesosiderites is a well-established – and enigmatic – feature of these meteorites (Powell, 1969; Bogard *et al*., 1990; Haack *et al*., 1996; Hopfe and Goldstein, 2001). The mesosiderites included in this study illustrate this slow cooling through both the exsolution textures in the metal clasts and homogeneous distribution of Ni in taenite (Tables 4, 6, 8-10; Figs. 18-22). This apparent disconnect between indicators of slow cooling in silicates and those in metal suggests that subgroup 1 mesosiderites could be further subdivided based on indicators of thermal history within the metal.

6.2 Metal-Silicate Mixing

The range of silicate lithologies observed in mesosiderites in general suggests that the basaltic material experienced fractional crystallization, whereas the restricted range of Ir

concentrations in the metal of class A and B mesosiderites suggests that the metal had not experienced fractional crystallization and was likely still molten at the time of mixing (Wasson *et al*., 1974, 1998; Hassanzedah *et al*., 1990). This mixing event had a profound influence not only on the metal-silicate textures of mesosiderites, but the chemistry and mineralogy as a result of mixing. Redox reactions have been suggested based on the Fe-Mg-Mn systematics of the silicates, which are consistent with reduction of FeO in the silicates to Fe and the corresponding oxidation of P in the metal to produce the abundant phosphates observed in mesosiderites (*e.g.*, Figs. 18-22) (Fuchs, 1969; Powell, 1971; Nehru *et al*., 1978; Mittlefehldt *et al*., 1979; Harlow *et al*., 1982; Agosto, 1985; Mittlefehldt, 1990). Although evidence for proposed reactions has come primarily from observations of silicates and phosphates, redox reactions of this type should also be apparent in the mineralogy and compositions of the metallic phases. In fact, we do observe evidence of such reactions. This evidence includes a marked depletion of P in the matrix metal relative to the elements of similar volatility (*e.g.*, Ga) (Tables 11-17; Figs. 23-29), the presence of phosphates primarily associated with the silicates in the matrix (Figs. 18-22), and the markedly higher kamacite/taenite ratio in the matrix compared to the metal clasts (Figs. 18-22). Harlow *et al*. (1982) presented thermodynamic calculations for the specific redox reaction proposed by Agosto (1985) (Table 3). These calculations predicted that this specific reaction would take place at temperatures between 970°C and 1030°C. The metal in mesosiderites would not begin to solidify and exsolve kamacite from taenite until it cooled to temperatures at least <800°C (Harlow *et al*., 1982). This allows the excess metallic Fe produced by this redox reaction to raise the initial Fe/Ni ratio of the matrix metal before it begins to exsolve kamacite, which results in the increased kamacite/taenite ratio of the matrix metal compared to metal clasts.

While the metal composition and mineralogy are broadly consistent with previously proposed redox reactions, the full range of elements analyzed by LA-ICP-MS provides a means to test these ideas. In particular, changes in the concentrations of other elements between the metal and silicates should be observed. Indeed, we observe significant depletions of Mo and Cu relative to elements of similar volatility (Table 11,13; Figs. 23, 25). For example, the Mo/Ir ratio of matrix metal in Crab Orchard is 0.47 and the Cu/Au ratio is 0.07 (Table 11). If these depletions are also related to redox, the T-fO_2 buffer curves for these elements should be similar to that of P, which was oxidized during metal-silicate mixing; in fact, they are not. The buffer curve for Mo-MoO_2 is ~ 1 log unit above iron-wüstite (Fig. 30) (Righter *et al*., 2017). For comparison, the W-WO_2 buffer curve is slightly below iron-wüstite (Fig. 30) (Righter *et al*., 2017). Thus, oxidation of Mo should produce a corresponding depletion in W. No such depletion is observed, with a W/Ir ratio of 0.97 in the Crab Orchard matrix metal (Table 11). Oxidation of Cu would require considerably more oxidizing conditions because the Cu-Cu_2O buffer curve approximates the hematite-magnetite curve (Fig. 30) (O'Neill and Pownceby, 1993), consistent with the presence of metallic Cu and absence of copper oxides in meteoritic materials.

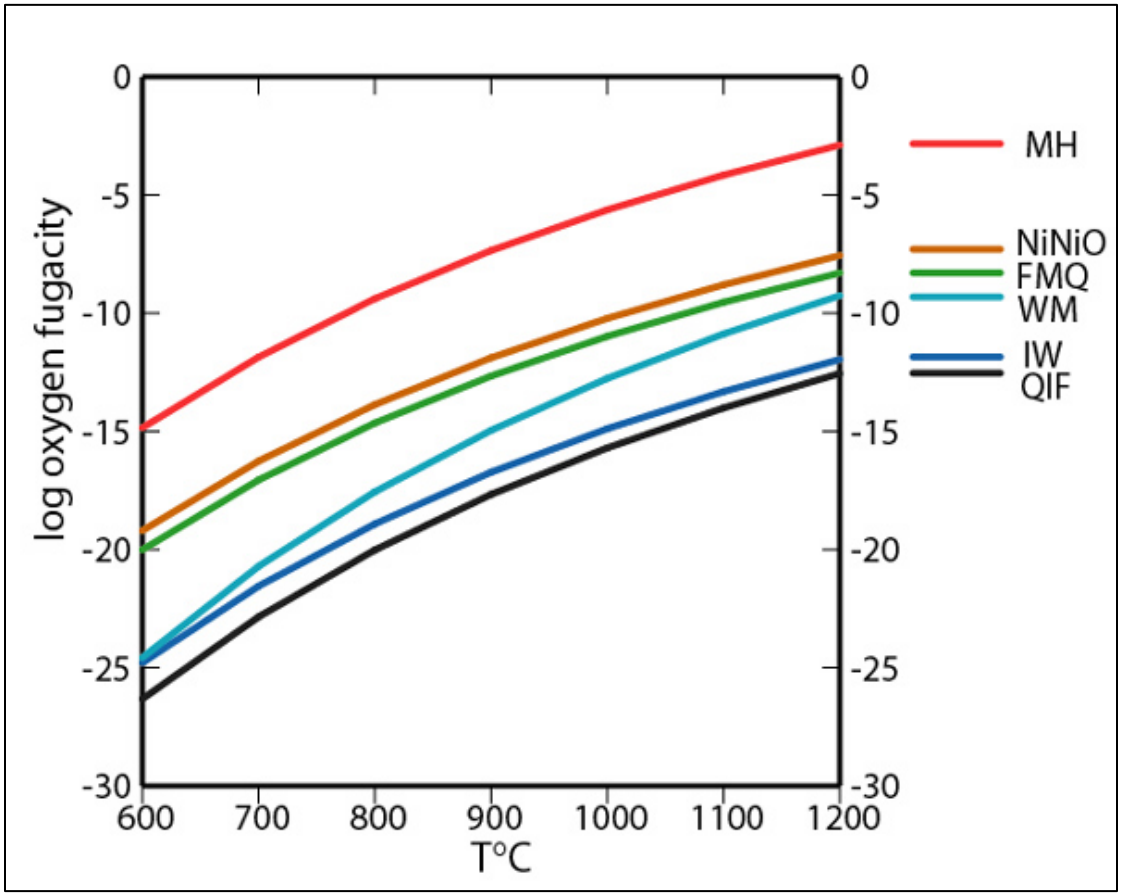

Figure 30. Oxygen fugacity buffer diagram of typical buffer curves used in geochemistry. The iron-wüstite buffer curve is labeled IW in dark blue. The Mo-MoO_2 buffer curve lies ~1 log unit above IW, and the W-WO_2 buffer curve lies slightly below IW. The Cu-Cu_2O approximates the hematite-magnetite buffer curve labeled as MH. Figure from Frost (1991).

The relatively oxidizing conditions required for oxidation of Mo and Cu suggest that additional processes operated during the formation of mesosiderites to explain the composition of the metal. One possible process for Cu depletion is the exsolution or crystallization of metallic Cu, as observed in the Newport pallasite (Buseck, 1968). Ramdohr (1965) observed metallic copper in the Patwar class A mesosiderite. Our multispectral elemental mapping of mesosiderites in this study did not reveal the presence of metallic Cu (Appendix B-F). Alternatively, sulfidization may have played a role in sequestering Mo and Cu from the metallic phase. Copper is known to partition into sulfides (Buseck, 1968; Papike, 1998; Chabot *et al*., 2003). However, our multispectral elemental mapping does not show any correlation of Cu with S (Appendix B-F). An elemental map of Mo was not produced in this study, and therefore we are not able to determine if there is a correlation of Mo with S. Further investigation is required to determine the possible effects of sulfidization in mesosiderites. The depletion of Cu in the matrix metal may also be a result of its affinity for taenite over kamacite. Taenite was not analyzed for the matrix metal, but our multispectral elemental mapping shows that Cu is correlated with Ni throughout all samples (Appendix B-F). This suggests that this Cu depletion may be superficial and is a result of partitioning of Cu between kamacite and taenite.

6.3 Initial Crystallization

Although the major impetus for this research was understanding redox reactions during metal-silicate mixing, Crab Orchard, RKPA79015, and Chaunskij exhibit remarkably similar concentrations of many of the moderately refractory and volatile siderophile elements, including Co, Ni, Fe, Pd, Au and Cu (Tables 12, 16, 17; Fig. 31, 32). In contrast, the highly refractory siderophile elements differ between the class A and B and anomalous samples. Although limited to only three samples, this range in highly refractory siderophile elements is reminiscent of the

range of highly refractory siderophile elements observed in IIIAB irons (Mullane *et al.*, 2004). In the IIIAB irons, the highly refractory siderophile elements (Re, Os, Ir, Ru, Pt, Rh) exhibit orders of magnitude variation owing to their strong preference for the solid phase compared to the liquid. For example, IIIAB iron Ir concentrations show four orders of magnitude variation (Mittlefehldt *et al.*, 1998), while the mesosiderites studied here show approximately two orders of variation (Tables 12, 16, 17; Fig. 31, 32). In contrast to the highly refractory siderophile elements, W and Mo show a much smaller range between the mesosiderites in this study. This is consistent with these elements exhibiting less affinity for the crystallizing metal, as reflected by their partition coefficients (Chabot *et al.*, 2017).

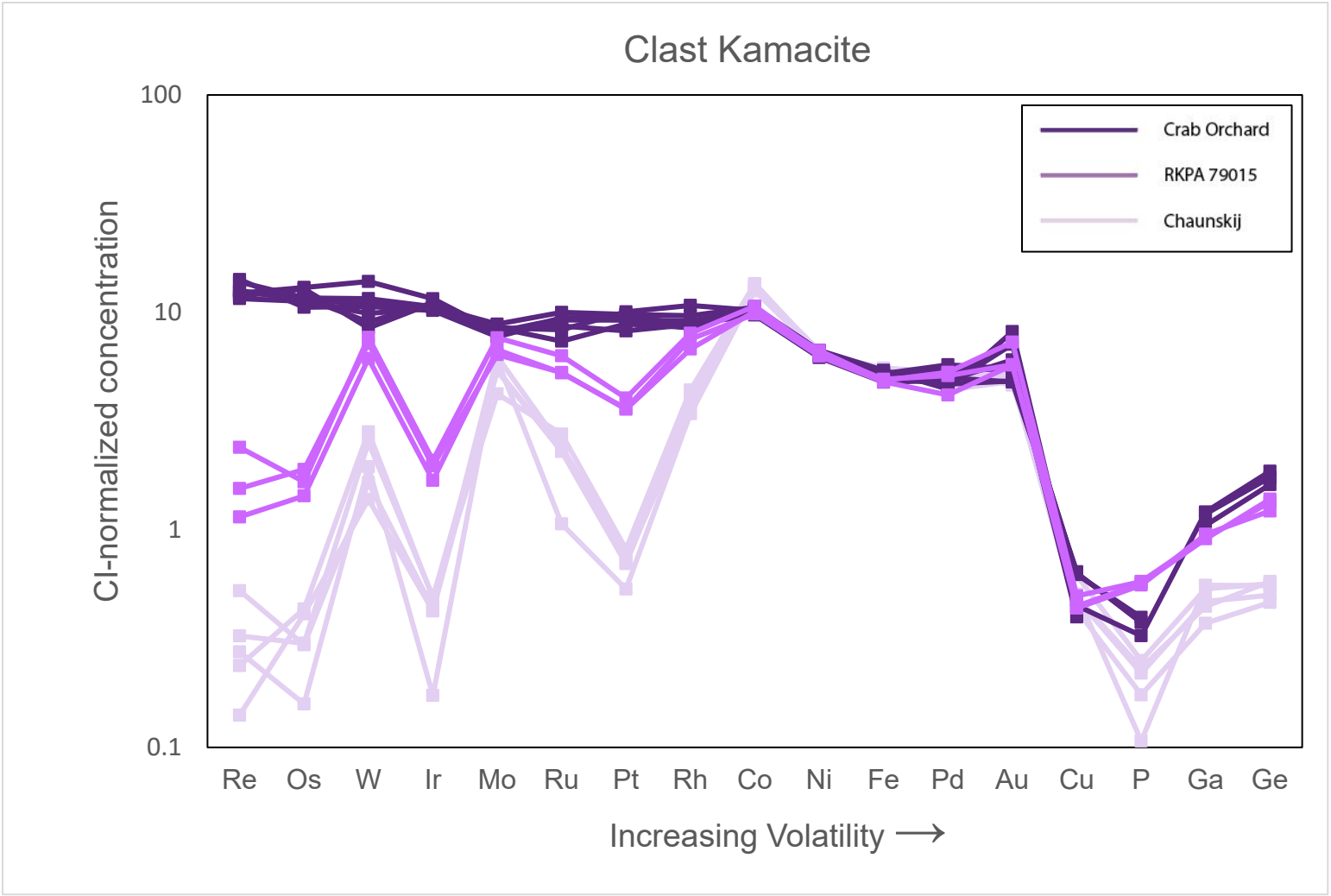

Figure 31. Comparison of metal clast kamacite compositions of class A and B and anomalous mesosiderites. Class A and B mesosiderite metal clasts (Crab Orchard) show high concentrations of highly refractory siderophile elements, Chaunskij shows low concentrations of highly refractory siderophile elements, and RKPA 79015 shows concentrations of highly siderophile elements that lie between classes A and B and Chaunskij. This trend is suggestive of fractional crystallization.

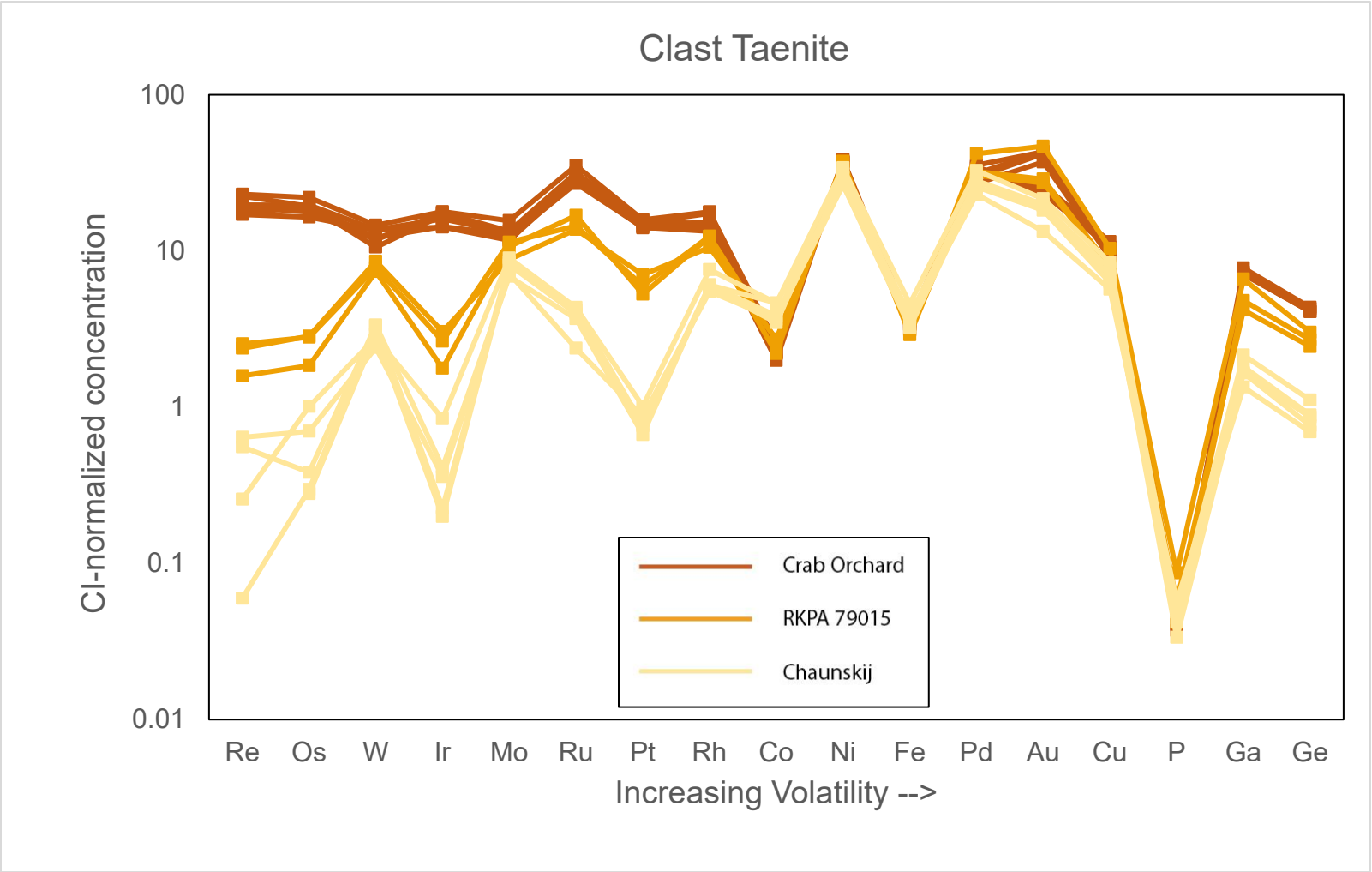

Figure 32. Comparison of metal clast taenite compositions of class A and B and anomalous mesosiderites. Class A and B mesosiderite metal clasts (Crab Orchard) show high concentrations of highly refractory siderophile elements, Chaunskij shows low concentrations of highly refractory siderophile elements, and RKPA 79015 shows concentrations of highly siderophile elements that lie between classes A and B and Chaunskij. This trend is suggestive of fractional crystallization.

The consensus in the mesosiderite literature is that the restricted range in Ir concentrations in mesosiderites suggests the metal was molten at the time of mixing and fractional crystallization did not occur (Wasson *et al*., 1974, 1998; Hassanzedah *et al*., 1990). Samples such as Chaunskij and RKPA 79015, with differing Ir concentrations, were identified as anomalous (Wasson *et al*., 1974, 1998; Hassanzedah *et al*., 1990). However, as stated above, the data presented here shows a range in Ir values, with class A and B having the highest concentrations, Chaunskij having the lowest, and class C (RKPA79015) lying in between (Tables 12, 16, 17; Figs. 31, 32). This is suggestive of fractional crystallization. If fractional crystallization is responsible for the siderophile element compositions of the metal in RKPA79015 and Chaunskij, it was unlikely to have involved the entire metallic mass sampled by mesosiderites. Extensive crystallization of this mass should have produced a range of Ir concentrations, while the vast majority of mesosiderites exhibit a similar and restricted range of the highly refractory siderophile elements. Instead, RKPA79015 and Chaunskij may have been the exceptions.

Kong *et al*. (2008) suggested that compositional differences between matrix and clast metal in the Dong Ujimqin Qi mesosiderite were indicative of fractional crystallization between the two components; the clast metal representing early-stage crystallization and the matrix metal representing late-stage crystallization. In this work, comparing matrix kamacite to clast kamacite, we do not observe a compositional difference between these two populations that can be attributed to this process (Tables 11-14; Figs. 23, 25). We note that the clasts and matrix differ in their kamacite/taenite ratio and that these two phases differ in composition. For example, Pd is enriched in the matrix metal relative to the clasts in Crab Orchard (Tables 11, 12; Fig. 23). This may reflect strong preference of Pd for taenite over kamacite (Hirata and Nesbitt, 1997). The matrix metal has

not exsolved to the same extent as the clasts, resulting in Pd enrichment in the kamacite phase. Thus, comparison of bulk matrix and clasts must be approached with caution.

RKPA79015 and Chaunskij are also unlikely to have been the crystallized outer surface of the metallic mass, as that early crystallizing material would be expected to have higher highly refractory siderophile element concentrations, while these meteorites have lower concentrations. Instead, we suggest that local fractional crystallization may have occurred in the metallic masses sampled by anomalous mesosiderites. One possible model for this is that an isolated portion of the metallic mass experienced extensive fractional crystallization, such as a mass isolated from the main portion by admixed or adhering mantle fragments (Fig. 33). An interesting alternative to this model is that the impact that produced the molten metallic mass sampled by class A and B mesosiderites produced a smaller mass, with a higher surface to volume ratio and faster cooling, that fractionally crystallized to produce RKPA79015 and Chaunskij (Fig. 34). Given the constraint that the metal in class A and B mesosiderites was molten, it is possible that the event that stripped the silicate shell from the molten metallic core occurred both temporally and proximally close to the differentiated asteroid from which the crustal silicates were derived. Production of molten metallic masses of a range of sizes is a natural consequence of hit-and-run collisions (Asphaug *et al.*, 2006; Scott *et al.*, 2015), perhaps providing a mechanism for producing compositionally related bodies that differed in their extent of crystallization.

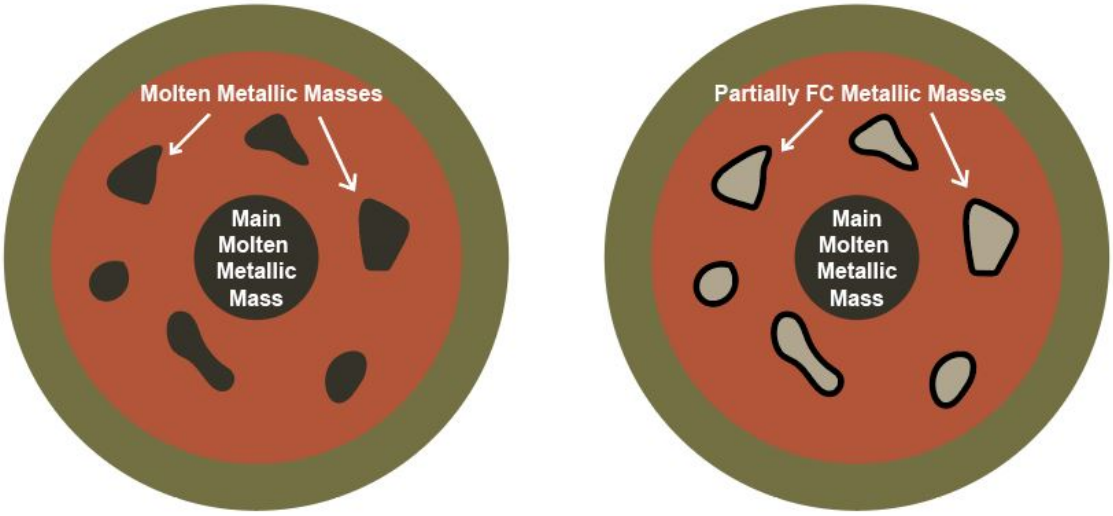

Figure 33. Formational model for mesosiderite metal. (Left) Smaller molten metallic masses are segregated and separated from the main molten metallic mass by adhering mantle fragments. (Right) Smaller molten metallic masses are able to lose heat more quickly allowing them to experience a certain degree of fractional crystallization.

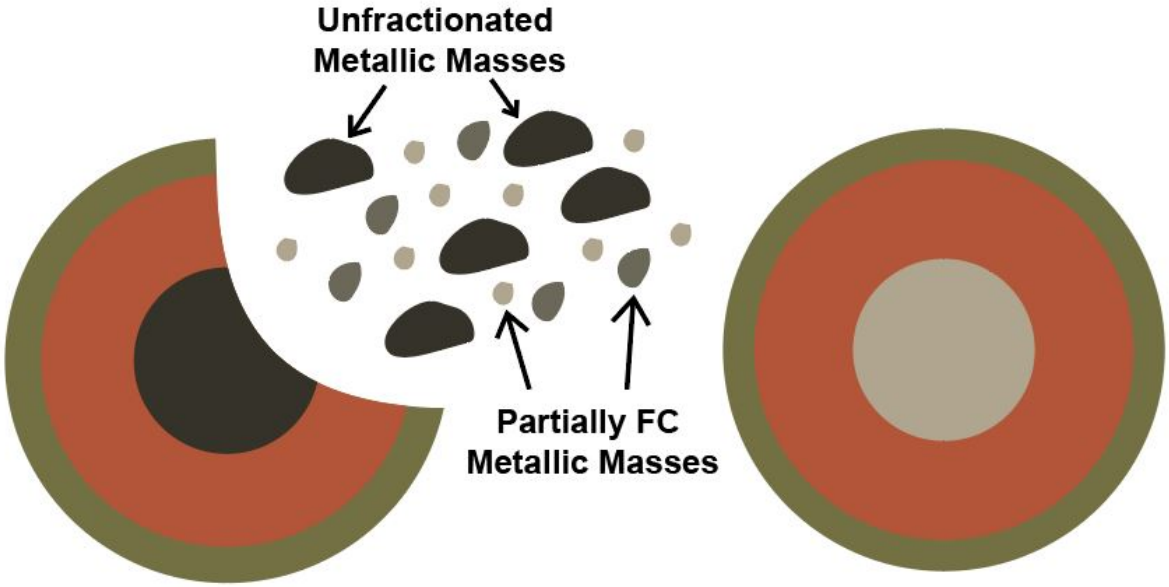

Figure 34. Hit-and-run formational model for mesosiderite metal. (Left) An impacted asteroid with a molten metallic core produces metallic fragments of varying sizes. Smaller metallic masses partially fractionally crystallize. (Right) Differentiated asteroid containing basaltic crust. Molten metallic fragments accrete onto the surface and mix with crustal silicates to form mesosiderites.

As previously stated, Wilson (1972) claims that the "random magnetic polarity" of metal nodules found in mesosiderites indicate that this metal was solid at the time of metal-silicate mixing. Iron loses all magnetic properties at temperatures above 770°C, which is below the temperature at which metal begins to solidify and form metallographic structures. If smaller metallic masses were able to begin fractional crystallization, the outer-most portion of the masses should be solid. These solid outer shells may be represented by nodules that have retained their magnetic properties; however, the fraction of metal that these outer shells represent compared to the amount of molten metal that would be produced by hit-and-run collisions is small. It is unlikely that metal representing this solidified outer shell would be abundant in the mesosiderite record.

The ratio of Ga/Ni varies significantly between mesosiderite petrologic classes (Fig. 4) (Hassanzadeh *et al*., 1990; Wasson *et al*., 1974, 1998). Class A mesosiderites show a large range in low to high Ga/Ni ratios, class B shows high Ga/Ni ratios, and class C (RKPA 79015) shows moderately high Ga/Ni ratios. Our data displayed in Figures 31 and 32 show that the volatile siderophile elements Ga and Ge are depleted compared to the moderately refractory siderophile elements. Chaunskij shows the strongest depletions of Ga and Ge, and the class A and B mesosiderites show the smallest depletion of Ga and Ge compared to the moderately refractory siderophile elements (Figs. 31, 32). RKPA 79015 Ga and Ge concentrations lie between class A and B and Chaunskij (Figs. 31, 32). We see a trend of depletion in our data showing that the anomalous samples are more depleted in volatile siderophile elements compared to class A and B mesosiderites. Depletions of Ga and Ge have been explained by major planetary impacts that excavated metal before it solidified resulting in the loss of volatiles (Goldstein *et al*., 2009). The trend of depletion we see in our data may show that the smaller metallic masses that produced the metal in the anomalous samples were able to lose Ga and Ge as volatiles during impacting more

effectively than the larger masses that produced the metal in the class A and B mesosiderites. The depletion of volatile siderophile elements in our data supports our theory that the mesosiderite metal originated from a body that experienced hit-and-run collisions, and that the metal was molten at the time of impacting.

7.0 Conclusions

This study examined the metallography of five sections that span the range of petrologic types sampled by mesosiderites and show the lowest degree of metamorphism.

- Our data indicate that redox reactions during metal-silicate mixing were localized within the matrix metal and did not occur within the metal clasts of mesosiderites.
- Evidence for these reactions includes: a marked depletion in P in the matrix metal; phosphates associated with silicates in the matrix; the high kamacite/taenite ratio of the matrix metal as a result of excess metallic Fe.
- Depletions of Mo and Cu in the matrix metal cannot be explained by redox reactions, suggesting that other processes, such as sulfidation, must have occurred.
- Metal clast compositions of classes A and B, C, and anomalous samples in this study produce a trend that is representative of fractional crystallization.
    - Previous studies have concluded that the restricted range in Ir concentrations within the mesosiderites indicated that the metal was molten at the time of mixing. RKPA 79015 and Chaunskij have differing Ir concentrations and have been classified as anomalous.
    - We suggest that these samples are not anomalous but may represent metal that has experienced a certain degree of fractional crystallization.
- We suggest that RKPA 79015 and Chaunskij could have formed as isolated metallic masses that experienced localized fractional crystallization on the mesosiderite parent body, or smaller metallic masses produced by hit-and-run collisions.

- Our model presented here favors the previously proposed formation models that invoke impact origins for molten mesosiderite metal that accreted onto a differentiated body with a basaltic crust (*e.g*. Wasson and Rubin, 1985).

8.0 Future Work

Future work is needed to better understand all possible redox reactions that could have taken place during the mesosiderite metal-silicate mixing event. Here we have only examined the effects of one redox reaction proposed by Agosto (1985). However, it is likely that many other redox reactions similar to this one took place at the same time. We have only examined the matrix metal for two samples in our data set. Examining the matrix metal of the full suite of samples, and possibly adding more subgroup 1 samples, would be helpful to examine the full suite of redox reactions in mesosiderites.

Updated research is also needed to explore other processes that could have taken place during metal-silicate mixing. Our results show depletions in elements that are not likely to be affected by redox reactions. For example, could the depletions of Mo in the matrix metal compared to metal clasts be due to sulfidization? If so, what reactions occur during this process? In addition, elemental concentrations of both metal phases, kamacite and taenite, in the matrix should be analyzed to determine if depletions of different elements can be explained by partitioning between the two phases.

Lastly, the redox reaction examined in this study has been suggested to be catalyzed by the Ca contained in the clinopyroxenes in the silicate portion of the mesosiderites (Agosto, 1985). The mesosiderites are classified by the composition of their silicate portion resulting in a variation of clinopyroxene abundance between the classes. The amount of phosphates that are suggested to be produced by this redox reaction should be quantified for each petrologic class. It has been noted that mesosiderite phosphates show only small amounts of REEs compared to achondritic phosphates that are produced by igneous fractionation (Harlow *et al*., 1982). This is important because it shows that the phosphates are not a product of igneous fractionation and must have

formed as a result of other processes, such as redox reactions. More work should be done to better understand these REE patterns and how they compare to REE patterns of the clinopyroxenes containing the necessary Ca to form the mesosiderite phosphates.

References

Agosto W.M. (1985) "Liquidus phosphorus reduction reactions in mesosiderite silicates." *Proc. Lunar Planet. Sci. Conf. 16th*, 7-8.

Agosto W.M., Hewins R.H., and Clarke R.S., Jr. (1980) "Allan Hills A77219, the first Antarctic mesosiderite." *Proc. Lunar Planet. Conf. 11th*, 1027-1045.

Asphaug E., Agnor C.B., and Williams Q. (2006) "Hit-and-run planetary collisions." *Nature* 439, 155-160.

Binzel R.P. and Xu S. (1993) "Chips off of Asteroid 4 Vesta: Evidence for the Parent Body of Basaltic Achondrite Meteorites." *Science* 260, 186-191.

Bogard D.D., Garrison D.H., Jordan J.L., and Mittlefehldt D.W. (1990) "^{39}Ar-^{40}Ar dating of mesosiderites: Evidence for major parent body disruption <4 Ga ago." *Geochim. Cosmochim. Acta* 54, 2549-2564.

Buseck P.R. (1968) "Mackinawite, pentlandite, and native copper from the Newport pallasite." *Mineral. Mag.* 36 (281), 717-725.

Chabot N.L. and Drake M.J. (1999) "Crystallization of magmatic iron meteorites: The role of mixing in the molten core." *Meteoritics Plan. Sci*. 34, 235-246.

Chabot N.L., Campbell A.J., Jones J.H., Humayun M., and Agee C.B. (2003) "An experimental test of Henry's Law in solid metal/liquid metal systems with implications for iron meteorites." *Meteoritics Plan. Sci.* 38,181–196.

Chabot N.L., Wollack A.E., McDonough W.F., Ash., R.D., and Saslow S.A. (2017) "Experimental determination of partitioning in the Fe-Ni system for applications to modeling meteoritic metals." *Meteoritics Plan. Sci.* 52, 1133-1145.

Chakraborty S. (2008) "Diffusion in solid silicates: A tool to track timescales of processes comes of age." *Annu. Rev. Earth Planet. Sci*. 36,153–90.

Clayton R.N. (2005) "Oxygen Isotopes in Meteorites." In *Meteorites, Comets, and Planets: Treatise on Geochemistry 2nd Ed.* 1, (ed. A.M. Davis) Elsevier Science, 129-142.

Consolmagno G.J. and Drake M.J. (1977) "Composition and evolution of the eucrite parent body: Evidence from rare earth elements." *Geochim. Cosmochim. Acta* 41, 1271-1282.

Delaney J.S., Nehru C.E., Prinz M., and Harlow G.E. (1981) "Metamorphism in mesosiderites." *Proc Lunar Planet. Sci.* 12B, 1315-1342.

Dodd R.T. Jr. and Van Schmus W.R. (1967) "A survey of the unequilibrated ordinary chondrites." *Geochim. Cosmochim. Acta* 31, 921-951.

Floran R.J. (1978) "Silicate petrography, classification, and origin of the mesosiderites: Review and new observations." *Proc Lunar Planet. Sci 9th*, 1053-1081.

Frost R.B. (1991) "Introduction to oxygen fugacity and its petrologic importance." *Reviews in Mineralogy and Geochemistry* 25, 1-9.

Fuchs L.H. (1969) “The phosphate mineralogy of meteorites.” In: *Meteorite Research*, (ed. P.M. Millman), 683-695.

Ganguly J. (2002) “Diffusion kinetics in minerals: Principles and applications to techtono-metamorphic processes.” *EMU Notes in Mineralogy* 4, 271-309.

Ganguly J., Yang H., and Ghose S. (1994) “Thermal history of mesosiderites: Quantitative constraints from compositional zoning and Fe-Mg ordering in orthopyroxenes.” *Geochim. Cosmochim. Acta* 58, 2711-2723.

Goldstein J.I., Scott E.R.D., and Chabot N.L. (2009) “Iron meteorites: Crystallization, thermal history, parent bodies, and origin.” *Chemie der Erde* 69, 293-325.

Goodrich C.A. and Delaney J.S. (2000) “Fe/Mg—Fe/Mn relations of meteorites and primary heterogeneity of primitive achondrite parent bodies.” *Geochim. Cosmochim. Acta* 64, 149-160.

Greenberg R. and Chapman C.R. (1984) “Asteroids and Meteorites: Origin of stony-iron meteorites at mantle-core boundaries”. *Icarus* 57, 267-279.

Greenwood R.C., Franchi I.A., Jambon A., Barrat J.A., and Burbine T.H. (2006) “Oxygen isotope variation in stony-iron meteorites.” *Science* 313, 1763-1765.

Haack H., Scott E.R.D., and Rasmussen K.L. (1996) “Thermal and shock history of mesosiderites and their large parent asteroid.” *Geochim. Cosmochim. Acta* 60, 2609-2619.

Hardersen P.S., Gaffey M.J., and Abell P.A. (2004) “Mineralogy of asteroid 1459 Magnya and implications for its origin.” *Icarus* 167, 170-177.

Harlow G.E., Delaney J.S., Nehru C.E., and Prinz M. (1982) “Metamorphic reactions in mesosiderites: origin of abundant phosphate and silica.” *Geochim. Cosmochim. Acta* 46, 339-348.

Hassanzadeh J., Rubin A.E., and Wasson J.T., (1990) “Compositions of large metal nodules in mesosiderites: Links to iron meteorite group IIIAB and the origin of mesosiderite subgroups.” *Geochim. Cosmochim. Acta* 54, 3197-3208.

Hewins R.H. (1983) “Impact versus internal origins for mesosiderites.” *Proc. Lunar Planet. Sci. Conf. 14th*, Part 1: *J Geophys. Res. 88 Suppl.*, B257-B266.

Hewins R.H. (1984) “The case for a melt matrix in plagioclase-POIK mesosiderites.” *Proc. Lunar Planet. Sci. Conf. 15th*, Part 1: *J Geophys. Res. 89 Suppl.*, C289-C297.

Hewins R.H. (1988) “Petrology and pairing of mesosiderites from Victoria Land, Antarctica.” *Meteoritics Plan. Sci.* 23, 123-129.

Hirata T. and Nesbitt R.W. (1997) “Distribution of platinum group elements and rhenium between metallic phases of iron meteorites.” *Earth and Planetary Science Letters* 147, 11-24.

Hopfe W.D. and Goldstein J.I. (2001) “The metallographic cooling rate method revised: Application to iron meteorites and mesosiderites.” *Meteoritics Plan. Sci.* 36, 135-154.

Jones J.H. (1983) “Mesosiderites: (1) reevaluation of cooling rates and (2) experimental results bearing on the origin of metal.” *Lunar Planet. Sci.*14, 351-352.

Kong P., Su W., Li X., Spettel B., Palme H., and Tao K. (2008) "Geochemistry and origin of metal, olivine clasts, and matrix in the Dong Ujimqin Qi mesosiderite." *Meteoritics Plan. Sci*. 43, 451-460.

Lazarro D., Michtchenko T., Carvano J.M., Binzel R.P., Bus S.J., Burbine T.H., Mothe-Dinz T., Florczak M., Angeli C.A., and Harris A.W. (2000) "Discovery of a basaltic asteroid in the outer main belt." *Science* 288, 2033-2035.

Mason B. (1949) "Oxidation and Reduction in Geochemistry." *J Geol.* 57, 62-72.

McCall G.J.H. (1966) "The petrology of the Mount Padbury mesosiderite and its achondritic enclaves." *Mineral. Mag.* 35, 1029-1060.

McCord T.B., Adams J.B., and Johnson T.V. (1970) "Asteroid Vesta: Spectral reflectivity and compositional implications." *Science* 168, 1445-1447.

McDonough W.F. and Sun S.-S. (1995) "The composition of the Earth." *Chem. Geol.* 120, 223-254.

McSween H.Y., Binzel R.P., De Sanctis M.C., Ammannito E., Prettyman T.H., Beck A.W., Reddy V., Le Corre L., Gaffey M.J., McCord T.B., Raymond C.A., Russell C.T., and the Dawn Science Team (2013) "Dawn; the Vesta-HED connection; and the geologic context for eucrites, diogenites, and howardites." *Meteoritics Plan. Sci.* 48, 2090-2104.

Mittlefehldt D.W. (1979) "Petrographic and chemical characterization of igneous lithic clasts from mesosiderites and howardites and comparison with eucrites and diogentites." *Geochim. Cosmochim. Acta* 43, 1917-1935.

Mittlefehldt D.W. (1990) "Petrogenesis of mesosiderites: I. Origin of mafic lithologies and comparison with basaltic achondrites." *Geochim. Cosmochim. Acta* 54, 1165-1173.

Mittlefehldt D.W., Chou C.L., and Wasson J.T. (1979) "Mesosiderites and howardites: Igenous formation and possible genetic relationships." *Geochim. Cosmochim. Acta* 43, 673-688.

Mittlefehldt D.W., McCoy T.J., Goodrich C.A., and Kracher A. (1998) "Non-chondritic meteorites from asteroidal bodies." In: *Planetary Materials*, (ed. J.J. Papike) *Mineralogical Society of America Reviews in Mineralogy* 36, 142-163.

Mullane E., Alard O., Gounelle M., and Russell S.S. (2004) "Laser ablation ICP-MS study of IIIAB irons and pallasites: constraints on the behaviour of highly siderophile elements during and after planetesimal core formation." *Chem. Geol.* 208, 5-28.

Narayan C., and Goldstein J.I. (1985) "A major revision iron meteorite cooling rates; an experimental study of the growth of the Widmanstätten pattern." *Geochim. Cosmochim. Acta* 49, 397-410.

Nehru C.E., Zucker S.M., Harlow G.E, and Hewins R.H. (1978) "The tridymite-phosphate-rich component in mesosiderites." (Abstract) *Meteoritics Plan. Sci.* 13, 573.

Nehru C.E., Zucker S.M., Harlow G.E., and Prinz M. (1980) "Olivines and olivine coronas in mesosiderites." *Geochim. Cosmochim. Acta* 44, 1103-1118.

O'Neill H.S.C. and Pownceby M.I. (1993) "Thermodynamic data from redox reactions at high temperatures. I. An experimental and theoretical assessment of the electrochemical method using stabilized zirconia electrolytes, with revised values for the Fe-'FeO', Co-CoO, Ni-

NiO, and Cu-Cu_2O oxygen buffers, and new data for the W-WO_2 buffer." *Contr. Mineral. and Petrol.* 114, 296-314.

Papike J.J. (1998) Planetary Materials. *Mineralogical Society of America Reviews in Mineralogy* 36.

Powell B.N. (1969) "Petrology and geochemistry of mesosiderites—I. Textures and composition of nickel-iron." *Geochim. Cosmochim. Acta* 33, 789-810.

Powell B.N. (1971) "Petrology and chemistry of mesosiderites—II: Silicate textures and compositions and metal silicate relationships." *Geochim. Cosmochim. Acta* 35, 5-34.

Prettyman T.H., Mittlefehldt D.W., Lawrence D.J., Yamashita N., Beck A.W., Feldman W.C., McCoy T. J., McSween H.Y., Toplis M.J., Titus T.N., Tricarico P., Reedy R.C., Hendricks J.S., Forni O., Le Corre L., LiJ.-Y., Mizzon H., Reddy V., Raymond C.A., and Russell C.T. (2012) "Elemental mapping by Dawn reveals exogenic H in Vesta's regolith." *Science* 338, 242-246.

Prior G.T. (1918) "On the mesosiderite-grahamite group of meteorites: with analyses of Vaca Muerta, Hainholz, Simondium, Powder Mill Creek." *Mineral Mag* 18, 151-172.

Ramdohr P. (1965) "Über mineralbestand von pallasiten und mesosideriten und einige genetische überlegungen." *Monatsber. Deutsch. Akad. Wiss.* 7, 923-938.

Righter K., Pando K.M., Ross D.K., Butterworth A.L., Gainsforth Z., Jilly-Rehak C.E., and Westphal A.J. (2017) "Oxygen buffering in high pressure solid media assemblies: New approach enabling study of fO_2 from IW +4.5." *80th Annual Met. Soc.*, abstract no. 1987.

Roig F., Nesvorný D., Gil-Hutton R., and Lazzaro D. (2008) "V-type asteroids in the middle main belt." *Icarus* 194, 125-130.

Rubin A.E. and Jerde E.A. (1987) "Diverse eucritic pebbles in the Vaca Muerta mesosiderite." *Earth and Planet. Sci. Lett.* 84, 1-14.

Rubin A.E. and Mittlefehldt D.W. (1992) "Classification of mafic clasts from mesosiderites: Implications for endogenous igneous processes." *Geochim. Cosmochim. Acta* 56, 827-840.

Scott E.R.D., Haack H., and Love S.G. (2001) "Formation of mesosiderites by fragmentation and reaccretion of a large differentiated asteroid." *Meteoritics Planet. Sci.* 36, 869-881.

Scott E.R.D., Keil K., Goldstein J.I., Asphaug E., Bottke W.F., and Moskovitz N.A (2015) "Early impact history and dynamical origin of differentiated meteorites and asteroids." In *Asteroids IV* (P. Michel *et al.*, eds.), 573–595.

Sunshine J.M., Bus S.J., McCoy T.J., Burbine T.H., Corrigan C.M., and Binzel R.P. (2004) "High-calcium pyroxene as an indicator of igneous differentiation in asteroids and meteorites." *Meteoritics Planet. Sci.* 39, 1343-1357.

Wasson J.T. (1999) "Trapped melt in IIIAB irons; solid/liquid elemental partitioning during the fractionation of the IIIAB magma." *Geochim. Cosmochim. Acta* 63, 2875–2889.

Wasson J.T. (2013) "Vesta and extensively melted asteroids: Why HED meteorites are probably not from Vesta." *Earth and Planetary Science Letters* 381, 138-146.

Wasson J.T., Choi B-G, Jerde E.A., and Ulff-Moller F. (1998) "Chemical classification of iron meteorites: XII. New members of the magmatic group." *Geochim. Cosmochim. Acta* 62, 715-724.

Wasson J.T. and Rubin A.E. (1985) "Formation of mesosiderites by low-velocity impacts as a natural consequence of planet formation." *Nature* 318, 168-170.

Wasson J.T., Schaudy R., Bild R.W., and Chou C-L (1974) "Mesosiderites-I. Compositions of their metallic portions and possible relationship to other metal-rich meteorite groups." *Geochim. Cosmochim. Acta* 38, 135-149.

Wasson J.T. and Wetherill G.W. (1979) "Dynamical chemical and isotopic evidence regarding the formation locations of asteroids and meteorites." *Asteroids: University of Arizona Press*, 926-974.

Wilson W.E. Jr. (1972) "The Bondoc mesosiderite: Mineralogy and petrology of the metal nodules." Master's thesis, Arizona State Univ., Tempe. 74.

Wisdom J. (1985) "Meteorites may follow a chaotic route to Earth." *Nature* 315, 731–733.

Appendix A- Supplemental Data

Appendix A-1. Crab Orchard Metal Clasts EMPA

Kamacite

Location	*Fe*	*Ni*	*Si*	*S*	*P*	*Co*	*Cu*	*Cr*	*Total*
12	94.59	6.24	0.00	0.00	0.03	0.74	0.03	0.00	101.63
10	93.53	6.51	0.00	0.01	0.02	0.72	0.04	0.00	100.83
34	92.72	6.56	0.00	0.00	0.03	0.73	0.05	0.00	100.08
23	92.80	6.62	0.00	0.00	0.04	0.76	0.04	0.00	100.25
33	92.68	6.64	0.00	0.01	0.03	0.72	0.03	0.01	100.11
38	92.28	6.70	0.00	0.00	0.03	0.69	0.05	0.02	99.77
18	93.03	6.77	0.00	0.01	0.03	0.78	0.02	0.00	100.63
6	92.61	6.79	0.00	0.00	0.02	0.76	0.02	0.00	100.20
9	92.43	6.79	0.00	0.01	0.04	0.74	0.03	0.00	100.05
32	92.56	6.80	0.00	0.00	0.02	0.72	0.05	0.00	100.15
13	92.91	6.84	0.00	0.00	0.03	0.72	0.06	0.00	100.57
22	92.35	6.85	0.00	0.00	0.03	0.72	0.03	0.00	99.97
25	92.59	6.85	0.00	0.01	0.03	0.71	0.03	0.00	100.23
39	92.78	6.86	0.00	0.00	0.02	0.74	0.05	0.00	100.43
8	92.64	6.87	0.00	0.00	0.03	0.72	0.03	0.00	100.28
5	92.77	6.88	0.00	0.00	0.03	0.73	0.05	0.01	100.46
20	92.31	6.89	0.00	0.00	0.04	0.70	0.04	0.00	99.99
35	95.81	6.93	0.00	0.00	0.04	0.71	0.03	0.00	103.52
2	92.31	6.96	0.00	0.01	0.04	0.74	0.02	0.00	100.08
30	92.40	6.97	0.01	0.00	0.02	0.73	0.07	0.01	100.21
19	93.94	6.99	0.00	0.00	0.04	0.77	0.07	0.00	101.79
36	95.31	6.99	0.00	0.00	0.03	0.72	0.00	0.01	103.07
3	92.43	7.01	0.00	0.00	0.03	0.75	0.04	0.00	100.25
21	92.22	7.03	0.01	0.00	0.03	0.76	0.03	0.00	100.08
4	93.32	7.05	0.00	0.00	0.04	0.73	0.05	0.00	101.18
29	91.94	7.09	0.00	0.01	0.03	0.71	0.04	0.01	99.84
28	92.92	7.10	0.00	0.01	0.05	0.70	0.02	0.01	100.80
31	92.94	7.11	0.00	0.00	0.08	0.76	0.05	0.00	100.94
7	92.17	7.12	0.00	0.02	0.03	0.72	0.07	0.01	100.13
Average	92.94	6.85	0.00	0.00	0.03	0.73	0.04	0.00	100.6
Std. Dev.	0.91	0.20	0.00	0.00	0.01	0.02	0.02	0.01	

Appendix A-1. Crab Orchard Metal Clasts EMPA (cont.)

Taenite

Location	*Fe*	*Ni*	*Si*	*S*	*P*	*Co*	*Cu*	*Cr*	*Total*
26	61.97	36.89	0.00	0.00	0.01	0.31	0.16	0.00	99.34
14	61.98	38.01	0.00	0.00	0.01	0.26	0.19	0.00	100.45
27	60.64	38.56	0.00	0.00	0.00	0.28	0.13	0.00	99.62
24	59.91	38.76	0.00	0.00	0.00	0.28	0.22	0.01	99.18
1	59.62	38.88	0.00	0.00	0.00	0.30	0.23	0.00	99.03
16	61.08	39.13	0.00	0.00	0.00	0.25	0.18	0.02	100.67
11	60.59	39.26	0.00	0.01	0.00	0.28	0.18	0.00	100.31
15	59.72	39.56	0.00	0.00	0.00	0.29	0.19	0.00	99.75
37	59.99	39.75	0.00	0.00	0.00	0.30	0.18	0.00	100.22
17	59.72	40.54	0.00	0.00	0.00	0.26	0.18	0.00	100.70
Average	60.52	38.93	0.00	0.00	0.00	0.28	0.18	0.00	99.93
Std. Dev.	0.90	1.00	0.00	0.00	0.00	0.02	0.03	0.01	

Appendix A-2. Crab Orchard Matrix Metal EMPA

Kamacite

Location	*Fe*	*Ni*	*Si*	*S*	*P*	*Co*	*Cu*	*Cr*	*Total*
111 G	94.85	4.29	0.00	0.00	0.00	0.17	0.00	0.00	99.31
166 G	81.08	4.32	0.00	0.00	0.02	0.18	0.00	0.01	85.60
171 G	94.59	4.47	0.00	0.00	0.01	0.19	0.00	0.01	99.27
167 G	94.25	4.66	0.00	0.01	0.00	0.17	0.00	0.00	99.10
127 G	93.65	4.81	0.00	0.00	0.01	0.20	0.00	0.00	98.67
163 G	94.67	4.81	0.00	0.00	0.01	0.17	0.00	0.00	99.66
115 G	95.17	4.84	0.00	0.01	0.01	0.17	0.00	0.00	100.19
158 G	84.99	4.90	0.00	0.01	0.02	0.21	0.00	0.00	90.12
165 G	94.46	4.97	0.00	0.01	0.01	0.18	0.00	0.00	99.62
176 G	93.72	5.02	0.00	0.01	0.00	0.16	0.00	0.00	98.91
145 G	94.66	5.04	0.00	0.01	0.01	0.17	0.00	0.00	99.89
89 G	92.78	5.06	0.00	0.00	0.01	0.18	0.00	0.00	98.02
209 G	94.35	5.08	0.00	0.01	0.02	0.19	0.00	0.01	99.65
226 G	93.58	5.09	0.00	0.00	0.02	0.20	0.00	0.00	98.88
146 G	94.07	5.09	0.00	0.00	0.01	0.18	0.00	0.00	99.35
151 G	94.99	5.11	0.00	0.00	0.00	0.19	0.00	0.00	100.28
105 G	93.78	5.12	0.00	0.01	0.03	0.16	0.00	0.00	99.10
170 G	93.59	5.12	0.00	0.01	0.02	0.17	0.00	0.01	98.92
149 G	93.77	5.19	0.00	0.02	0.02	0.17	0.00	0.01	99.16
155 G	94.03	5.22	0.00	0.00	0.01	0.18	0.00	0.01	99.45
123 G	94.42	5.23	0.00	0.01	0.01	0.18	0.00	0.00	99.86
147 G	94.40	5.25	0.00	0.01	0.01	0.15	0.00	0.00	99.82
135 G	94.29	5.26	0.00	0.00	0.01	0.17	0.00	0.00	99.73
208 G	94.02	5.26	0.00	0.01	0.01	0.17	0.00	0.00	99.47
162 G	93.63	5.28	0.00	0.01	0.02	0.17	0.00	0.00	99.10
150 G	94.31	5.28	0.00	0.01	0.02	0.16	0.00	0.00	99.78
119 G	93.69	5.29	0.00	0.00	0.01	0.15	0.00	0.00	99.14
59 G	93.71	5.30	0.00	0.01	0.02	0.18	0.00	0.00	99.22
107 G	93.04	5.32	0.00	0.00	0.01	0.18	0.00	0.00	98.56
148 G	94.61	5.33	0.00	0.00	0.01	0.17	0.00	0.00	100.11
164 G	93.83	5.33	0.00	0.00	0.02	0.16	0.00	0.01	99.35
108 G	93.53	5.35	0.00	0.00	0.01	0.17	0.00	0.01	99.06
172 G	93.38	5.36	0.00	0.01	0.01	0.16	0.00	0.01	98.93
120 G	93.97	5.36	0.00	0.01	0.01	0.15	0.00	0.00	99.50
126 G	94.14	5.36	0.00	0.00	0.01	0.18	0.00	0.00	99.69
218 G	94.16	5.38	0.00	0.01	0.01	0.17	0.00	0.00	99.73
125 G	94.33	5.41	0.00	0.00	0.02	0.15	0.00	0.00	99.91
173 G	94.39	5.41	0.00	0.01	0.01	0.17	0.00	0.00	99.99
177 G	93.80	5.42	0.00	0.00	0.01	0.17	0.00	0.00	99.41
104 G	94.01	5.42	0.00	0.01	0.01	0.17	0.00	0.01	99.64

Appendix A-2. Crab Orchard Matrix Metal EMPA (cont.)

Location	*Fe*	*Ni*	*Si*	*S*	*P*	*Co*	*Cu*	*Cr*	*Total*
117 G	93.73	5.45	0.00	0.01	0.01	0.18	0.00	0.01	99.38
207 G	93.13	5.45	0.00	0.01	0.00	0.17	0.00	0.00	98.76
114 G	93.16	5.45	0.00	0.00	0.01	0.16	0.00	0.01	98.78
169 G	93.94	5.46	0.00	0.02	0.02	0.16	0.00	0.01	99.59
112 G	93.83	5.47	0.00	0.00	0.02	0.20	0.00	0.00	99.51
168 G	93.36	5.48	0.00	0.00	0.02	0.16	0.00	0.00	99.03
110 G	92.72	5.51	0.00	0.00	0.02	0.17	0.00	0.00	98.42
116 G	93.47	5.51	0.00	0.00	0.02	0.18	0.00	0.00	99.18
124 G	94.13	5.58	0.00	0.00	0.01	0.14	0.00	0.00	99.86
106 G	93.60	5.59	0.00	0.00	0.02	0.15	0.00	0.00	99.36
215 G	94.05	5.61	0.00	0.00	0.01	0.19	0.00	0.00	99.86
88 G	93.72	5.61	0.00	0.01	0.02	0.16	0.00	0.01	99.53
194 G	92.79	5.61	0.00	0.00	0.01	0.18	0.00	0.01	98.60
134 G	93.93	5.62	0.00	0.00	0.01	0.18	0.00	0.00	99.73
181 G	93.21	5.62	0.00	0.00	0.02	0.16	0.00	0.01	99.02
113 G	93.29	5.63	0.00	0.00	0.01	0.16	0.00	0.00	99.09
178 G	93.25	5.63	0.00	0.00	0.03	0.15	0.00	0.00	99.07
199 G	93.05	5.64	0.00	0.00	0.01	0.18	0.00	0.00	98.88
118 G	93.18	5.65	0.00	0.00	0.02	0.15	0.00	0.00	99.00
85 G	93.59	5.65	0.00	0.00	0.02	0.16	0.00	0.01	99.43
156 G	93.75	5.65	0.00	0.00	0.02	0.17	0.00	0.00	99.60
86 G	92.73	5.66	0.00	0.00	0.01	0.16	0.00	0.00	98.56
202 G	92.37	5.67	0.00	0.00	0.01	0.17	0.00	0.00	98.21
159 G	93.23	5.68	0.00	0.01	0.01	0.15	0.00	0.01	99.09
103 G	94.07	5.69	0.00	0.00	0.02	0.15	0.00	0.00	99.93
87 G	92.50	5.71	0.00	0.02	0.02	0.16	0.00	0.00	98.41
128 G	93.25	5.72	0.00	0.01	0.02	0.18	0.00	0.00	99.17
109 G	94.26	5.73	0.00	0.00	0.01	0.17	0.00	0.00	100.16
83 G	92.71	5.74	0.00	0.00	0.02	0.17	0.00	0.00	98.64
161 G	92.96	5.75	0.00	0.01	0.01	0.16	0.00	0.00	98.89
77 G	92.81	5.76	0.00	0.00	0.01	0.17	0.00	0.00	98.75
75 G	92.31	5.76	0.00	0.01	0.01	0.17	0.00	0.00	98.27
195 G	92.33	5.77	0.00	0.01	0.01	0.18	0.00	0.00	98.30
144 G	93.26	5.77	0.00	0.01	0.02	0.16	0.00	0.00	99.22
102 G	93.43	5.78	0.00	0.01	0.02	0.16	0.00	0.00	99.40
197 G	92.50	5.79	0.00	0.01	0.02	0.16	0.00	0.00	98.48
152 G	93.75	5.80	0.00	0.00	0.03	0.18	0.00	0.00	99.76
216 G	94.07	5.81	0.00	0.01	0.01	0.17	0.00	0.00	100.07
76 G	92.38	5.81	0.00	0.00	0.03	0.17	0.00	0.01	98.39
160 G	92.96	5.82	0.00	0.01	0.01	0.18	0.00	0.00	98.99
60 G	93.14	5.82	0.00	0.01	0.02	0.16	0.00	0.00	99.15
136 G	92.64	5.83	0.00	0.01	0.02	0.19	0.00	0.00	98.68

Appendix A-2. Crab Orchard Matrix Metal EMPA (cont.)

Location	*Fe*	*Ni*	*Si*	*S*	*P*	*Co*	*Cu*	*Cr*	*Total*
133 G	93.86	5.83	0.00	0.01	0.01	0.17	0.00	0.00	99.88
82 G	92.73	5.83	0.00	0.00	0.01	0.16	0.00	0.00	98.73
90 G	93.00	5.84	0.00	0.00	0.01	0.19	0.00	0.00	99.04
201 G	93.23	5.84	0.00	0.01	0.01	0.17	0.00	0.00	99.27
187 G	92.73	5.85	0.00	0.00	0.02	0.18	0.00	0.00	98.78
84 G	93.07	5.87	0.00	0.00	0.02	0.14	0.00	0.00	99.10
154 G	93.56	5.87	0.00	0.00	0.03	0.18	0.00	0.01	99.63
186 G	93.36	5.88	0.00	0.00	0.01	0.18	0.00	0.00	99.44
229 G	93.02	5.89	0.00	0.00	0.01	0.15	0.00	0.00	99.07
184 G	93.50	5.89	0.00	0.00	0.01	0.16	0.00	0.00	99.57
74 G	93.38	5.90	0.00	0.01	0.01	0.17	0.00	0.00	99.47
227 G	93.10	5.90	0.00	0.01	0.02	0.16	0.00	0.00	99.19
188 G	92.59	5.92	0.00	0.00	0.02	0.18	0.00	0.00	98.70
81 G	92.83	5.93	0.00	0.01	0.01	0.17	0.00	0.00	98.94
210 G	93.89	5.93	0.00	0.01	0.03	0.17	0.00	0.01	100.05
185 G	92.72	5.94	0.00	0.02	0.01	0.18	0.00	0.00	98.86
70 G	92.87	5.94	0.00	0.00	0.02	0.16	0.00	0.00	98.98
175 G	93.71	5.94	0.00	0.00	0.02	0.18	0.00	0.00	99.86
62 G	91.96	5.95	0.00	0.00	0.01	0.17	0.00	0.00	98.09
196 G	92.20	5.95	0.00	0.00	0.01	0.17	0.00	0.00	98.33
217 G	93.39	5.95	0.00	0.00	0.01	0.18	0.00	0.00	99.53
61 G	92.06	5.96	0.00	0.01	0.02	0.16	0.00	0.00	98.21
153 G	93.24	5.96	0.00	0.00	0.01	0.15	0.00	0.00	99.37
78 G	92.61	5.98	0.00	0.01	0.01	0.16	0.00	0.00	98.78
193 G	93.09	6.01	0.00	0.00	0.02	0.15	0.00	0.00	99.27
100 G	92.09	6.01	0.00	0.01	0.01	0.18	0.00	0.00	98.30
228 G	93.24	6.01	0.00	0.00	0.02	0.18	0.00	0.00	99.44
179 G	93.13	6.01	0.00	0.00	0.02	0.17	0.00	0.01	99.33
198 G	92.09	6.01	0.00	0.01	0.02	0.17	0.00	0.00	98.31
79 G	93.16	6.02	0.00	0.00	0.03	0.15	0.00	0.00	99.36
132 G	92.78	6.03	0.00	0.00	0.01	0.18	0.00	0.00	99.00
91 G	92.14	6.03	0.00	0.00	0.02	0.16	0.00	0.00	98.34
80 G	93.13	6.04	0.00	0.00	0.02	0.16	0.00	0.00	99.35
182 G	92.47	6.04	0.00	0.00	0.02	0.17	0.00	0.00	98.70
101 G	93.11	6.05	0.00	0.00	0.02	0.16	0.00	0.00	99.34
225 G	93.42	6.05	0.00	0.02	0.02	0.18	0.00	0.00	99.69
180 G	92.98	6.05	0.00	0.00	0.02	0.17	0.00	0.00	99.22
63 G	92.69	6.06	0.00	0.01	0.01	0.17	0.00	0.00	98.95
72 G	92.39	6.06	0.00	0.01	0.02	0.17	0.00	0.00	98.65
183 G	93.22	6.07	0.00	0.00	0.02	0.17	0.00	0.01	99.49
174 G	92.84	6.08	0.00	0.01	0.02	0.17	0.00	0.00	99.12
129 G	93.77	6.08	0.00	0.00	0.02	0.16	0.00	0.01	100.04

Appendix A-2. Crab Orchard Matrix Metal EMPA (cont.)

Location	*Fe*	*Ni*	*Si*	*S*	*P*	*Co*	*Cu*	*Cr*	*Total*
223 G	92.31	6.09	0.00	0.01	0.02	0.18	0.00	0.00	98.60
200 G	92.25	6.09	0.00	0.00	0.01	0.18	0.00	0.00	98.54
130 G	92.82	6.10	0.00	0.01	0.02	0.16	0.00	0.00	99.11
206 G	93.15	6.10	0.00	0.00	0.02	0.17	0.00	0.01	99.45
92 G	91.91	6.11	0.00	0.00	0.01	0.17	0.00	0.00	98.20
143 G	93.33	6.11	0.00	0.01	0.02	0.17	0.00	0.01	99.64
192 G	92.11	6.12	0.00	0.00	0.02	0.18	0.00	0.00	98.43
69 G	92.64	6.13	0.00	0.01	0.01	0.16	0.00	0.00	98.95
73 G	93.37	6.13	0.00	0.00	0.01	0.17	0.00	0.00	99.69
224 G	93.37	6.13	0.00	0.00	0.02	0.17	0.00	0.00	99.70
214 G	93.21	6.14	0.00	0.00	0.01	0.17	0.00	0.00	99.54
219 G	92.98	6.14	0.00	0.02	0.01	0.18	0.00	0.00	99.33
211 G	93.35	6.14	0.00	0.00	0.02	0.16	0.00	0.00	99.68
203 G	92.33	6.15	0.00	0.01	0.02	0.19	0.00	0.00	98.70
71 G	92.40	6.17	0.00	0.00	0.02	0.16	0.00	0.00	98.75
137 G	93.55	6.18	0.00	0.02	0.02	0.17	0.00	0.00	99.93
221 G	92.76	6.18	0.00	0.01	0.02	0.15	0.00	0.00	99.12
220 G	92.64	6.19	0.00	0.00	0.02	0.20	0.00	0.00	99.05
68 G	93.01	6.19	0.00	0.00	0.03	0.15	0.00	0.00	99.38
205 G	92.52	6.20	0.00	0.01	0.02	0.17	0.00	0.00	98.90
99 G	92.97	6.21	0.00	0.00	0.02	0.16	0.00	0.00	99.36
191 G	92.36	6.21	0.00	0.00	0.03	0.18	0.00	0.00	98.77
157 G	92.76	6.22	0.00	0.01	0.02	0.18	0.00	0.00	99.19
93 G	92.76	6.22	0.00	0.01	0.01	0.17	0.00	0.00	99.17
189 G	92.10	6.22	0.00	0.01	0.02	0.19	0.00	0.00	98.54
64 G	92.44	6.23	0.00	0.02	0.02	0.20	0.00	0.00	98.90
190 G	92.53	6.23	0.00	0.00	0.02	0.16	0.00	0.00	98.95
96 G	92.76	6.24	0.00	0.00	0.03	0.16	0.00	0.00	99.19
95 G	92.88	6.25	0.00	0.00	0.02	0.17	0.00	0.01	99.32
222 G	92.76	6.25	0.00	0.01	0.01	0.17	0.00	0.00	99.20
94 G	92.85	6.25	0.00	0.00	0.02	0.16	0.00	0.00	99.29
140 G	92.99	6.25	0.00	0.00	0.02	0.17	0.00	0.01	99.44
213 G	92.81	6.26	0.00	0.00	0.02	0.19	0.00	0.00	99.27
131 G	93.04	6.27	0.00	0.00	0.02	0.16	0.00	0.00	99.49
65 G	93.11	6.29	0.00	0.01	0.00	0.15	0.00	0.00	99.56
97 G	92.84	6.29	0.00	0.01	0.02	0.16	0.00	0.01	99.32
67 G	93.30	6.30	0.00	0.01	0.03	0.17	0.00	0.00	99.82
204 G	91.99	6.31	0.00	0.01	0.02	0.17	0.00	0.00	98.49
66 G	93.04	6.31	0.00	0.00	0.02	0.15	0.00	0.00	99.51
142 G	92.77	6.31	0.00	0.01	0.03	0.16	0.00	0.00	99.28
98 G	92.61	6.32	0.00	0.00	0.03	0.15	0.00	0.00	99.10
141 G	93.21	6.33	0.00	0.00	0.03	0.18	0.00	0.00	99.74

Appendix A-2. Crab Orchard Matrix Metal EMPA (cont.)

Location	*Fe*	*Ni*	*Si*	*S*	*P*	*Co*	*Cu*	*Cr*	*Total*
139 G	92.50	6.34	0.00	0.00	0.03	0.16	0.00	0.00	99.02
212 G	93.36	6.36	0.00	0.00	0.02	0.16	0.00	0.00	99.90
138 G	93.45	6.37	0.00	0.01	0.02	0.17	0.00	0.00	100.02
Average	93.12	5.75	0.00	0.00	0.02	0.17	0.00	0.00	99.07
Std. Dev.	1.32	0.44	0.00	0.00	0.01	0.01	0.00	0.00	

Appendix A-2. Crab Orchard Matrix Metal EMPA (cont.)

Taenite

Location	*Fe*	*Ni*	*Si*	*S*	*P*	*Co*	*Cu*	*Cr*	*Total*
121 G	50.07	47.59	0.00	0.03	0.00	0.00	0.00	0.01	97.70
122 G	49.45	47.87	0.00	0.04	0.00	0.00	0.00	0.02	97.37
Average	49.76	47.73	0.00	0.03	0.00	0.00	0.00	0.01	97.54
Std. Dev.	0.43	0.20	0.00	0.00	0.00	0.00	0.00	0.00	

Appendix A-3. Chinguetti Metal Clast EMPA

Kamacite

Location	*Fe*	*Ni*	*Si*	*S*	*P*	*Co*	*Cu*	*Cr*	*Total*
23	93.82	5.53	0.00	0.01	0.02	0.77	0.01	0.02	100.18
32	93.93	5.59	0.00	0.01	0.02	0.82	0.06	0.00	100.42
30	94.20	5.63	0.00	0.00	0.01	0.76	0.03	0.00	100.63
33	94.23	5.78	0.00	0.00	0.01	0.80	0.03	0.01	100.87
1	93.50	6.02	0.00	0.01	0.02	0.78	0.00	0.01	100.35
28	93.74	6.15	0.00	0.01	0.02	0.79	0.08	0.01	100.80
22	93.13	6.17	0.00	0.00	0.02	0.80	0.05	0.00	100.17
39	93.00	6.20	0.00	0.00	0.03	0.80	0.08	0.00	100.10
24	93.40	6.23	0.00	0.01	0.02	0.76	0.02	0.01	100.45
38	92.94	6.25	0.00	0.00	0.02	0.84	0.06	0.00	100.10
29	93.36	6.26	0.00	0.00	0.02	0.79	0.03	0.00	100.45
19	92.99	6.35	0.00	0.00	0.04	0.82	0.05	0.00	100.25
9	92.60	6.38	0.00	0.01	0.02	0.82	0.02	0.00	99.86
8	92.69	6.41	0.00	0.01	0.04	0.80	0.04	0.01	99.99
25	93.27	6.41	0.00	0.01	0.02	0.78	0.04	0.00	100.53
37	92.53	6.43	0.00	0.00	0.02	0.80	0.05	0.00	99.83
40	92.78	6.46	0.00	0.01	0.03	0.80	0.03	0.00	100.10
18	93.18	6.46	0.00	0.01	0.03	0.77	0.03	0.00	100.48
34	93.21	6.60	0.00	0.01	0.03	0.81	0.05	0.00	100.70
4	93.04	6.62	0.00	0.01	0.04	0.79	0.03	0.00	100.52
7	93.15	6.62	0.01	0.01	0.03	0.82	0.03	0.00	100.67
12	92.33	6.63	0.00	0.00	0.02	0.78	0.01	0.00	99.78
11	92.45	6.65	0.00	0.00	0.02	0.77	0.04	0.01	99.93
5	93.39	6.66	0.00	0.01	0.02	0.80	0.05	0.01	100.95
10	92.53	6.72	0.00	0.00	0.02	0.81	0.03	0.00	100.12
2	93.00	6.75	0.00	0.01	0.02	0.75	0.03	0.00	100.55
6	92.64	6.82	0.00	0.00	0.03	0.78	0.05	0.00	100.31
Average	93.15	6.33	0.00	0.00	0.02	0.79	0.04	0.00	100.34
Std. Dev.	0.52	0.36	0.00	0.00	0.01	0.02	0.02	0.01	

Appendix A-3. Chinguetti Metal Clast EMPA (cont.)

Taenite

Location	*Fe*	*Ni*	*Si*	*S*	*P*	*Co*	*Cu*	*Cr*	*Total*
13	63.65	35.43	0.00	0.00	0.00	0.38	0.14	0.00	99.60
16	63.85	35.56	0.00	0.01	0.01	0.33	0.19	0.00	99.95
26	63.64	35.74	0.00	0.00	0.01	0.36	0.17	0.00	99.91
35	62.07	37.03	0.00	0.00	0.01	0.33	0.19	0.01	99.63
15	61.82	37.41	0.00	0.01	0.01	0.33	0.20	0.01	99.79
31	61.57	37.58	0.00	0.01	0.00	0.29	0.21	0.00	99.66
21	61.00	38.10	0.00	0.01	0.01	0.32	0.20	0.00	99.63
36	60.77	38.44	0.00	0.00	0.00	0.32	0.20	0.00	99.73
14	60.67	38.63	0.00	0.00	0.01	0.34	0.18	0.00	99.83
17	59.13	40.25	0.00	0.00	0.00	0.27	0.23	0.00	99.87
20	58.85	40.27	0.00	0.01	0.00	0.26	0.18	0.00	99.57
27	58.57	40.75	0.00	0.00	0.01	0.30	0.20	0.00	99.83
Average	61.30	37.93	0.00	0.00	0.01	0.32	0.19	0.00	99.75
Std. Dev.	1.84	1.85	0.00	0.01	0.01	0.04	0.02	0.00	

Appendix A-4. Chinguetti Matrix Metal EMPA

Kamacite

Location	*Fe*	*Ni*	*Si*	*S*	*P*	*Co*	*Cu*	*Cr*	*Total*
237 G	96.86	3.64	0.00	0.00	0.01	0.24	0.00	0.00	100.75
243 G	95.45	4.21	0.00	0.02	0.01	0.24	0.00	0.00	99.92
239 G	95.71	4.37	0.00	0.01	0.02	0.22	0.00	0.00	100.33
245 G	96.41	4.44	0.00	0.01	0.01	0.24	0.00	0.00	101.11
274 G	97.21	4.54	0.00	0.00	0.01	0.26	0.00	0.00	102.03
242 G	95.35	4.58	0.00	0.00	0.02	0.24	0.00	0.00	100.20
238 G	95.54	4.69	0.00	0.00	0.01	0.23	0.00	0.00	100.48
241 G	95.81	4.84	0.00	0.01	0.00	0.22	0.00	0.00	100.89
318 G	96.89	4.90	0.00	0.01	0.02	0.23	0.00	0.00	102.05
277 G	97.53	4.97	0.00	0.01	0.02	0.26	0.00	0.00	102.77
255 G	95.96	5.00	0.00	0.00	0.03	0.21	0.00	0.01	101.21
262 G	96.11	5.10	0.00	0.02	0.01	0.20	0.00	0.00	101.44
261 G	96.03	5.10	0.00	0.01	0.02	0.22	0.00	0.00	101.39
254 G	96.81	5.21	0.00	0.01	0.01	0.22	0.00	0.01	102.27
249 G	94.44	5.33	0.00	0.01	0.02	0.23	0.00	0.00	100.04
240 G	94.28	5.34	0.00	0.00	0.01	0.20	0.00	0.00	99.84
267 G	97.01	5.40	0.00	0.01	0.01	0.23	0.00	0.00	102.66
258 G	95.27	5.42	0.00	0.00	0.01	0.22	0.00	0.00	100.93
250 G	95.22	5.45	0.00	0.01	0.02	0.25	0.00	0.00	100.95
256 G	94.82	5.50	0.00	0.01	0.02	0.22	0.00	0.01	100.58
259 G	95.18	5.53	0.00	0.01	0.01	0.22	0.00	0.00	100.93
253 G	97.58	5.55	0.00	0.01	0.02	0.21	0.00	0.00	103.36
299 G	96.64	5.55	0.00	0.01	0.03	0.24	0.00	0.00	102.47
257 G	95.30	5.56	0.00	0.01	0.01	0.23	0.00	0.01	101.12
235 G	97.53	5.60	0.00	0.02	0.02	0.20	0.00	0.00	103.36
260 G	94.83	5.60	0.00	0.00	0.01	0.23	0.00	0.00	100.67
236 G	98.54	5.61	0.00	0.02	0.02	0.23	0.00	0.00	104.41
244 G	95.25	5.67	0.00	0.00	0.01	0.23	0.00	0.00	101.17
331 G	95.61	5.69	0.00	0.00	0.02	0.25	0.00	0.00	101.57
314 G	96.51	5.70	0.00	0.01	0.02	0.24	0.00	0.00	102.48
265 G	96.16	5.71	0.00	0.01	0.02	0.24	0.00	0.00	102.15
278 G	95.56	5.74	0.00	0.00	0.02	0.25	0.00	0.00	101.57
285 G	94.80	5.75	0.00	0.01	0.02	0.22	0.00	0.00	100.81
290 G	94.46	5.78	0.00	0.00	0.03	0.23	0.00	0.00	100.50
282 G	95.92	5.79	0.00	0.00	0.02	0.27	0.00	0.01	102.01
269 G	94.81	5.82	0.00	0.01	0.02	0.24	0.00	0.00	100.90
284 G	94.79	5.82	0.00	0.03	0.01	0.24	0.00	0.00	100.88
266 G	96.03	5.83	0.00	0.01	0.02	0.25	0.00	0.00	102.14
271 G	96.02	5.88	0.00	0.01	0.02	0.26	0.00	0.00	102.19
280 G	95.77	5.88	0.00	0.01	0.01	0.24	0.00	0.00	101.92

Appendix A-4. Chinguetti Matrix Metal EMPA (cont.)

Location	*Fe*	*Ni*	*Si*	*S*	*P*	*Co*	*Cu*	*Cr*	*Total*
247 G	94.82	5.90	0.00	0.00	0.02	0.23	0.00	0.00	100.98
279 G	95.77	5.90	0.00	0.01	0.02	0.26	0.00	0.00	101.96
246 G	94.74	5.91	0.00	0.00	0.02	0.23	0.00	0.00	100.89
297 G	95.95	5.91	0.00	0.00	0.03	0.24	0.00	0.01	102.13
330 G	96.16	5.95	0.00	0.00	0.02	0.24	0.00	0.00	102.36
298 G	95.39	5.96	0.00	0.01	0.01	0.28	0.00	0.00	101.64
272 G	95.36	5.97	0.00	0.01	0.02	0.25	0.00	0.00	101.61
323 G	95.63	5.97	0.00	0.01	0.02	0.26	0.00	0.01	101.89
292 G	95.44	5.98	0.00	0.01	0.02	0.27	0.00	0.01	101.73
268 G	95.56	6.01	0.00	0.02	0.03	0.22	0.00	0.00	101.84
291 G	95.00	6.01	0.00	0.00	0.02	0.25	0.00	0.00	101.27
321 G	96.45	6.03	0.00	0.00	0.02	0.24	0.00	0.01	102.75
281 G	96.10	6.06	0.00	0.00	0.02	0.25	0.00	0.00	102.43
332 G	95.13	6.06	0.00	0.01	0.01	0.24	0.00	0.01	101.46
283 G	95.51	6.07	0.00	0.01	0.02	0.26	0.00	0.00	101.87
325 G	96.43	6.08	0.00	0.01	0.02	0.25	0.00	0.00	102.78
329 G	96.32	6.09	0.00	0.01	0.01	0.23	0.00	0.00	102.66
293 G	94.85	6.12	0.00	0.00	0.02	0.25	0.00	0.00	101.25
319 G	95.98	6.12	0.00	0.01	0.04	0.24	0.00	0.00	102.38
328 G	96.09	6.13	0.00	0.00	0.02	0.24	0.00	0.00	102.48
300 G	95.98	6.14	0.00	0.00	0.01	0.24	0.00	0.00	102.37
320 G	95.40	6.19	0.00	0.00	0.02	0.25	0.00	0.00	101.86
294 G	94.43	6.20	0.00	0.01	0.02	0.27	0.00	0.00	100.93
326 G	95.95	6.23	0.00	0.01	0.01	0.24	0.00	0.01	102.44
313 G	95.54	6.23	0.00	0.00	0.02	0.24	0.00	0.00	102.03
296 G	95.82	6.24	0.00	0.01	0.02	0.25	0.00	0.00	102.35
301 G	95.57	6.27	0.00	0.01	0.02	0.25	0.00	0.00	102.11
295 G	96.01	6.28	0.00	0.01	0.03	0.24	0.00	0.00	102.57
304 G	95.46	6.30	0.00	0.02	0.02	0.24	0.00	0.01	102.04
302 G	96.06	6.30	0.00	0.01	0.02	0.23	0.00	0.00	102.62
307 G	95.11	6.32	0.00	0.02	0.02	0.24	0.00	0.00	101.69
324 G	95.56	6.34	0.00	0.02	0.02	0.22	0.00	0.00	102.16
306 G	95.47	6.35	0.00	0.00	0.02	0.24	0.00	0.00	102.09
322 G	95.97	6.36	0.00	0.01	0.03	0.23	0.00	0.00	102.59
335 G	94.83	6.36	0.00	0.01	0.03	0.23	0.00	0.00	101.46
303 G	96.01	6.38	0.00	0.00	0.01	0.25	0.00	0.00	102.66
305 G	95.77	6.41	0.00	0.00	0.01	0.24	0.00	0.00	102.43
312 G	95.51	6.42	0.00	0.01	0.02	0.24	0.00	0.00	102.20
308 G	95.23	6.42	0.00	0.01	0.02	0.24	0.00	0.01	101.93
315 G	95.67	6.44	0.00	0.01	0.02	0.27	0.00	0.00	102.39
309 G	94.39	6.50	0.00	0.00	0.01	0.25	0.00	0.00	101.16
327 G	95.50	6.52	0.00	0.01	0.03	0.25	0.00	0.00	102.30

Appendix A-4. Chinguetti Matrix Metal EMPA (cont.)

Location	*Fe*	*Ni*	*Si*	*S*	*P*	*Co*	*Cu*	*Cr*	*Total*
317 G	94.66	6.57	0.00	0.01	0.01	0.25	0.00	0.01	101.51
310 G	94.27	6.63	0.00	0.01	0.02	0.24	0.00	0.00	101.18
311 G	94.56	6.67	0.00	0.01	0.02	0.25	0.00	0.00	101.51
316 G	94.71	6.69	0.00	0.01	0.02	0.26	0.00	0.00	101.69
248 G	88.24	7.38	0.00	0.02	0.03	0.23	0.00	0.00	95.90
Average	95.59	5.81	0.00	0.01	0.02	0.24	0.00	0.00	101.67
Std. Dev.	1.13	0.63	0.00	0.01	0.01	0.02	0.00	0.00	

Appendix A-4. Chinguetti Matrix Metal EMPA (cont.)

Taenite

Location	*Fe*	*Ni*	*Si*	*S*	*P*	*Co*	*Cu*	*Cr*	*Total*
287 G	63.03	38.22	0.00	0.00	0.01	0.00	0.00	0.00	101.26
288 G	61.71	39.01	0.00	0.01	0.00	0.00	0.00	0.00	100.73
231 G	60.51	39.95	0.00	0.01	0.00	0.00	0.00	0.00	100.46
273 G	60.99	40.21	0.00	0.01	0.00	0.00	0.00	0.00	101.22
270 G	61.14	40.24	0.00	0.01	0.01	0.00	0.00	0.00	101.40
286 G	61.48	40.24	0.00	0.00	0.01	0.00	0.00	0.00	101.73
232 G	59.83	40.91	0.00	0.00	0.01	0.00	0.00	0.00	100.76
275 G	59.24	41.50	0.00	0.00	0.01	0.00	0.00	0.00	100.75
264 G	58.81	42.14	0.00	0.02	0.00	0.00	0.00	0.00	100.97
251 G	56.80	43.29	0.00	0.01	0.02	0.00	0.00	0.00	100.12
276 G	56.15	44.78	0.00	0.00	0.01	0.00	0.00	0.00	100.93
233 G	55.23	44.84	0.00	0.02	0.01	0.00	0.00	0.01	100.10
230 G	53.50	47.44	0.00	0.01	0.01	0.00	0.00	0.01	100.96
289 G	51.84	49.88	0.00	0.00	0.01	0.00	0.00	0.00	101.72
234 G	49.97	50.54	0.00	0.01	0.01	0.00	0.00	0.00	100.53
252 G	50.46	51.24	0.00	0.01	0.00	0.00	0.00	0.00	101.71
263 G	49.54	51.75	0.00	0.01	0.00	0.00	0.00	0.00	101.29
Average	57.07	43.89	0.00	0.01	0.01	0.00	0.00	0.00	100.98
Std. Dev.	4.55	4.61	0.00	0.01	0.00	0.00	0.00	0.00	

Appendix A-5. Vaca Muerta Metal Clast EMPA

Kamacite

Location	*Fe*	*Ni*	*Si*	*S*	*P*	*Co*	*Cu*	*Cr*	*Total*
8	94.60	5.01	0.00	0.00	0.03	0.82	0.03	0.00	100.49
11	94.69	5.05	0.00	0.01	0.03	0.78	0.04	0.00	100.60
4	94.61	5.08	0.00	0.00	0.01	0.80	0.04	0.00	100.53
3	94.69	5.15	0.00	0.01	0.01	0.80	0.01	0.00	100.67
2	94.69	5.28	0.00	0.01	0.03	0.80	0.03	0.00	100.84
9	94.31	5.38	0.00	0.00	0.03	0.86	0.05	0.01	100.63
15	94.37	5.43	0.00	0.01	0.02	0.82	0.04	0.00	100.68
1	94.28	5.46	0.00	0.00	0.02	0.81	0.05	0.01	100.63
13	93.93	5.55	0.00	0.01	0.03	0.80	0.04	0.00	100.35
14	94.19	5.56	0.02	0.01	0.01	0.85	0.05	0.00	100.68
20	93.98	6.25	0.00	0.01	0.03	0.80	0.04	0.01	101.13
17	93.55	6.34	0.00	0.01	0.03	0.81	0.03	0.00	100.75
19	94.03	6.45	0.00	0.00	0.02	0.79	0.04	0.00	101.33
21	93.87	6.55	0.00	0.01	0.03	0.84	0.03	0.01	101.33
16	93.56	6.58	0.00	0.00	0.05	0.79	0.02	0.02	101.02
18	93.81	6.69	0.00	0.02	0.02	0.83	0.04	0.00	101.41
Average	94.20	5.74	0.00	0.01	0.03	0.81	0.04	0.00	100.82
Std. Dev.	0.39	0.62	0.00	0.01	0.01	0.02	0.01	0.01	

Appendix A-5. Vaca Muerta Metal Clast EMPA (cont.)

Taenite

Location	*Fe*	*Ni*	*Si*	*S*	*P*	*Co*	*Cu*	*Cr*	*Total*
7	56.78	42.47	0.00	0.01	0.01	0.25	0.20	0.00	99.72
5	56.33	42.55	0.00	0.00	0.01	0.27	0.21	0.00	99.37
6	56.50	42.77	0.00	0.00	0.01	0.25	0.21	0.00	99.75
12	55.58	43.17	0.00	0.00	0.01	0.27	0.23	0.01	99.27
10	50.70	48.26	0.00	0.01	0.00	0.24	0.26	0.01	99.47
Average	55.18	43.84	0.00	0.00	0.01	0.26	0.22	0.00	99.51
Std. Dev.	2.54	2.48	0.00	0.00	0.00	0.01	0.02	0.01	

Appendix A-6. RKPA 79015 Metal Clast EMPA

Kamacite

Location	*Fe*	*Ni*	*Si*	*S*	*P*	*Co*	*Cu*	*Cr*	*Total*
24	94.25	6.28	0.00	0.01	0.03	0.80	0.04	0.00	101.39
18	93.62	6.49	0.00	0.01	0.03	0.78	0.03	0.00	100.95
9	93.03	6.56	0.00	0.01	0.03	0.73	0.04	0.00	100.41
21	92.44	6.61	0.00	0.00	0.04	0.78	0.06	0.00	99.93
8	93.15	6.61	0.00	0.00	0.02	0.80	0.05	0.00	100.63
23	93.65	6.62	0.00	0.00	0.05	0.81	0.06	0.00	101.18
19	92.50	6.62	0.00	0.01	0.03	0.82	0.03	0.00	100.01
27	93.40	6.68	0.00	0.00	0.02	0.78	0.01	0.00	100.89
22	92.74	6.69	0.00	0.00	0.03	0.80	0.04	0.01	100.29
1	92.56	6.72	0.00	0.00	0.03	0.77	0.04	0.01	100.13
26	93.30	6.72	0.00	0.00	0.03	0.77	0.03	0.00	100.85
10	93.01	6.73	0.00	0.00	0.03	0.79	0.02	0.00	100.59
11	93.19	6.74	0.00	0.00	0.04	0.81	0.03	0.00	100.81
25	93.41	6.76	0.00	0.00	0.03	0.79	0.06	0.02	101.06
4	93.14	6.79	0.00	0.02	0.03	0.84	0.04	0.00	100.86
3	92.63	6.80	0.00	0.01	0.03	0.79	0.04	0.00	100.30
28	93.32	6.81	0.00	0.00	0.02	0.77	0.03	0.00	100.96
15	92.70	6.85	0.00	0.01	0.02	0.76	0.05	0.00	100.40
31	92.66	6.88	0.00	0.00	0.02	0.79	0.04	0.00	100.39
32	93.06	6.94	0.00	0.00	0.04	0.79	0.02	0.00	100.84
33	92.83	6.96	0.00	0.01	0.02	0.78	0.02	0.00	100.62
2	92.70	7.01	0.00	0.00	0.04	0.80	0.05	0.00	100.59
29	93.10	7.02	0.00	0.02	0.04	0.78	0.07	0.02	101.04
16	92.83	7.08	0.03	0.01	0.04	0.77	0.04	0.00	100.80
Average	93.05	6.75	0.00	0.00	0.03	0.79	0.04	0.00	100.66
Std. Dev.	0.43	0.18	0.01	0.01	0.01	0.02	0.01	0.01	

Appendix A-6. RKPA 79015 Metal Clast EMPA (cont.)

Taenite

Location	*Fe*	*Ni*	*Si*	*S*	*P*	*Co*	*Cu*	*Cr*	*Total*
12	66.98	32.26	0.00	0.02	0.02	0.46	0.15	0.01	99.89
20	65.98	32.94	0.00	0.01	0.02	0.35	0.15	0.02	99.46
7	64.94	34.61	0.00	0.00	0.02	0.38	0.17	0.00	100.11
6	64.66	34.63	0.00	0.00	0.01	0.38	0.17	0.00	99.85
17	64.66	34.68	0.00	0.00	0.00	0.34	0.18	0.01	99.87
5	64.59	34.69	0.00	0.01	0.00	0.35	0.16	0.00	99.80
36	63.47	35.62	0.00	0.00	0.01	0.34	0.17	0.01	99.60
34	62.36	36.84	0.00	0.00	0.01	0.29	0.17	0.00	99.66
35	61.58	37.75	0.00	0.00	0.02	0.32	0.15	0.00	99.80
14	60.65	38.59	0.00	0.01	0.00	0.34	0.23	0.01	99.84
30	59.87	39.32	0.00	0.00	0.02	0.29	0.21	0.01	99.71
Average	63.61	35.63	0.00	0.00	0.01	0.35	0.17	0.01	99.78
Std. Dev.	2.24	2.25	0.00	0.01	0.01	0.05	0.03	0.01	

Appendix A-7. Chaunskij Metal Clast EMPA

Kamacite

Location	*Fe*	*Ni*	*Si*	*S*	*P*	*Co*	*Cu*	*Cr*	*Total*
29	94.65	4.98	0.00	0.00	0.02	0.84	0.04	0.01	100.54
7	94.04	6.07	0.00	0.00	0.03	0.80	0.01	0.01	100.96
12	93.57	6.22	0.00	0.01	0.00	0.83	0.04	0.00	100.67
1	93.49	6.29	0.00	0.02	0.02	0.80	0.02	0.01	100.65
3	93.73	6.49	0.00	0.00	0.02	0.83	0.04	0.01	101.12
36	93.61	6.61	0.00	0.01	0.02	0.91	0.05	0.00	101.21
32	93.74	6.62	0.00	0.00	0.04	0.84	0.04	0.00	101.28
22	92.87	6.72	0.00	0.01	0.03	0.82	0.04	0.01	100.48
33	93.37	6.74	0.00	0.02	0.02	0.87	0.05	0.00	101.06
14	92.65	6.75	0.00	0.00	0.01	0.91	0.06	0.00	100.37
13	92.70	6.77	0.00	0.00	0.03	0.84	0.04	0.00	100.37
2	93.29	6.78	0.00	0.01	0.03	0.85	0.05	0.00	101.01
40	92.84	6.78	0.00	0.00	0.02	0.91	0.07	0.00	100.62
11	92.97	6.81	0.00	0.00	0.01	0.83	0.05	0.00	100.67
38	92.83	6.86	0.00	0.00	0.03	0.89	0.02	0.00	100.63
23	94.07	6.86	0.00	0.00	0.03	0.90	0.05	0.00	101.91
37	92.30	6.87	0.00	0.00	0.01	0.94	0.01	0.00	100.13
9	93.11	6.93	0.00	0.00	0.02	0.79	0.02	0.00	100.86
30	92.68	6.93	0.00	0.00	0.02	0.84	0.05	0.02	100.54
39	92.38	6.95	0.00	0.00	0.03	0.90	0.00	0.00	100.26
18	92.92	6.96	0.00	0.00	0.03	0.84	0.04	0.00	100.79
35	91.93	7.00	0.00	0.01	0.03	0.84	0.05	0.01	99.86
16	92.61	7.01	0.00	0.01	0.02	0.86	0.06	0.01	100.58
17	92.61	7.02	0.00	0.01	0.02	0.88	0.06	0.00	100.61
31	93.07	7.03	0.00	0.00	0.03	0.83	0.05	0.03	101.04
10	94.14	7.03	0.00	0.00	0.02	0.85	0.06	0.00	102.10
34	92.27	7.09	0.00	0.00	0.03	0.89	0.05	0.00	100.32
Average	93.13	6.17	0.00	0.00	0.02	0.86	0.04	0.00	100.76
Std. Dev.	0.66	0.43	0.00	0.01	0.01	0.04	0.02	0.01	

Appendix A-7. Chaunskij Metal Clast EMPA (cont.)

Taenite

Location	*Fe*	*Ni*	*Si*	*S*	*P*	*Co*	*Cu*	*Cr*	*Total*
27	75.76	23.41	0.01	0.01	0.02	0.52	0.10	0.00	99.83
26	74.55	24.68	0.00	0.00	0.02	0.51	0.13	0.00	99.88
25	73.51	25.72	0.00	0.01	0.02	0.47	0.12	0.02	99.87
20	72.03	27.65	0.00	0.00	0.01	0.42	0.14	0.01	100.25
19	71.23	27.85	0.00	0.01	0.01	0.46	0.12	0.00	99.67
28	71.50	27.92	0.00	0.01	0.01	0.49	0.13	0.00	100.04
24	70.91	28.34	0.00	0.01	0.00	0.47	0.13	0.00	99.86
8	68.54	31.05	0.00	0.00	0.01	0.38	0.15	0.00	100.13
15	67.78	32.11	0.00	0.00	0.00	0.38	0.14	0.03	100.43
4	68.01	32.51	0.00	0.00	0.00	0.36	0.18	0.00	101.06
6	65.56	34.04	0.00	0.00	0.00	0.37	0.17	0.01	100.15
5	64.87	34.95	0.00	0.00	0.00	0.35	0.17	0.00	100.35
21	63.35	35.79	0.00	0.00	0.01	0.36	0.22	0.01	99.74
Average	69.81	29.69	0.00	0.00	0.01	0.43	0.15	0.01	100.10
Std. Dev.	3.83	4.00	0.00	0.00	0.01	0.06	0.03	0.01	

Appendix B

Individual SEM Elemental X-ray maps for Crab Orchard

The entire section was analyzed for seventeen elements:

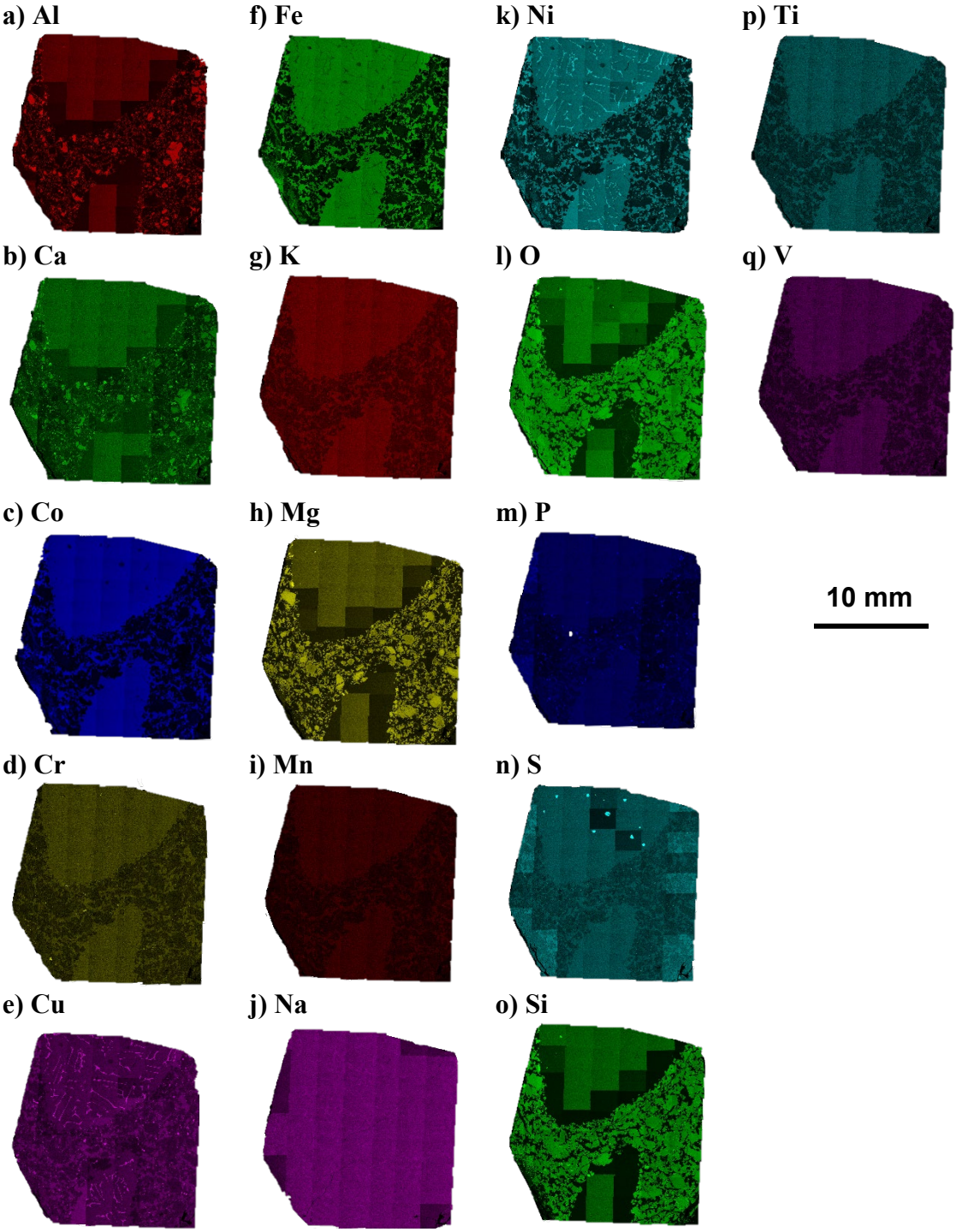

B-a) Crab Orchard – Al

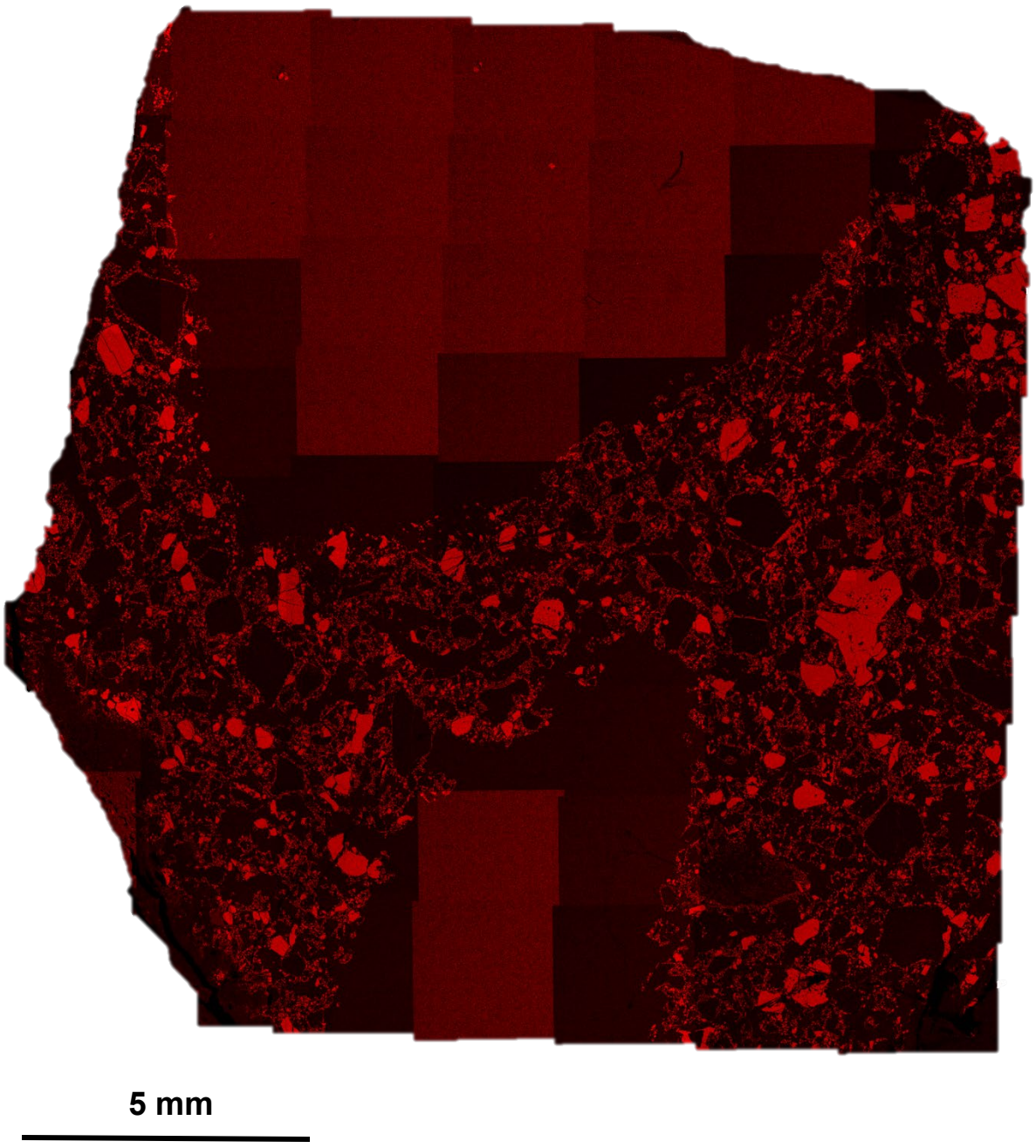

B-b) Crab Orchard – Ca

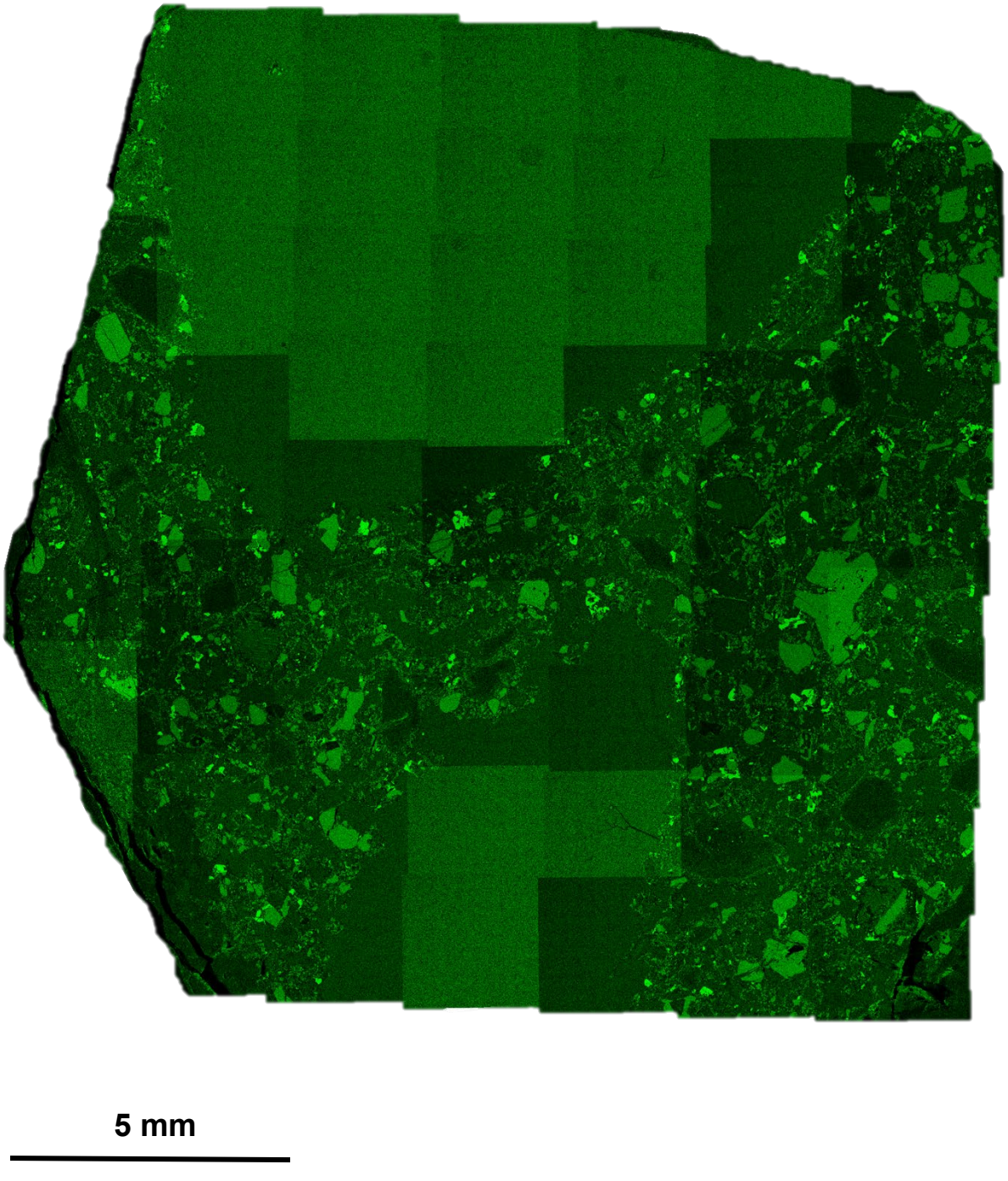

B-c) Crab Orchard – Co

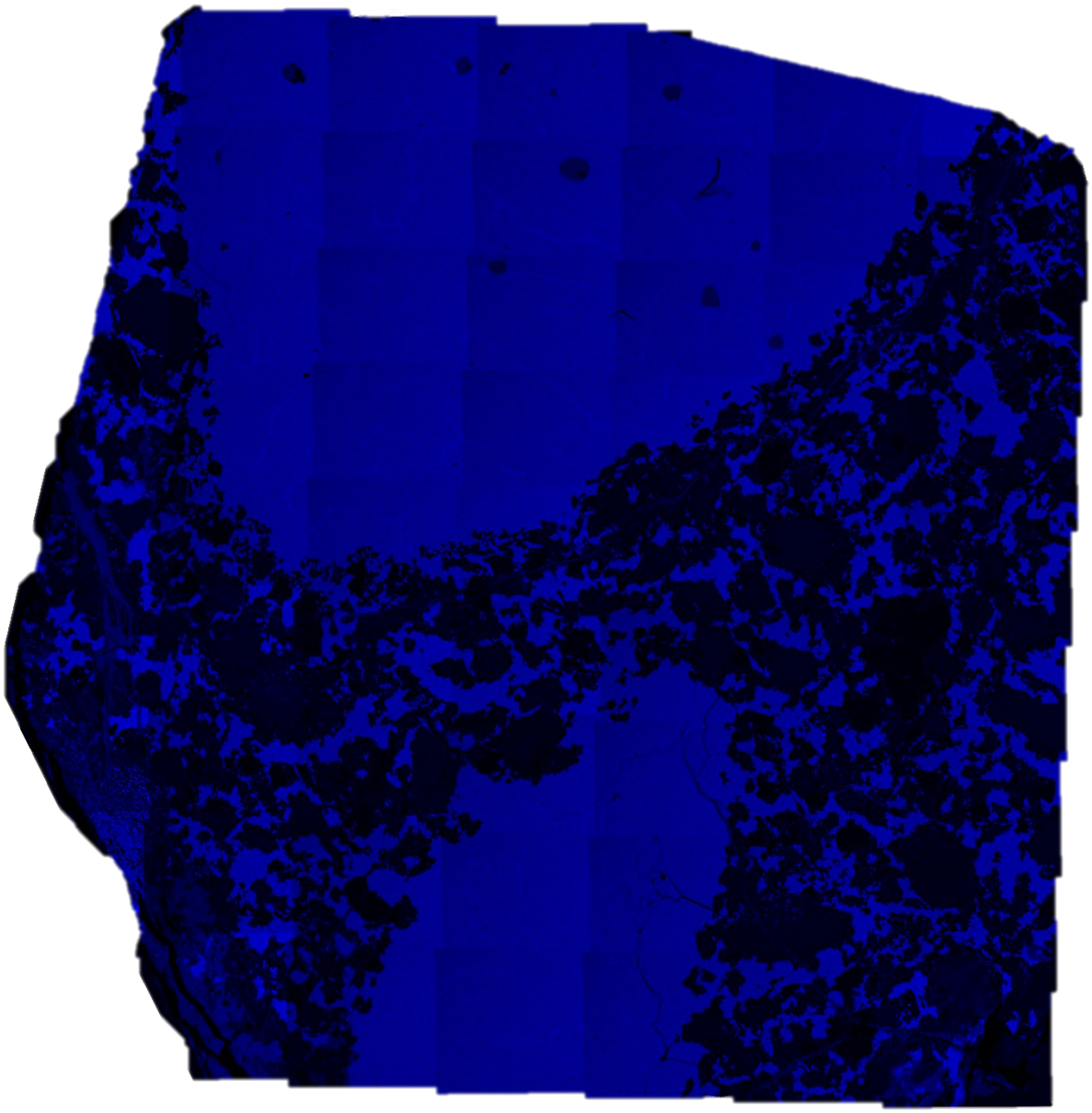

5 mm

B-d) Crab Orchard – Cr

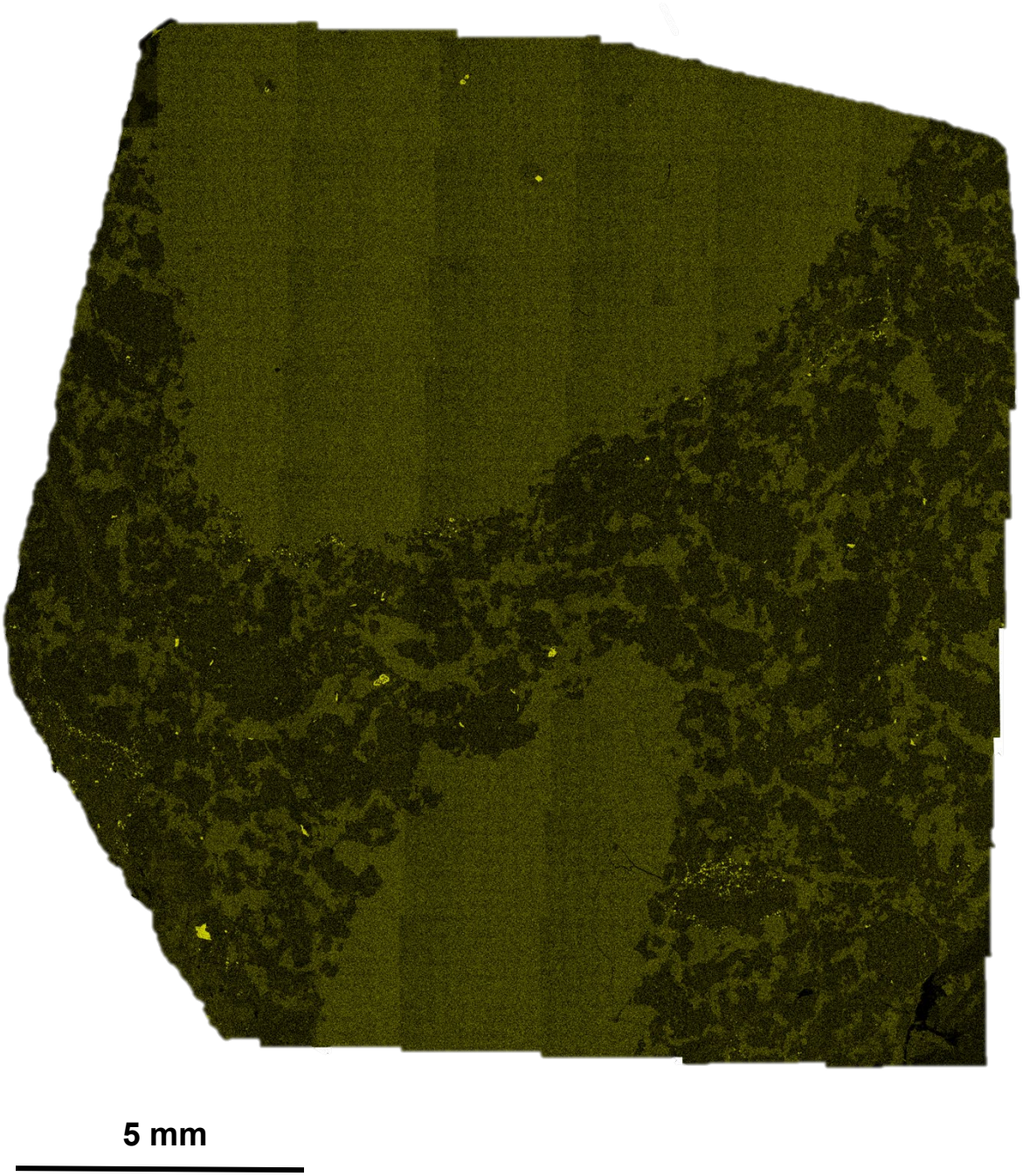

B-e) Crab Orchard – Cu

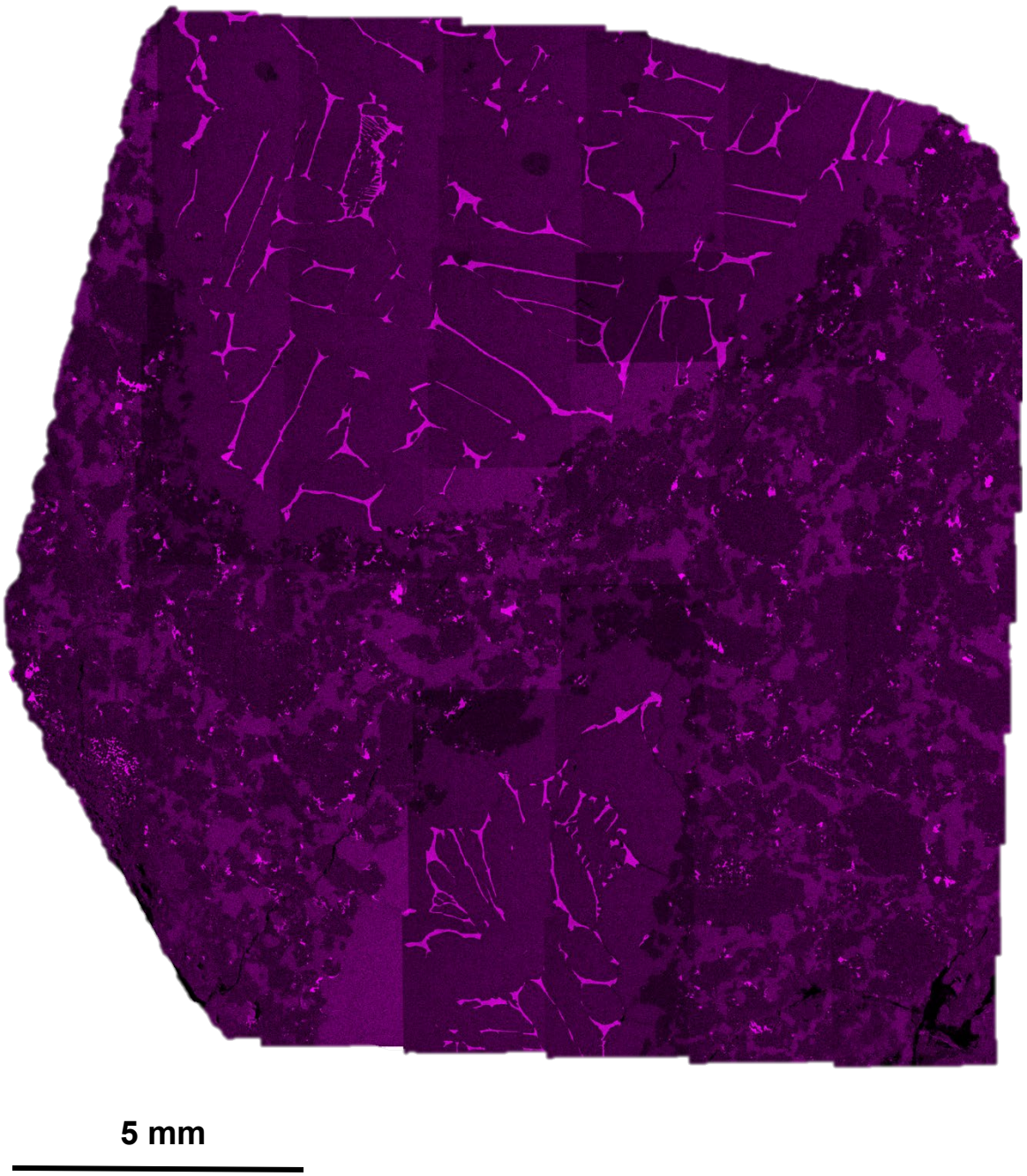

B-f) Crab Orchard – Fe

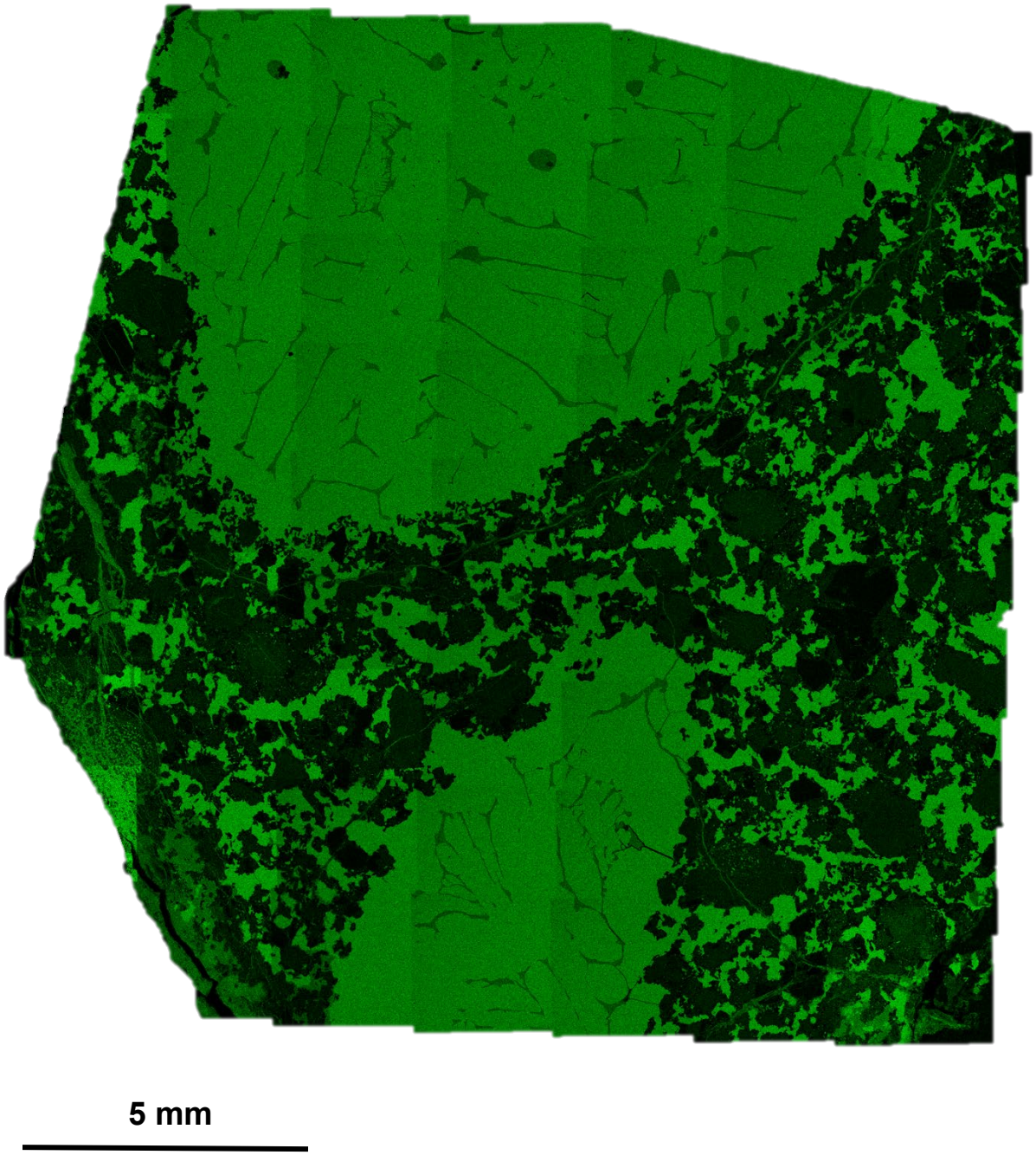

B-g) Crab Orchard – K

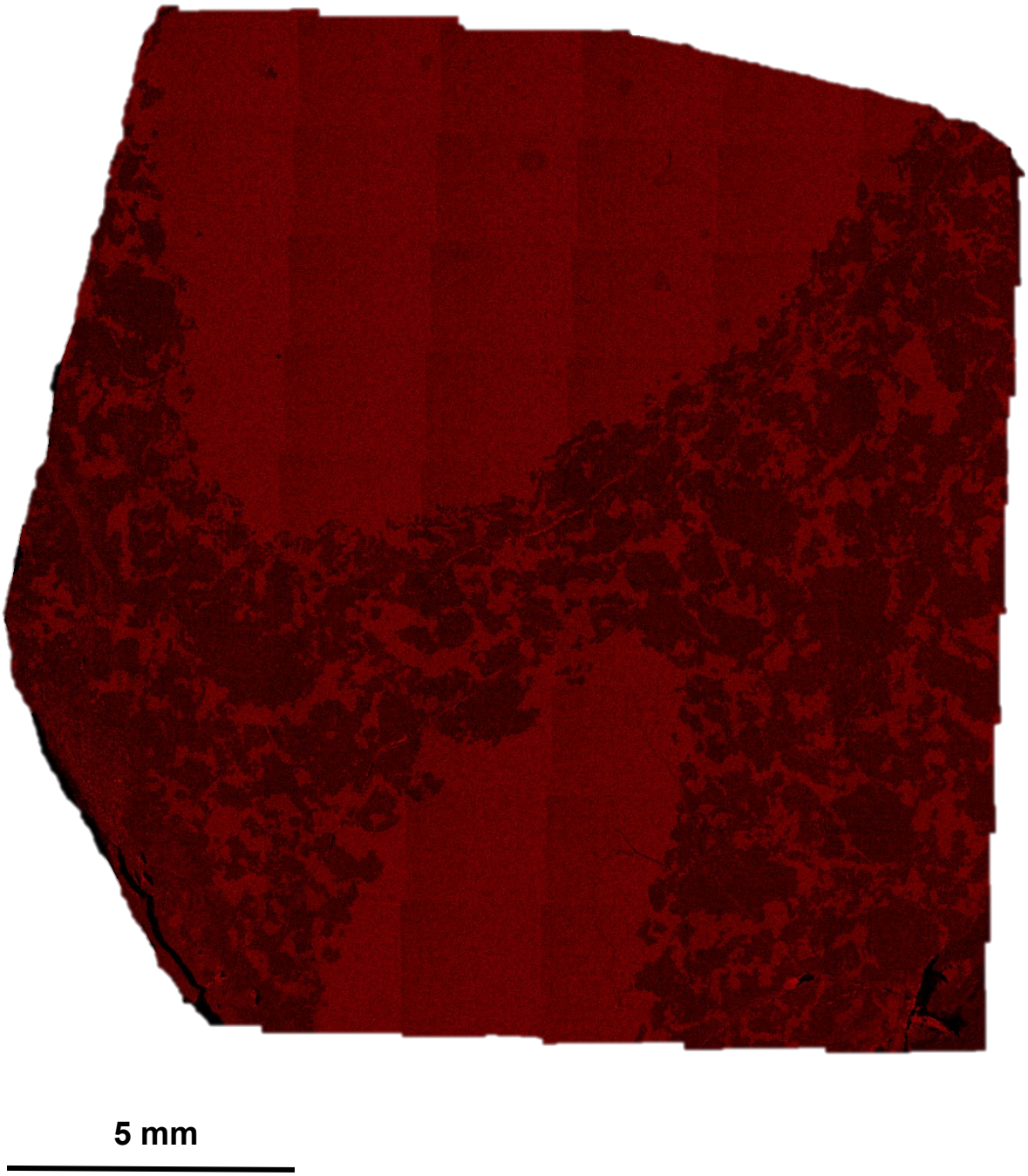

B-h)Crab Orchard – Mg

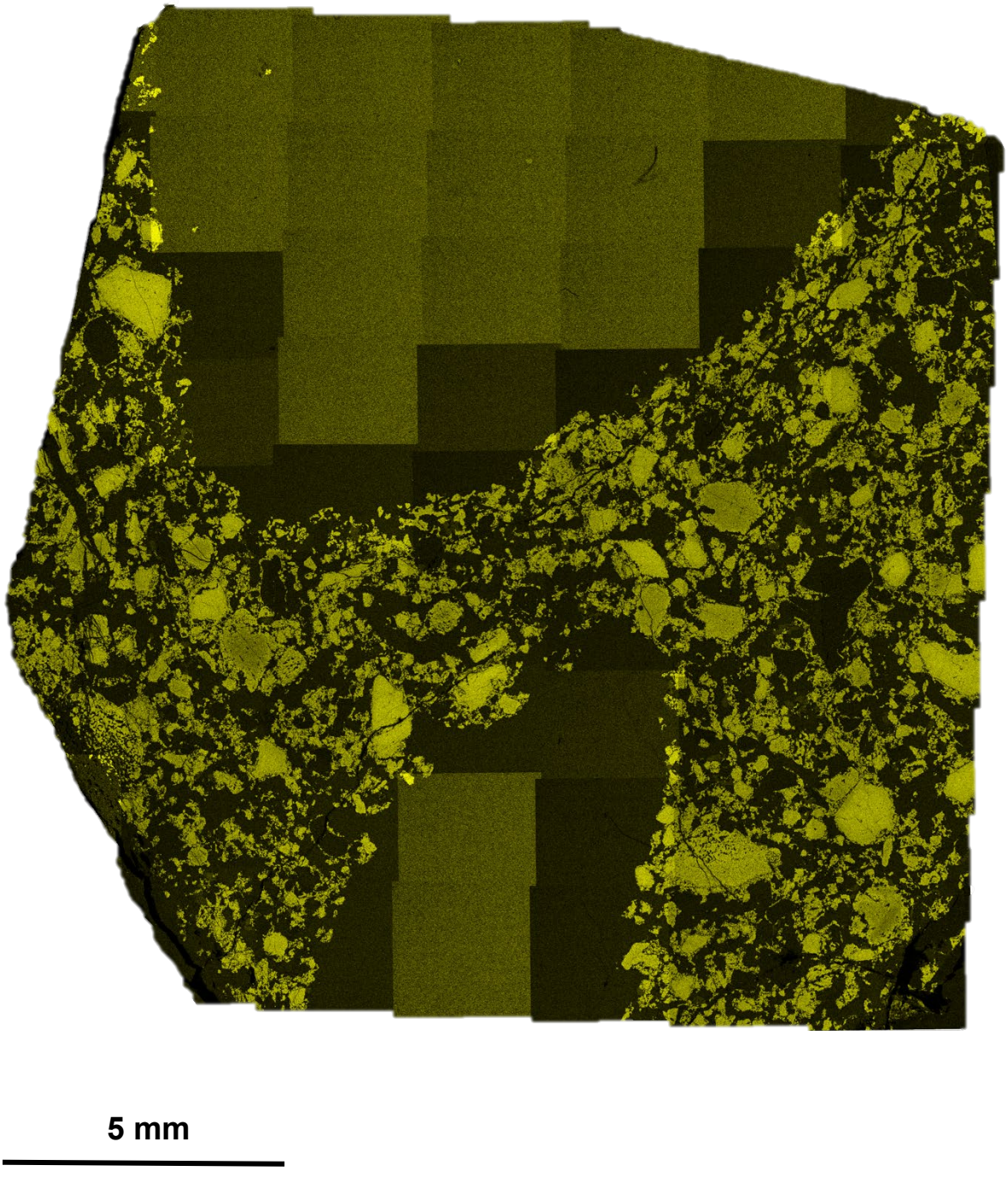

B-i) Crab Orchard – Mn

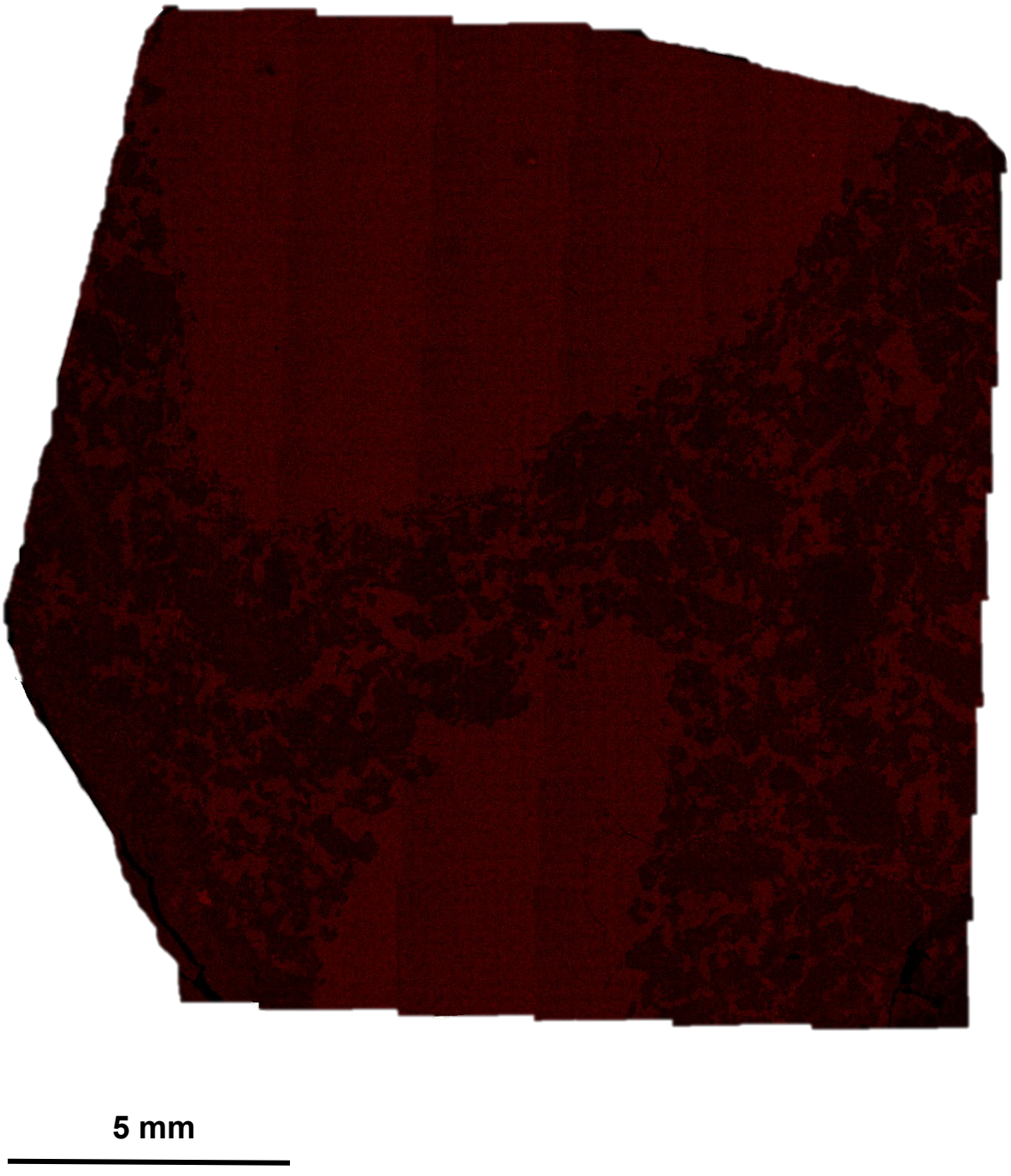

B-j) Crab Orchard – Na

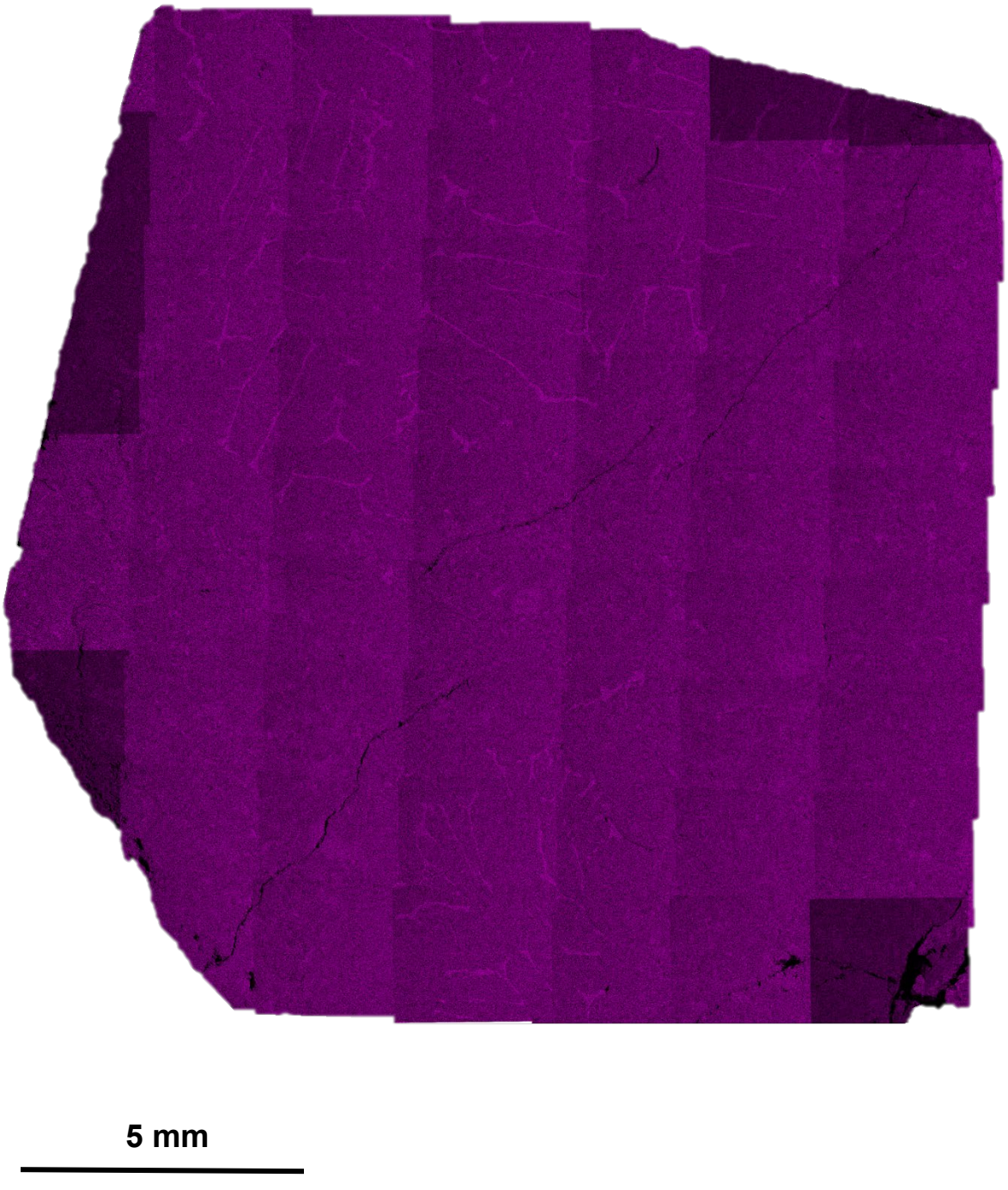

B-k) Crab Orchard – Ni

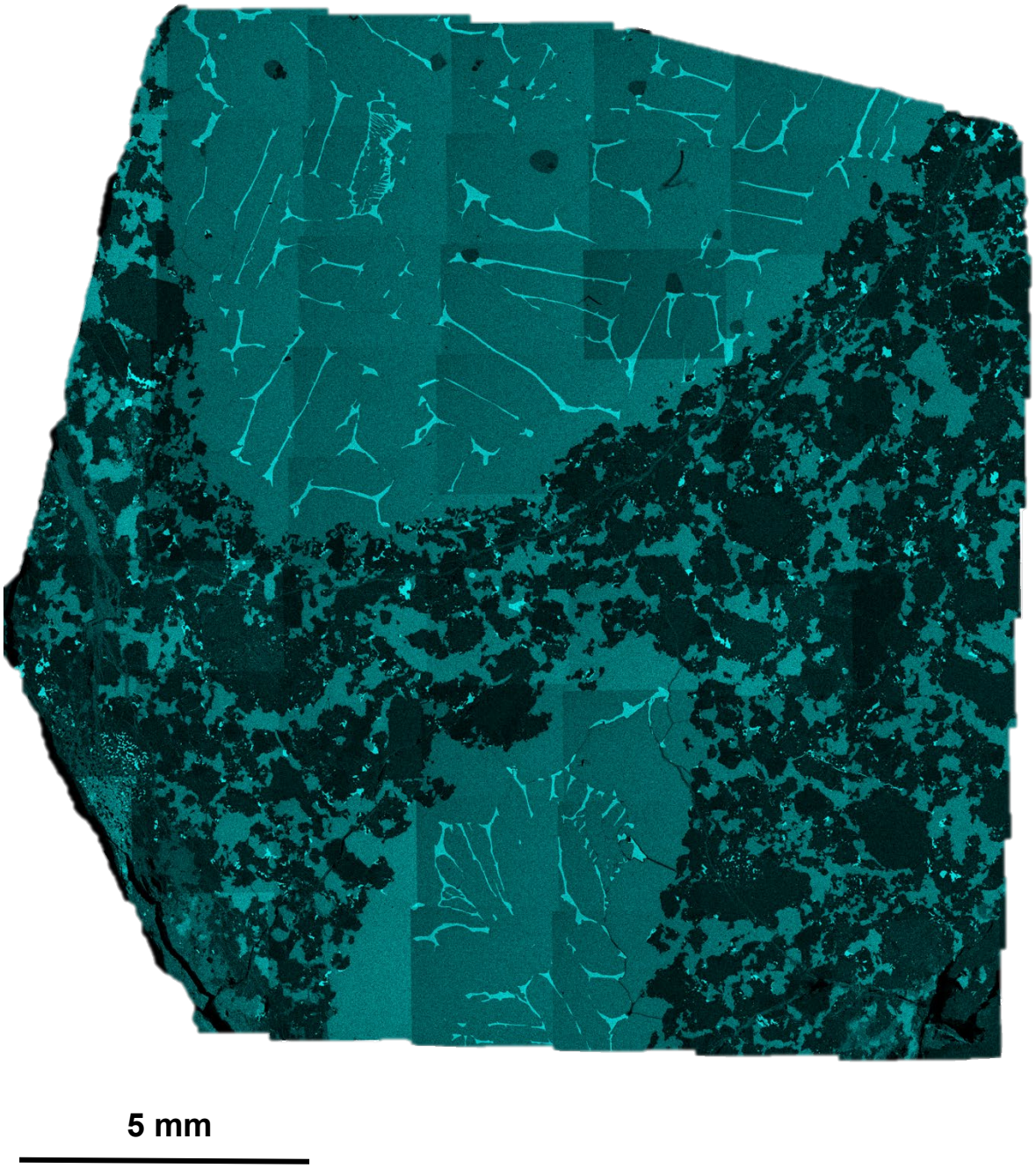

B-l) Crab Orchard – O

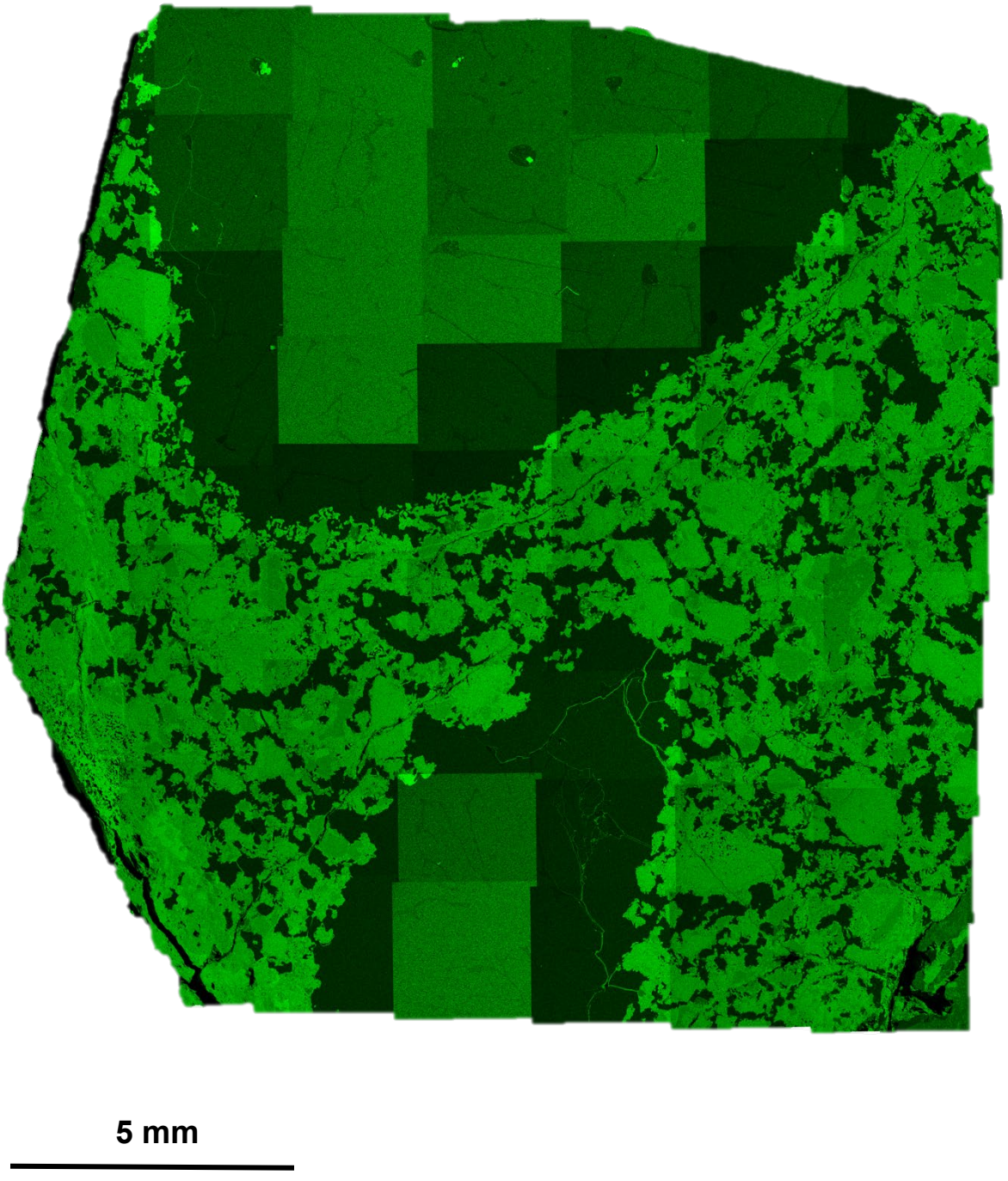

B-m) Crab Orchard – P

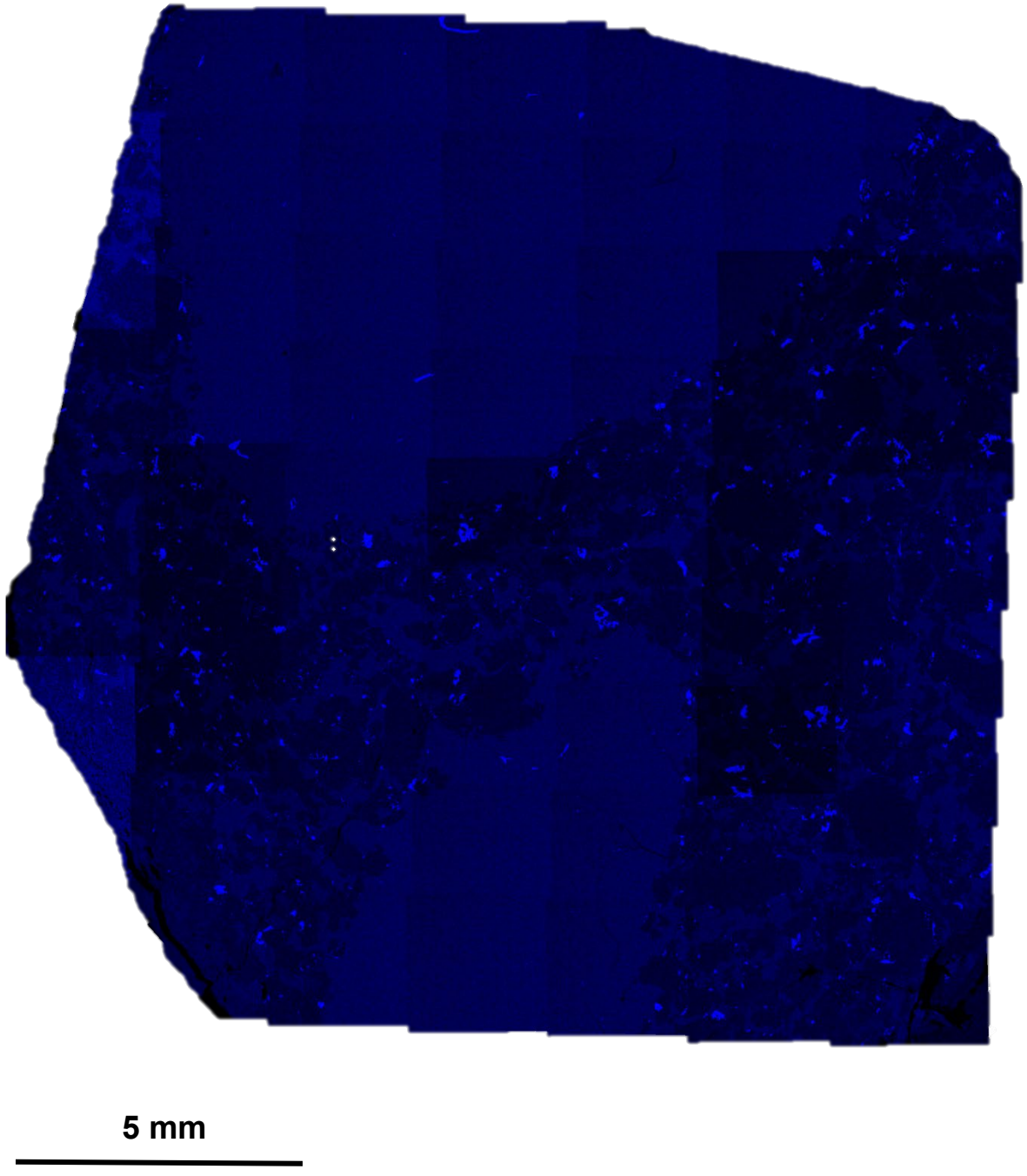

B-n) Crab Orchard – S

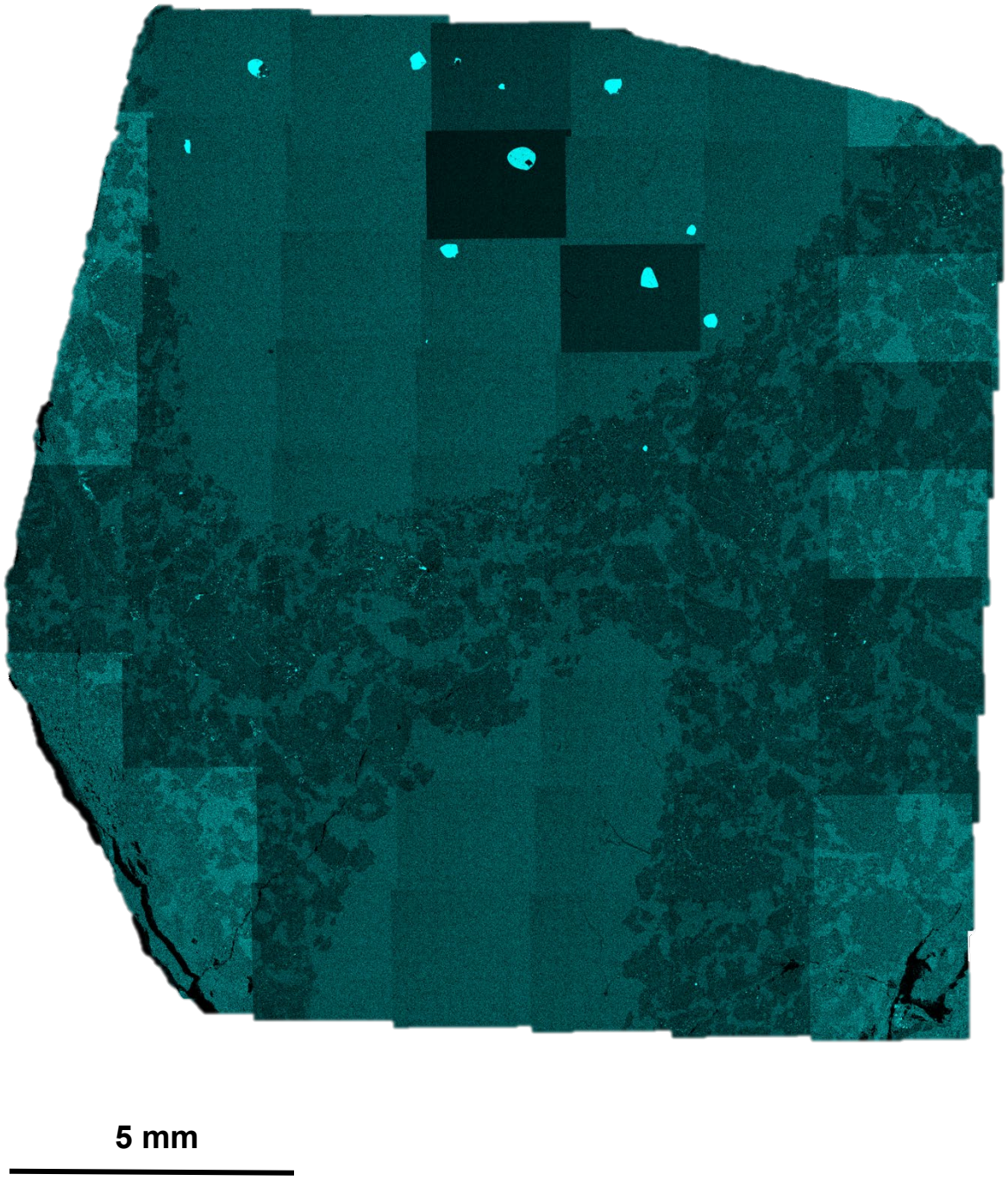

B-o) Crab Orchard – Si

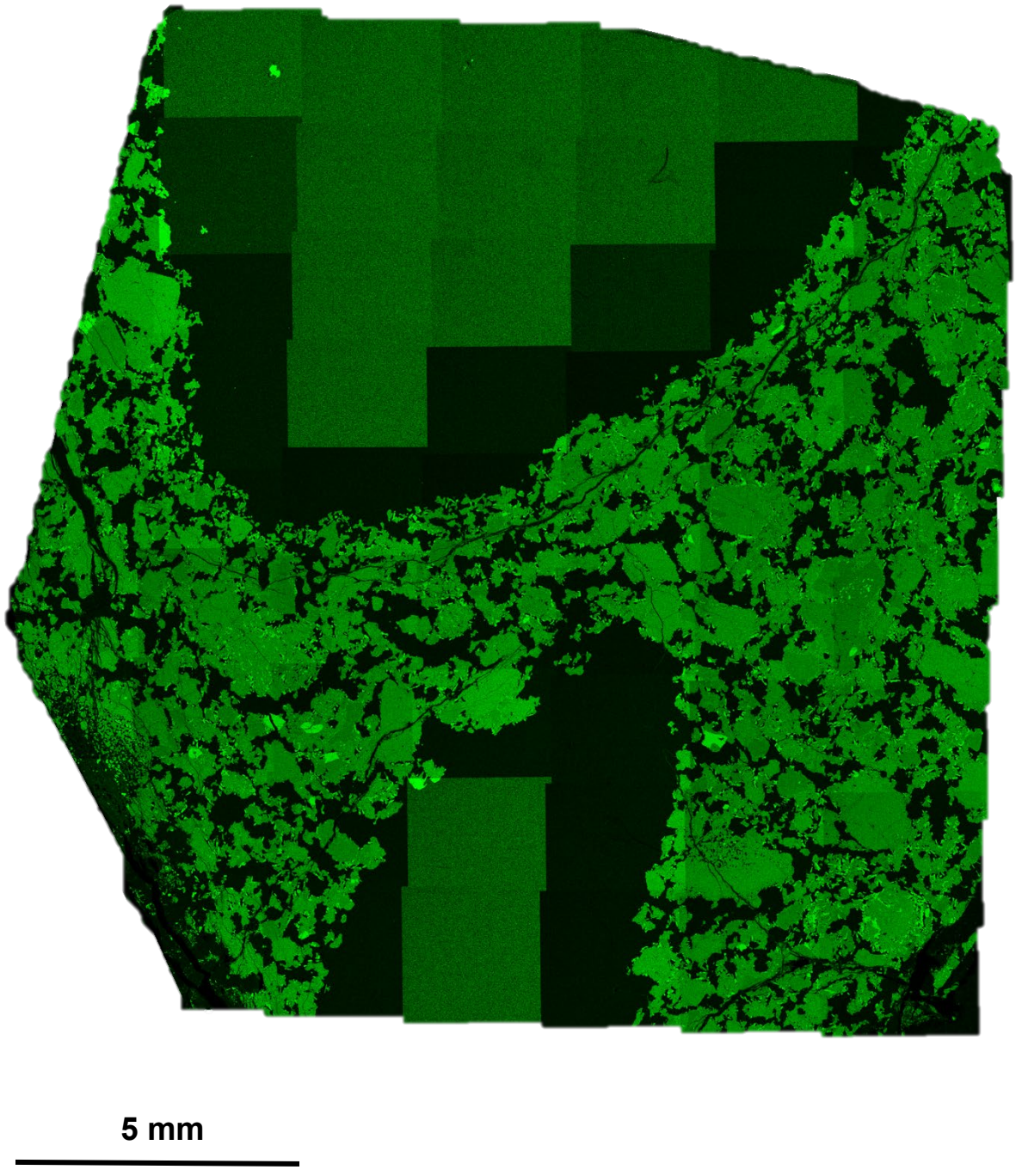

B-p) Crab Orchard – Ti

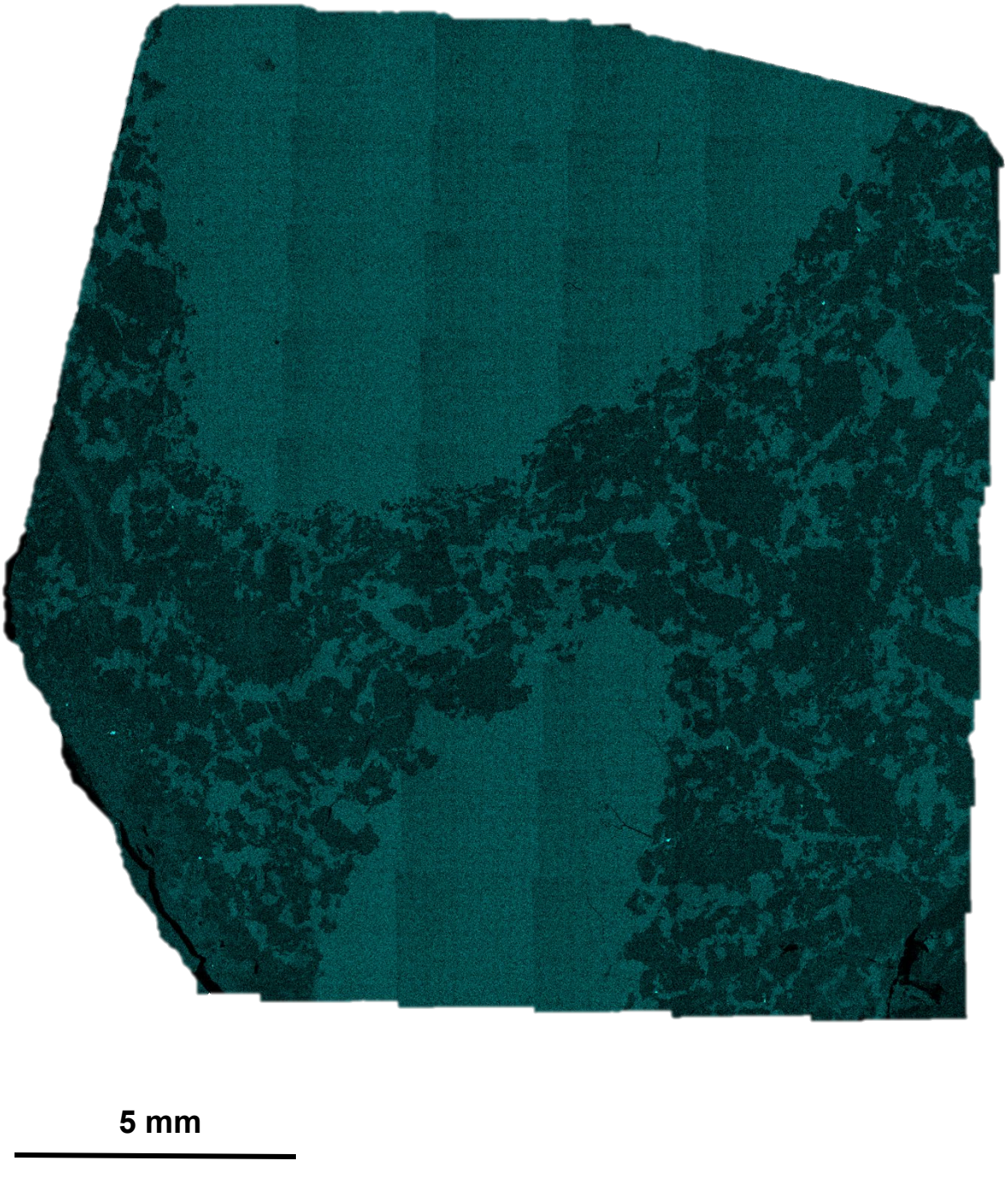

B-q) Crab Orchard – V

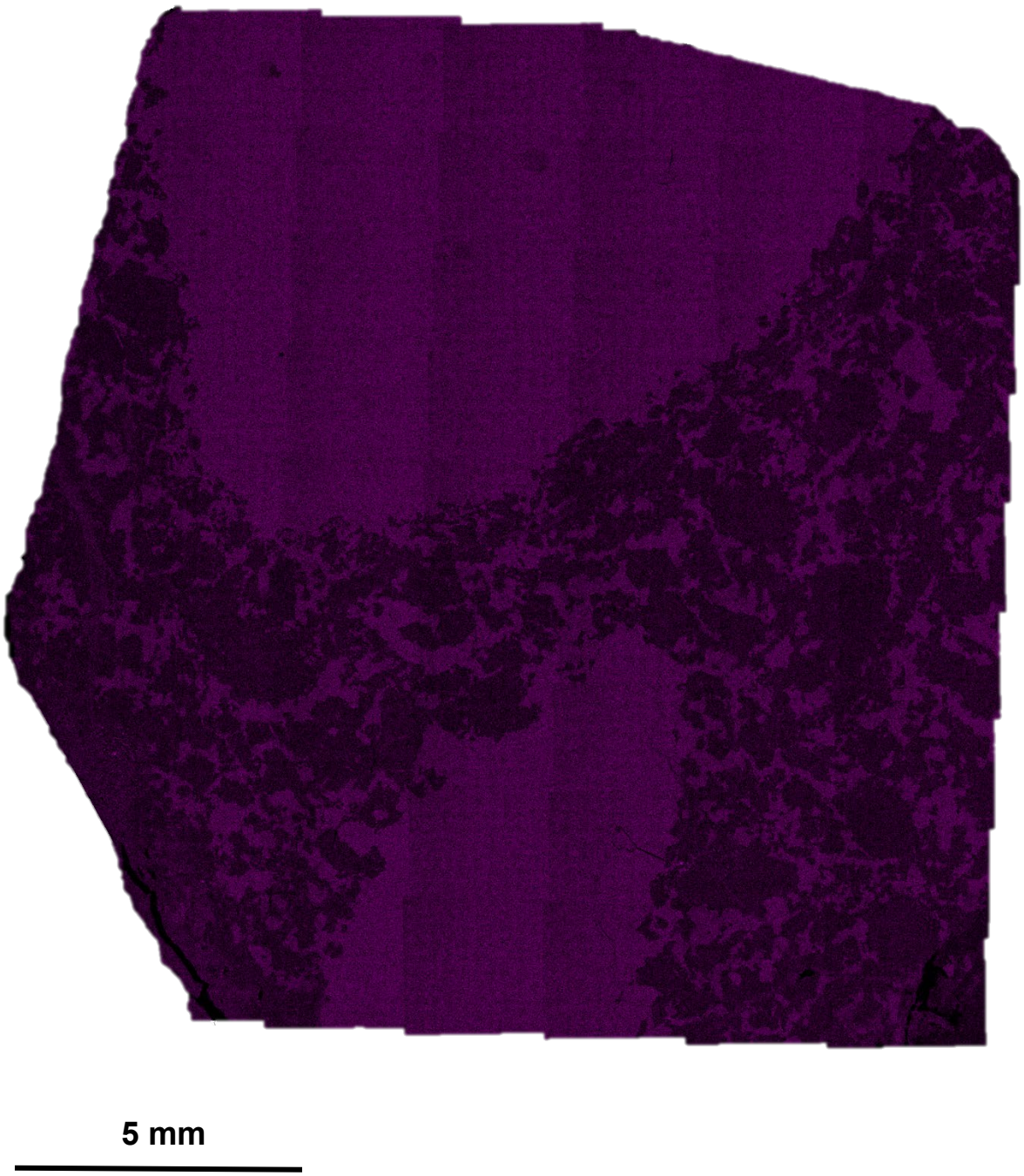

Appendix C

Individual SEM Elemental X-ray maps for Chinguetti

The entire section was analyzed for seventeen elements:

a) Al

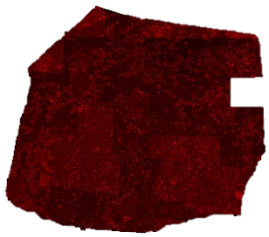

f) Fe

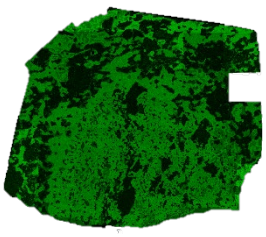

k) Ni

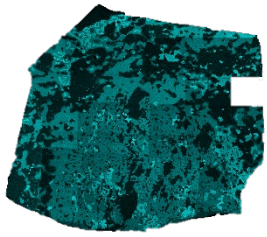

p) Ti

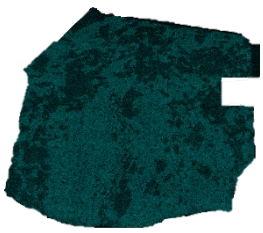

b) Ca

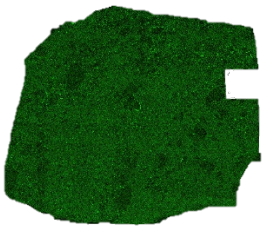

g) K

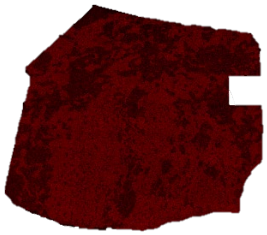

l) O

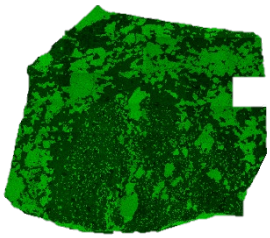

q) V

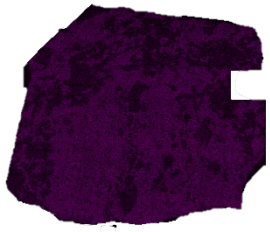

c) Co

h) Mg

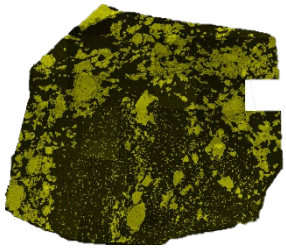

m) P

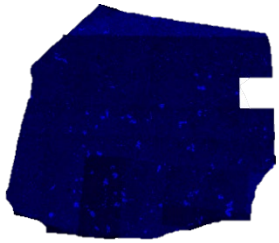

10 mm

d) Cr

i) Mn

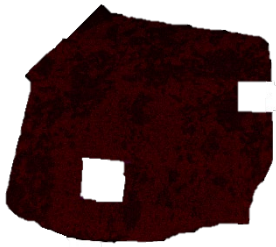

n) S

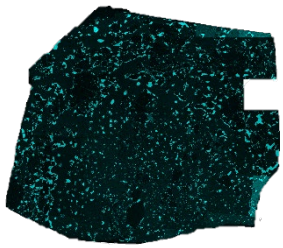

e) Cu

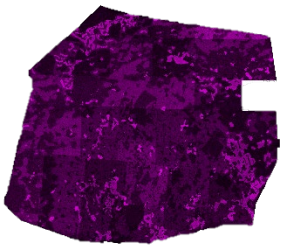

j) Na

o) Si

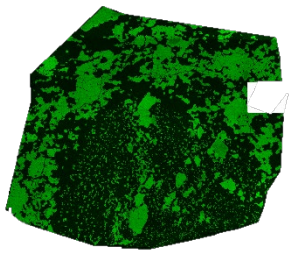

C-a) Chinguetti – Al

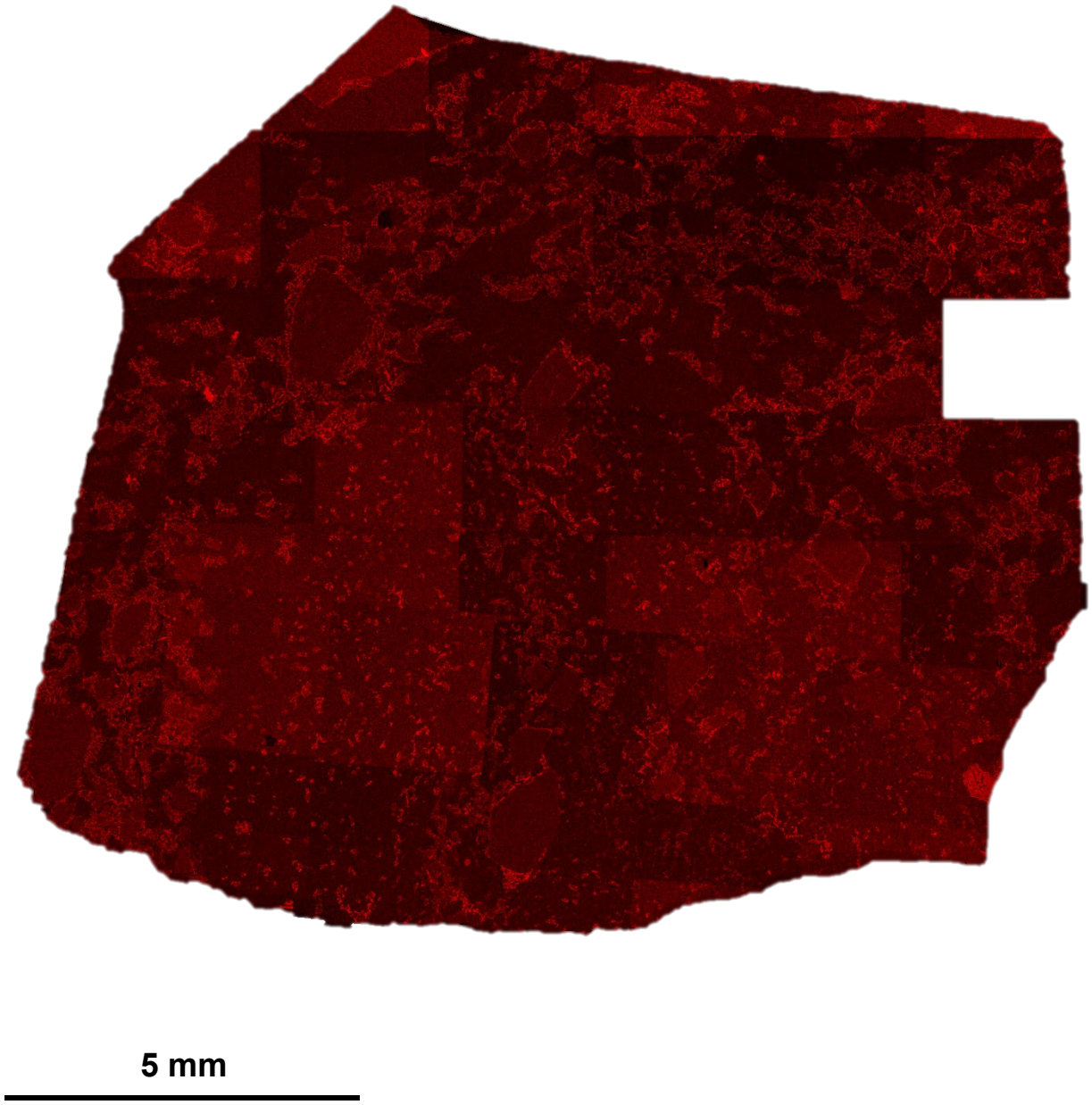

C-b) Chinguetti – Ca

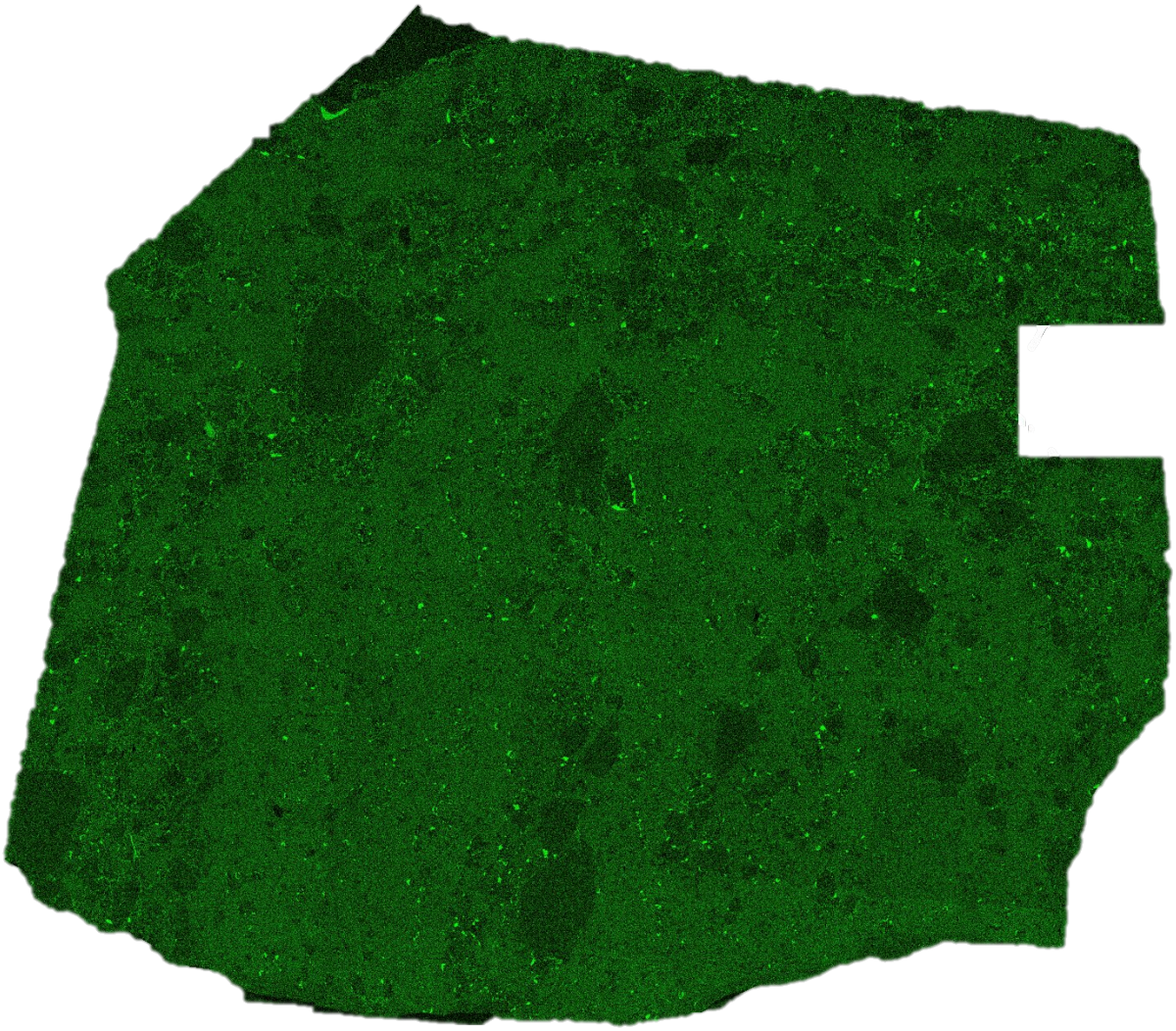

5 mm

C-c) Chinguetti – Co

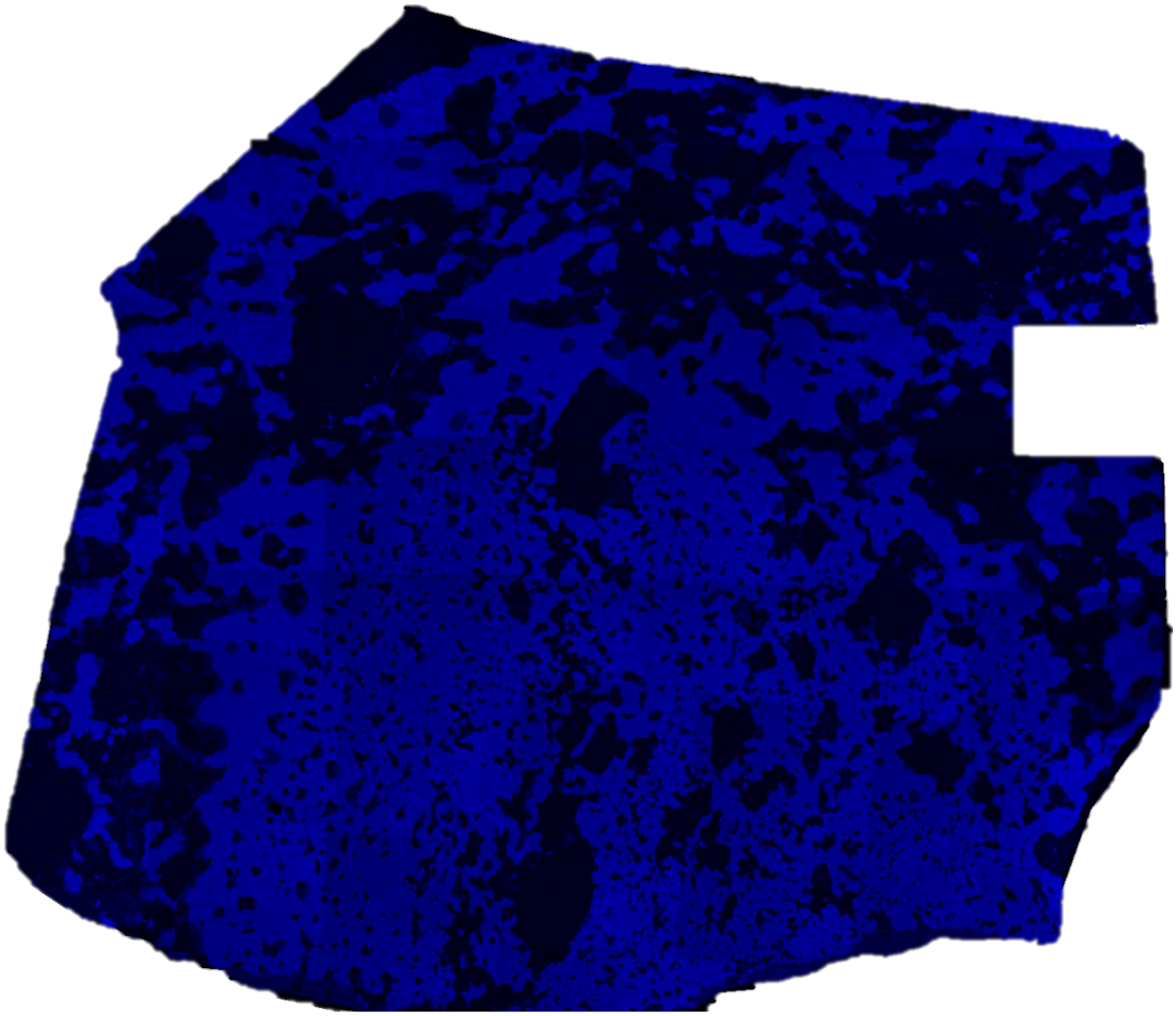

5 mm

C-d) Chinguetti – Cr

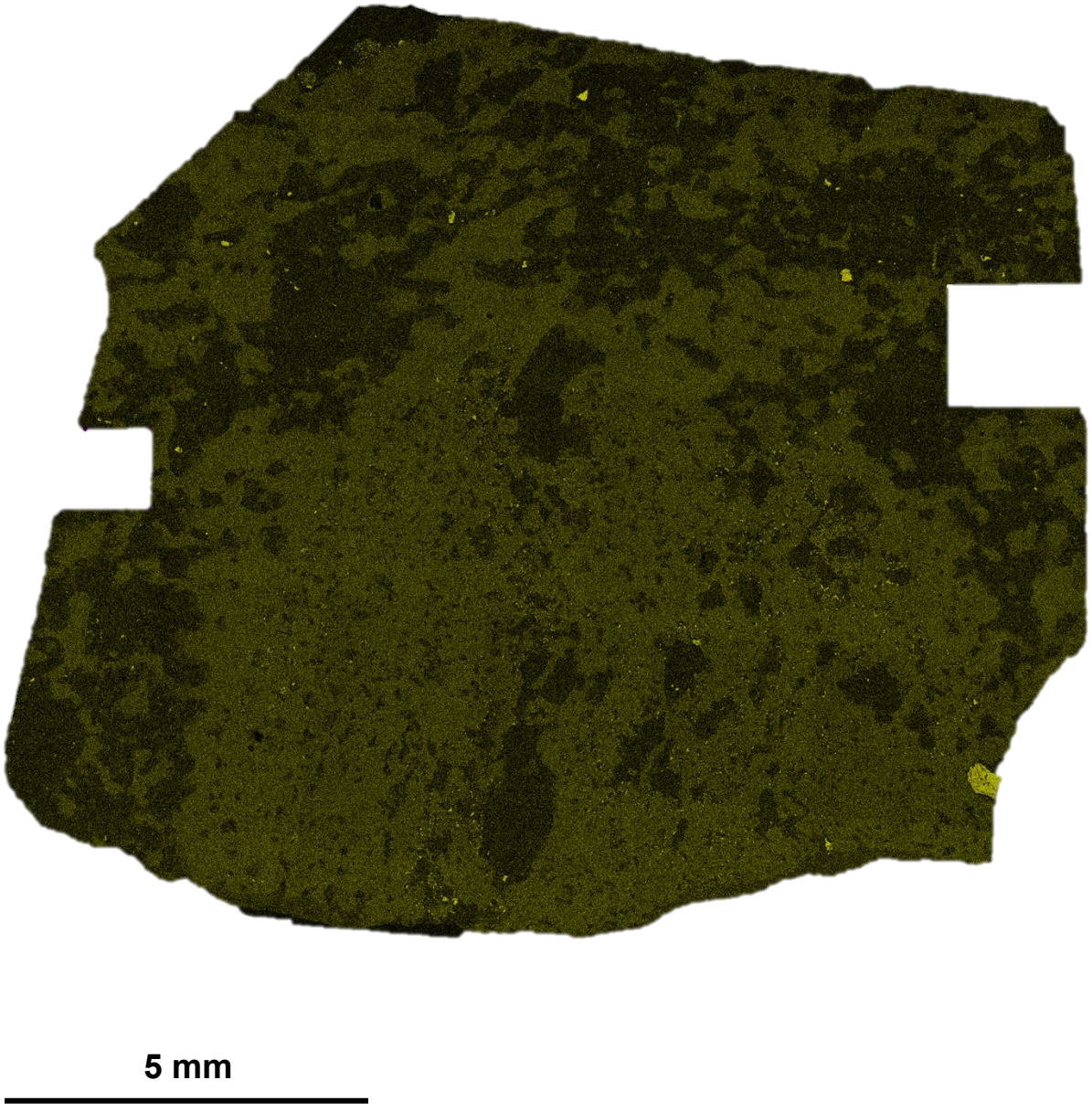

C-e) Chinguetti – Cu

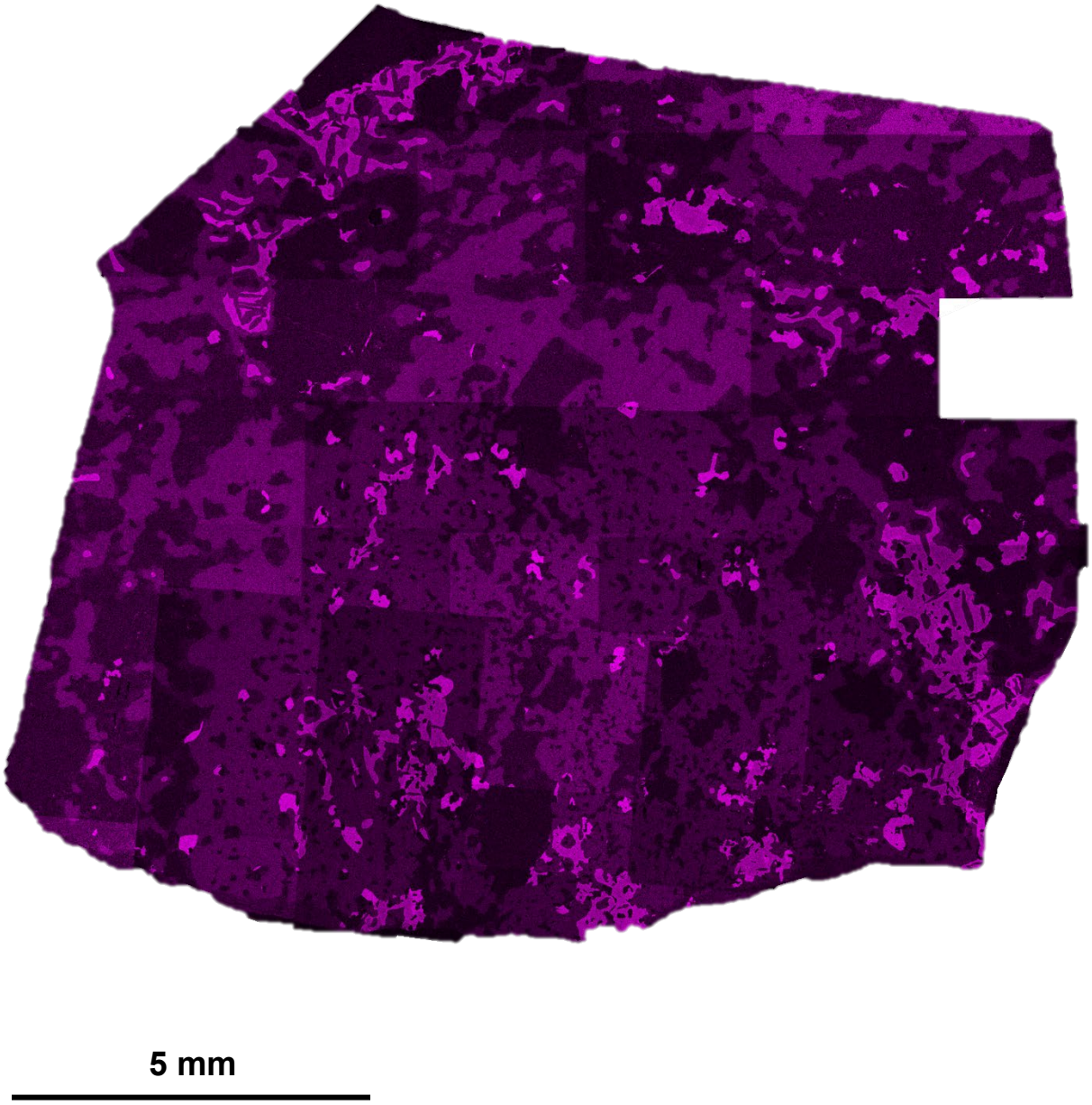

C-f) Chinguetti – Fe

5 mm

C-g) Chinguetti – K

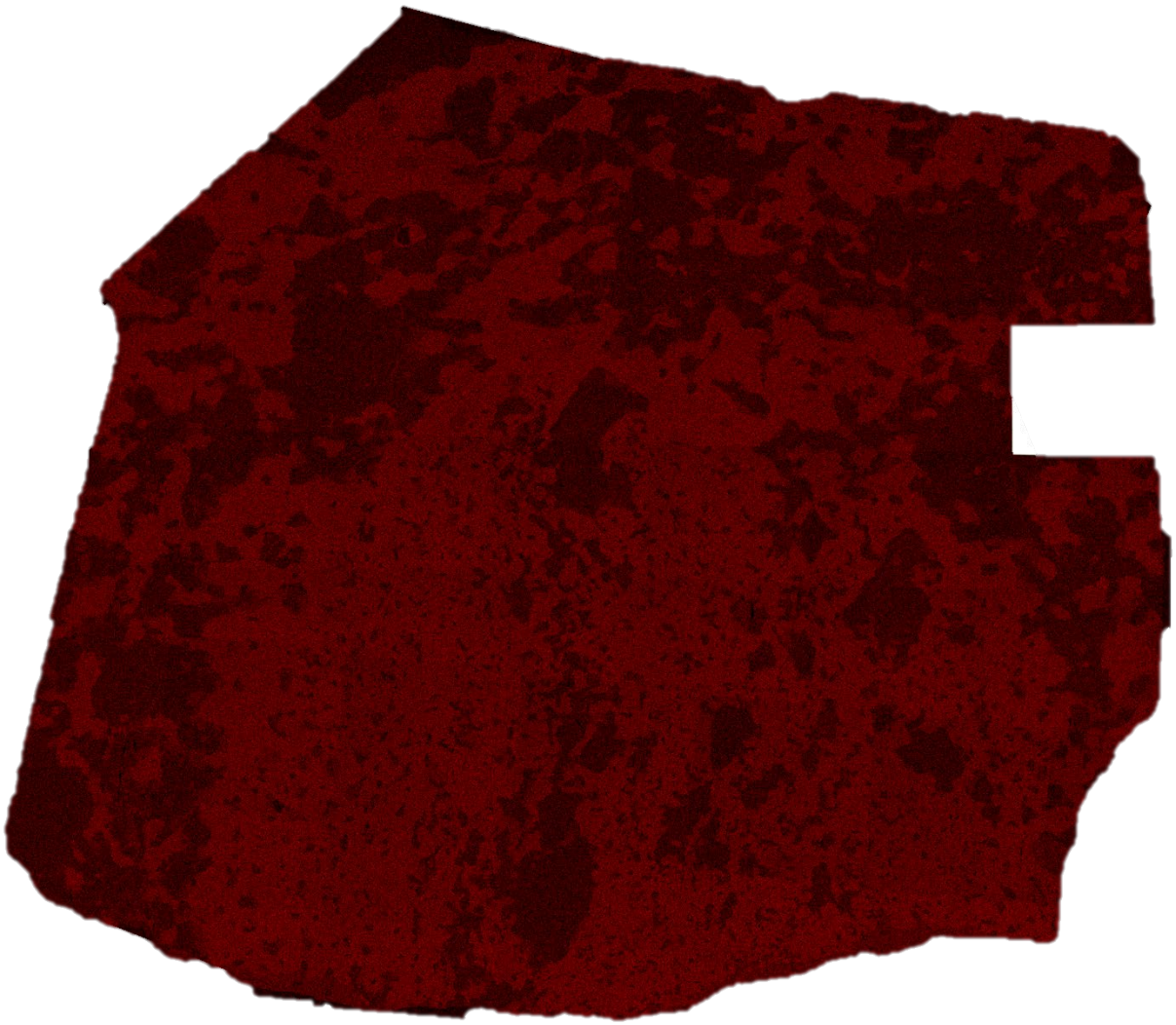

5 mm

C-h) Chinguetti – Mg

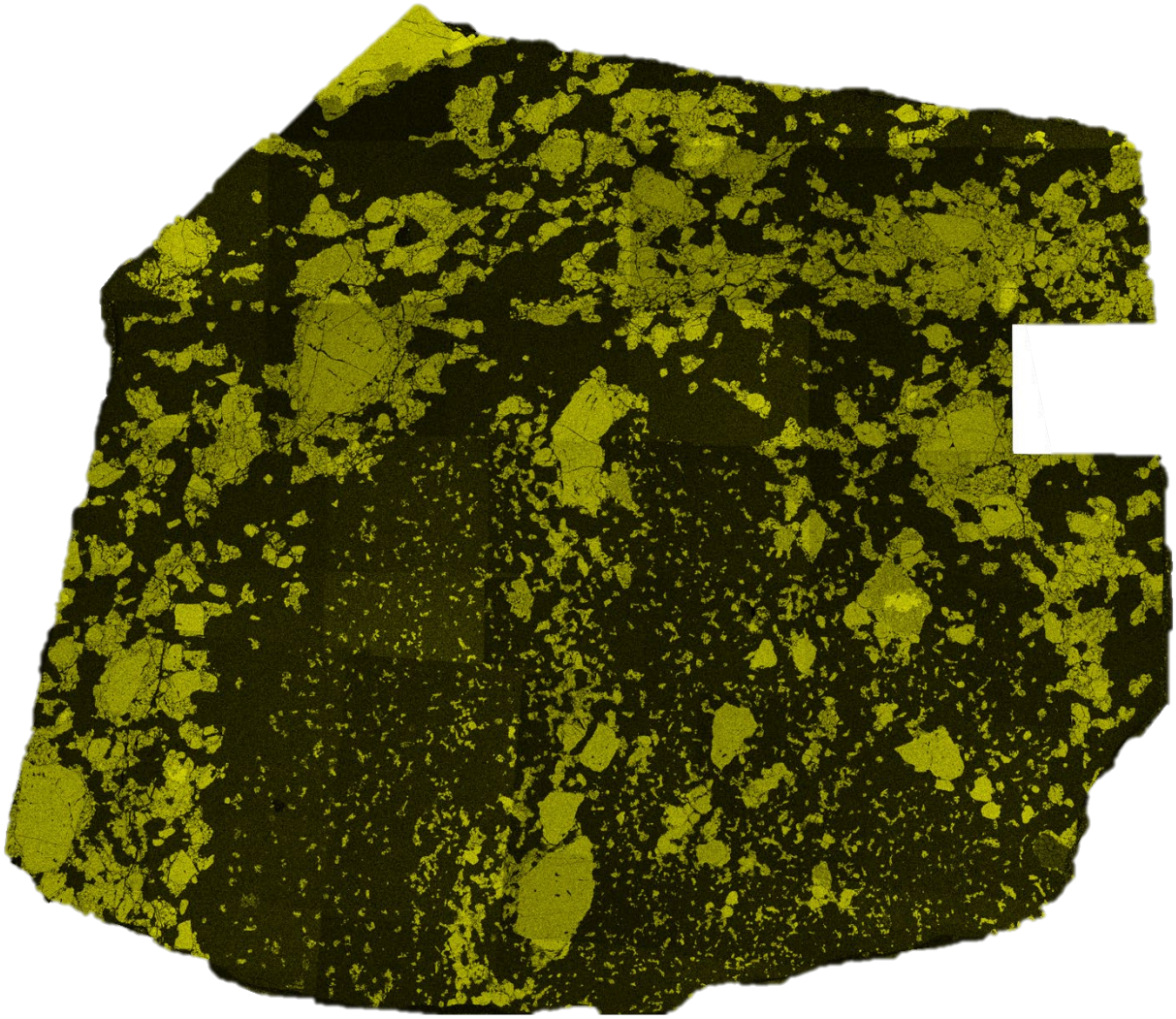

5 mm

C-i) Chinguetti – Mn

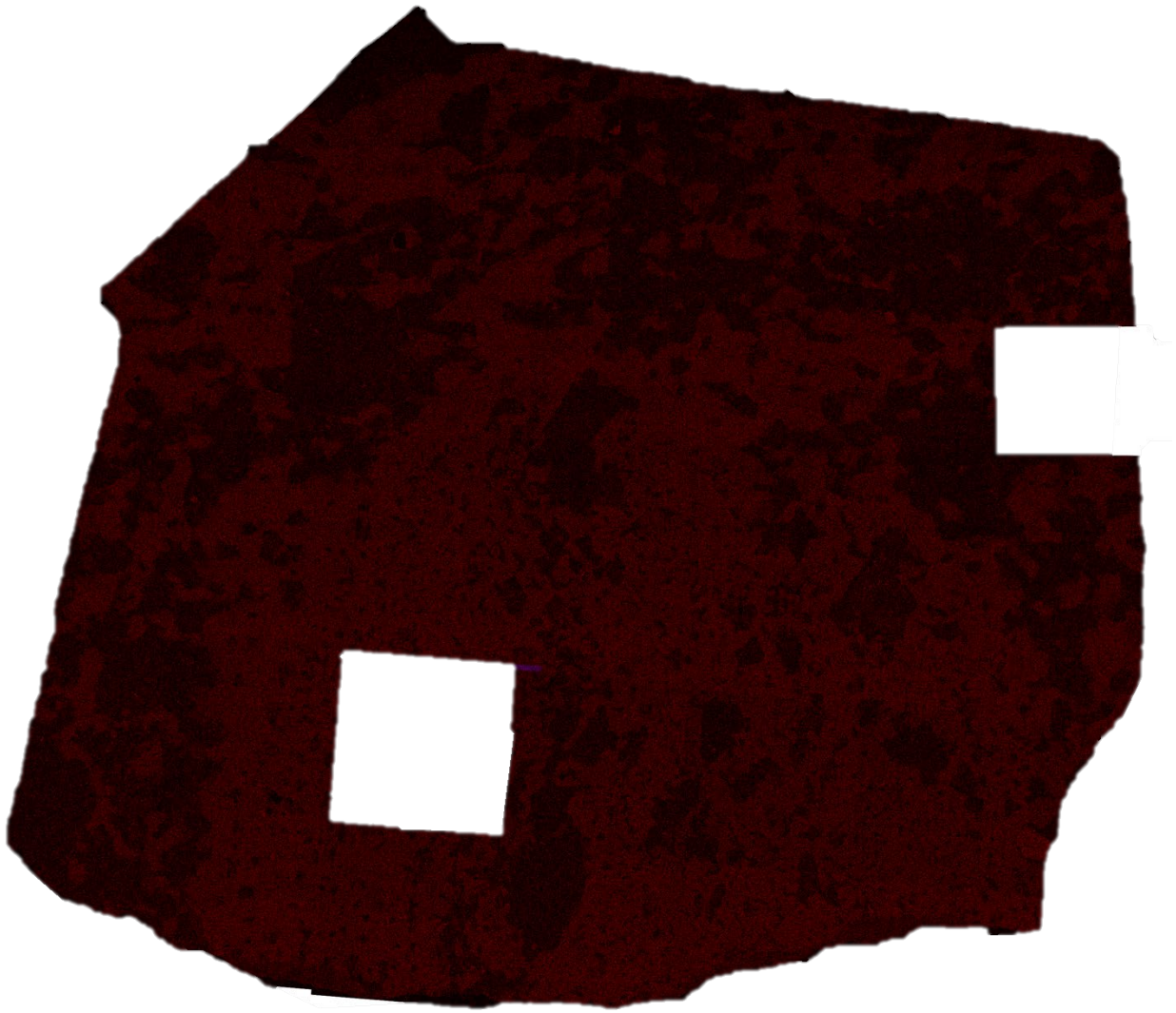

5 mm

C-j) Chinguetti – Na

5 mm

C-k) Chinguetti – Ni

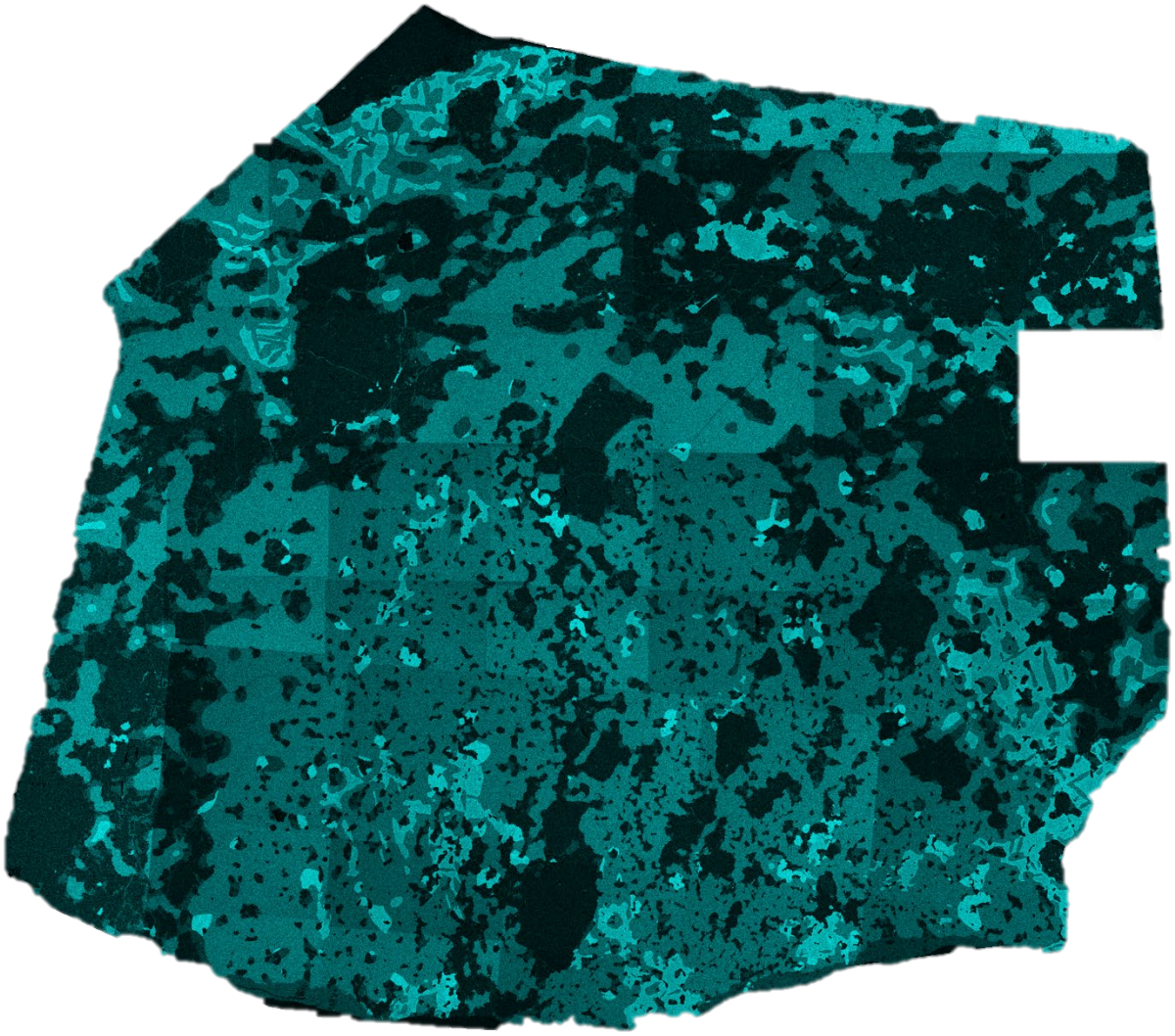

5 mm

C-l) Chinguetti – O

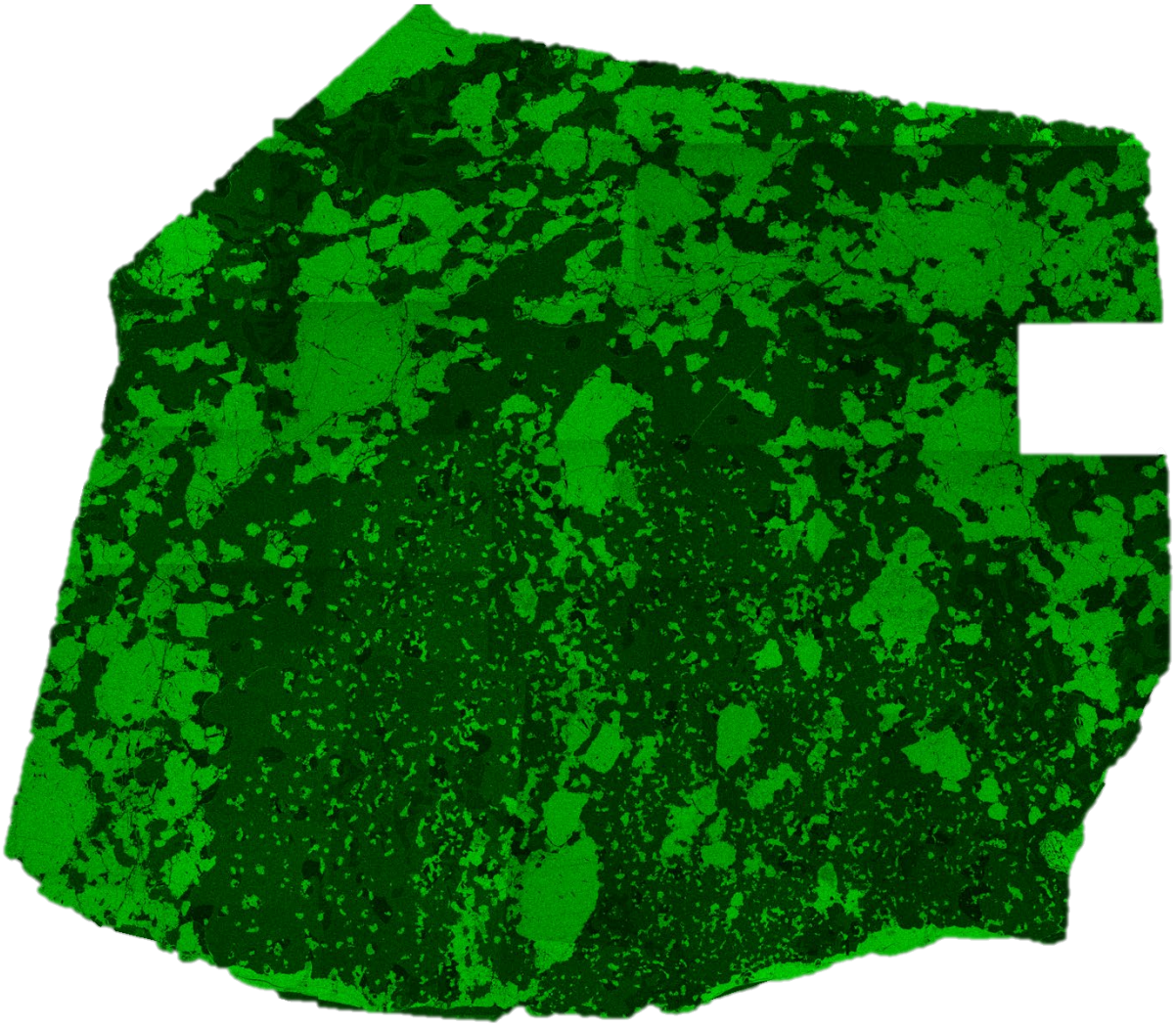

C-m) Chinguetti – P

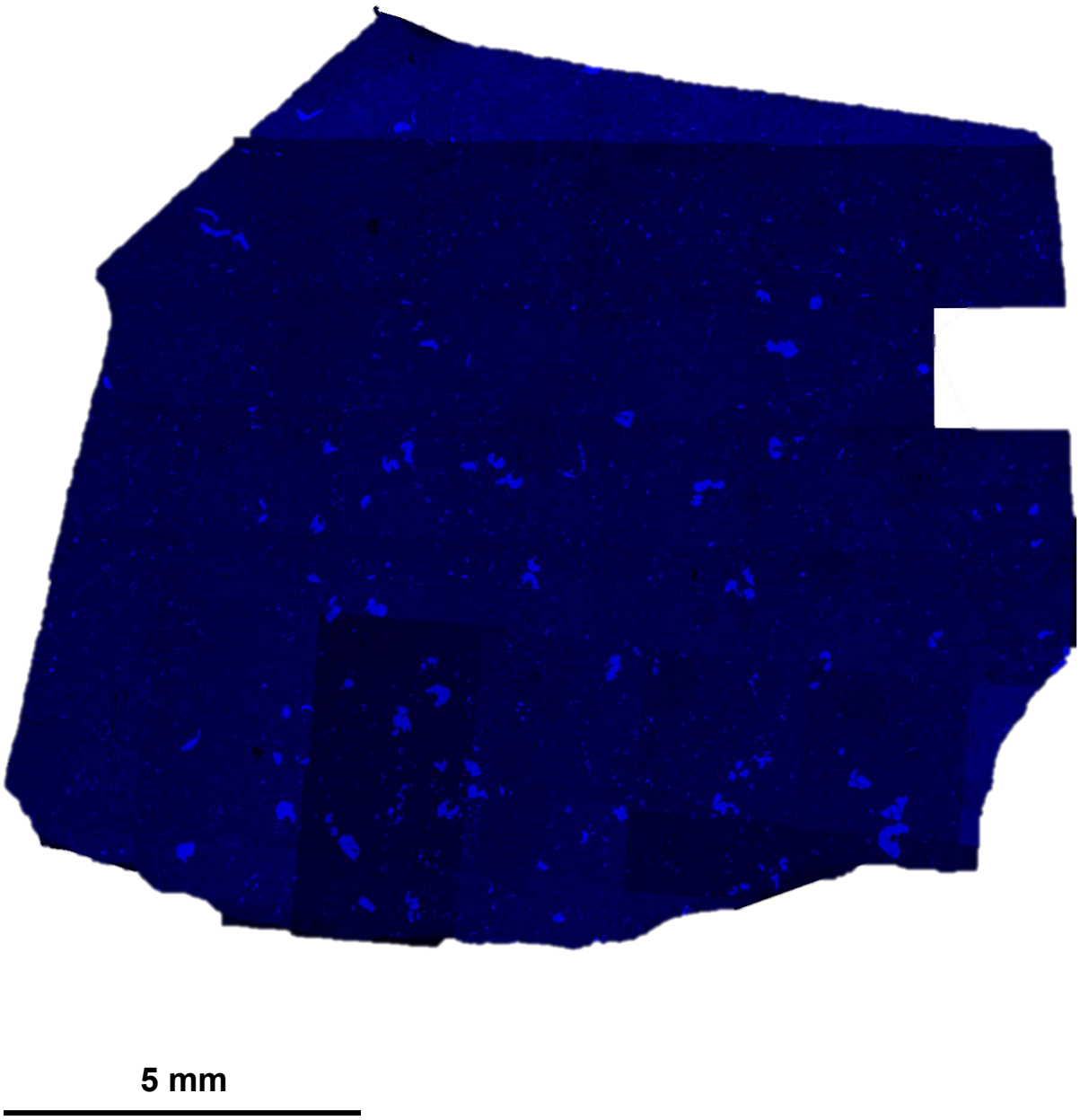

C-n) Chinguetti – S

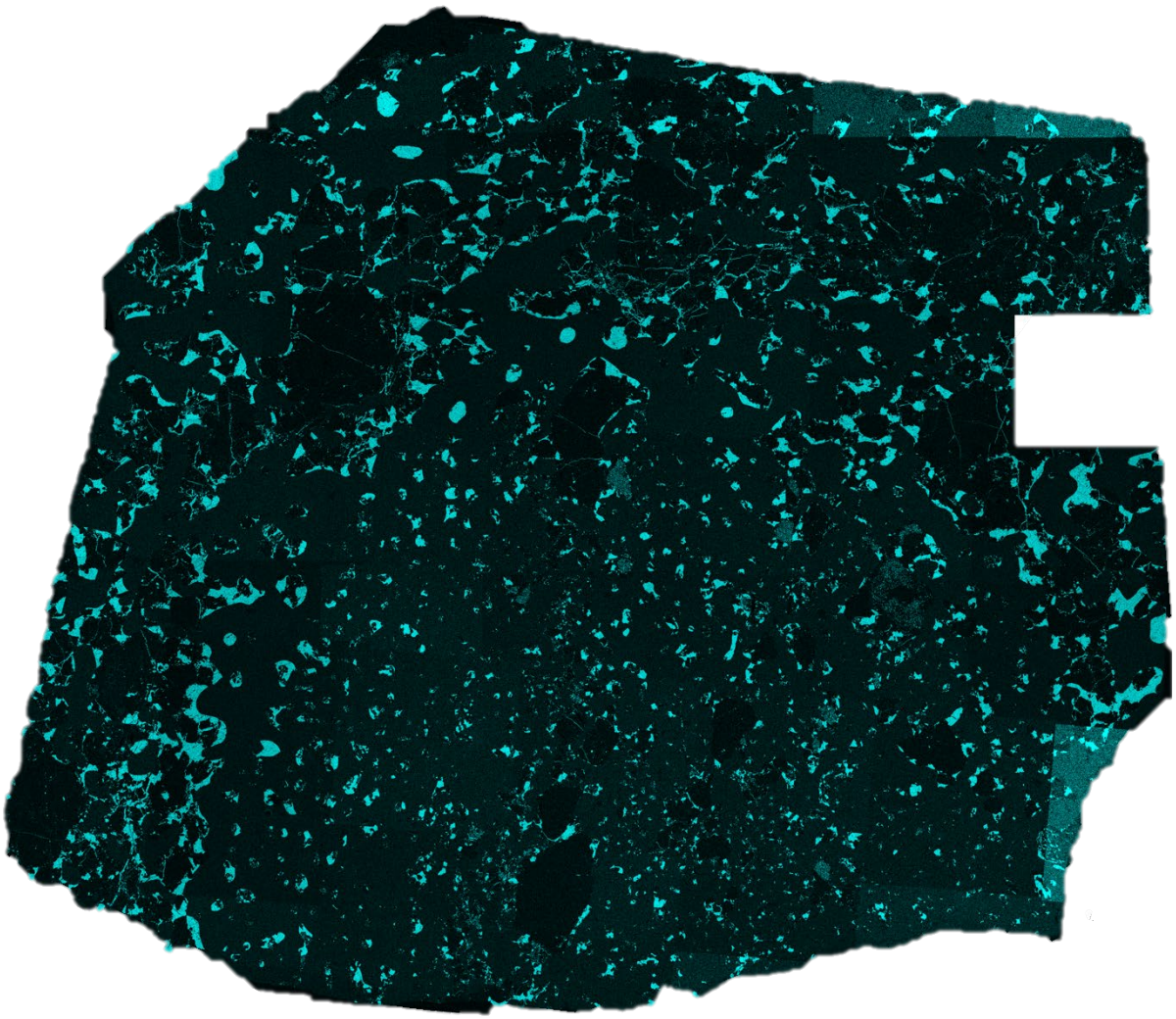

5 mm

C-o) Chinguetti – Si

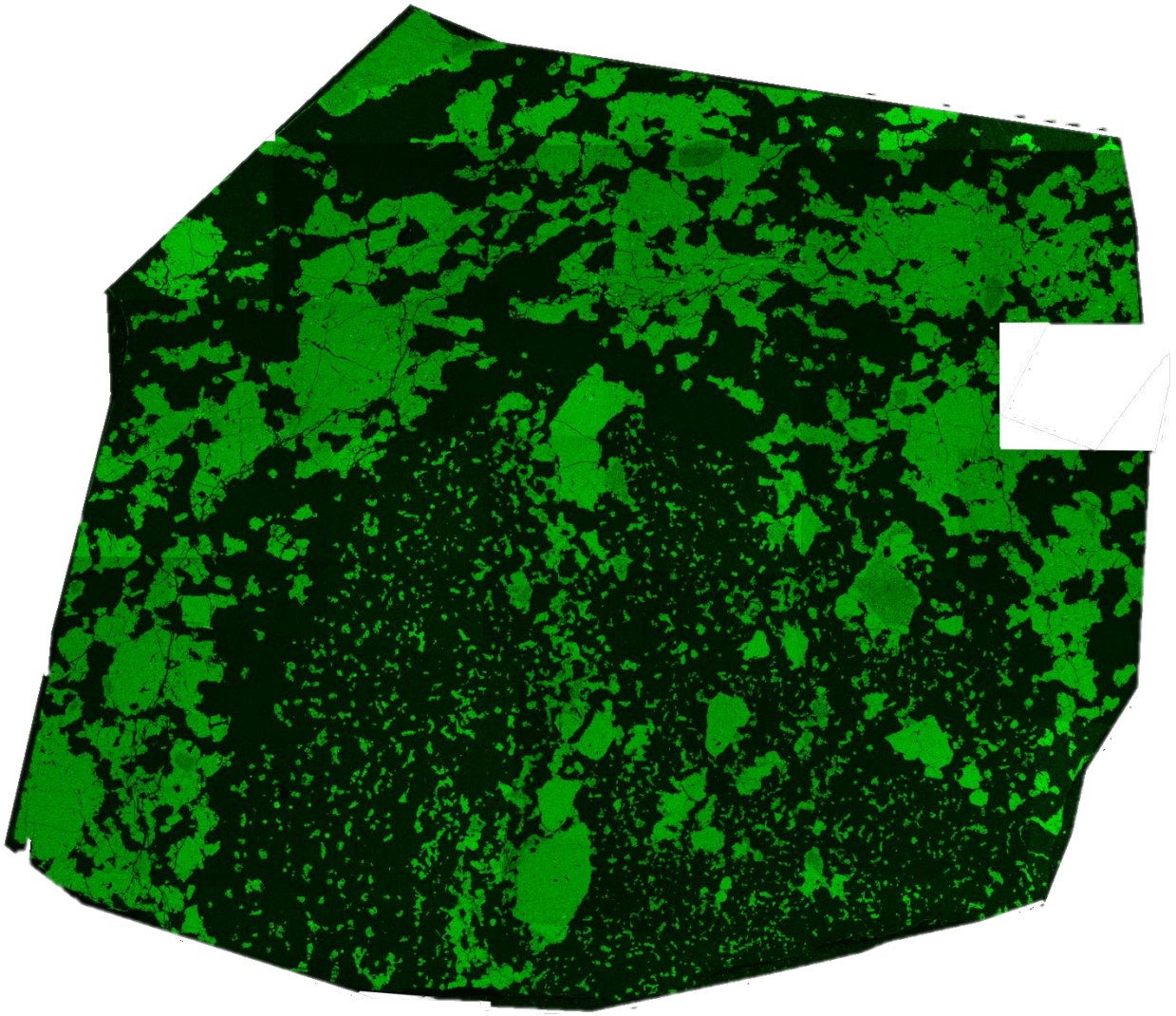

5 mm

C-p) Chinguetti – Ti

5 mm

C-q) Chinguetti – V

5 mm

Appendix D

Individual SEM Elemental X-ray maps for Vaca Muerta

The entire section was analyzed for seventeen elements:

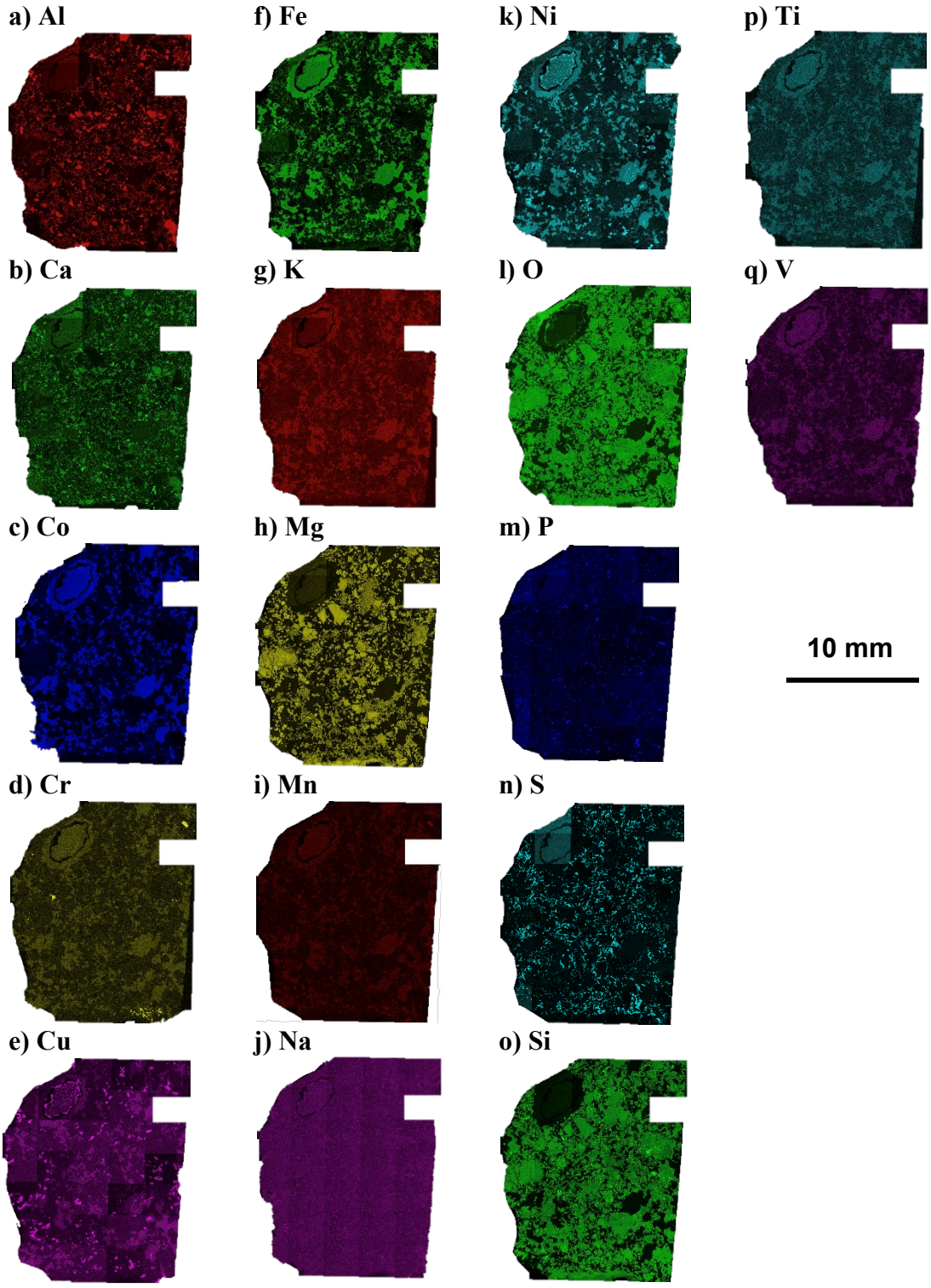

D-a) Vaca Muerta – Al

5 mm

D-b) Vaca Muerta – Ca

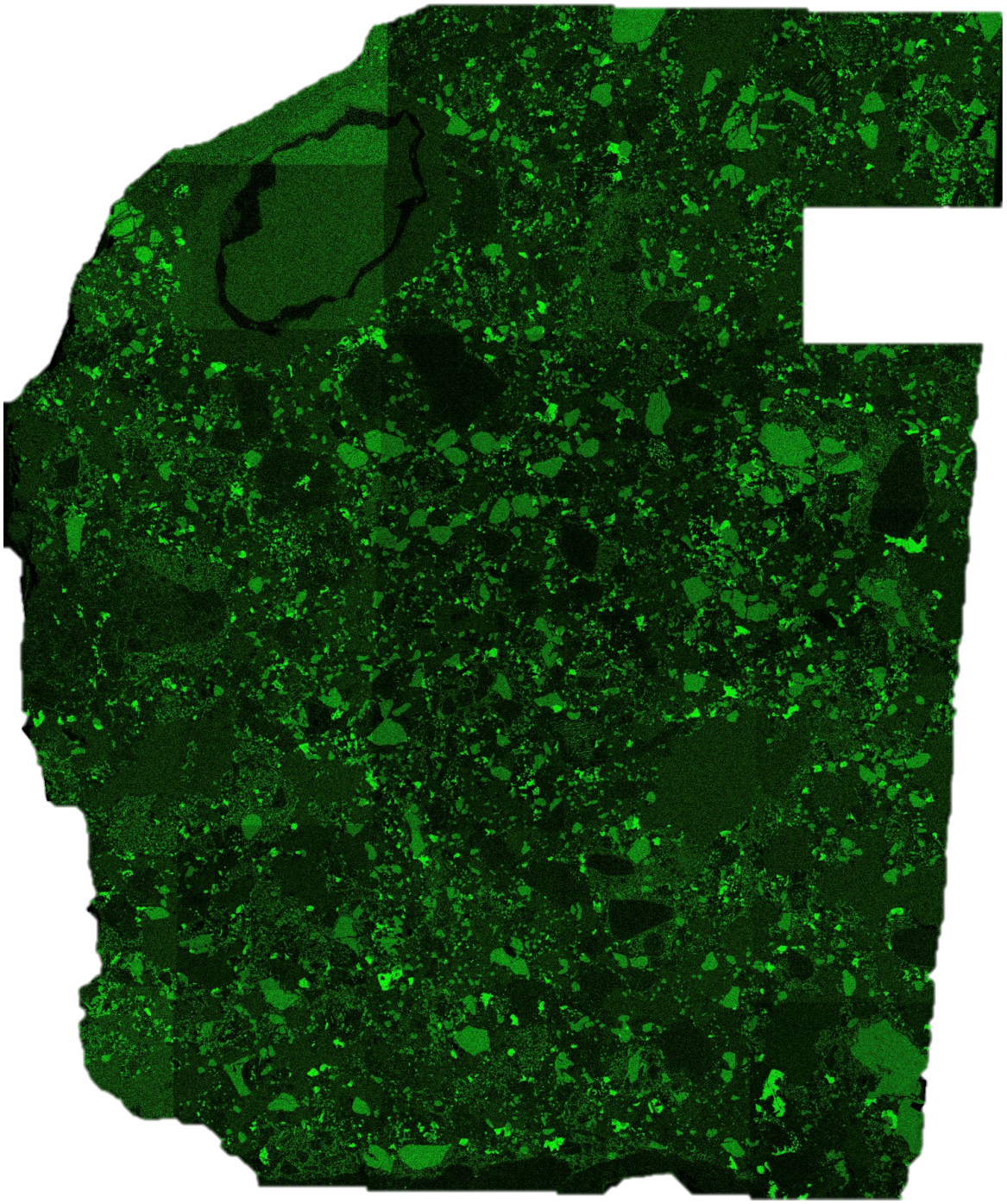

5 mm

D-c) Vaca Muerta – Co

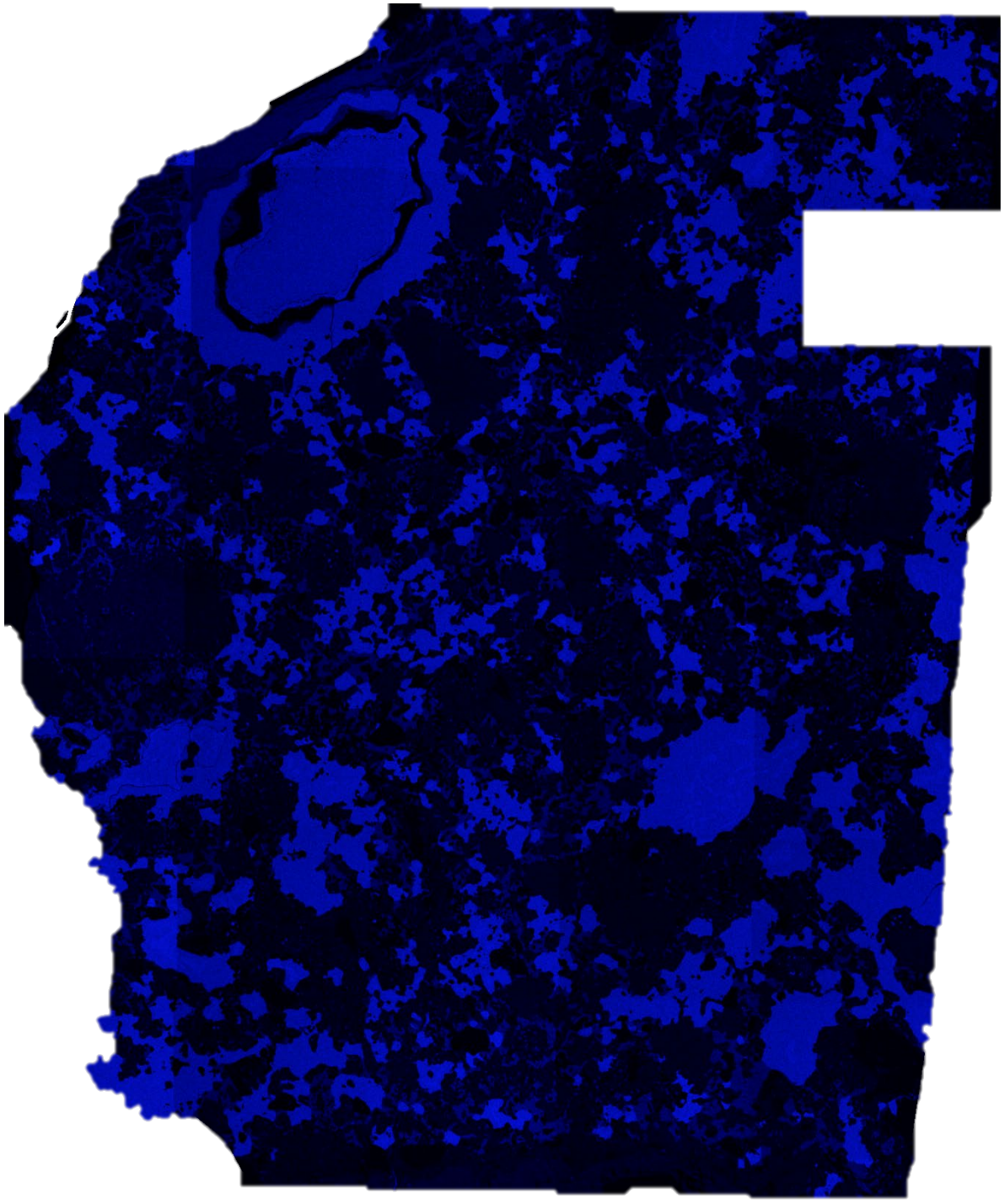

5 mm

D-d) Vaca Muerta – Cr

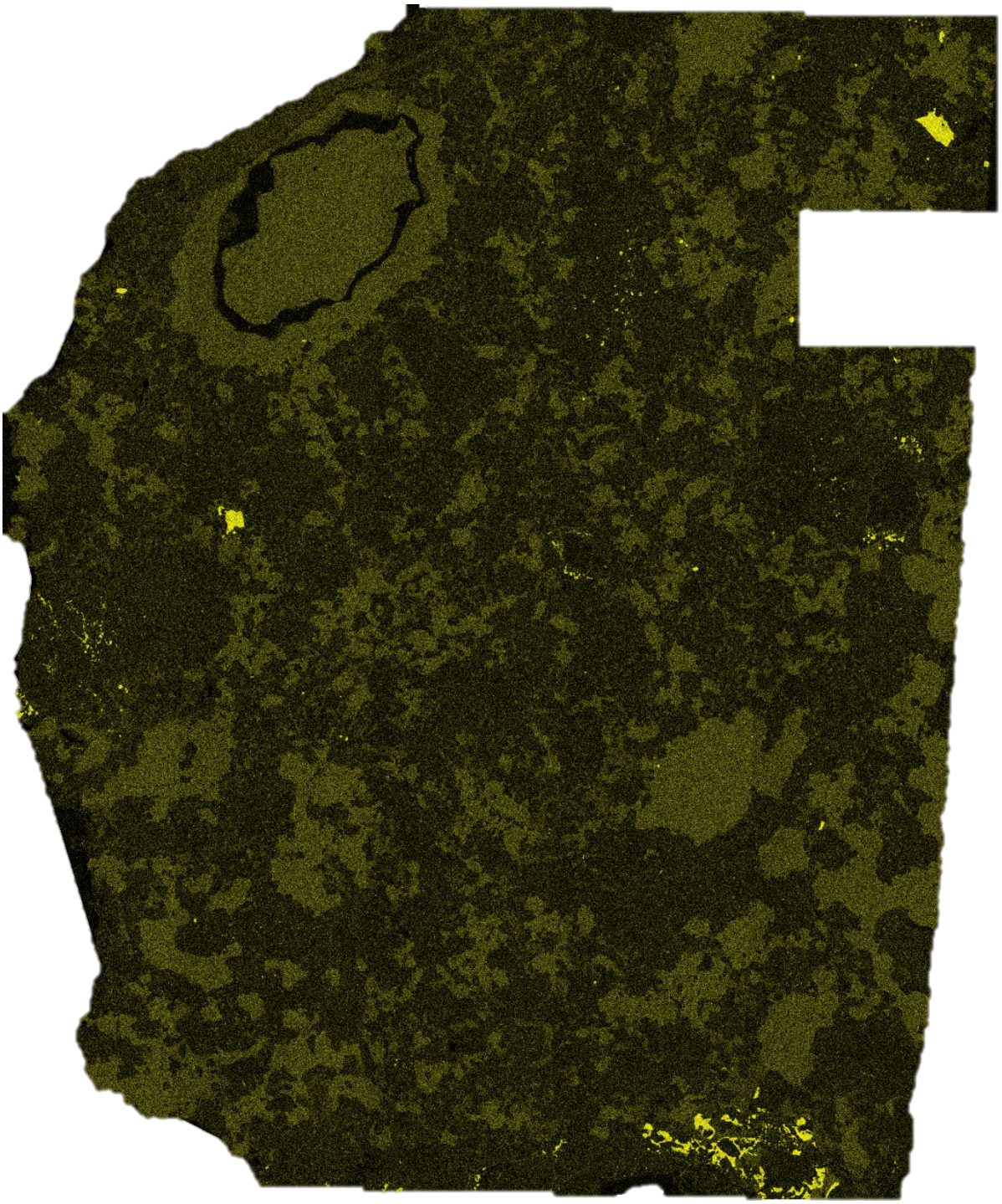

5 mm

D-e) Vaca Muerta – Cu

5 mm

D-f) Vaca Muerta – Fe

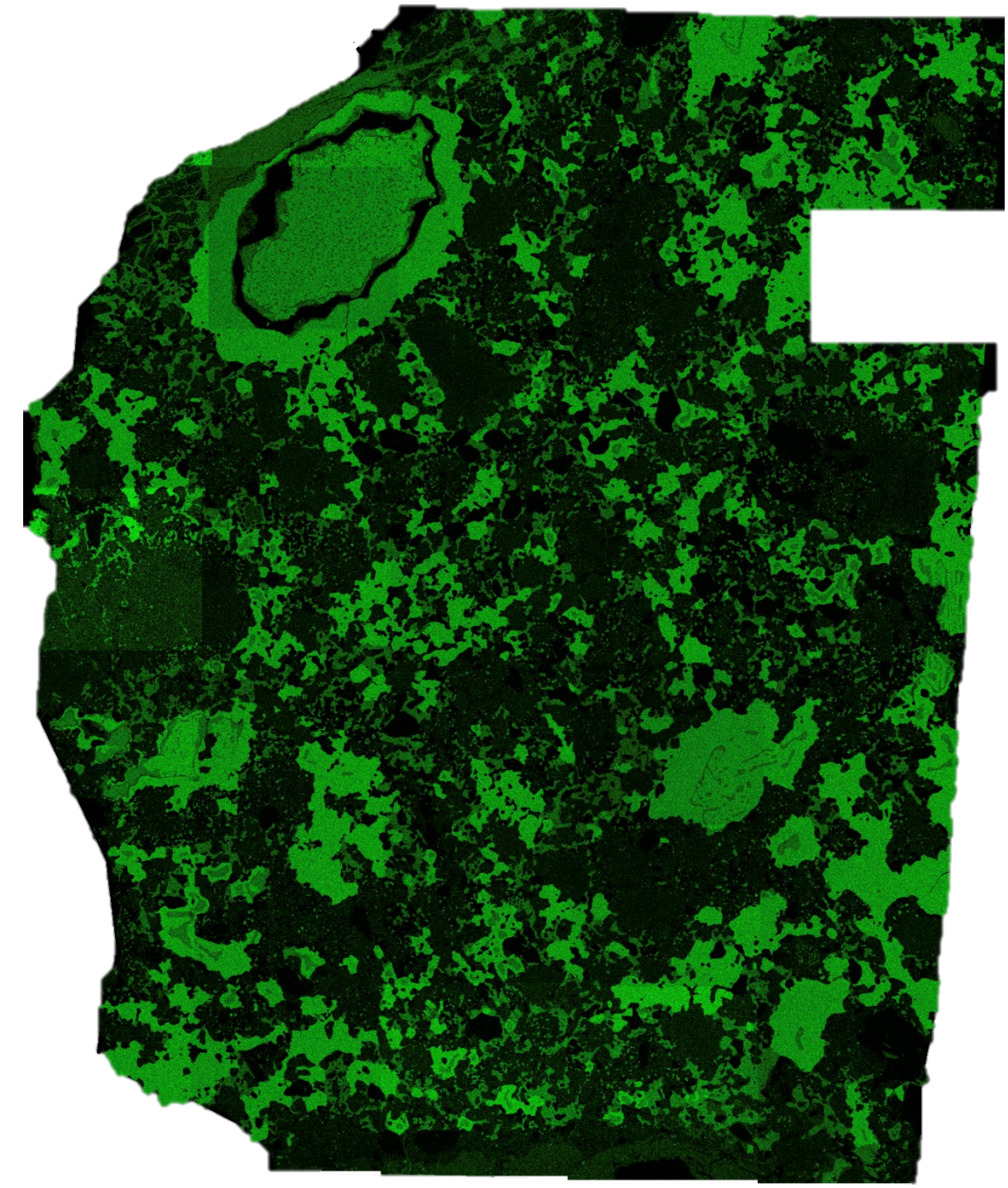

5 mm

D-g) Vaca Muerta – K

5 mm

D-h) Vaca Muerta – Mg

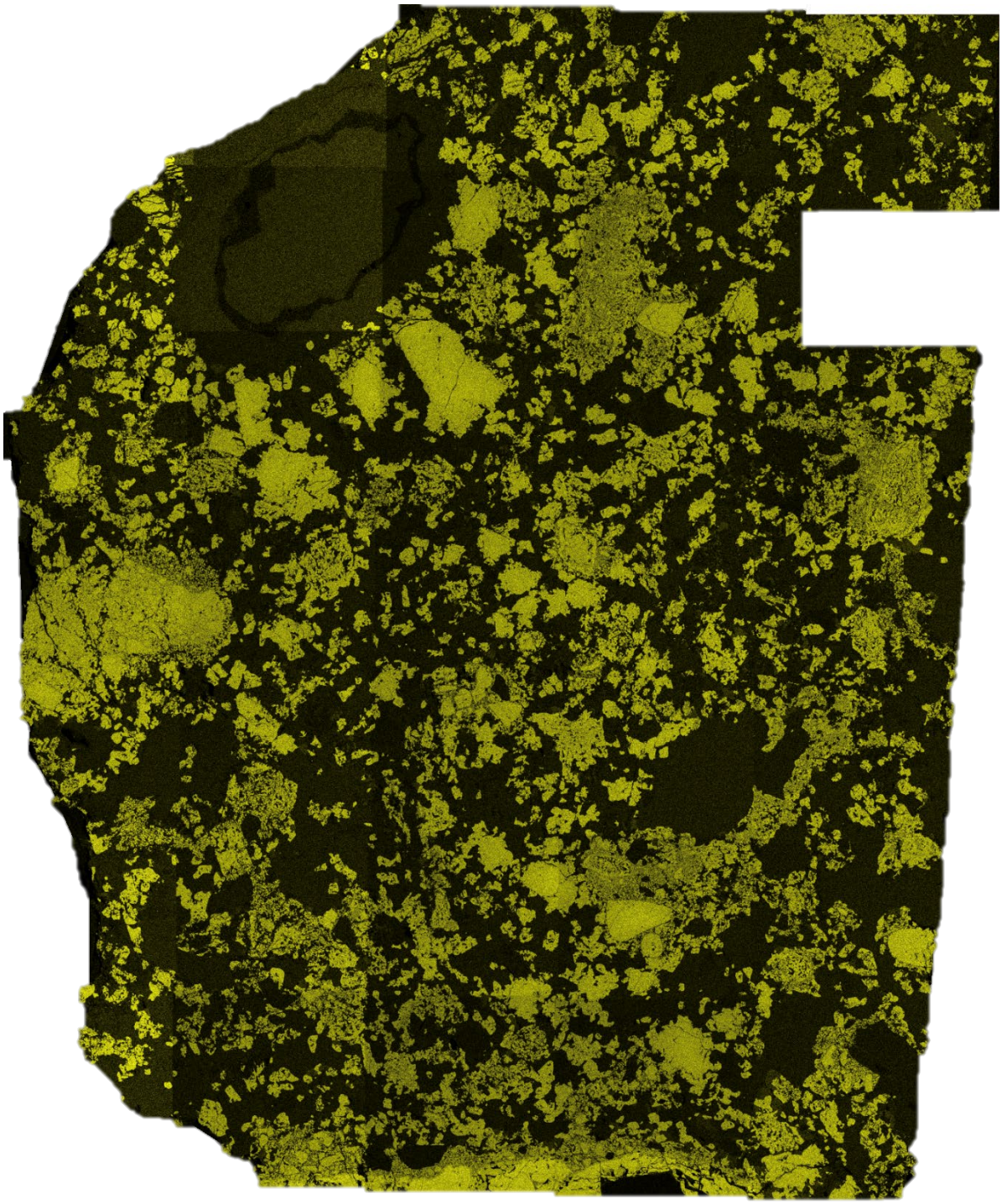

5 mm

D-i) Vaca Muerta – Mn

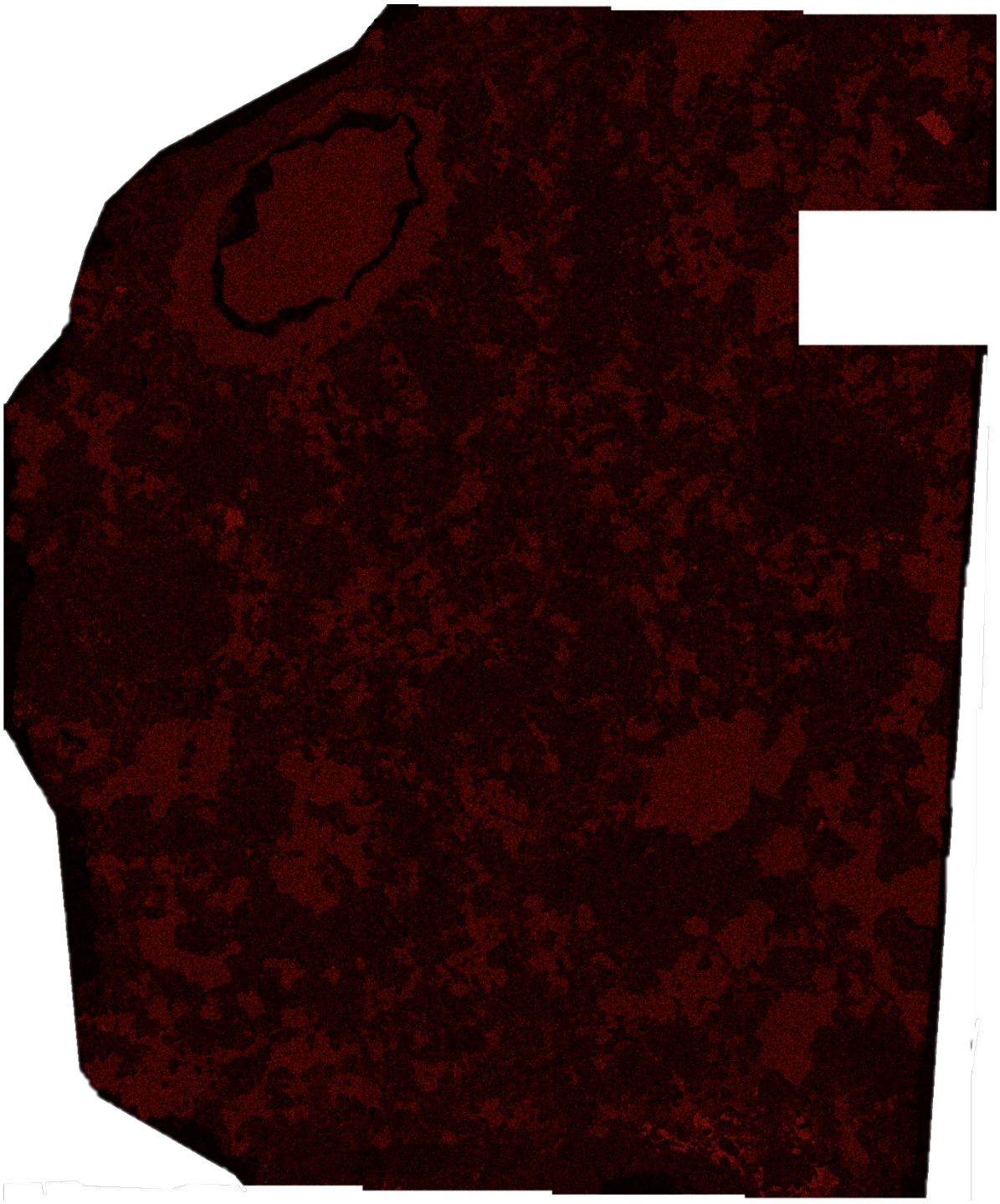

5 mm

D-j) Vaca Muerta – Na

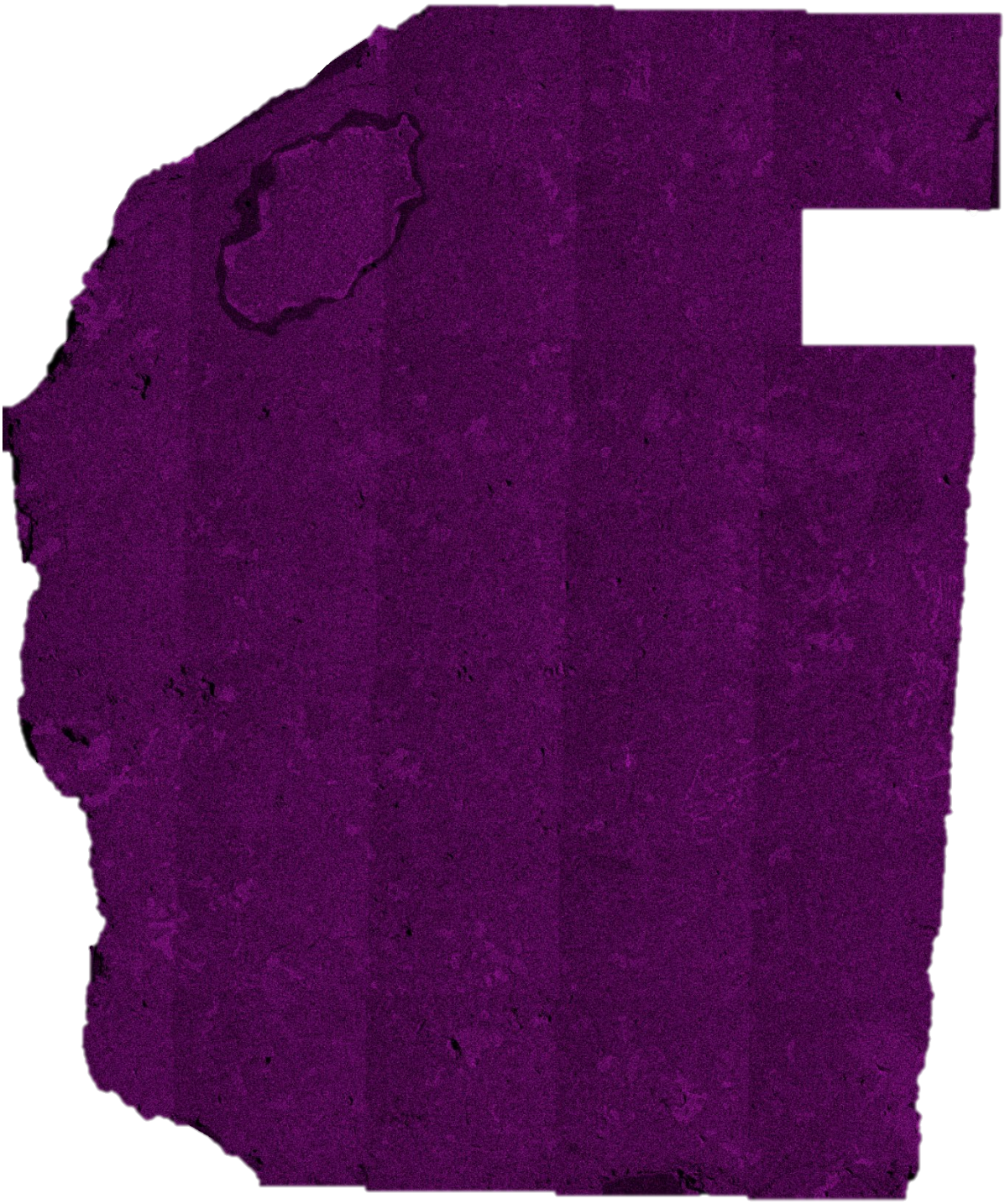

5 mm

D-k) Vaca Muerta – Ni

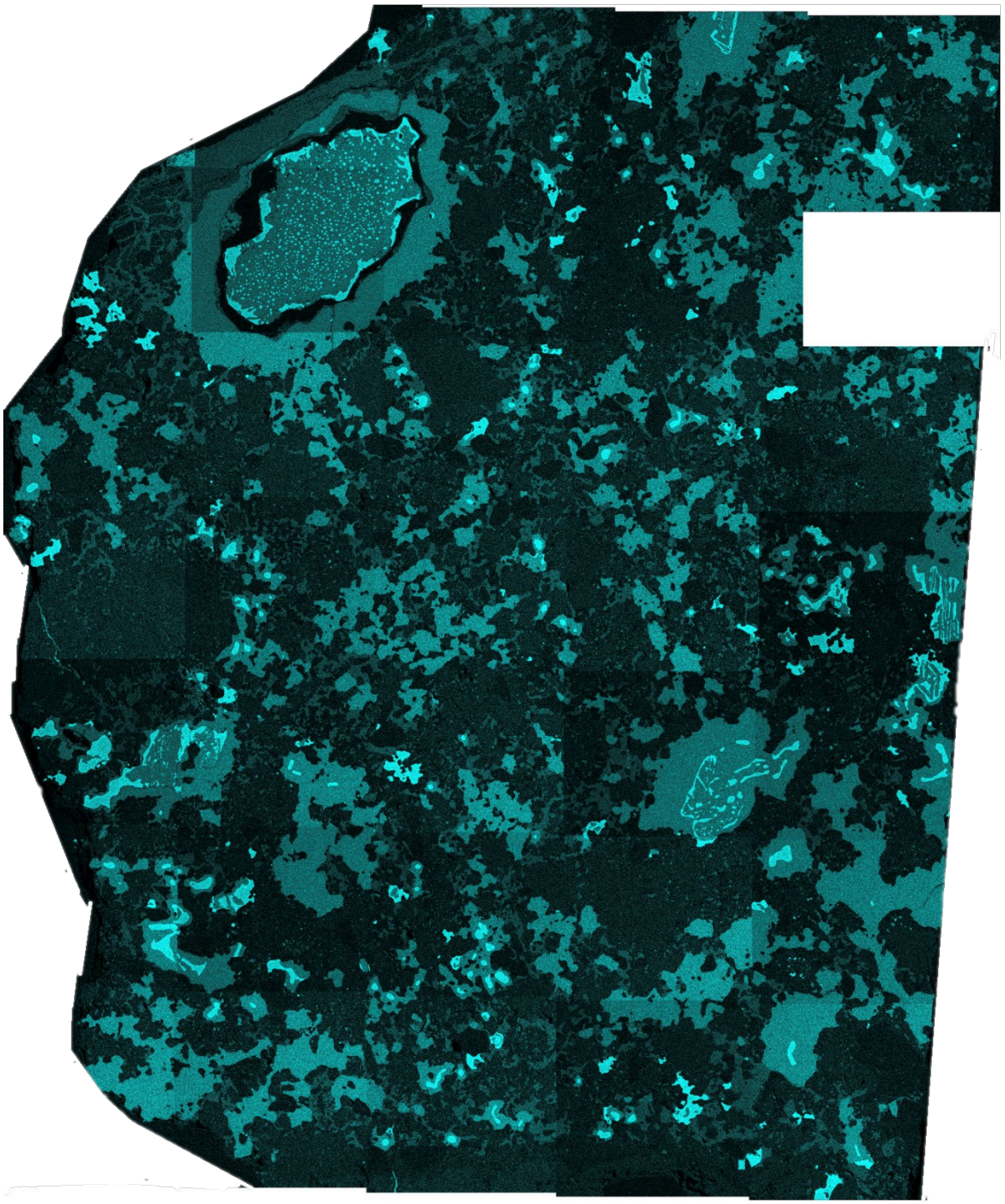

5 mm

D-l) Vaca Muerta – O

5 mm

D-m) Vaca Muerta – P

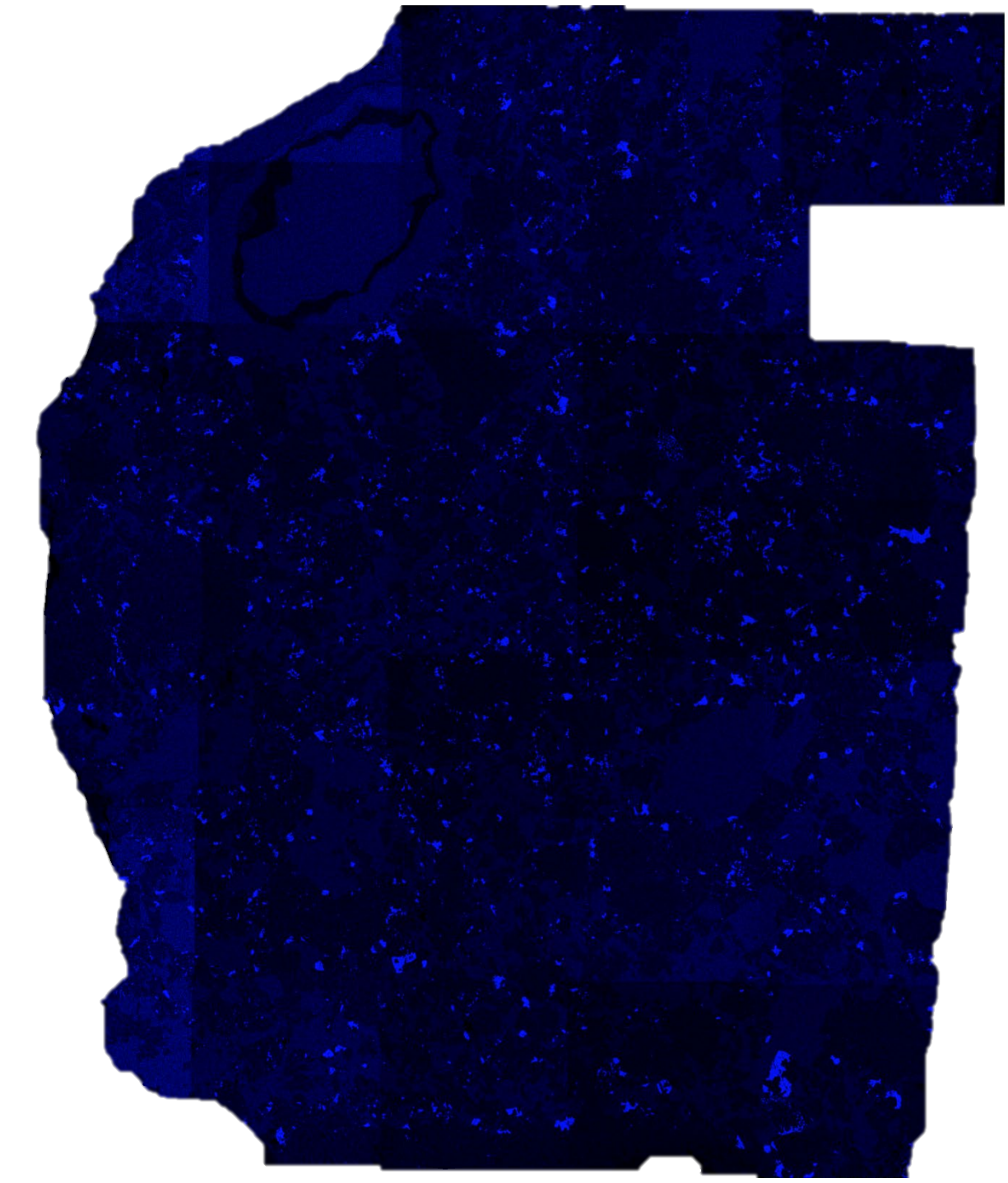

5 mm

D-n) Vaca Muerta – S

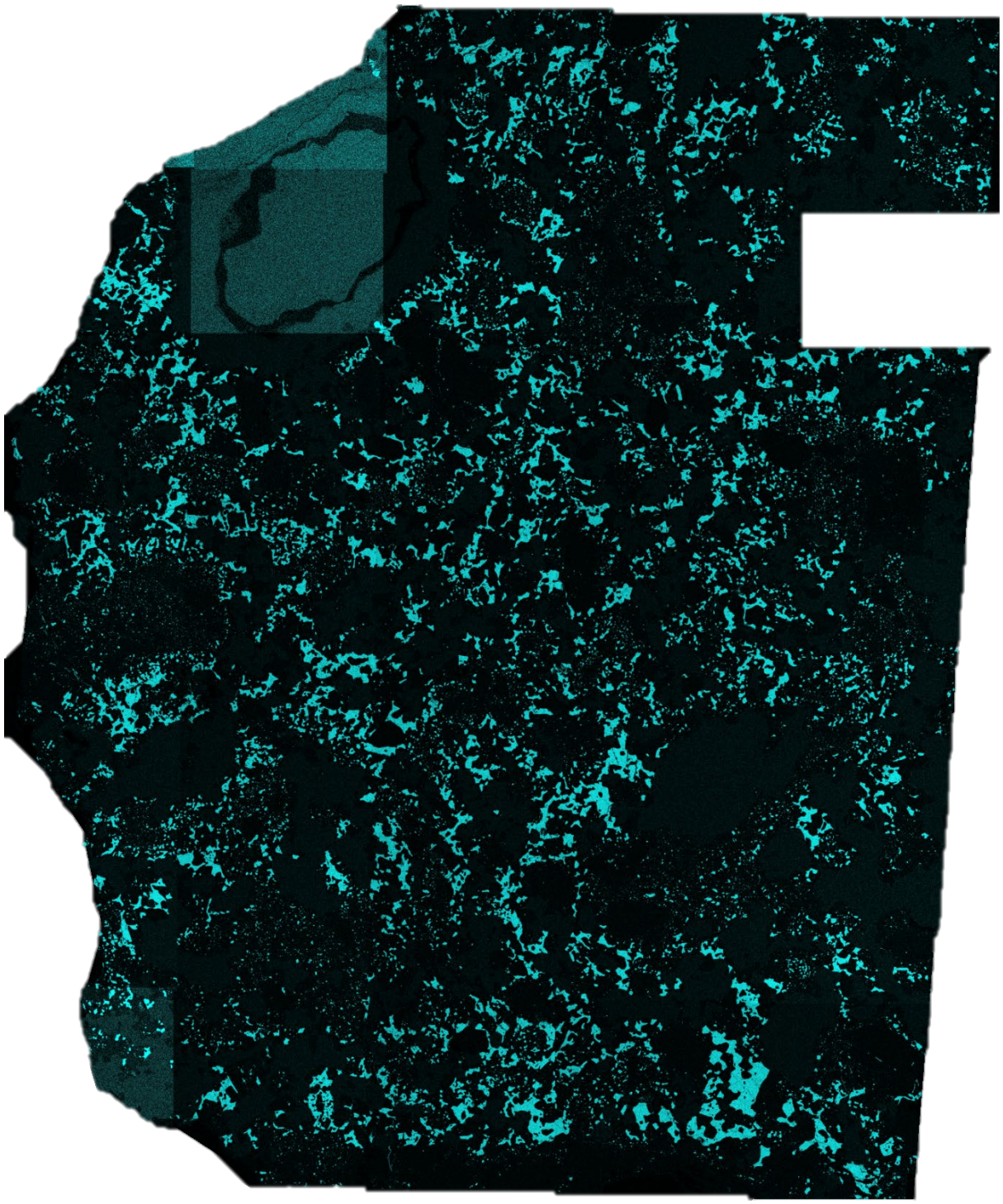

5 mm

D-o) Vaca Muerta – Si

D-p) Vaca Muerta – Ti

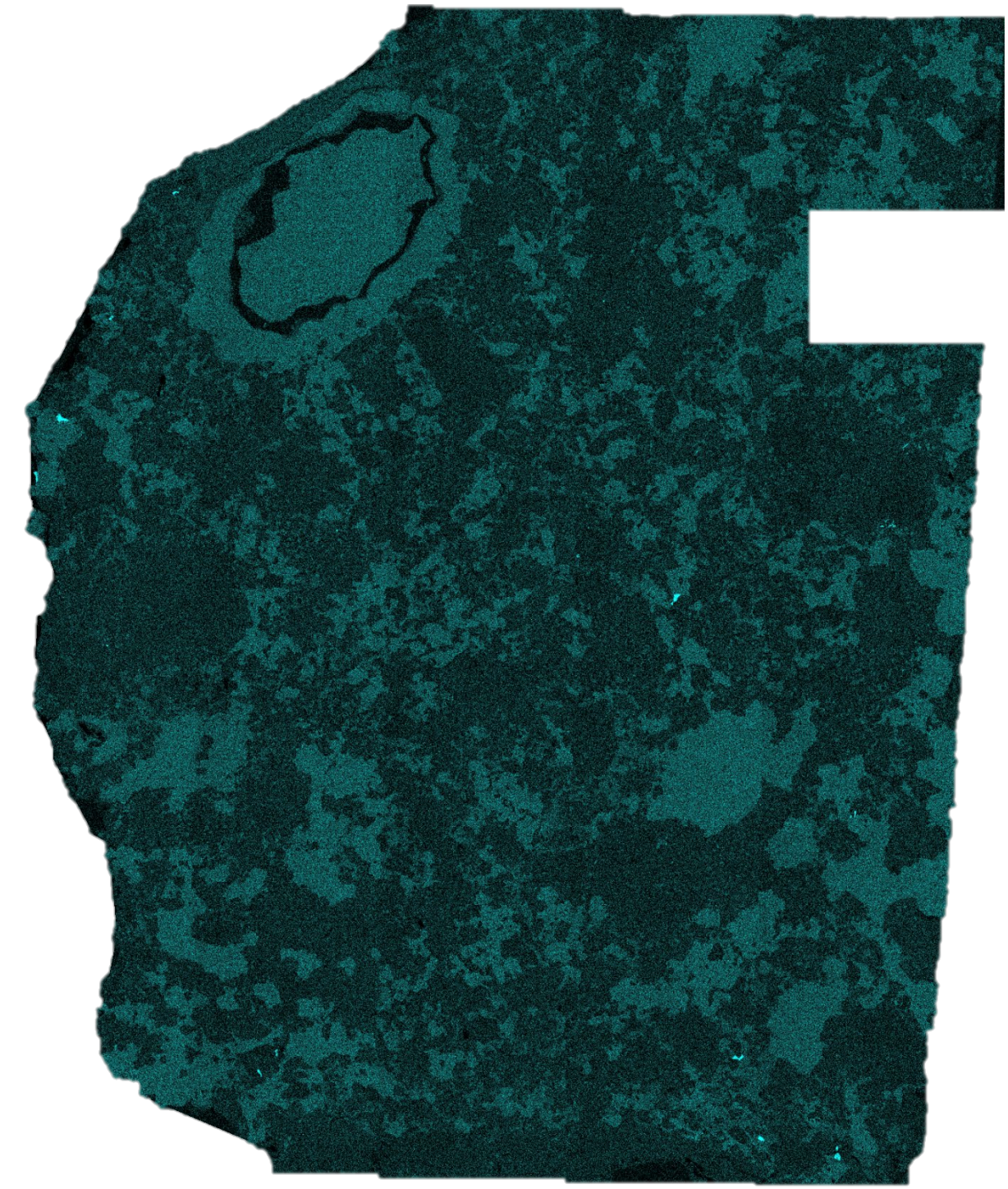

5 mm

D-q) Vaca Muerta – V

5 mm

Appendix E

Individual SEM Elemental X-ray maps for RKPA 79015

The entire section was analyzed for seventeen elements:

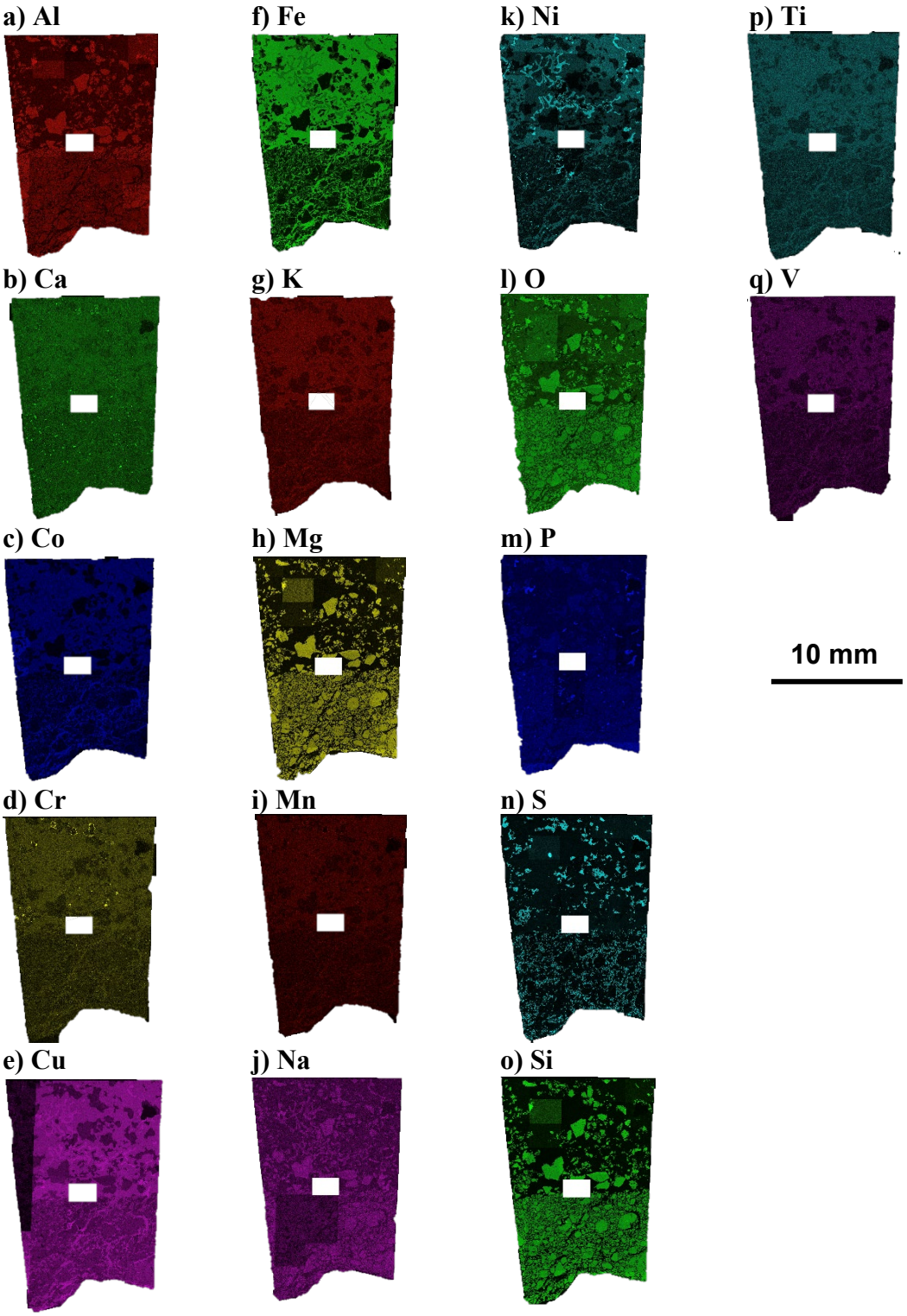

E-a) RKPA 79015 – Al

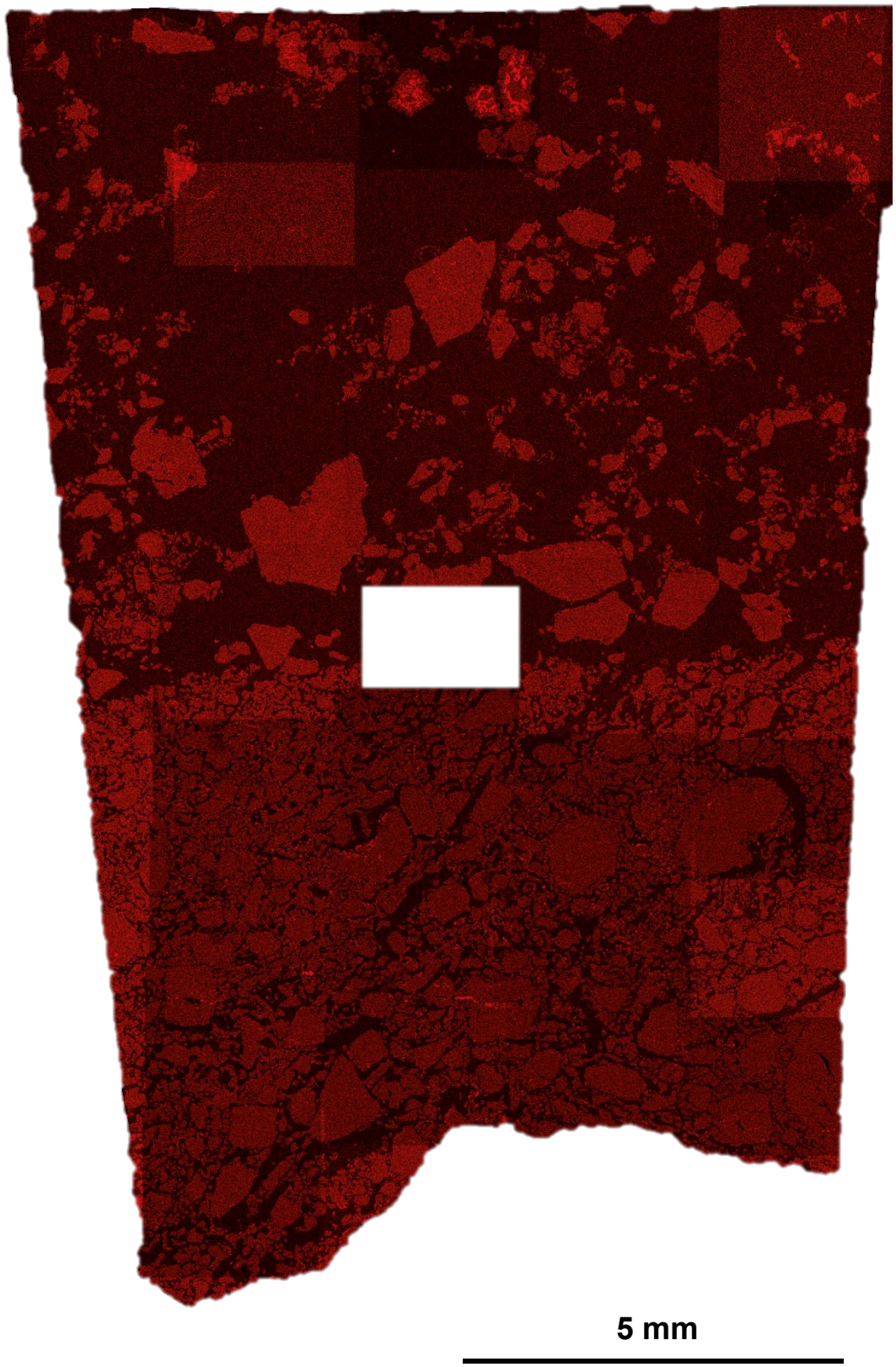

E-b) RKPA 79015 – Ca

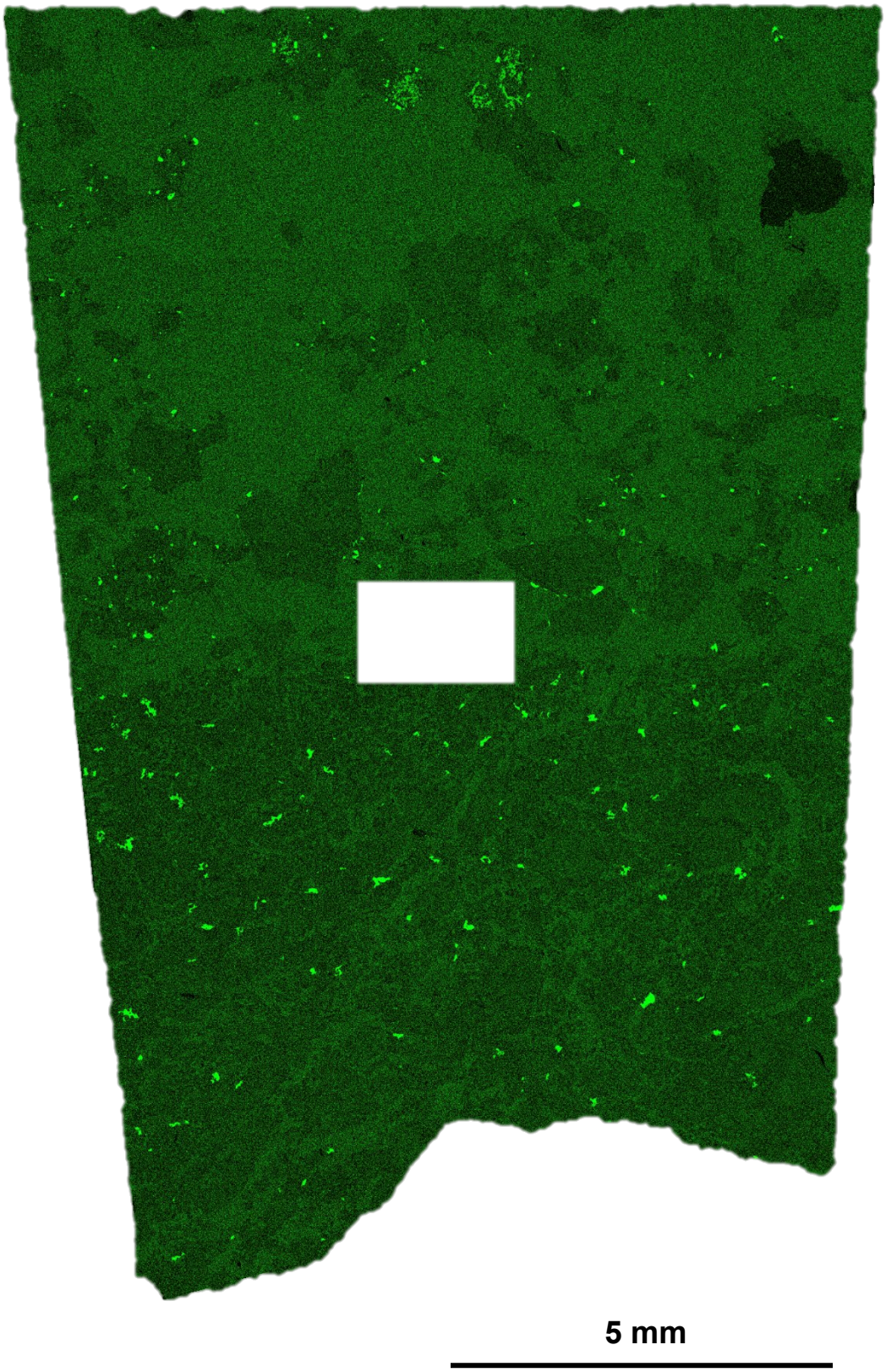

E-c) RKPA 79015 – Co

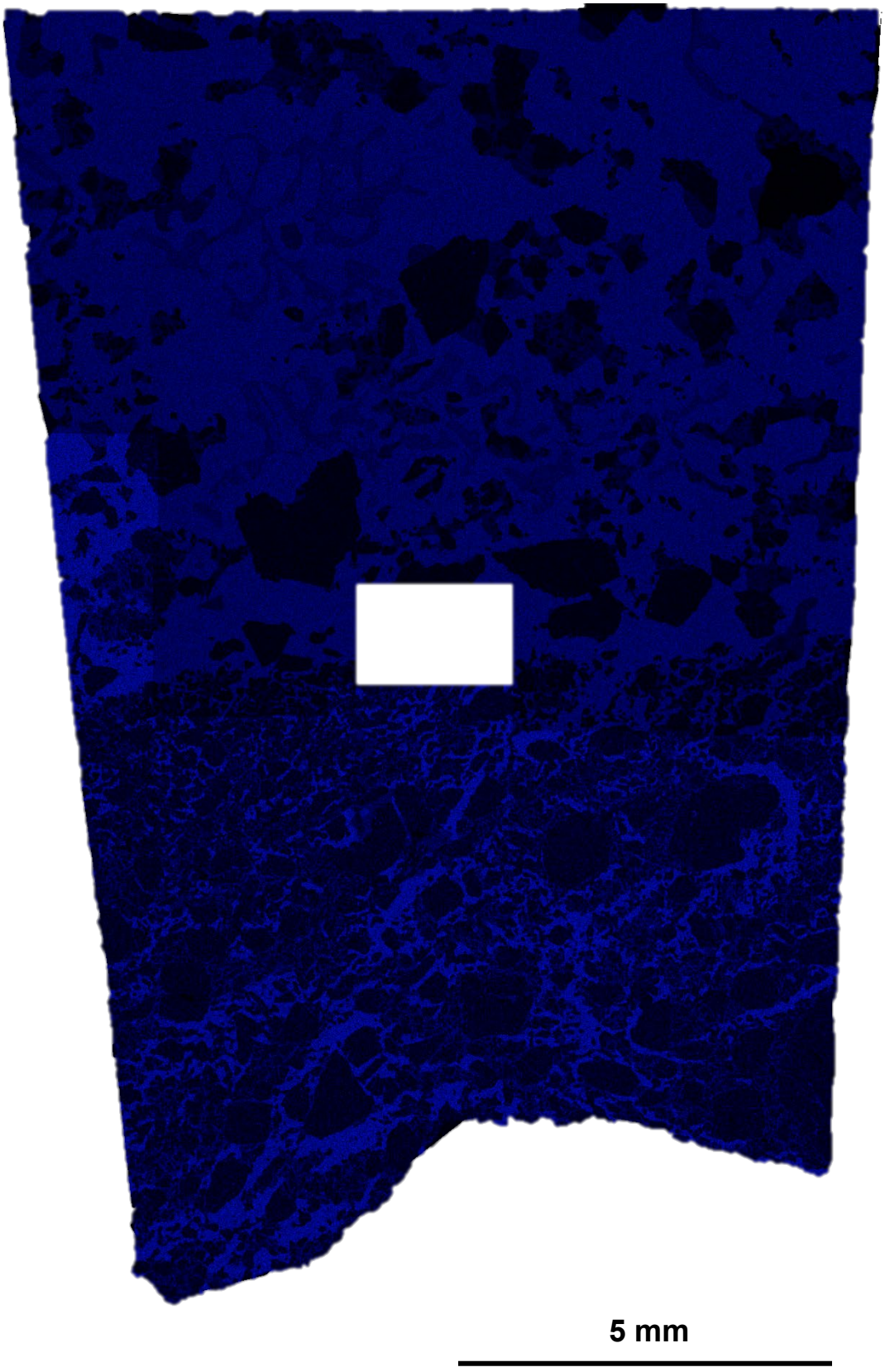

E-d) RKPA 79015 – Cr

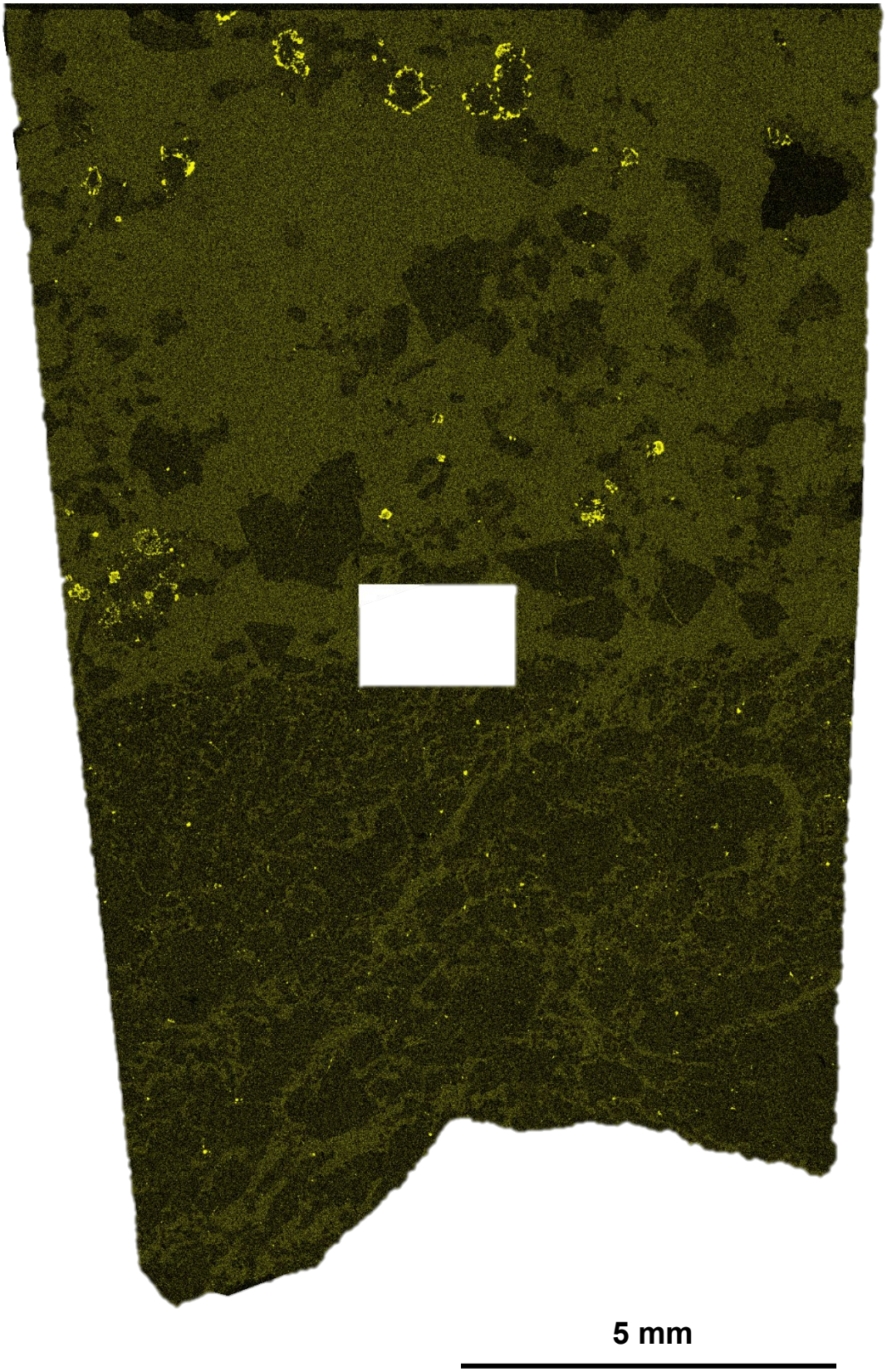

E-e) RKPA 79015 – Cu

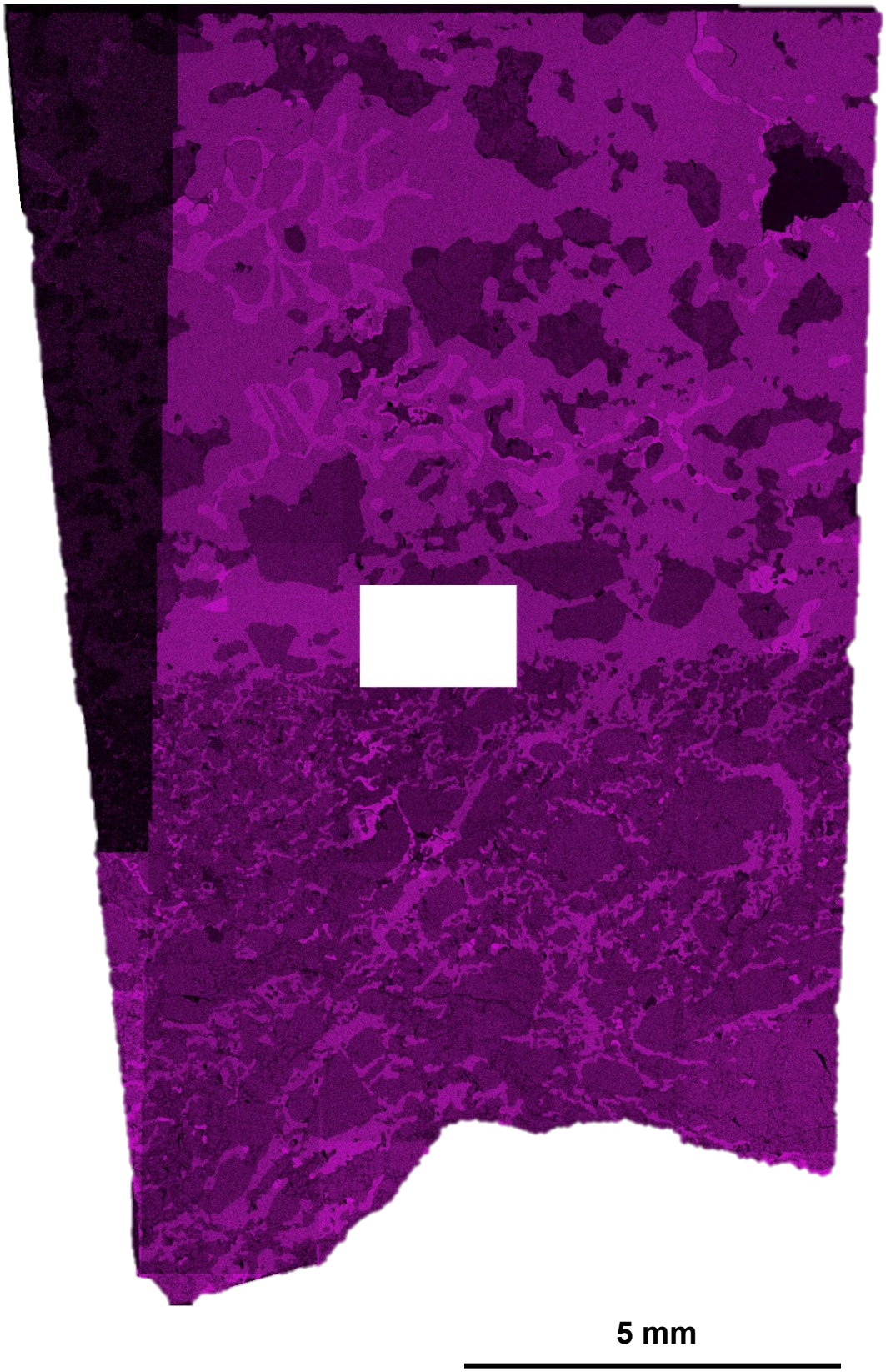

E-f) RKPA 79015 – Fe

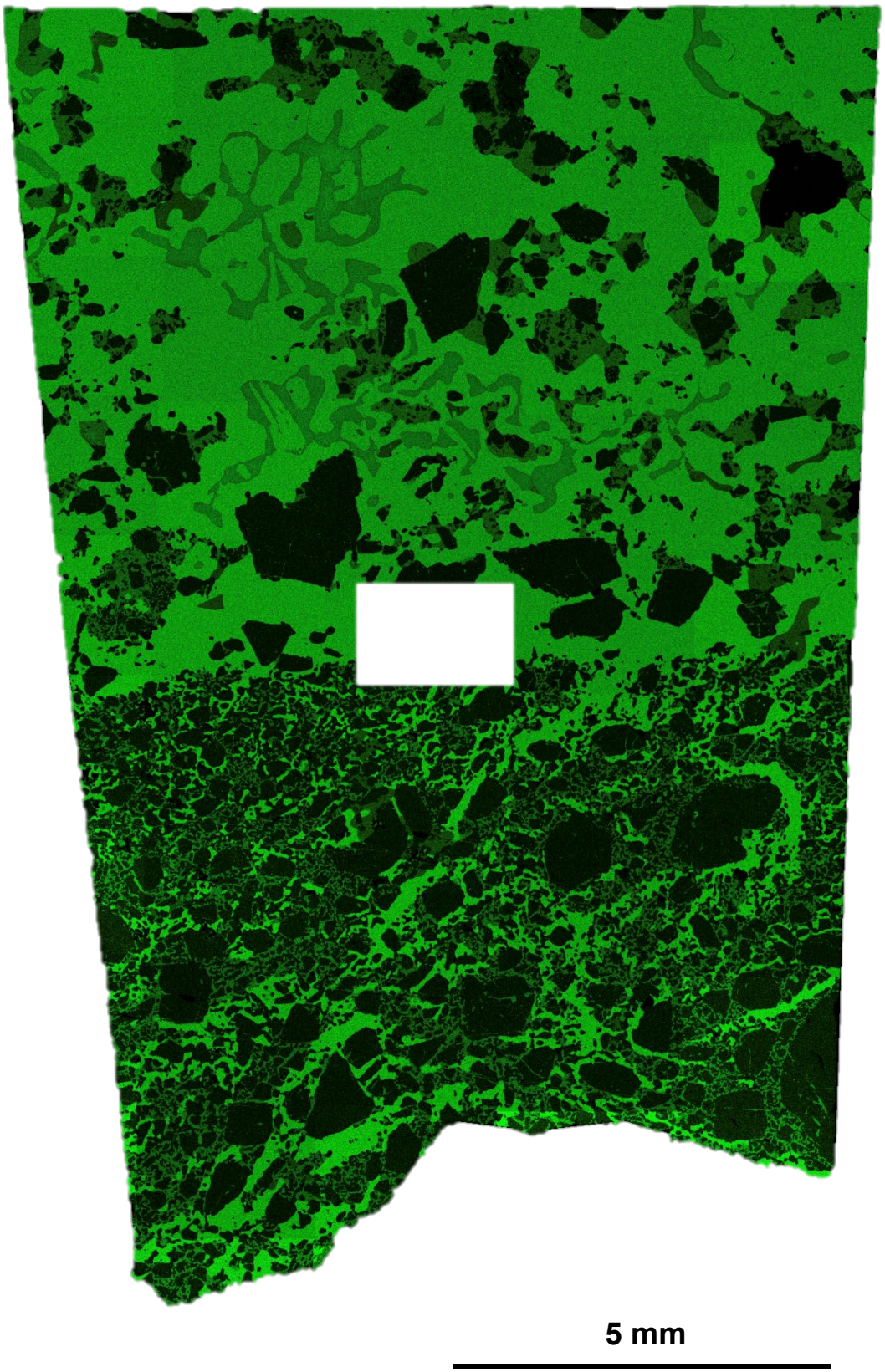

E-g) RKPA 79015 – K

E-h) RKPA 79015 – Mg

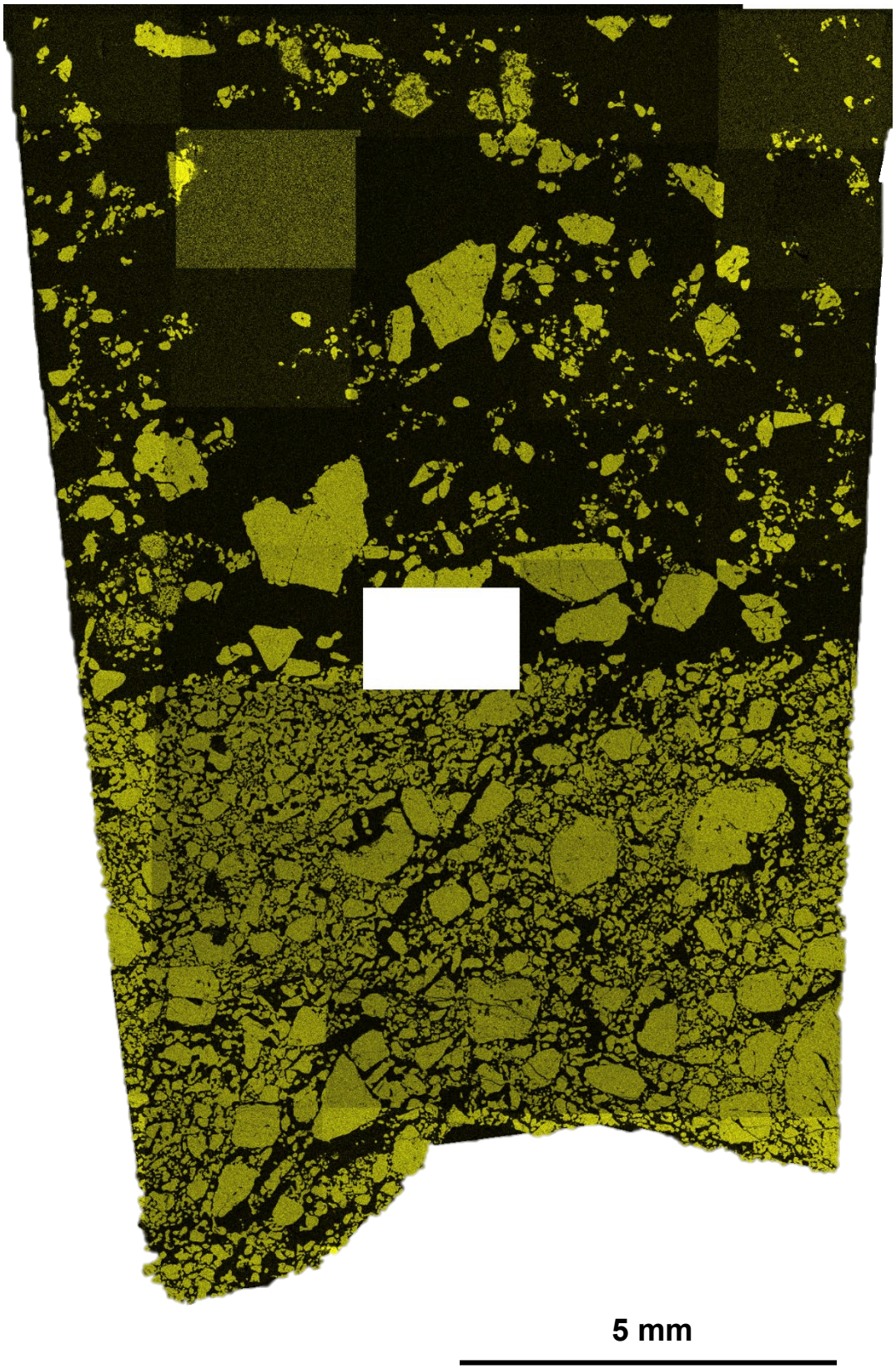

E-i) RKPA 79015 – Mn

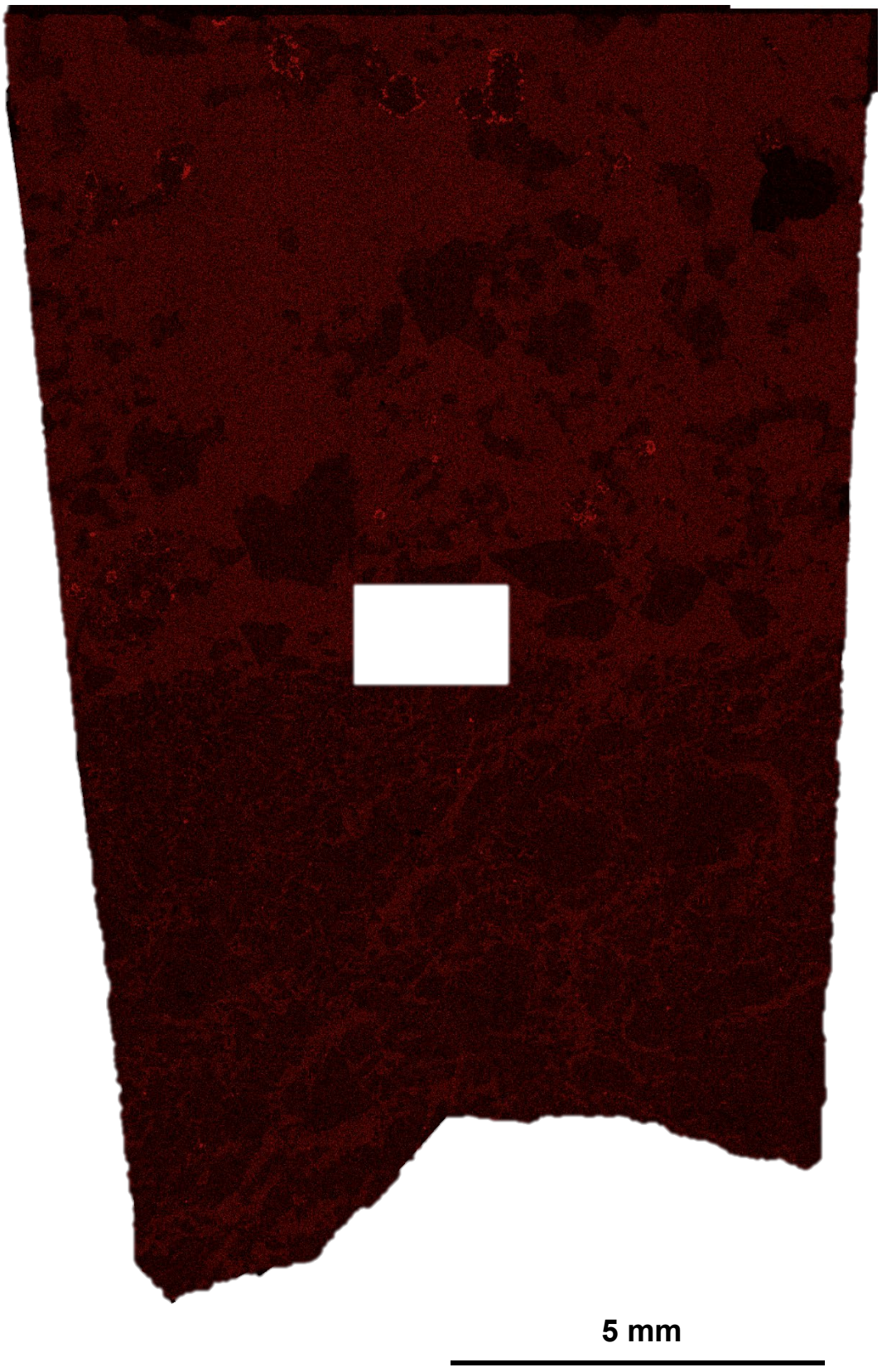

E-j) RKPA 79015 – Na

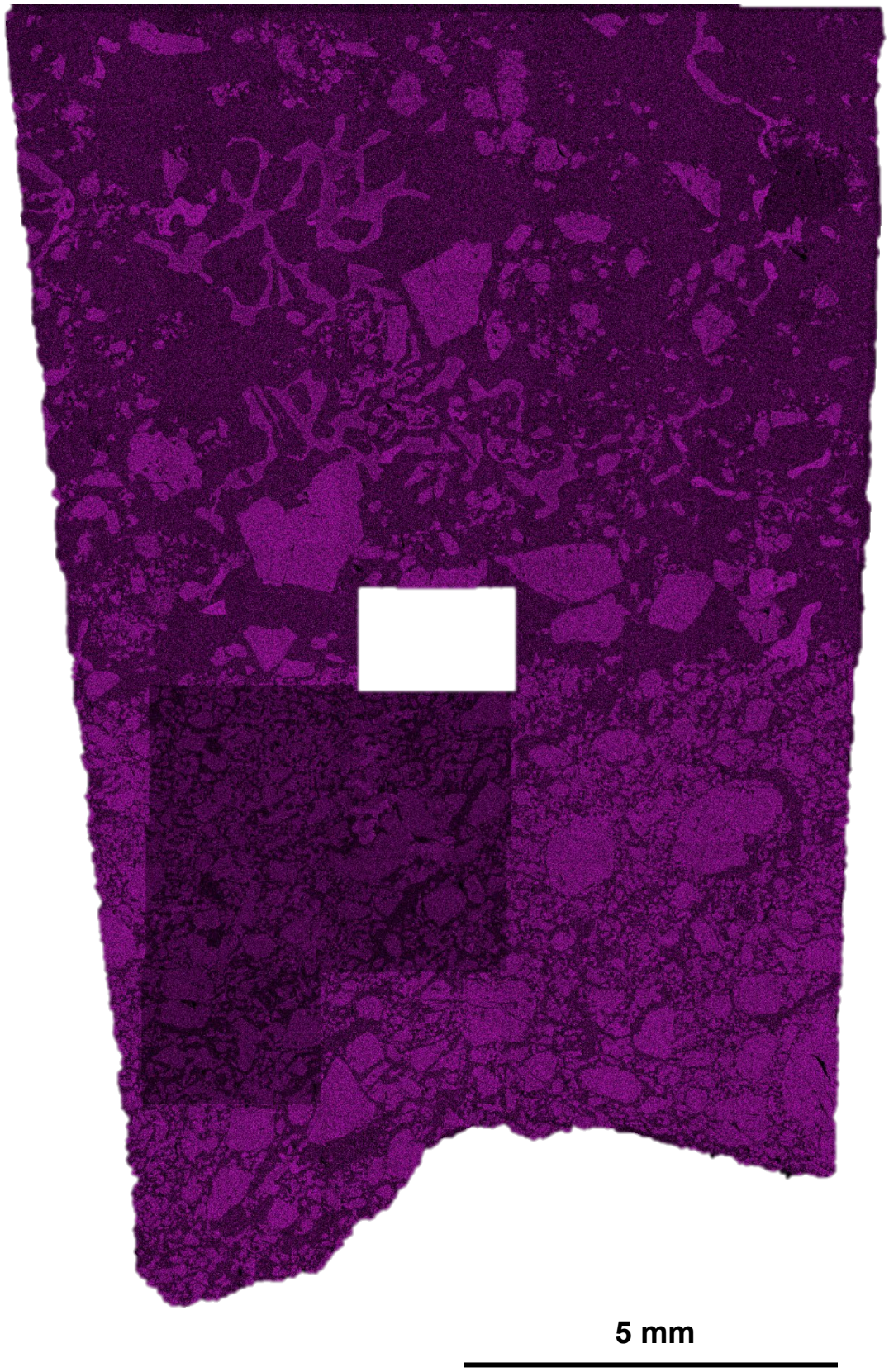

E-k) RKPA 79015 – Ni

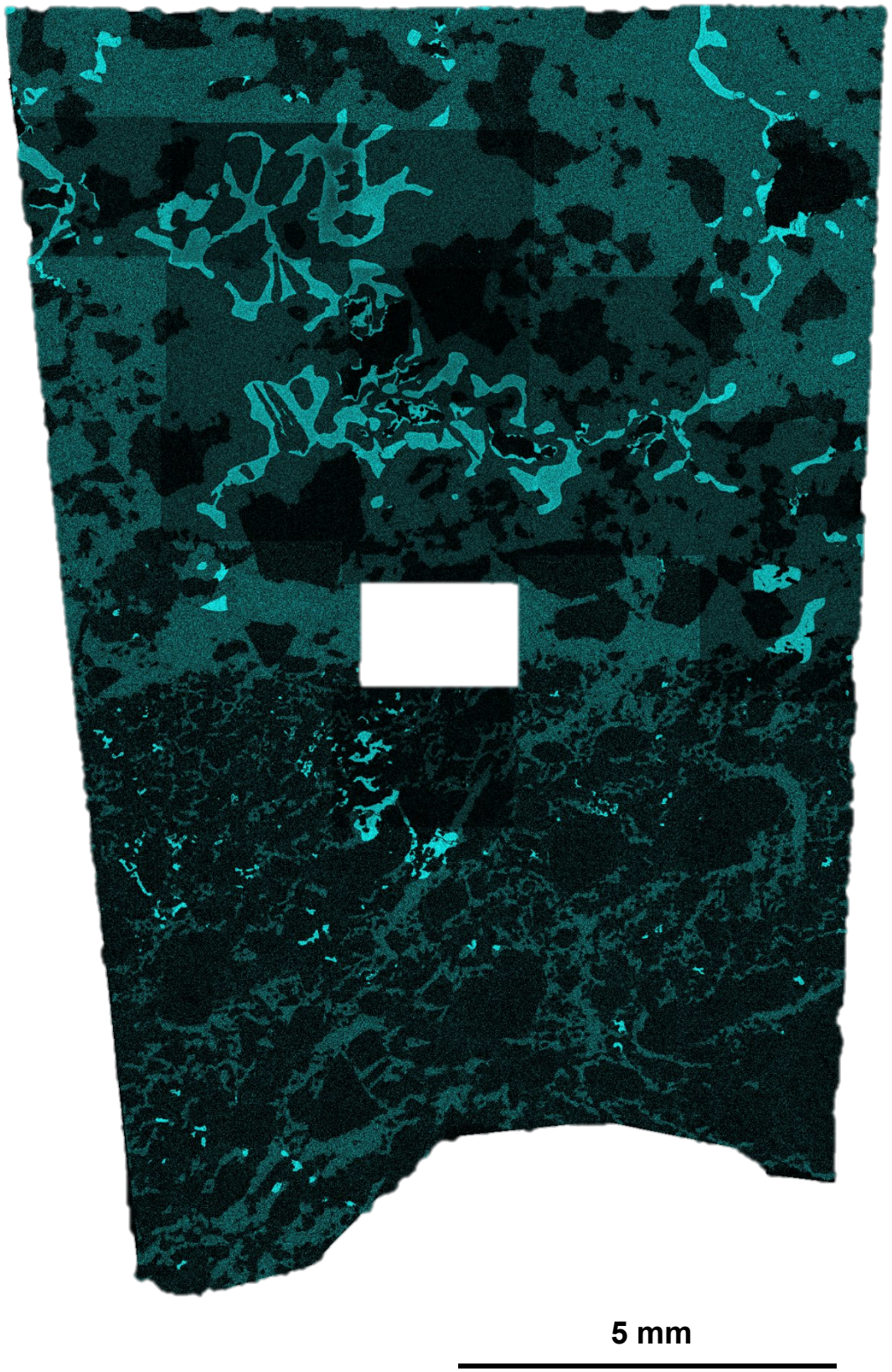

E-l) RKPA 79015 – O

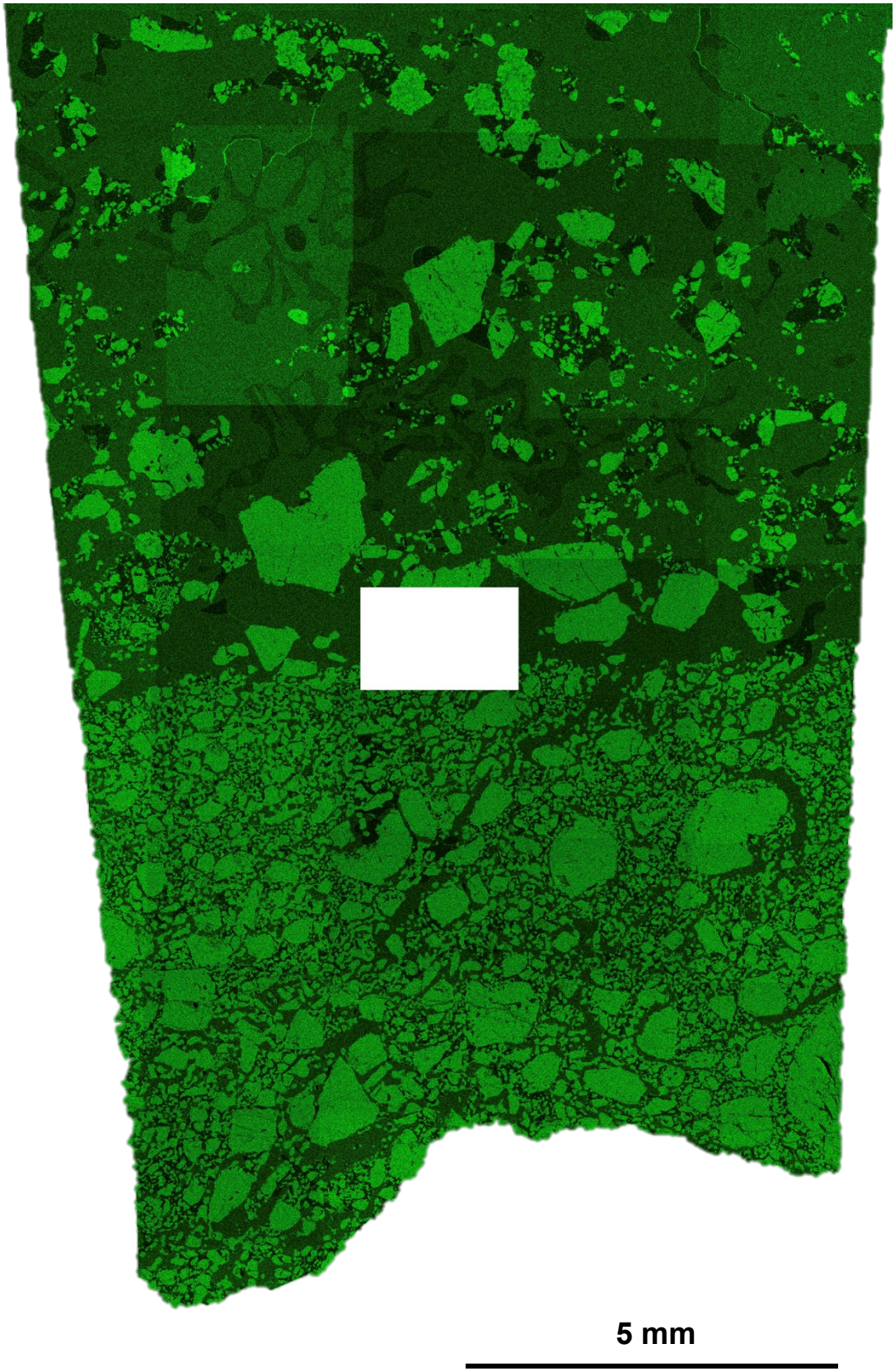

E-m) RKPA 79015 – P

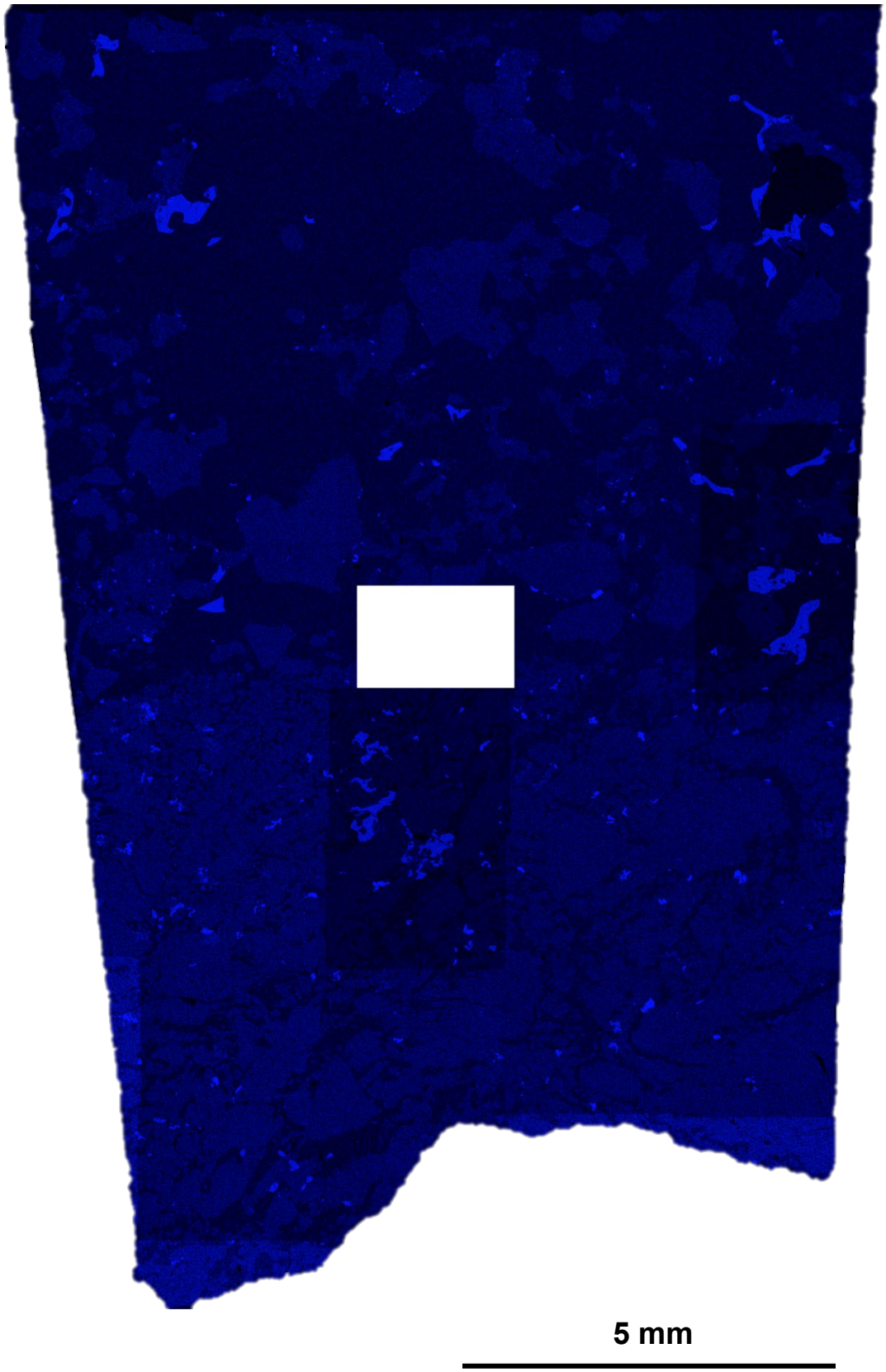

E-n) RKPA 79015 – S

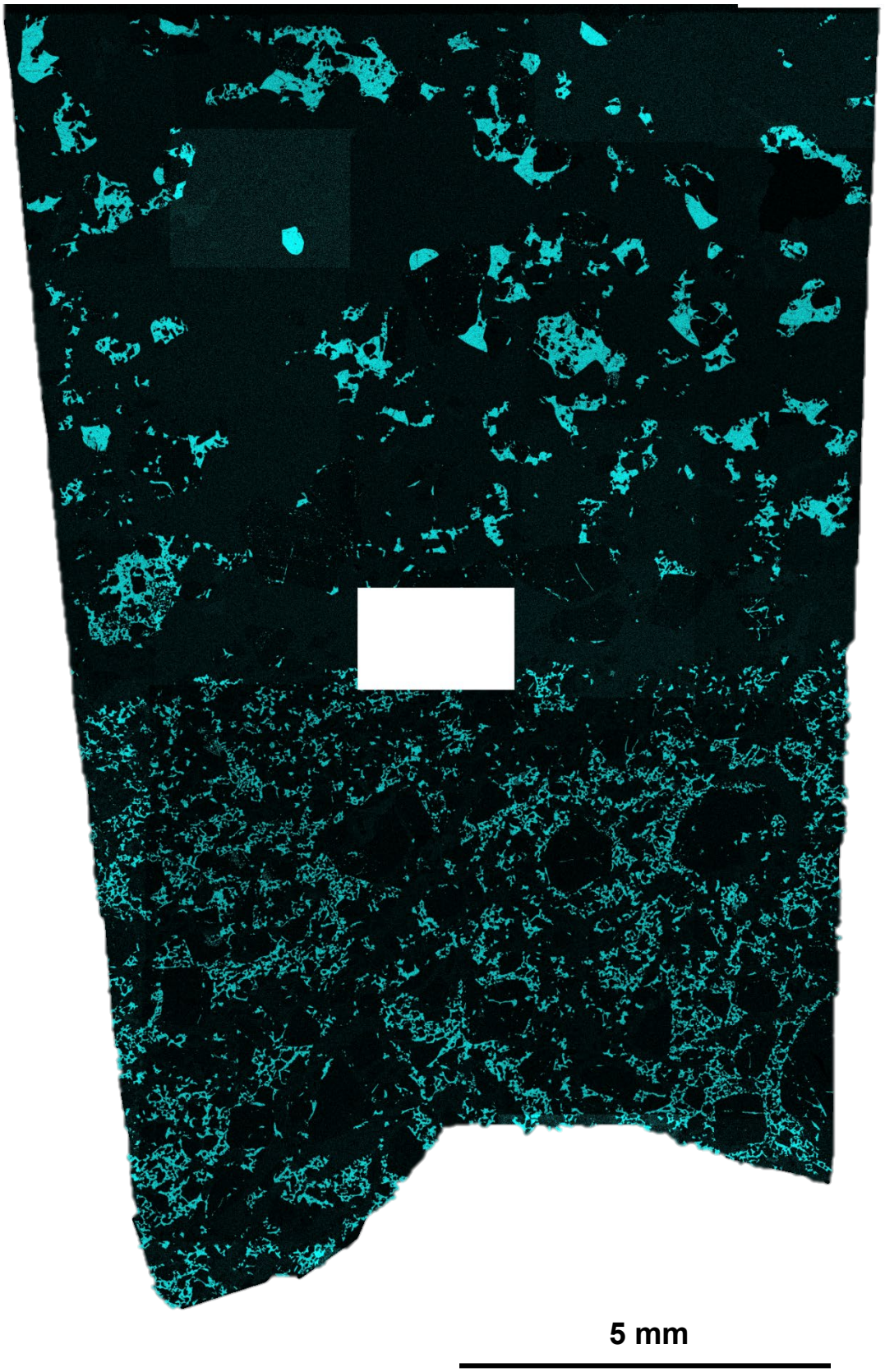

E-o) RKPA 79015 – Si

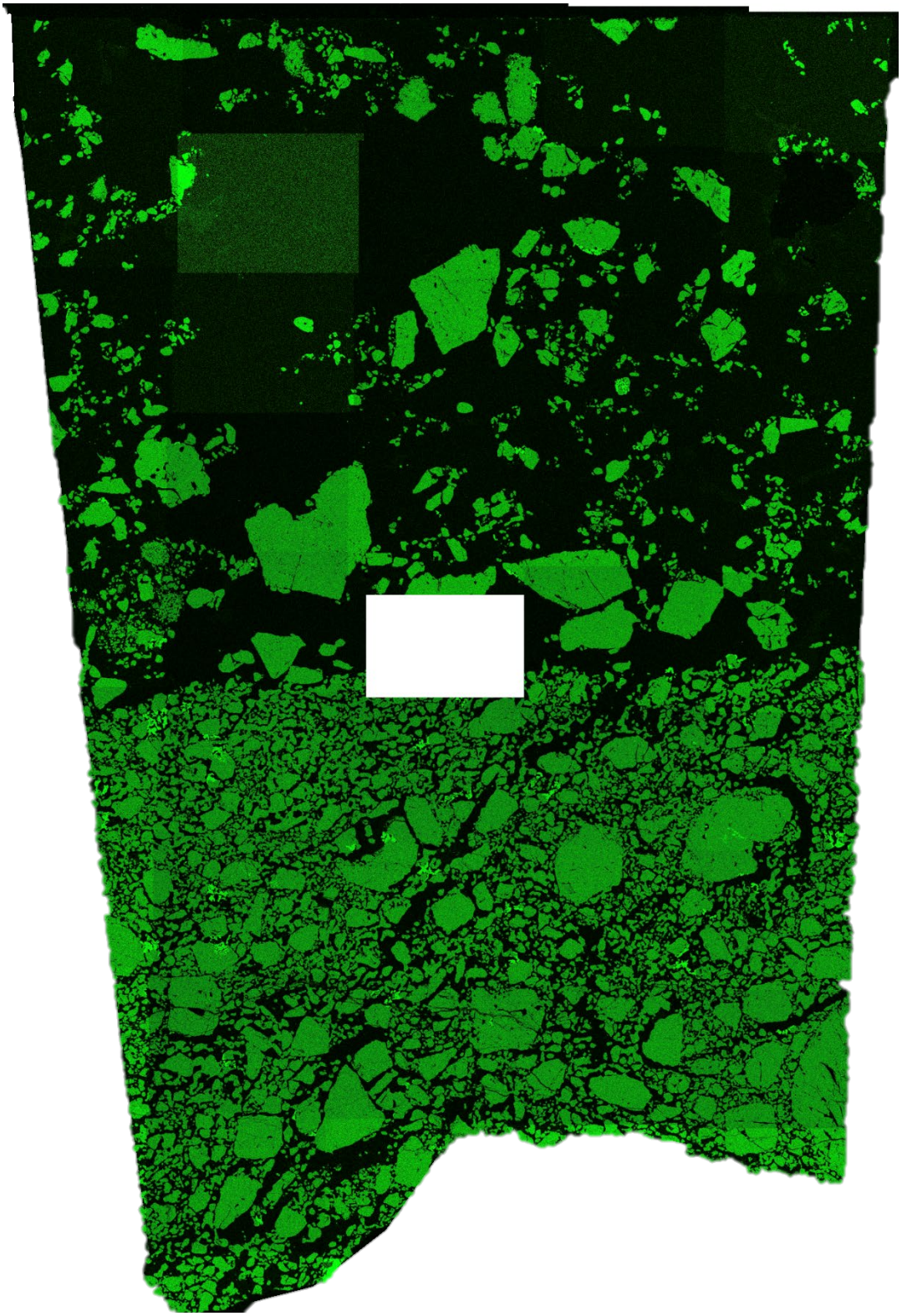

E-p) RKPA 79015 – Ti

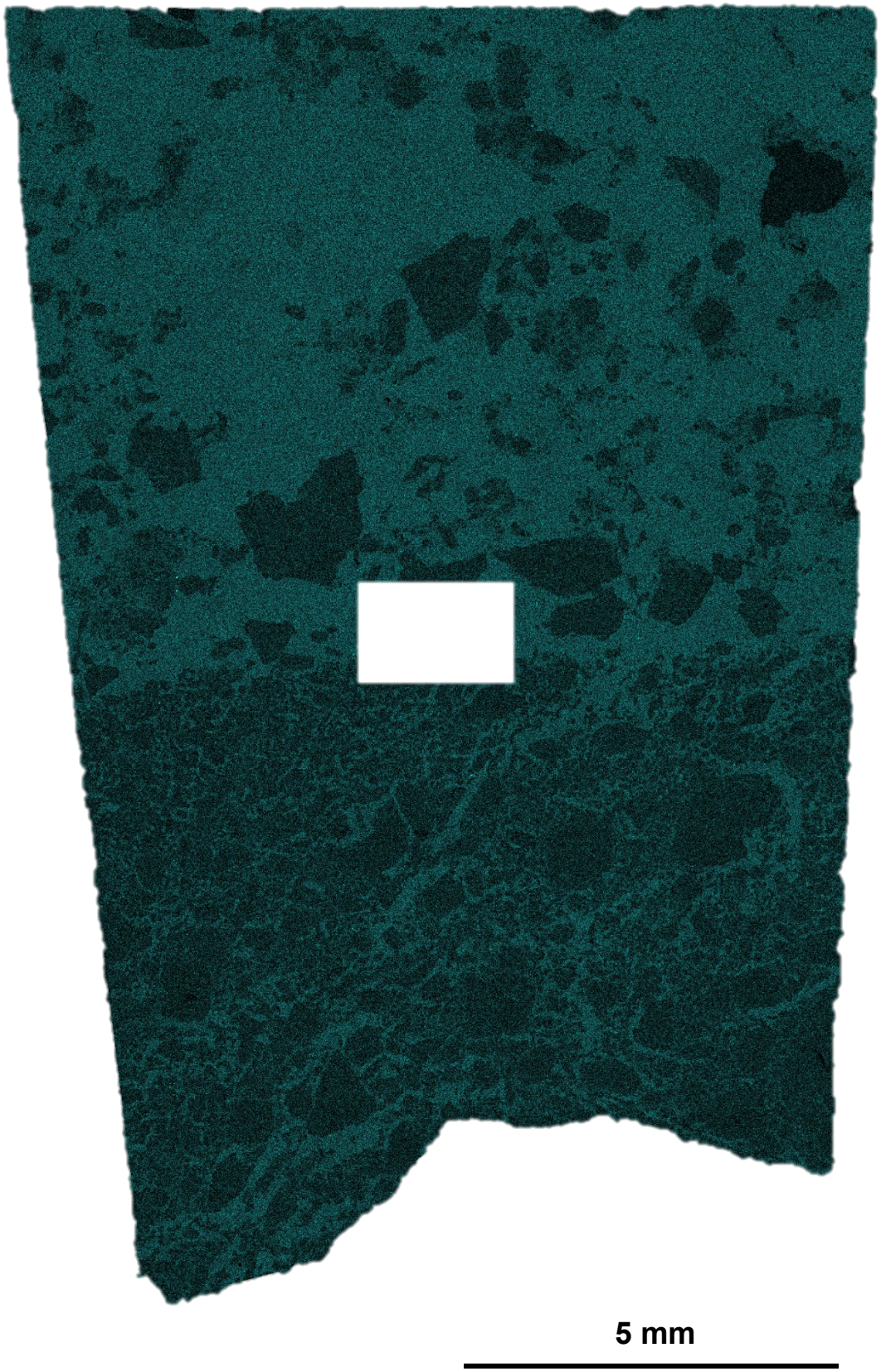

E-q) RKPA 79015 – V

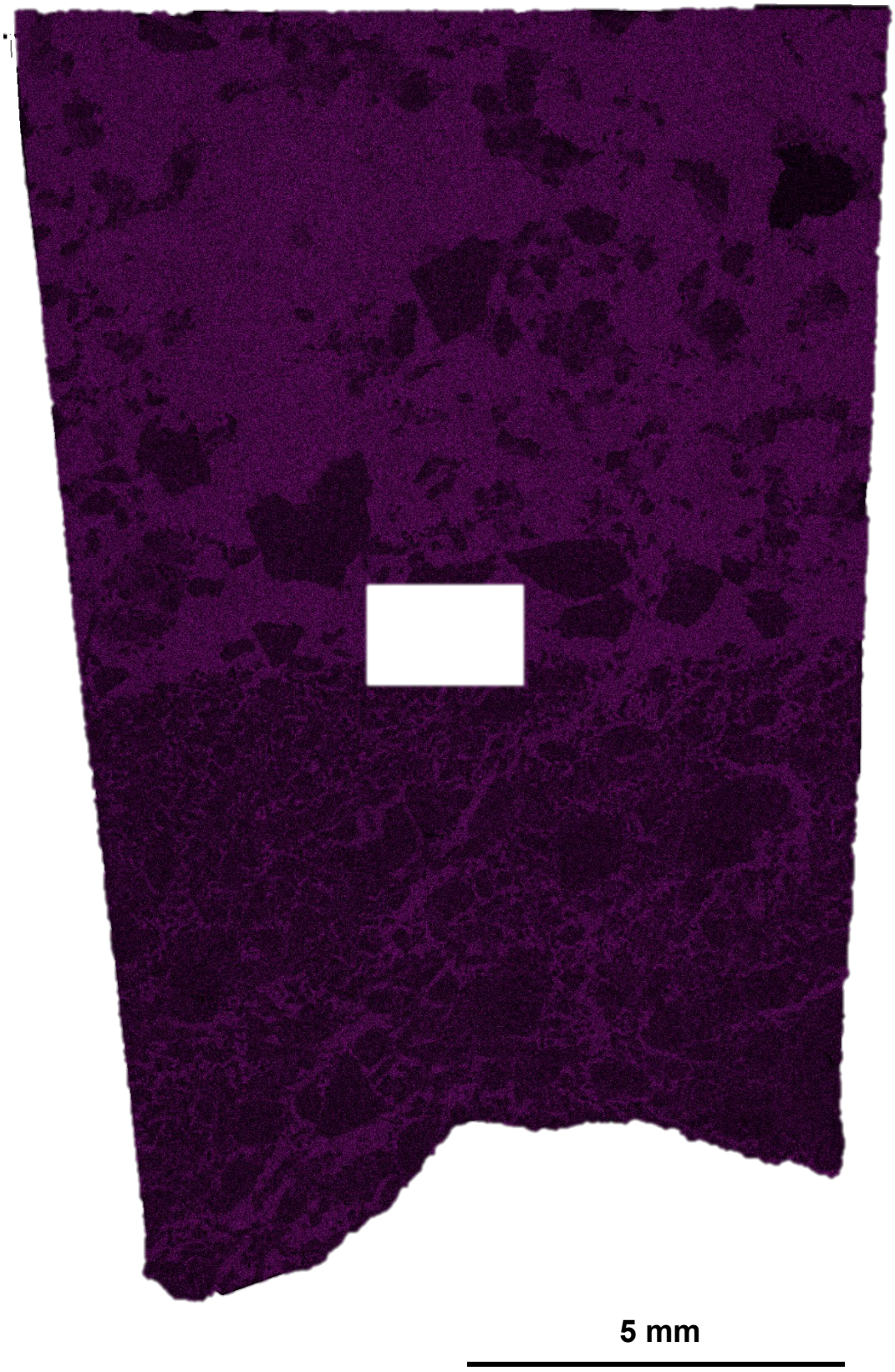

Appendix F

Individual SEM Elemental X-ray maps for Chaunskij

The entire section was analyzed for seventeen elements:

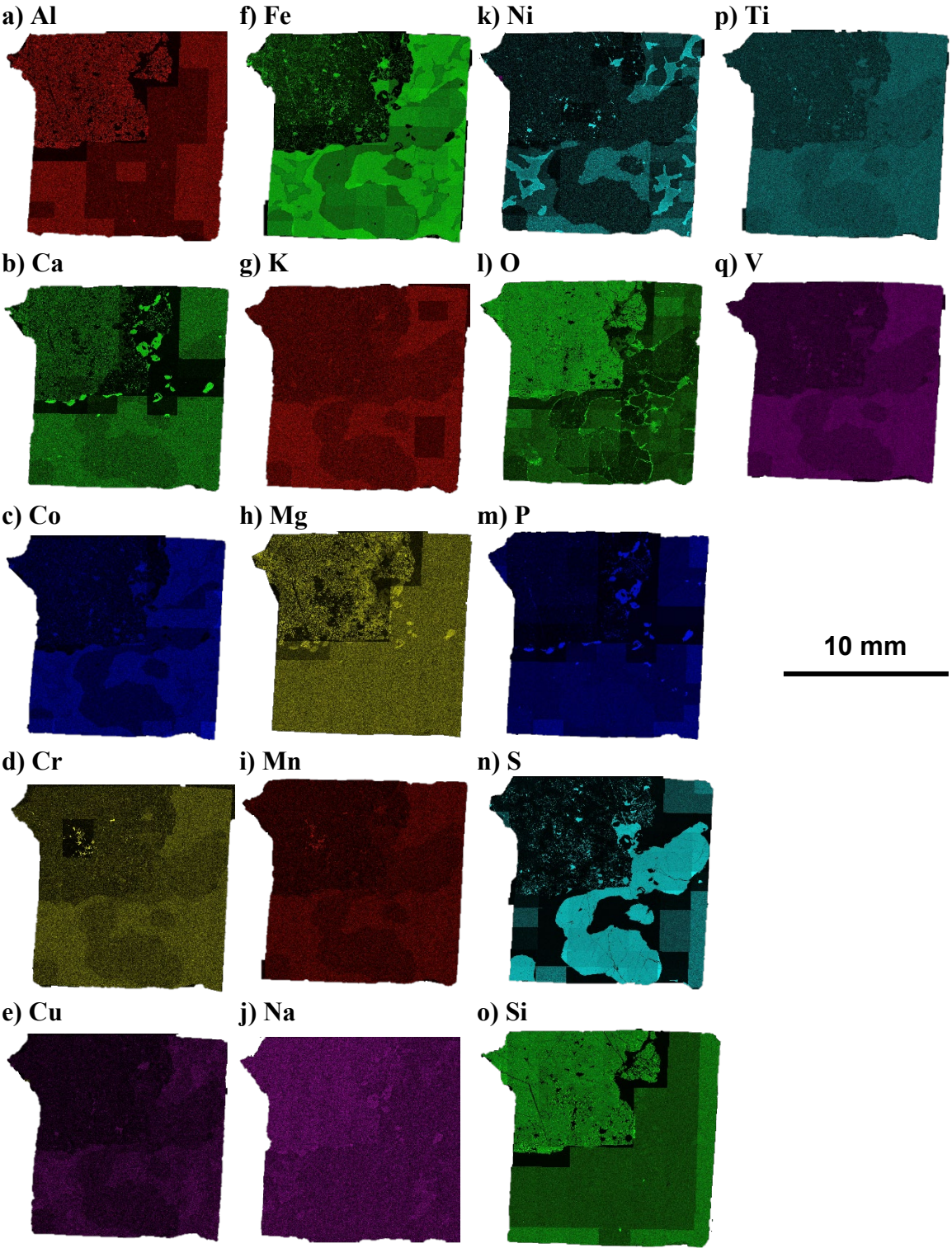

F-a) Chaunskij – Al

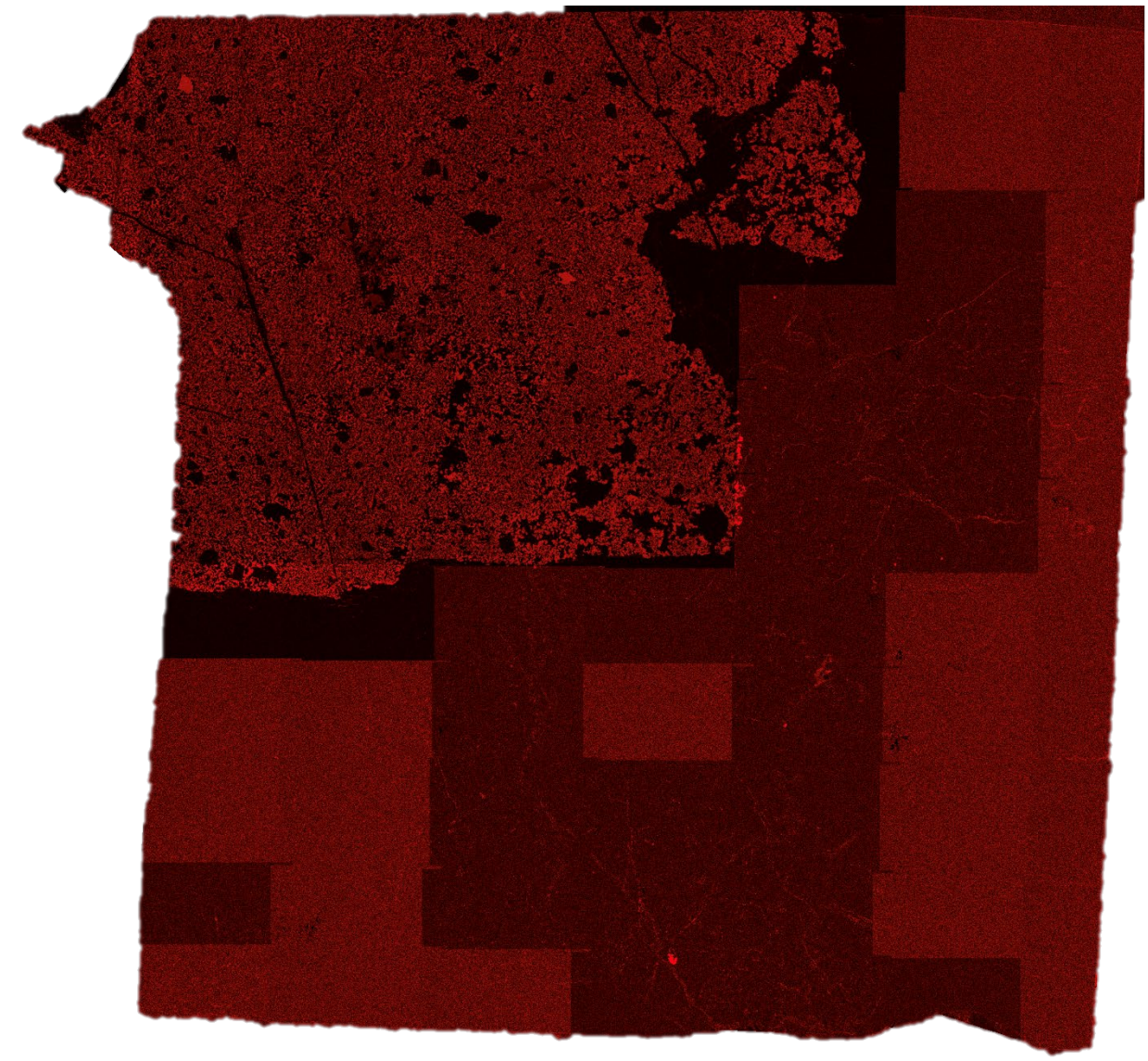

5 mm

F-b) Chaunskij – Ca

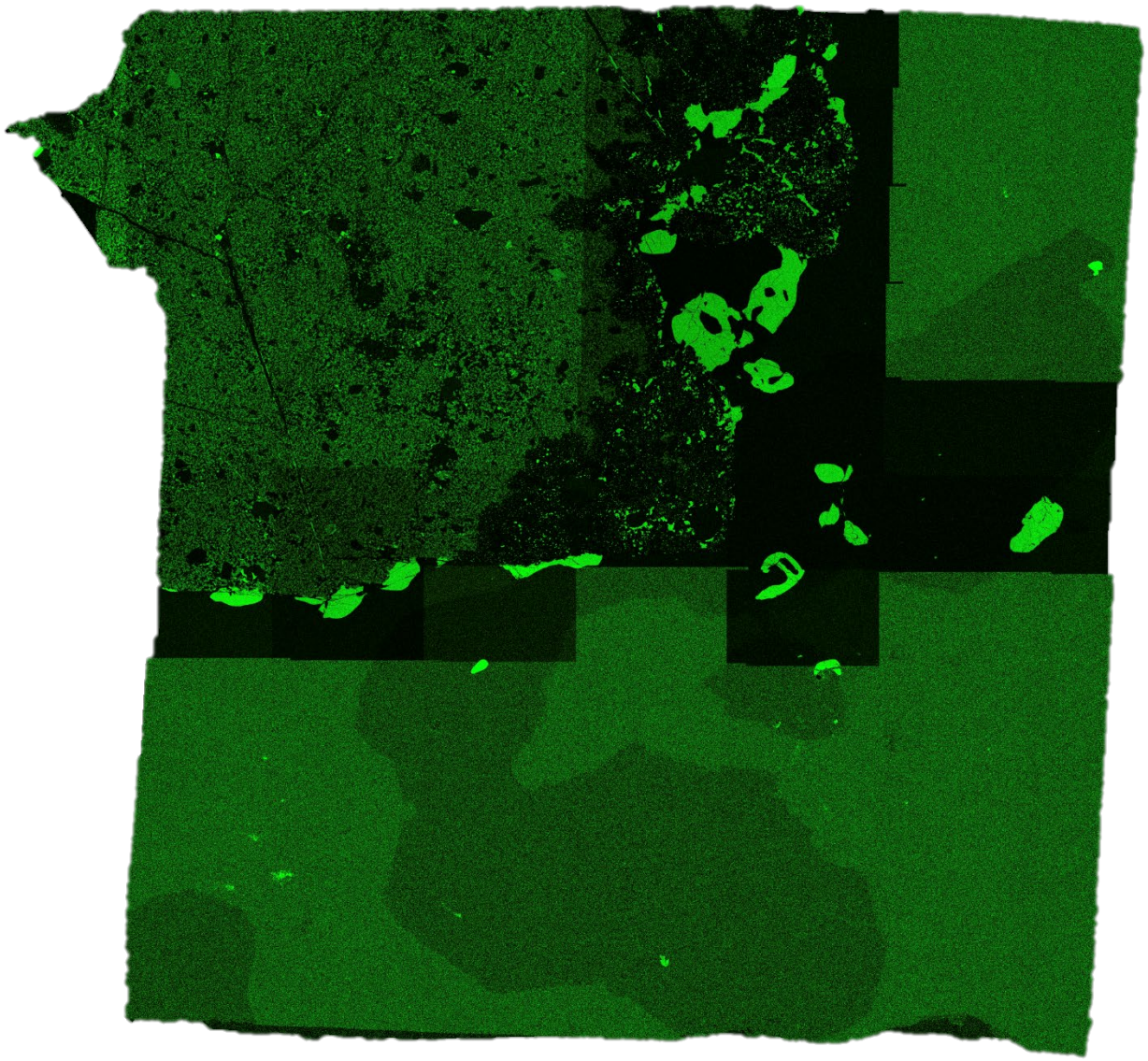

5 mm

F-c) Chaunskij – Co

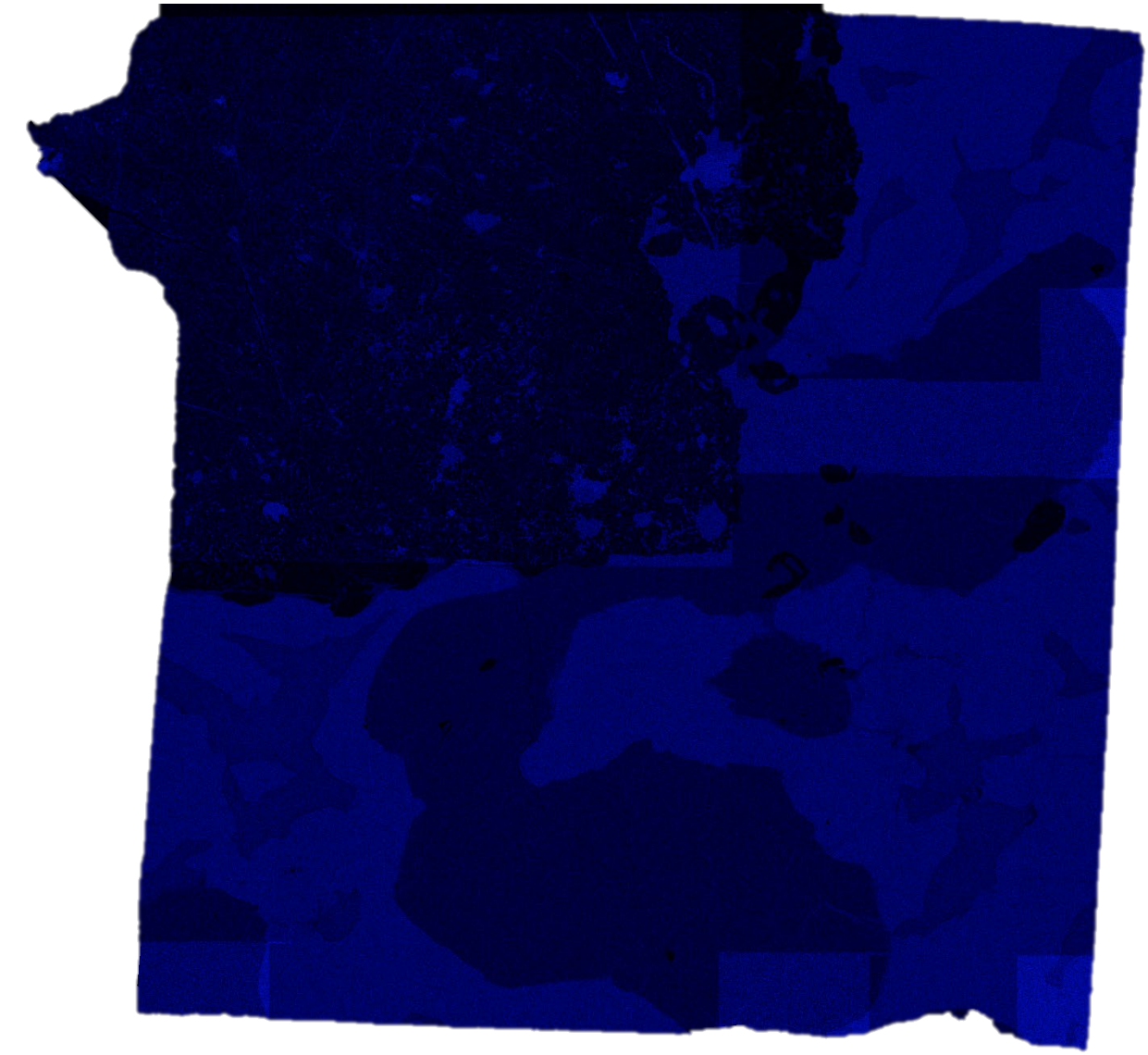

5 mm

F-d) Chaunskij – Cr

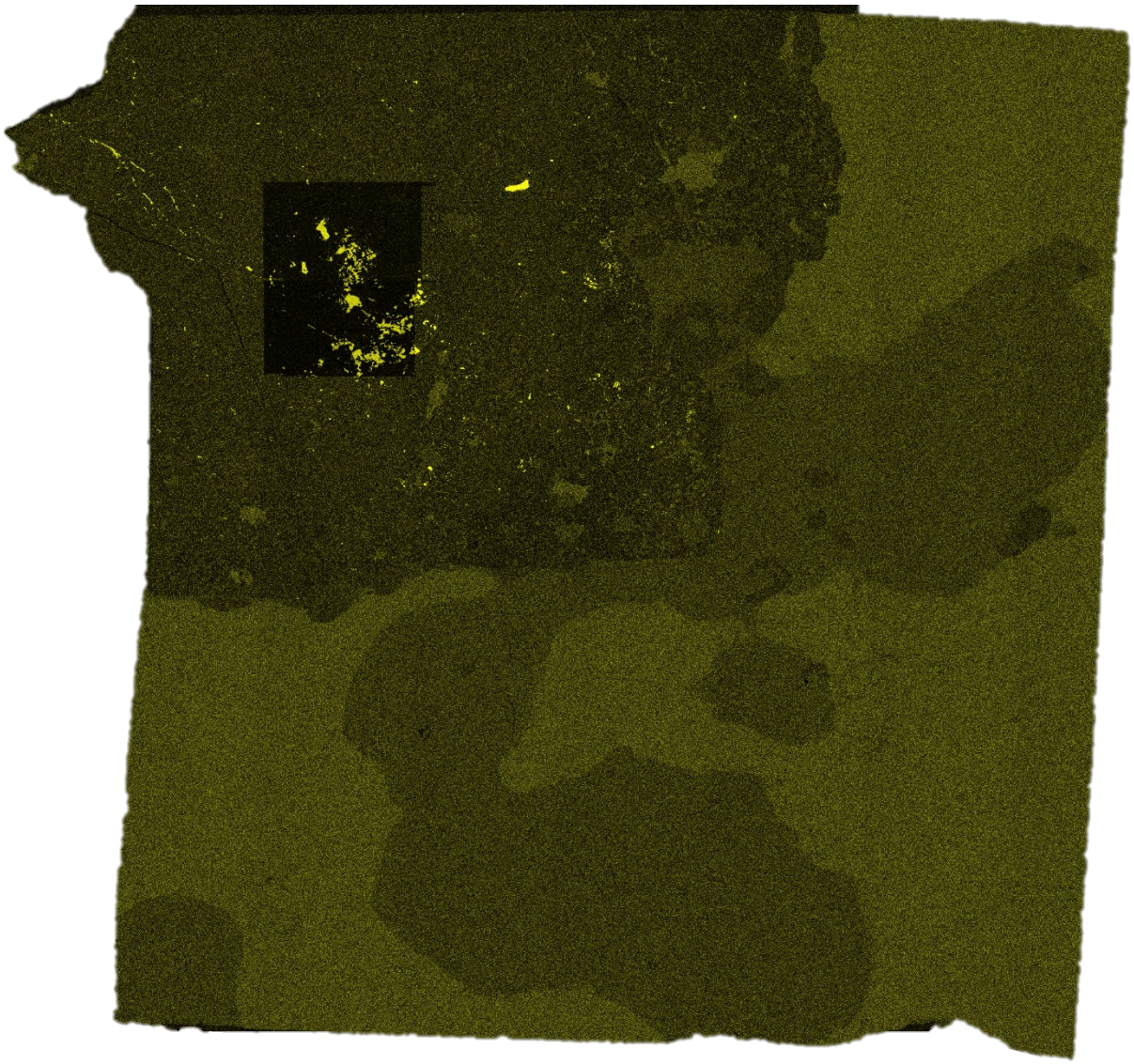

5 mm

F-e) Chaunskij – Cu

5 mm

F-f) Chaunskij – Fe

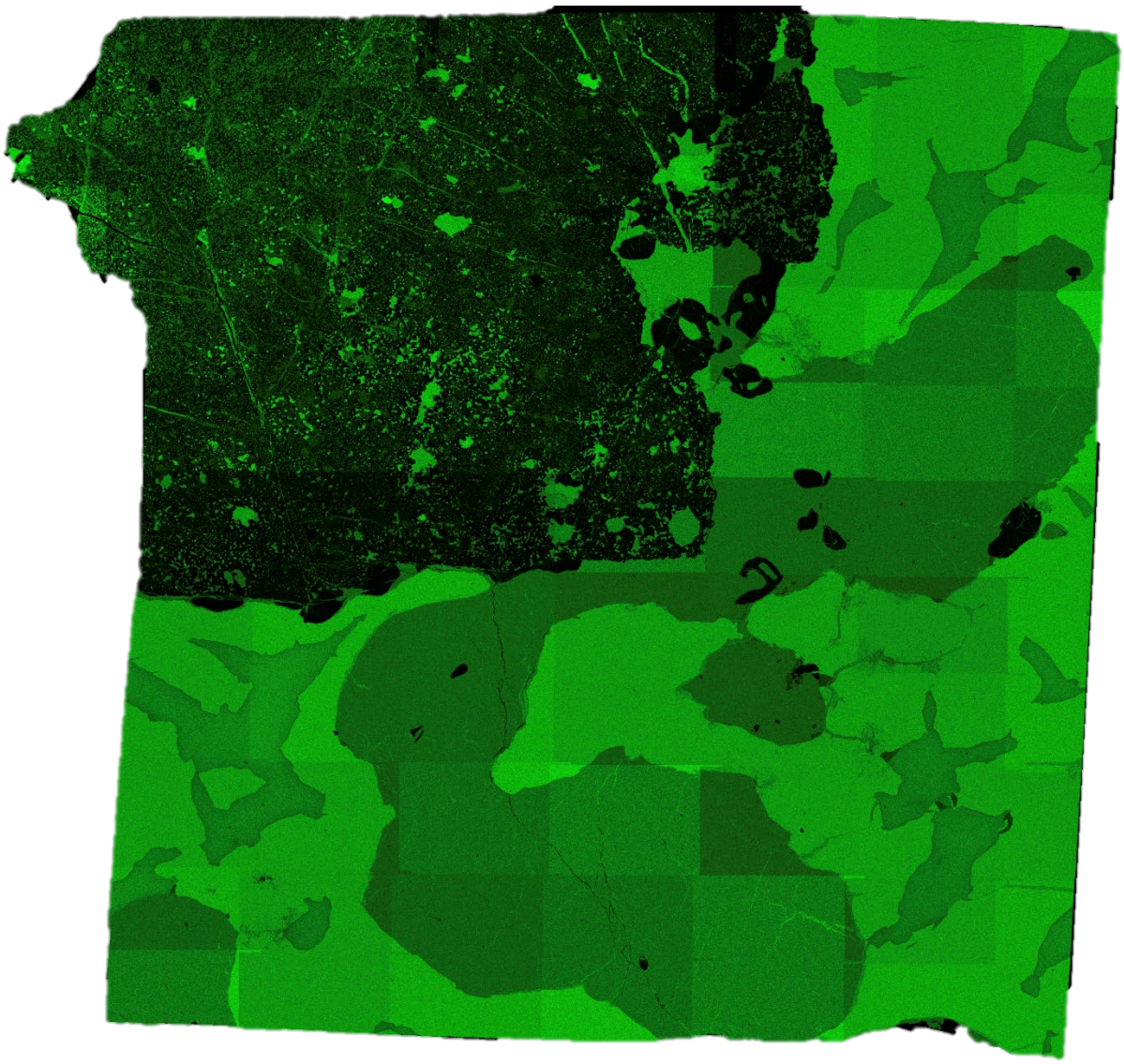

5 mm

F-g) Chaunskij – K

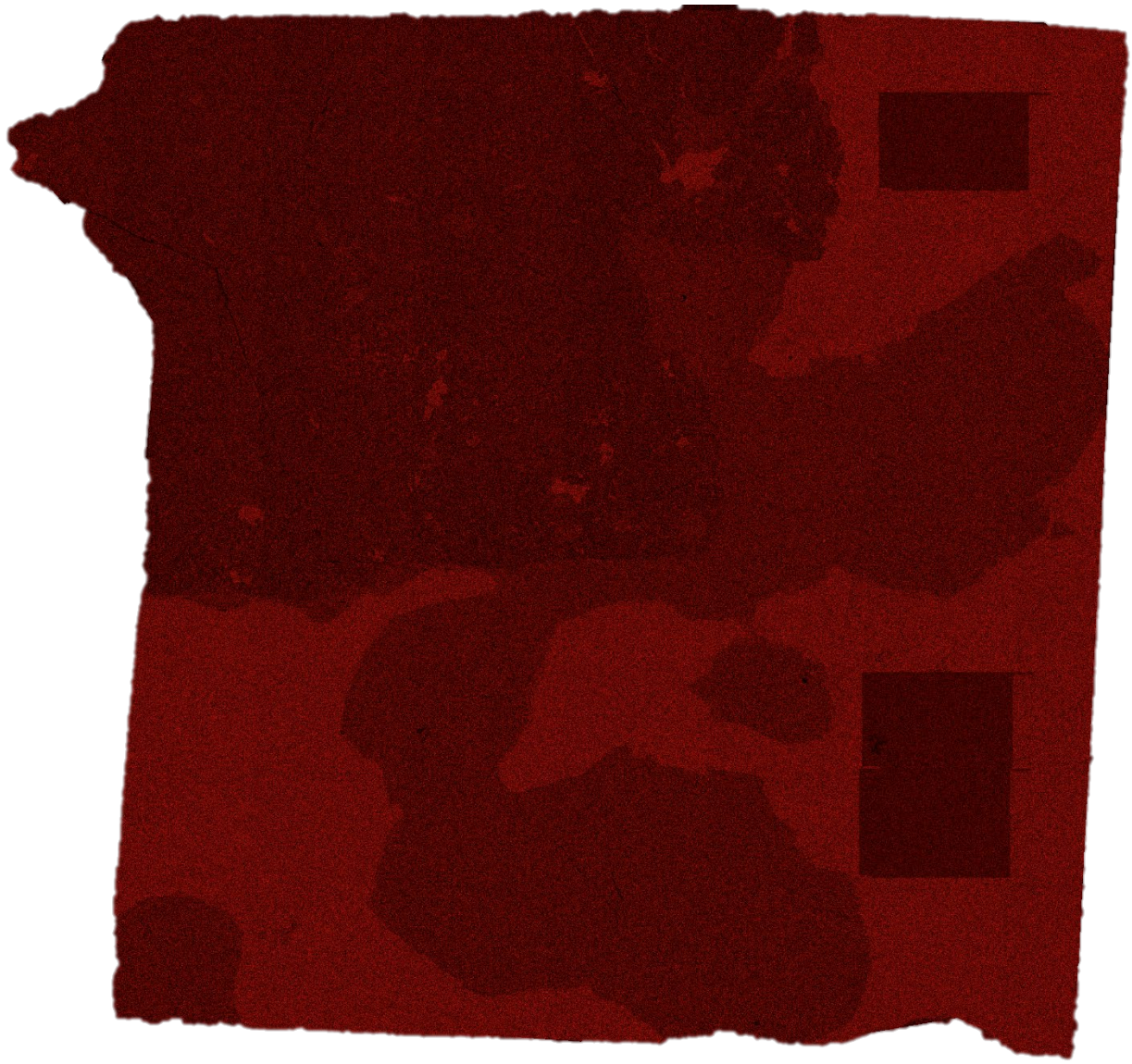

F-h) Chaunskij – Mg

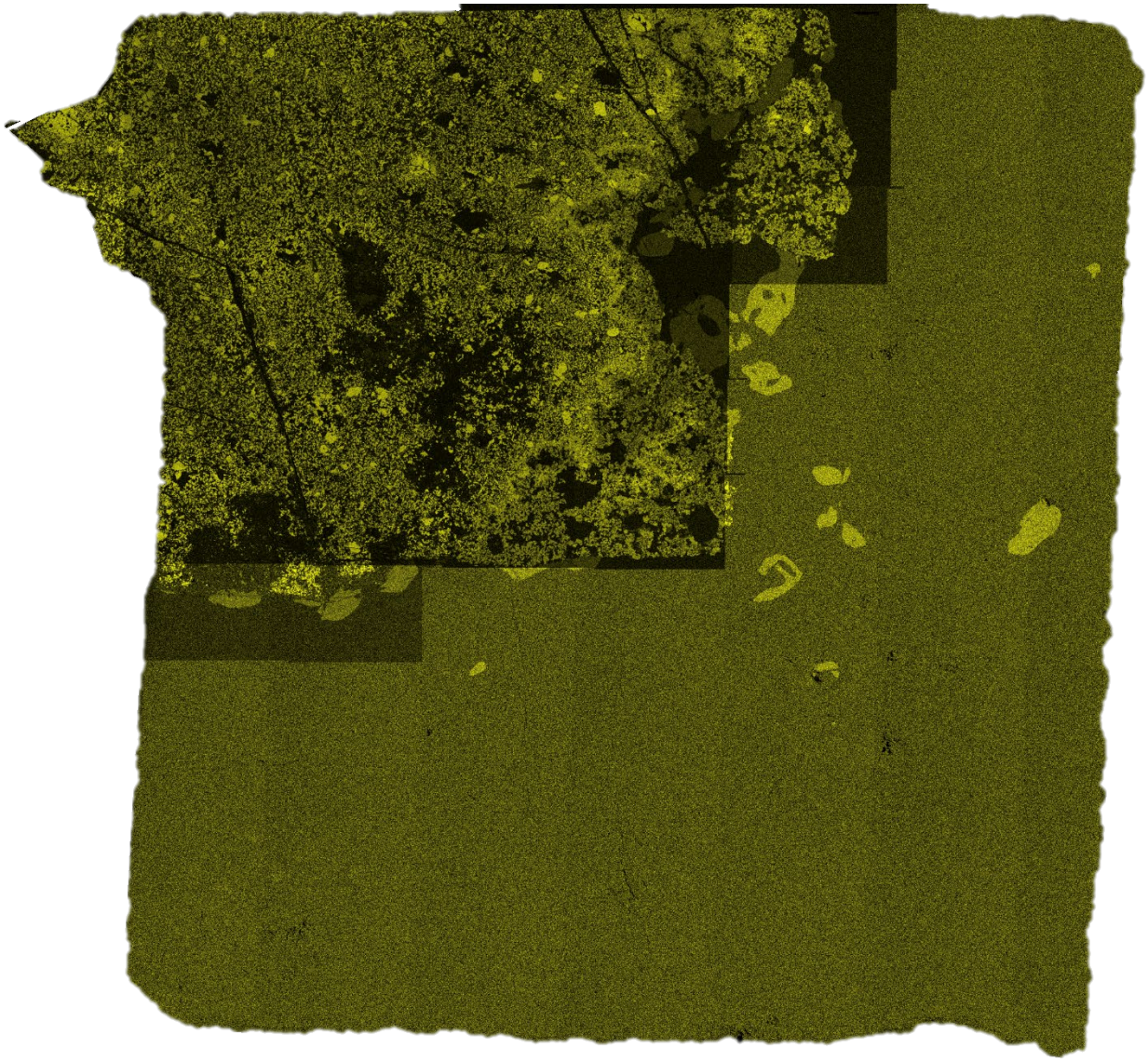

5 mm

F-i) Chaunskij – Mn

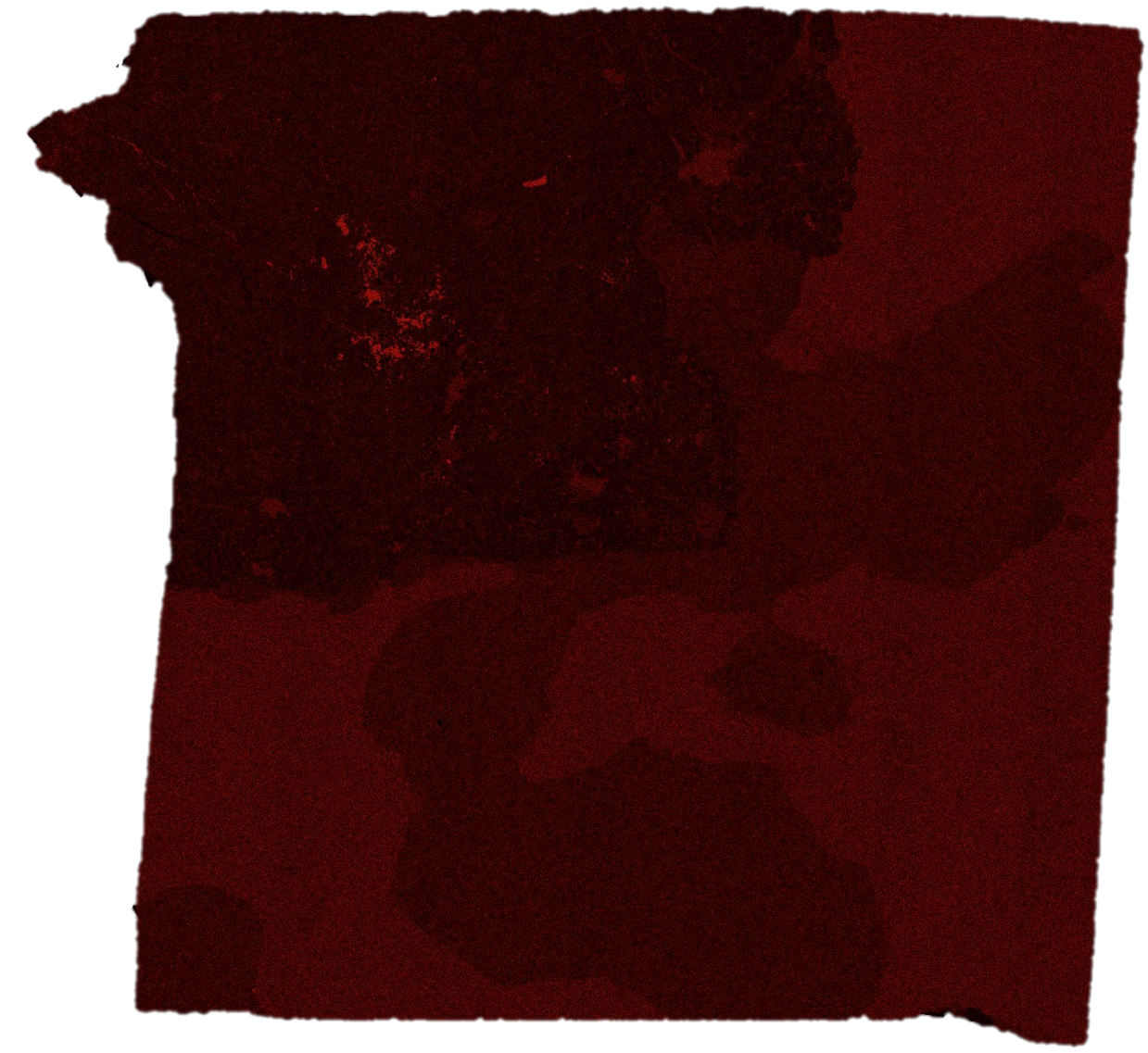

5 mm

F-j) Chaunskij – Na

5 mm

F-k) Chaunskij – Ni

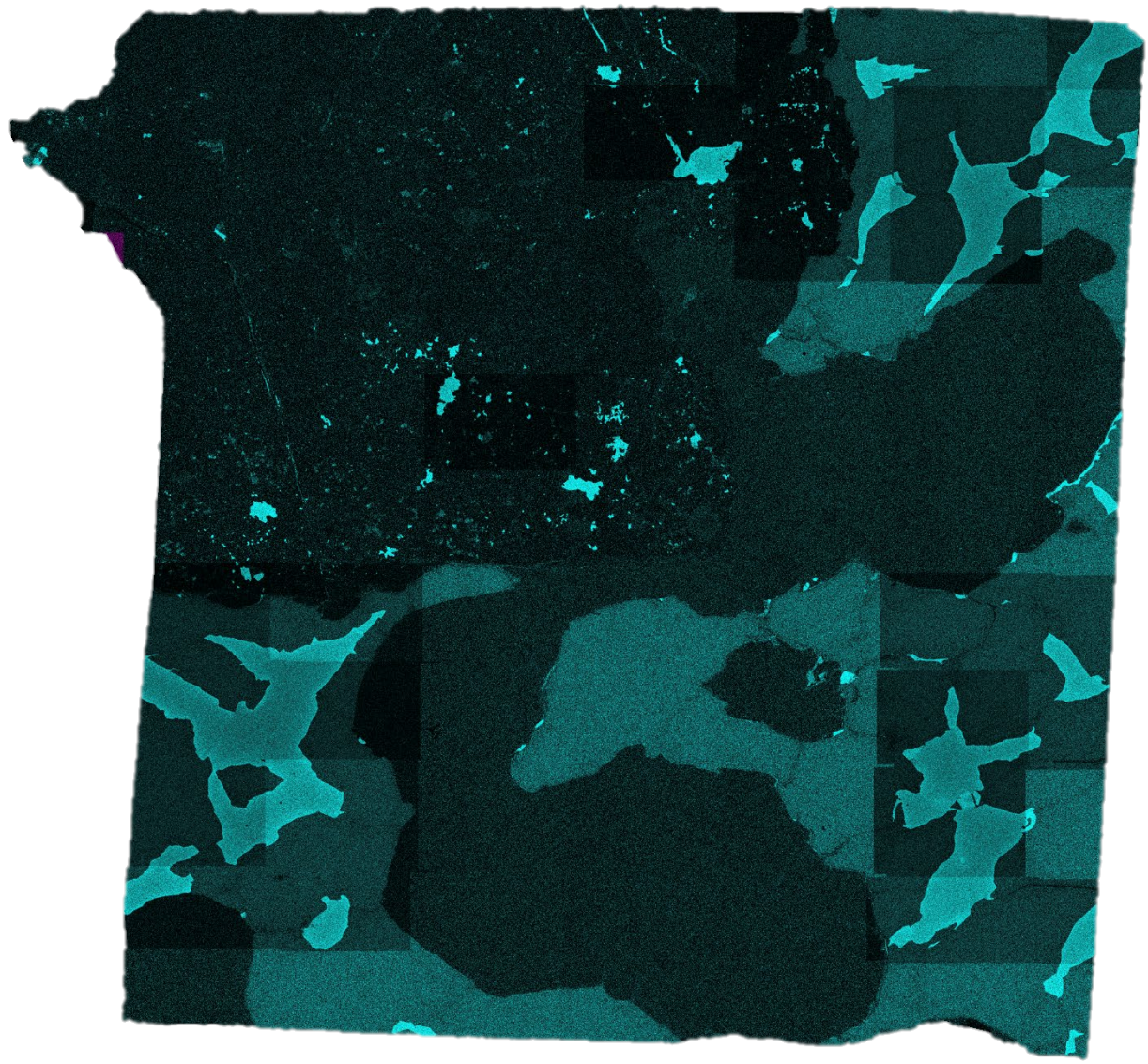

5 mm

F-l) Chaunskij – O

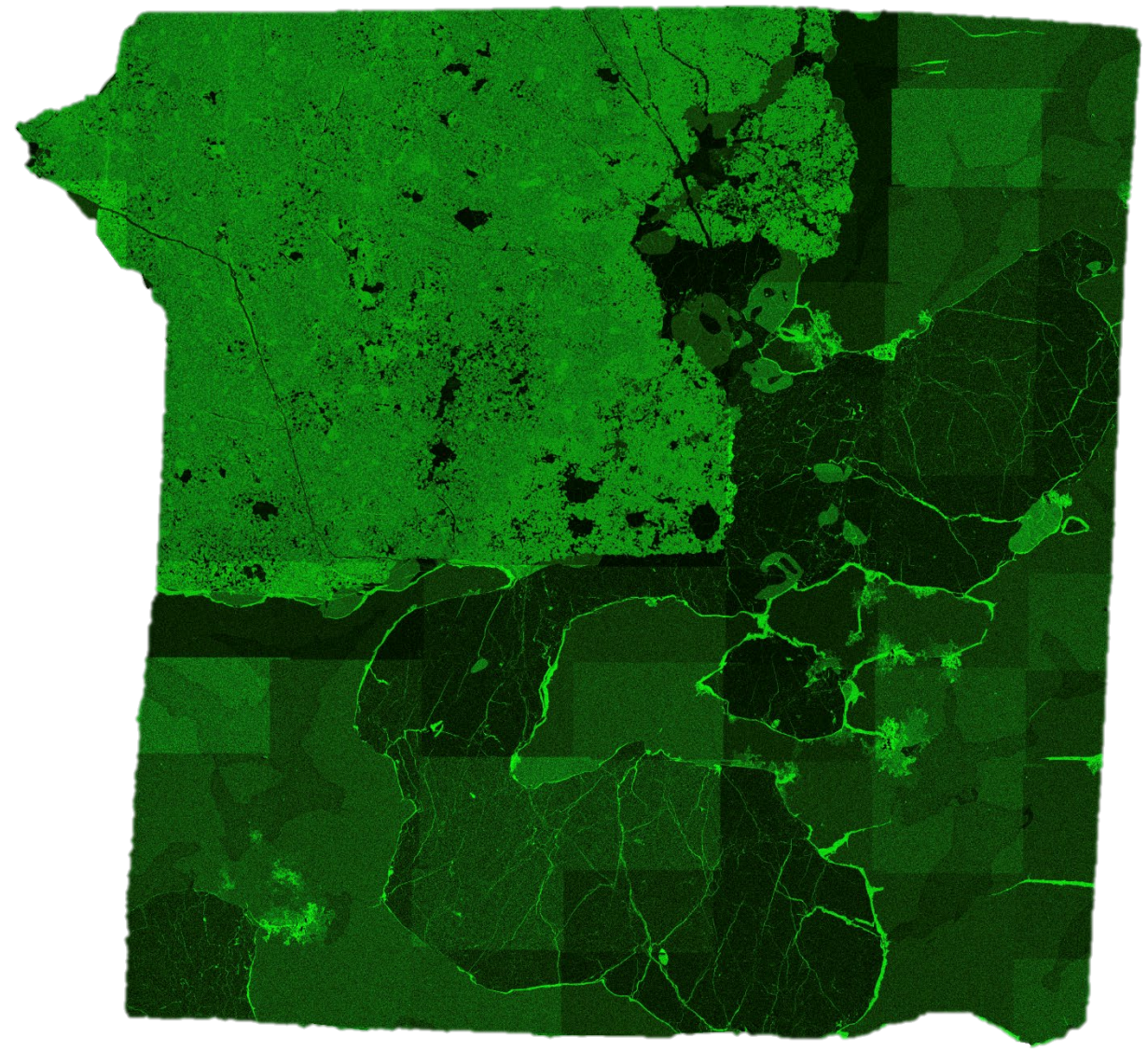

F-m) Chaunskij – P

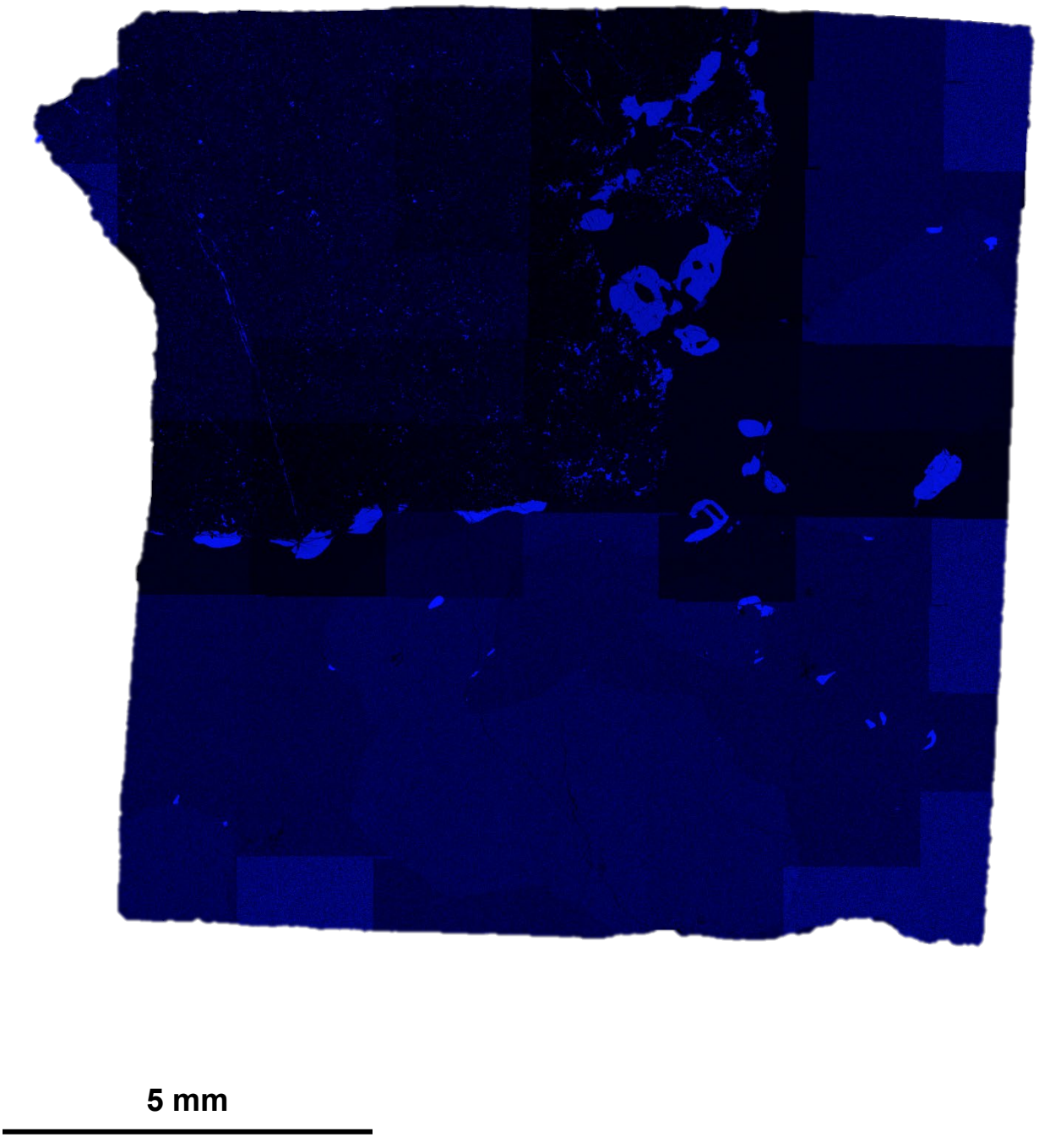

F-n) Chaunskij – S

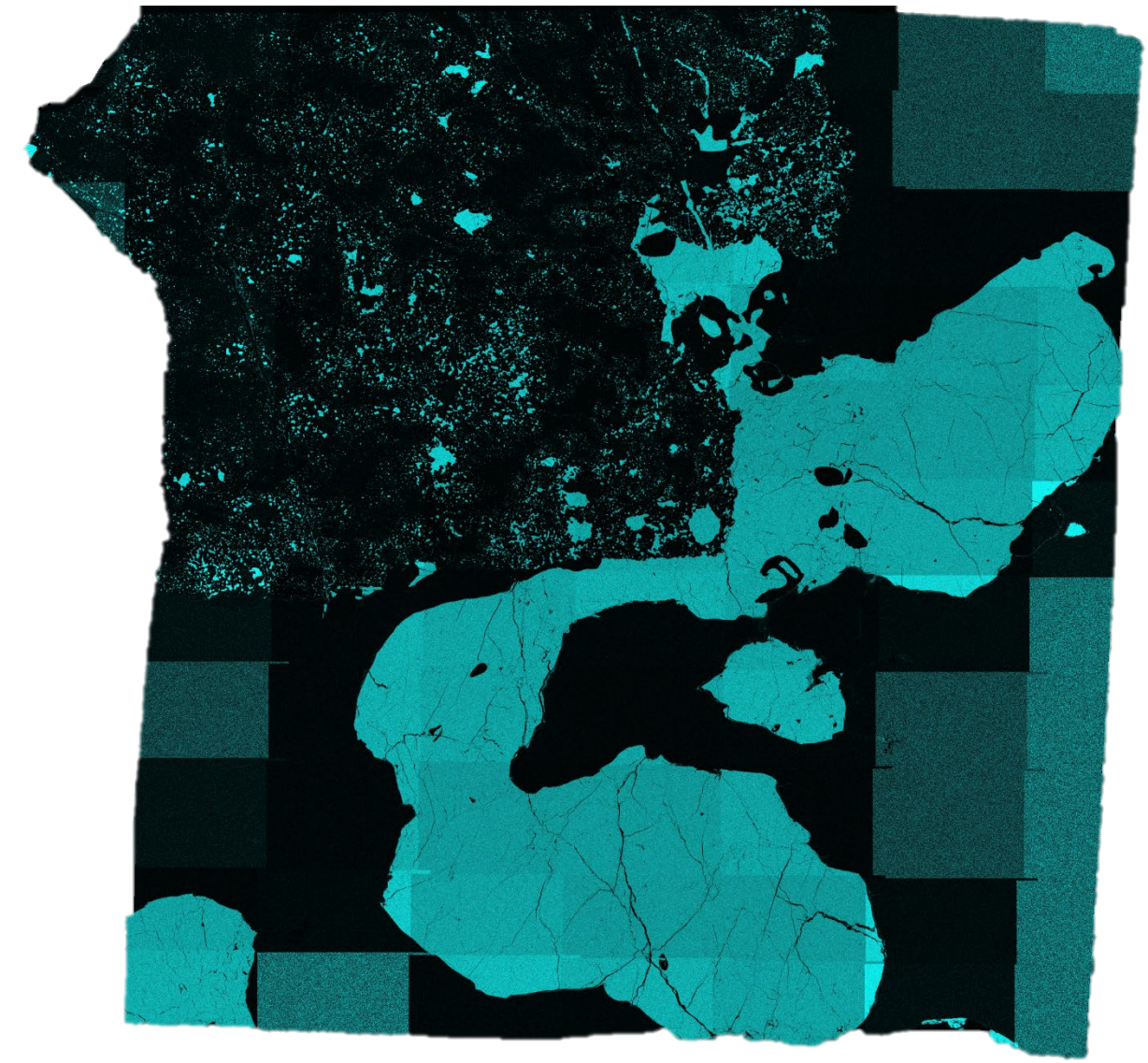

5 mm

F-o) Chaunskij – Si

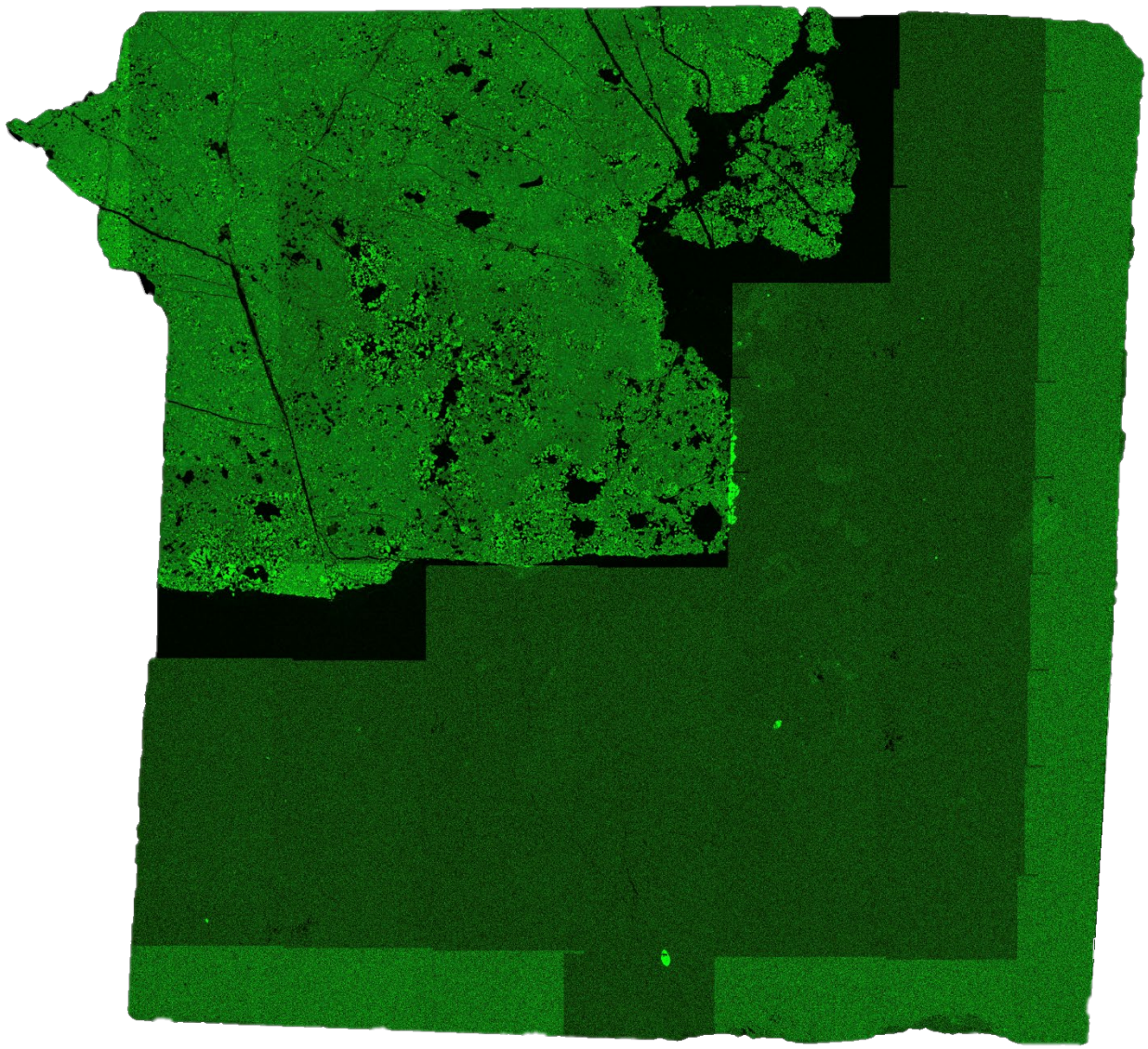

F-p) Chaunskij – Ti

F-q) Chaunskij – V

Vita

Personal	Lindsay Caves Born February 1, 1994, Knoxville, TN Daughter of Ken and Laura Caves
Education	Texas Christianity University, Geology, M.S. 2019 Advisor: Dr. Rhiannon G. Mayne University of Tennessee-Knoxville, Geology and Environmental Studies- Geology conc., B.S. 2016 Advisors: Dr. Harry Y. McSween and Dr. Lawrence A. Taylor
Experience	Served as an executive secretary for a NASA mission review panel, Spring 2019 Teaching Assistant, Texas Christian University, Fall 2018-Spring 2019 Field Assistant, Texas Christian University, Summer 2018

MESOSIDERITE FORMATION: REDOX FROM THE METAL PERSPECTIVE

By Lindsay Caves, M.S., 2019
Department of Geological Sciences
Texas Christian University

Thesis Advisor: Rhiannon Mayne, Associate Professor of Environmental Science

Richard Hanson, Professor of Geology

Timothy McCoy, Geologist and Curator of Meteorites
(Smithsonian National Museum of Natural History)

While mesosiderite formation is not well understood, it is widely believed that redox reactions occurred during metal-silicate mixing. Previous studies focused on evaluating redox reactions by studying the silicates within mesosiderites, but little attention has been given to the metal for complementary evidence of such processes. Here, the evidence for redox reactions in the metal portion of mesosiderites is evaluated. Five mesosiderites were chosen that span the range of petrologic classes (A, B, C, Anomalous) and that have experienced the lowest grade of metamorphism (subgroup 1). The metal compositions of both matrix metal and clast (nodule) metal were compared and examined for evidence of redox reactions. A deletion of P in the matrix metal relative to clast metal was observed, which along with the FeO reduction in silicates noted by previous workers, indicates that redox reactions did occur during metal-silicate mixing. However, depletions of Cu and Mo in the matrix metal cannot be explained by these reactions and require other processes, such as sulfidization, to have occurred. Metal clast compositions produce a trend that is suggestive of fractional crystallization; however, it is unlikely that the whole metallic portion sampled by these meteorites experienced fractional crystallization. It appears to be constrained to the anomalous samples measured here. This trend could be explained by isolated metallic masses that underwent fractional crystallization before mixing or by hit-and-run collisions that produced metallic masses that ranged in size.